

CHARACTERIZING THE EFFECT OF NEUTRON-RICHNESS ON THE REACTION
DYNAMICS IN CHROMIUM AND TUNGSTEN SYSTEMS.

By

Kalee Michelle Hammerton

A DISSERTATION

Submitted to
Michigan State University
in partial fulfillment of the requirements
for the degree of

Chemistry — Doctor of Philosophy

2017

ABSTRACT

CHARACTERIZING THE EFFECT OF NEUTRON-RICHNESS ON THE REACTION DYNAMICS IN CHROMIUM AND TUNGSTEN SYSTEMS.

By

Kalee Michelle Hammerton

Superheavy elements are primarily formed through heavy-ion fusion reactions [1, 2, 3]. Formation of a fully equilibrated compound nucleus is a critical step in the heavy-ion fusion reaction mechanism but can be hindered by orders of magnitude by quasifission, a process in which the dinuclear system breaks apart prior to full equilibration [1, 4, 5, 6, 7, 8]. To provide a complete description of heavy-ion fusion it is important to characterize the quasifission process. The interplay between the fusion-fission and quasifission reaction channels was explored by measuring mass distributions in eight different combinations of Cr + W reactions, with varying neutron-richness, at the Australian National University. The reactions were measured in two energy regimes: one at center-of-mass energies ($E_{c.m.}$) 13% above the Bass interaction barrier [9] and one at 52.0 MeV of excitation energy in the compound nucleus (E_{CN}^*). For the systems measured at the higher energies at $E_{c.m.}/V_{Bass} = 1.13$ the dependence on the neutron-richness is clear and an increase in the neutron-richness of the entrance channel decreases the likelihood of quasifission [10]. However, for the reactions at $E_{CN}^* = 52.0$ MeV, the dependence is less clear and additional factors are shown to play a vital role, especially the influence of deformation on the effective fusion barrier. The present work demonstrates that quasifission is an important process in competition with fusion in reactions with intermediate mass projectiles, particularly with more neutron-rich systems.

for my family

ACKNOWLEDGMENTS

This work was accomplished because of the support I received from many people. It is impossible to thank everyone so here I will highlight a few key contributors.

First and foremost, I would like to thank my advisor Dave Morrissey. Words cannot describe how much I appreciate you taking on this project with me midway through and helping me complete it all in 3.5 years. Thanks for reminding me to keep the cart behind the horse and for helping me improve my writing skills.

I would like to thank my committee members, Paul Mantica, Wolfie Mittag, and Sean Liddick for their support and suggestions. Additionally, I would like to thank Brad Sherrill for being a great mentor and encouraging me to explore policy and start the nuclear policy working group chapter at MSU. I would also like to acknowledge Michigan State University, the Department of Chemistry, the NSCL, the National Science Foundation, the NSSC, and IGCC for their financial support of this work.

This work would not have been possible without the support of my research group Adi Wakhle and Krystin Stiefel. Thanks for being there through all of our craziness, including experiments. Krystin, thanks for being an amazing friend and great roommate through some tough times in grad school. Thanks for all of your help along the way. Adi, thanks for being there to answer all of my many questions about the ANU set-up and experiment. I would also like to thank Zach Kohley for proposing the idea for the experiment and giving me the opportunity to be involved so early in my career.

John Yurkon, thanks so much for your patience in teaching me about making detectors. Some of my best grad school memories come from building detectors. The support from the NSCL faculty and staff was unparalleled. Thank you all for looking out for me.

Grad school would not have been the same with the awesome Nuclear Chemistry group: Becky Lewis, Nicki Larson, Katie Childers, Chris Prokop, Kortney Cooper, Ben Crider, and Paige Able. Thanks for great Friday lunches and some memorable Wine Nights. I will miss being a part of this community! Becky, thanks for being an awesome friend, listening to me vent, acting as a sounding board for all sorts of ideas, and always being up for a trip to Starbucks! Nicki, thanks for being a great friend, teaching me to be a better swimmer, and helping me sort through all of the grad school requirements. Chris, thanks for being a great friend and office mate and always pushing me to be my best throughout grad school. Thanks to all of the NSCL grad students, including Wei Jia Ong, Amy Lovell, Jenna Smith, Chris Morse, and Zach Meisel for being amazing friends.

Thanks to the MSU running group (Jill Berryman, Renan Fontus, and Jon Bonofiglio, and Michelle Kuchera) for helping me run off the stress of grad school stress. Jill thanks for listening and offering great advice on navigating grad school. Michelle Kuchera, thanks for pushing me to be a better runner and for not accepting any of my many excuses as to why we should not run all through Michigan winters! Our long run chats, track Tuesdays, and trail therapy are some of my favorite grad school memories.

Thanks to the ANU group, David Hinde and Nanda Dasgupta for all of your support in the experiment and analysis. This work would not have been possible without the amazing staff at the ANU Heavy Ion Accelerator Facility. Thanks to Ian Carter and Joe Walshe for being great friends and entertaining me while at ANU.

Grad school would not have been possible without my amazing family. Thanks to the Fenkers for many interesting nuclear physics discussions and help. Kelsey, thanks for showing me grad school was an option and getting me started on a good path.

I would not be where I am today with out the amazing support of my parents! You

definitely set me up for success. Thanks for never letting me sell my self short and pushing me to be who I am today. I could not do all of this without your support.

Finally, Alex, grad school would not have been possible without you. Thanks for listening to all of my stress. Thanks for being my biggest cheerleader. Thanks for staying positive and making all the dinners during my oral exam. Thanks for being there when I needed to escape for grad school life.

TABLE OF CONTENTS

LIST OF TABLES	x
LIST OF FIGURES	xii
Chapter 1 Introduction	1
1.1 Superheavy Elements	1
1.2 Heavy-Ion Fusion Reactions	3
1.2.1 Capture, σ_{cap}	5
1.2.1.1 Angular Momentum	5
1.2.1.2 Impact Parameter	7
1.2.1.3 Bass Barrier	9
1.2.2 Survival against Fission, W_{sur}	10
1.2.2.1 Liquid Drop Model	11
1.2.3 Probability of forming a Compound Nucleus, P_{CN}	13
1.2.3.1 Quasifission	14
1.3 Experimental Signatures of Quasifission	14
1.3.1 Mass Distributions	15
1.3.1.1 Excitation Energy and Fusion-Fission	20
1.3.2 Angular Distributions	21
1.3.3 Mass-Angle Distributions	22
1.3.3.1 Types of Mass Angle Distributions	24
1.3.4 Entrance Channel Energy and Quasifission	29
1.4 Heavy-Ion Fusion Reactions with Neutron-rich Rare Isotope Beams	30
1.5 Organization of Dissertation	31
Chapter 2 Experimental Details	32
2.1 System Selection	32
2.1.1 Two Energy Regimes	33
2.1.2 Cr + W Systems	35
2.2 The ANU Heavy-Ion Accelerator Facility	36
2.2.1 Ion Source	39
2.2.2 14 UD Pelletron	42
2.2.3 Superconducting LINAC	44
2.3 The CUBE Detector System	44
2.3.1 MWPCs	46
2.3.2 Structure of the CUBE MWPCs	46
Chapter 3 Data Analysis Techniques	49
3.1 Coordinate System Definition	49
3.2 Position Information	53

3.2.1	Position Calibrations	53
3.2.2	Transformation Among the Coordinate Systems	60
3.3	Timing Information	64
3.4	Kinematic Coincidence Method	69
3.5	Velocity Determination	73
3.5.1	Using Φ to demonstrate v_{perp} is zero	74
3.5.2	Calculating M_R	75
3.5.3	Energy Calculation	78
3.5.4	Total Kinetic Energy Gates	79
3.5.5	Determination of M_R and $\theta_{c.m.}$	81
Chapter 4	Results	82
4.1	Cr + W: $E_{c.m.}/V_B = 1.13$	82
4.1.1	Mass-Angle Distributions	82
4.1.1.1	Symmetrization	87
4.1.1.2	Symmetrized MADs for Cr + W systems	88
4.1.2	Mass Distributions	93
4.1.2.1	Determination of Mass Width from Mass Distribution	93
4.1.2.2	Statistical Approximation of Pure Fusion-Fission	96
4.1.3	Angular Distributions	100
4.1.3.1	Normalization of the Angular Distribution	103
4.1.3.2	Quantities needed in Angular Distribution Determination	106
4.1.3.3	Relative Detector Efficiencies	109
4.2	Cr + W: $E^* = 52.0$ MeV	111
4.2.1	Mass-Angle Distributions	114
4.2.2	Mass Distributions	114
4.2.2.1	Curvature Analysis Techniques	123
4.2.2.2	Verification with $E_{c.m.}/V_B = 1.13$ systems	123
4.2.3	Angular Distributions	124
Chapter 5	Discussion	128
5.1	Bohr Independence Hypothesis	128
5.2	Cr + W: $E_{c.m.}/V_B = 1.13$	130
5.2.1	Fissility and Mass Asymmetry	132
5.2.2	Mass Widths Compared to Theoretical Calculations	135
5.2.3	Comparison with Analytical Calculations of P_{CN}	138
5.2.3.1	Armbruster's Analytical Description of P_{CN}	138
5.2.3.2	Zagrebaev's Analytical Description of P_{CN}	140
5.2.3.3	Siwek-Wilczynska's Analytical Description of P_{CN}	141
5.2.3.4	Comparison of Results of Analytical Calculations	142
5.3	Cr + W: $E^* = 52.0$ MeV	142
5.3.1	Angular Momentum	144
5.3.2	Rotational Energy	145
5.3.3	Effect of Nuclear Orientations	147
5.3.3.1	Shape Evolution and Mass Asymmetry	149

5.4	Angular Distributions	152
5.5	Previously Studied Reactions forming ^{238}Cf and ^{240}Cf	156
Chapter 6	Conclusions	164
BIBLIOGRAPHY	167

LIST OF TABLES

Table 2.1:	Chromium and tungsten isotopic information including percent abundances (half-lives), β_2 values, and any magic numbers in the nucleus.	34
Table 2.2:	Tungsten target and carbon backing thickness, and reaction [84] . . .	34
Table 2.3:	Cr + W systems, compound nuclei, relative change in neutrons (ΔN), fusion Q value (Q_{fus}), Bass interaction barrier (V_B) [9], $E_{\text{c.m.}}$ for both energy regimes	39
Table 2.4:	Cr + W systems, compound nuclei, relative change in neutrons (ΔN), $E_{\text{c.m.}}$, E_{CN}^* , interaction cross section (mb) [88], l_{max} , and l_{crit} [88] for both energy regimes	40
Table 3.1:	Coordinates in each of the three systems defined in this work for the center and four positions around the edge of the two MWPCs. The edge positions listed are at the center of the edges of the top, bottom, left, and right sides of the active area of the two MWPCs. In the Cartesian systems and in r in the spherical system the values are give in mm. In the spherical coordinate system the values θ and Φ are given in degrees.	53
Table 3.2:	The experimentally determined positions in channel numbers and the defined positions in mm for the edges of the active area of the Front and Back MWPCs.	55
Table 3.3:	Slopes and Intercepts determined for the linear conversion from channel number to millimeters for the MWPCs.	60
Table 3.4:	Component definitions for the projections $v_{i,\text{lab}}$ along the X and Z axes in the $(X, 0, Z)$ plane and along the X axis in the $(X, Y, 0)$ plane. The components in the $(X, 0, Z)$ plane are defined relative to θ , while X_Φ is defined in the $(X, Y, 0)$ plane relative to Φ . See text for full descriptions of planes and angles.	71
Table 4.1:	Calculated values used in the determination of E_{sci}^*	98
Table 4.2:	Calculated values used in the determination of $E_{\text{pre}}^{\text{sci}}$	99
Table 4.3:	Calculated values used in the determination of the $E_{\text{rot}}^{\text{sci}}$	99

Table 4.4:	Experimental mass widths σ_{exp} , statistical estimate for the pure fusion-fission mass width σ_{ff} , and the ratio of $\sigma_{\text{exp}}/\sigma_{\text{ff}}$ (upper limit of P_{CN}) for all 8 systems measured at the same $E_{\text{c.m.}}/V_{\text{B}} = 1.13$	100
Table 4.5:	The number of counts in the two monitors (M), the number of pulser events in the Back MWPC (P), and the scalers values for the monitors (M_{scal}) and pulser (P_{scal}) from the measurement of $^{50}\text{Cr} + ^{180}\text{W}$ as an example and the calibration measurement of $^{50}\text{Cr} + ^{184}\text{W}$	111
Table 4.6:	Relative peak intrinsic efficiencies of the Back MWPC and the Si monitor detectors for all systems measured in the present work relative to the calibration run of $^{50}\text{Cr} + ^{184}\text{W} \rightarrow ^{234}\text{Cf}$ at $E_{\text{lab}} = 186.0$ MeV.	114
Table 4.7:	Curvature parameters and errors determined for all 8 systems measured at center-of-mass energies resulting in compound nuclei with $E_{\text{CN}} = 52.0$ MeV.	124
Table 5.1:	Compound nuclear fissility (χ_{CN}) and mass asymmetry (α) values of each of the eight Cr+W systems presented in this work. The determined upper limits of P_{CN} , capture cross section, and evaporation residue cross sections are also included.	135
Table 5.2:	Average radii, β_2 values [86], semi-major radii, and semi-minor radii determined for chromium and tungsten isotopes considered in the present work.	152
Table 5.3:	Bass interaction barriers [9] for the average and limiting orientations determined for the Cr + W reactions considered in the present work.	154
Table 5.4:	Entrance channel system, fissility (χ_{CN}), mass asymmetry (α), center-of-mass energy, energy relative to the interaction barrier [9] ($E_{\text{c.m.}} / V_{\text{B}}$), excitation energy (E^*), and upper limit of P_{CN} for the relevant systems measured in the present work and the systems previously measured at ANU where the compound nucleus formed was ^{238}Cf or ^{240}Cf	158

LIST OF FIGURES

Figure 1.1:	Illustration of an example heavy-ion fusion reaction showing various reaction channels. Key points in the reaction path are emphasized by the dashed lines. The arrows indicate the progression of the reaction with time.	4
Figure 1.2:	Illustration of three possible reaction outcomes from a heavy-ion reaction. Panel A depicts elastic scattering, Panel B depicts deep inelastic scattering, and Panel C depicts capture.	6
Figure 1.3:	Illustration of the cross section of a heavy-ion reaction as a function of angular momentum. The black, dashed line represents the line $\sigma = \pi\lambda^2(2l + 1)$. The various hashed regions indicate the various angular momentum values where different processes are prominent. The most prominent type of reaction in each angular momentum region is indicated. Four different angular momentum values are called out (l_{crit} , l_f , l_D , and l_{max}). See text for the definition of each of the indicated angular momentum values. Adapted from [32]	8
Figure 1.4:	Cartoon example of the definition of impact parameter. Panel A shows a side view of a heavy-ion collision. Panel B shows a beam view of a collision. As presented in the cartoon, the dark blue sphere is the target and the light blue sphere is the projectile.	9
Figure 1.5:	Illustration of a mass distribution. The various circles indicate the exit channel fragments expected at various mass ratios. See text for explanation.	16
Figure 1.6:	Mass distribution deduced from the reaction of $^{12}\text{C} + ^{208}\text{Pb}$ at $E_{\text{lab}} = 66.0$ MeV [47].	18
Figure 1.7:	Mass distribution deduced from the reaction of $^{48}\text{Ti} + ^{192}\text{Os}$ at $E_{\text{lab}} = 259.9$ MeV [46].	19
Figure 1.8:	Mass distributions reported in [48] from the reaction of helium and uranium-233. Reprinted figure with permission from [48] Copyright (1961) by the American Physical Society. http://dx.doi.org/10.1103/PhysRev.121.1415	20
Figure 1.9:	Schematic image of angular momentum coupling coordinate system for a deformed nucleus. Adapted from [51]	21

Figure 1.10:	The mass angle distribution previously deduced from the reaction of $^{12}\text{C} + ^{208}\text{Pb}$ at $E_{\text{lab}} = 66.0$ MeV [47].	24
Figure 1.11:	The mass angle distribution deduced from the reaction of $^{48}\text{Ti} + ^{192}\text{Os}$ at $E_{\text{lab}} = 259.9$ MeV [46]. The dashed, grey line is included to highlight the correlation between mass and angle.	25
Figure 1.12:	Three example quasifission reactions. Illustrating the influence of impact parameter of and angle of rotation of the mass and angle of the emitted fragments.	26
Figure 1.13:	Plot of the 42 MADs reported in [40]. In the top left corner, the MAD deduced from the measurement of $^{48}\text{Ti} + ^{170}\text{Er}$ at $E_{\text{lab}} = 225.0$ MeV is enlarged to highlight the axis labels. Systems that fall along the same vertical, red, dashed- or diagonal, blue, dashed-lines were formed with the same projectile or target, respectively. Systems along the same horizontal, black, dashed lines formed the same compound nucleus. Reprinted figure with permission from [40] Copyright (2013) by the American Physical Society. http://dx.doi.org/10.1103/PhysRevC.88.054618	27
Figure 1.14:	MADs representative of Types I, II, III as identified by Du Rietz <i>et al.</i> [40] are shown in Panels A, B, and C, respectively. The corresponding mass distributions are shown in Panels D, E, and F. Reprinted figure with permission from [40] Copyright (2013) by the American Physical Society. http://dx.doi.org/10.1103/PhysRevC.88.054618	28
Figure 1.15:	Z_{CN} as a function of $Z_{\text{p}}Z_{\text{t}}$ for the 42 reactions included in [40]. The identified boundaries between the Types of MADs are indicated by the solid, blue-and long-dashed, red-lines. Reprinted figure with permission from [40] Copyright (2013) by the American Physical Society. http://dx.doi.org/10.1103/PhysRevC.88.054618	29
Figure 2.1:	Schematic diagram of the ANU heavy-ion accelerator facility. The ion source is shown at the top (more detail in Figure 2.3). The 14UD Pelletron Tandem accelerator is in the center, followed by an analyzing magnet and the connection to the CUBE beam line. Only the LINAC magnet is indicated here and a schematic diagram of the complete LINAC is shown in Figure 2.2	37
Figure 2.2:	Schematic diagram of the ANU LINAC. The cryostats are depicted as well as many beam line components including the two achromats and the pre and post bunchers.	38

Figure 2.3:	Schematic diagram of the operation of the SNICS showing the active volume of the source, the ionizers, the cathode, the path of ionized Cs and the path of sputtered sample material.	41
Figure 2.4:	Schematic scale diagram of the layout of the detectors inside the CUBE detector system as viewed from above. One monitor detector is above the beam path and the other is below, see text.	45
Figure 2.5:	Rendering of the CUBE detector setup as used in the present work. The Front and Back MWPCs, the beam direction, the target ladder support, and the two Si monitor detectors are indicated.	47
Figure 3.1:	Schematic scale diagram of the individual MWPC coordinate systems used in the present work. The gray borders represent the MWPC support structure and the white inner regions represent the active area of the MWPCs. The four position quadrants of the MWPCs cathodes are indicated. The coordinates at the center of the detector and the center of each edge of the active area are indicated in units of mm.	50
Figure 3.2:	Schematic scale diagram of the Cartesian coordinate system used in the present work in relation to the CUBE detector setup. Panel A shows a diagram of the CUBE detectors setup from above illustrating the $(X, 0, Z)$ plane. Panel B shows a diagram of the CUBE detector setup from the beam axis upstream of the target illustrating the $(X, Y, 0)$ plane. The coordinates at the center of the CUBE and at the center of the two MWPCs are indicated.	52
Figure 3.3:	Schematic scale diagram of the spherical coordinate system used in the present work in relation to the CUBE detector setup. Panel A shows a diagram of the CUBE detector setup from above. The definitions of θ and r are indicated. Panel B shows a view from the beam axis upstream of the CUBE and the definition of Φ is indicated. The coordinates at the center of the CUBE and at the center of the two MWPCs are indicated.	52
Figure 3.4:	Position distributions in the x and y dimensions in channel number observed from the calibration measurement of $^{50}\text{Cr} + ^{184}\text{W}$ at $E_{\text{Lab}} = 186.0$ MeV that was used to determine the detector edges in Front and Back detectors. Panels A and B correspond to the x and y position distributions for the Back MWPC and Panels C and D correspond to the x and y position distributions for the Front MWPC.	56

Figure 3.5:	Two dimensional position spectra for the Back MWPC. Panel A shows the raw position information and the solid black rectangle reflects the gate applied to the data sets. Panel B shows the position spectra after the gate was applied. Both are for $^{50}\text{Cr} + ^{180}\text{W}$ at $E_{\text{Lab}} = 284.0$ MeV as an example.	58
Figure 3.6:	Two dimensional position spectra for the Front MWPC. Panel A shows the raw position information and the solid black rectangle reflects the gate applied to the data sets. Panel B shows the position spectra after the gate was applied. Both are for $^{50}\text{Cr} + ^{180}\text{W}$ at $E_{\text{Lab}} = 284.0$ MeV as an example.	59
Figure 3.7:	Two dimensional position spectra following the conversion from channel number to mm for the Back (A) and Front (B) MWPCs observed during the measurement of $^{50}\text{Cr} + ^{180}\text{W}$ at $E_{\text{Lab}} = 284.0$ MeV as an example.	61
Figure 3.8:	Angular coverage of the Back (A) and Front (B) MWPCs shown as θ_{lab} on the x-axis and Φ on the y-axis for $^{50}\text{Cr} + ^{180}\text{W}$ at $E_{\text{Lab}} = 284.0$ MeV.	63
Figure 3.9:	Panel A shows the raw timing signals observed for coincident fragments in the Front (x-axis) and Back (y-axis) MWPCs from the measurement of $^{50}\text{Cr} + ^{180}\text{W}$ at $E_{\text{Lab}} = 284.0$ MeV. Panel B shows the observed timing signals following conversion to ns. See text for details on this conversion.	65
Figure 3.10:	Time spectra in channel numbers observed in the Back (A) and Front (B) MWPCs from the TAC calibrations with 10 ns pulses.	66
Figure 3.11:	Illustration of an example set of timing signals including, RF signals in the top panel, a timing signal from the Back MWPC in the middle panel, and a timing signal from the Front MWPC in the bottom panel. t_0 and δ_t are the time parameters used in the CUBE calibration. See text for discussion.	68

Figure 3.12: Illustration of the primary vectors considered in the kinematic coincidence method for two emitted fragments. Panel A shows the projection of one possible combination of vectors on to a plane $(X, 0, Z)$ along the beam axis. The Z -axis represents the beam axis. The solid, black vectors represent a possible set of $V_{i,c.m.}$ for two fragments i . The dashed, purple vectors represent one possible set of $v_{i,lab}$. As an example, the two components of the two $V_{i,c.m.}$ are shown. The dot-dashed, red vectors represent $u_{i,c.m.}$ and the dotdashed, blue vectors represent $w_{i,c.m.}$. $\theta_{i,lab}$ is shown as an example of the definition of θ . Panel B shows a projection of one possible combination of velocity vectors on to a plane $(X, Y, 0)$ perpendicular to the beam axis. The dashed, black vectors represent one possible combination of $V_{i,c.m.}$ for fragments i . The dotdotdashed, sky blue vectors represent possible $V_{i,dev}$. The projection of each $V_{i,dev}$ on the z -axis is represented by the dotdotdashed, dark purple vectors (shown just off the z axis for clarity). The solid, orange vectors represent v_{perp} , which should be zero in binary kinematics. $\phi_{i,dev}$ are also indicated. 70

Figure 3.13: Perpendicular velocity determined for $^{50}\text{Cr} + ^{180}\text{W}$ at $E_{\text{Lab}} = 284.0$ MeV as a function of the difference between v_{par} and v_{cn} . The solid, black circle in Panel A represents the gate applied to the data set and has a 1 mm/ns radius. Panel A shows the distribution before the gate was applied. Panel B shows the distribution after the gate was applied to the data set. 76

Figure 3.14: The number of counts observed for $^{50}\text{Cr} + ^{180}\text{W}$ at $E_{\text{Lab}} = 284.0$ MeV shown as a function of the difference between the determined values of Φ from the Back detector and the Front detector for gated coincident events. The data is represented as the solid blue line and shows a strong peak at a Φ difference of 180° . A Gaussian function fitted to the data is shown as the dashed, red line and the box in the upper right corner provides the means and RMS from the fit. 77

Figure 3.15: Ratio of the deduced total kinetic energy from binary fragments to the total kinetic energy calculated for fission fragments for $^{50}\text{Cr} + ^{180}\text{W}$ at $E_{\text{Lab}} = 284.0$ MeV shown as a function the determined mass ratios. The solid, black polygon in Panel A represents the gates used to remove scattering events with mass ratios in the fission-like region. Panel A shows the distribution before the gate was applied. Panel B shows the distribution after the gate was applied. 80

Figure 4.1:	Unsymmetrized MADs of the eight Cr + W reactions in the Back MWPC at $E_{c.m.}/V_B = 1.13$. Δn is the change in the number of neutrons in the compound nucleus relative to $^{50}\text{Cr} + ^{180}\text{W}$, where $N = 132$	83
Figure 4.2:	Unsymmetrized MADs generated for the Cr + W reactions in the Front MWPC at $E_{c.m.}/V_B = 1.13$. Δn is the change in the number of neutrons in the compound nucleus relative to the lightest system, $^{50}\text{Cr} + ^{180}\text{W}$, where $N = 132$	85
Figure 4.3:	Evolution of a mass angle distribution through various separation angles. Panel A shows the full 360 degree coverage. Panel B shows a symmetrized MAD with a 0-180 degree scale in θ	88
Figure 4.4:	The mass angle distribution, where $\theta_{c.m.}$ is shown as a function of mass ratio, for coincident events from the reaction of $^{50}\text{Cr} + ^{180}\text{W}$ at $E_{lab} = 284.6$ MeV. The solid, black rectangle highlights the mass symmetric region ($M_R = 0.35 - 0.65$) across the full angular coverage of the symmetrized MAD. See text for discussion. Δn is the change in the number of neutrons in the compound nucleus relative to the lightest system, $^{50}\text{Cr} + ^{180}\text{W}$, where $N = 132$	90
Figure 4.5:	The symmetrized MAD from the reaction of $^{54}\text{Cr} + ^{186}\text{W}$ at $E_{lab} = 281.7$ MeV. As in Figure 4.4, the solid, black rectangle was drawn to highlight the region of mass symmetric events between $M_R = 0.35 - 0.65$ across the angular coverage of the MWPCs.	91
Figure 4.6:	Symmetrized MADs of the remaining six Cr + W reactions at $E_{c.m.}/V_B = 1.13$. Δn is the change in the number of neutrons in the compound nucleus relative to $^{50}\text{Cr} + ^{180}\text{W}$, where $N = 132$	92
Figure 4.7:	Mass distributions for all eight Cr + W systems from the present work at $E_{c.m.}/V_B = 1.13$. The solid red line represent a Gaussian fit to the data. The dashed blue line represents a Gaussian function with the widths calculated from a statistical approximations for pure Fusion-fission. This Gaussian function has been normalized to the peak of the experimental mass distribution. Δn is the change in the number of neutrons in the compound nucleus relative to $^{50}\text{Cr} + ^{180}\text{W}$, where $N = 132$	94
Figure 4.8:	Unsymmetrized mass angle distribution for calibration run of $^{50}\text{Cr} + ^{184}\text{W}$ at $E_{lab} = 186.0$ MeV. The dashed, black box indicates the angular region included in the angular distribution calculations.	102

Figure 4.9:	Unsymmetrized mass angle distribution for $^{50}\text{Cr} + ^{180}\text{W}$ at $E_{\text{lab}} = 284.6$ MeV as an example of the events included in the determination of the angular distribution. The solid, black box represents the gate used to exclude all events outside the fission-like region.	103
Figure 4.10:	Unsymmetrized mass angle distribution after the gate on the fission-like region was applied to the data set for $^{50}\text{Cr} + ^{180}\text{W}$ at $E_{\text{lab}} = 284.6$ MeV as an example of the angular region included in the determination of the angular distribution. The dashed, black box represents the angular region included in the angular distribution calculations.	104
Figure 4.11:	Counts in the two monitor detectors for the reaction of $^{50}\text{Cr} + ^{180}\text{W}$ at $E_{\text{lab}} = 284.6$ MeV shown as a function of channel number.	107
Figure 4.12:	$\theta_{\text{c.m.}}$ distributions for the reaction of $^{50}\text{Cr} + ^{180}\text{W}$ at $E_{\text{lab}} = 284.6$ MeV.	108
Figure 4.13:	Distribution of $\theta_{\text{c.m.}}$ for each deduced θ_{lab} for the $^{50}\text{Cr} + ^{180}\text{W}$ at $E_{\text{lab}} = 284.6$ MeV. The solid, red line represents a fourth degree polynomial fit to the distribution.	109
Figure 4.14:	$\theta_{\text{c.m.}}$ distributions for the calibration measurement of $^{50}\text{Cr} + ^{184}\text{W}$ at $E_{\text{lab}} = 186.0$ MeV.	110
Figure 4.15:	The angular distribution ($d\sigma(\theta_{\text{lab}}, E)/d\Omega$) for all eight Cr + W systems measure in the present work at $E_{\text{c.m.}}/V_{\text{B}} = 1.13$ shown as a function of $\theta_{\text{c.m.}}$ is represented by the black data points. The solid, red line is a sine function fit to the experimental data points using a χ^2 minimization.	112
Figure 4.16:	Unsymmetrized MADs observed in the Back MWPC for all eight systems presented in this work at $E_{\text{CN}}^* = 52.0$ MeV. Δn is the change in the number of neutrons in the compound nucleus relative to $^{50}\text{Cr} + ^{180}\text{W}$, where $N = 132$	115
Figure 4.17:	Unsymmetrized MADs observed in the Front MWPC for all eight systems presented in this work at $E_{\text{CN}}^* = 52.0$ MeV.	117
Figure 4.18:	Symmetrized MADs for the Cr + W systems measured in this work at $E_{\text{CN}}^* = 52.0$ MeV.	119

Figure 4.19:	Mass distributions for Cr + W systems presented in this work at $E_{\text{CN}}^* = 52.0$ MeV. The solid green line represents the second degree polynomial fit to the data.	121
Figure 4.20:	Comparison of the results from the two methods for determining the relative shapes experimental mass distributions applied to the Cr + W data at $E_{\text{c.m.}}/V_{\text{B}} = 1.13$	125
Figure 4.21:	The angular distribution ($d\sigma(\theta_{\text{lab}}, E)/d\Omega$) for Cr + W systems measure in the present work at $E_{\text{CN}}^* = 52.0$ MeV shown as a function of $\theta_{\text{c.m.}}$ is represented by the black data points. The solid, red line is a sine function fit to the experimental data points using a χ^2 minimization.	126
Figure 5.1:	Upper limit of P_{CN} determined for the Cr + W systems forming ^{236}Cf measured in the present work as a function of the mass of the projectile. These systems were measured at $E_{\text{c.m.}}/V_{\text{B}} = 1.13$. The colors of the upper limit markers correspond to the projectile used in the reaction.	131
Figure 5.2:	Curvature parameter determined for the Cr + W systems forming ^{236}Cf measured in the present work as a function of the mass of the projectile. These systems were measured at $E_{\text{CN}}^* = 52.0$ MeV. The colors of the upper limit markers correspond to the projectile used in the reaction.	131
Figure 5.3:	Upper limit of P_{CN} for each system measured at $E_{\text{c.m.}}/V_{\text{B}} = 1.13$ is shown as a function of $(N/Z)_{\text{CN}}$. The color of the upper limit markers correspond to the projectile used in the reaction.	132
Figure 5.4:	The mass asymmetry of the systems measured in the present work shown as a function of the systems fissility. The colors of the markers correspond to the projectile used in the reaction.	134
Figure 5.5:	Deduced upper limits for P_{CN} shown as a function of the compound nuclear fissility for the systems measured at $E_{\text{c.m.}}/V_{\text{B}} = 1.13$. The colors of the upper limit markers correspond to the projectile used in the reaction.	136
Figure 5.6:	Deduced upper limits for P_{CN} shown as a function of the mass asymmetry for the systems measured at $E_{\text{c.m.}}/V_{\text{B}} = 1.13$. The colors of the upper limit markers correspond to the projectile used in the reaction.	136

Figure 5.7:	TDHF calculations for mass ratio M_R , charge ratio Z_R (a) and contact time (b) for $^{50}\text{Cr} + ^{180}\text{W} \rightarrow ^{240}\text{Cf}$ and $^{54}\text{Cr} + ^{186}\text{W} \rightarrow ^{240}\text{Cf}$ shown as a function of impact parameter b [10]. The insert in panel (a) shows an example of a density plot where the dinuclear system separates. The insert in panel b shows an example of a density plot where the system fuses, see the text. Reprinted figure with permission from [10] Copyright (2015) by the American Physical Society. http://dx.doi.org/10.1103/PhysRevC.91.041602	139
Figure 5.8:	P_{CN} calculated from three analytical functions [119, 29, 120] shown as a function of $(N/Z)_{\text{CN}}$. The upper limits deduced for the systems in the present work are included as the horizontal lines.	143
Figure 5.9:	Curvature parameter in arbitrary units deduced from the mass distribution for each system measured at $E_{\text{CN}}^* = 52.0$ MeV as a function $(N/Z)_{\text{CN}}$	145
Figure 5.10:	Curvature parameter deduced for the Cr + W systems at $E_{\text{CN}}^* = 52.0$ MeV in the present work as a function of the l_{max} . The colors of the data points indicate the projectile used in the reaction.	146
Figure 5.11:	Curvature parameter deduced for the Cr + W systems at $E_{\text{CN}}^* = 52.0$ MeV in the present work as a function of the l_{crit} . The colors of the data points indicate the projectile used in the reaction.	146
Figure 5.12:	Curvature parameter determined for the Cr + W systems at $E_{\text{CN}}^* = 52.0$ MeV measured in the present work as a function of the maximum available rotational energy determined as in eq. 5.9 in MeV. The colors of the data points indicate the projectile used in the reaction.	148
Figure 5.13:	The two limiting case of collision with a deformed target nucleus. Panel A shows a collision where the nuclear symmetry axes are aligned. Panel B shows the case where the axes are anti-aligned.	149
Figure 5.14:	Curvature parameters determined for the Cr + W reactions measured in the present work as a function of $E_{\text{c.m.}}/V_{\text{B}}$ (aligned) in Panel A, $E_{\text{c.m.}}/V_{\text{B}}$ (average) in Panel B, and $E_{\text{c.m.}}/V_{\text{B}}$ (anti-aligned) in Panel C.	153
Figure 5.15:	Angular anisotropy, determined as the ratio of $W(142^\circ)$ to $W(102^\circ)$ for the systems measured at $E_{\text{c.m.}}/V_{\text{B}} = 1.13$ shown as a function of $(N/Z)_{\text{CN}}$ in the present work. The colors of the data points correspond to the projectile used in the reaction. The solid, green line indicates the ratio of $W(142^\circ)$ to $W(102^\circ)$ for a $1/\sin(\theta)$ function.	155

Figure 5.16:	Angular anisotropy, determined as the ratio of $W(142^\circ)$ to $W(102^\circ)$ for the systems measured at $E_{\text{CN}}^* = 52.0$ MeV shown as a function of $(N/Z)_{\text{CN}}$ in the present work. The colors of the data points correspond to the projectile used in the reaction. The solid, green line indicates the ratio of $W(142^\circ)$ to $W(102^\circ)$ for a $1/\sin(\theta)$ function. .	156
Figure 5.17:	Mass distributions for previously measured systems forming ^{238}Cf or ^{240}Cf at comparable energies to the Cr+W systems measured at $E_{\text{c.m.}}/V_{\text{B}} \approx 1.13$ (panels A, C, and E) and $E_{\text{CN}}^* \approx 52.0$ MeV (panels B, D, and F).	159
Figure 5.18:	The upper limit of P_{CN} determined for the systems in the present work and previously measured at ANU forming ^{238}Cf or ^{240}Cf as the compound nucleus are shown as a function of the fissility of the compound nucleus. The systems are distinguished in in the legend. .	160
Figure 5.19:	The upper limit of P_{CN} determined for the systems in the present work and previously measured at ANU forming ^{238}Cf or ^{240}Cf as the compound nucleus are shown as a function of the entrance channel mass asymmetry. The systems are distinguished in in the legend. . .	161
Figure 5.20:	The curvature parameters determined for the systems in the present work and previously measured at ANU forming ^{238}Cf or ^{240}Cf as the compound nucleus are shown as a function of the fissility of the compound nucleus. The systems forming ^{238}Cf are indicated by the solid markers, while the systems forming ^{240}Cf are indicated by the open markers. The systems are distinguished in in the legend. The inset in the lower right corner is the same plot zoomed in on the systems other than $^{32}\text{S} + ^{208}\text{Pb}$	162
Figure 5.21:	The curvature parameters determined for the systems in the present work and previously measured at ANU forming ^{238}Cf or ^{240}Cf as the compound nucleus are shown as a function of the entrance channel mass asymmetry. The systems forming ^{238}Cf are indicated by the solid markers, while the systems forming ^{240}Cf are indicated by the open markers. The systems are distinguished in in the legend. The inset in the lower right corner is the same plot zoomed in on the systems other than $^{32}\text{S} + ^{208}\text{Pb}$	163

Chapter 1

Introduction

1.1 Superheavy Elements

In 2016 four new superheavy elements were named [11, 2, 12, 13, 14, 15]. The four new elements help answer one of the overarching questions in nuclear physics: How large can a nucleus become and still be held together by the nuclear force?

In superheavy element research in the 1970's a method, called "cold fusion" was proposed, where a medium mass projectile is impinged on a ^{208}Pb or ^{209}Bi target at energies such that the compound nucleus is formed with approximately 20 MeV of excitation energy [16, 17]. The term "cold" is a result of the relatively small excitation energies of the compound nuclei. While cold fusion reactions were successful in the production of superheavy elements with Z between 104 and 113 the production cross sections decrease by more than four orders of magnitude over that Z range [1]. Hot fusion reactions, where doubly magic ^{48}Ca is impinged on heavy actinide targets, have significantly larger cross sections compared to the previously used cold fusion reactions [1]. These reactions are termed "hot" fusion reactions due to the relatively high excitation energy of the compound nucleus and were used to produce superheavy elements with Z of 114 to 118 [15, 14, 11]. Beyond a Z of 118 the superheavy element production cross sections for both hot and cold fusion reactions continue to decrease [18]. Additionally, to reach higher Z with hot fusion reactions, heavier actinide targets are needed and the next actinides, einsteinium, fermium, and beyond, do not have

isotopes with long enough half lives to easily prepare a target [19]. While some work is focused on trying to produce these heavier targets [20], a larger research effort is exploring alternative methods for the production of superheavy nuclei [18].

In addition to the desire to increase the nuclear charge of new superheavy nuclei, there is a strong motivation to move towards more neutron-rich superheavy nuclei. This motivation comes from the theoretical prediction made in the 1960s [21], that there exists a region of enhanced stability around neutron number 184 termed the “Island of Stability” [1, 22, 23, 24, 2, 25]. The most neutron-rich nuclei produced to date are still several neutrons away from $N = 184$, but an enhancement in stability has already been observed [13, 14, 15, 12].

One proposed mechanism to reach the more neutron-rich superheavy nuclei is to use neutron-rich radioactive isotopes as the projectile beams [26, 27, 28, 29]. Loveland et al. [29] used analytical calculations to compare the production rates of superheavy nuclei from reactions of stable and radioactive projectile beams based on the predicted production intensities at the proposed RIA facility. This work concluded that stable beams generally have larger productions rates for a given nucleus than radioactive beams due to beam intensity. However, there are many nuclei that simply cannot be produced from reactions of stable projectiles and targets. It is particularly difficult to reach the more neutron-rich superheavy nuclei with stable beams, thus neutron-rich radioactive beams may be the best possible mechanism to reach the “island of stability”. At the writing of this document the use of radioactive beams in superheavy element production is limited due to extremely low beam intensities. However, future facilities may make superheavy production reactions with neutron-rich, radioactive beams possible. To assess the feasibility of using radioactive isotope beams in the production of superheavy elements, it is important to have a full understanding of how increasing the neutron number of the projectile will impact the mechanism for producing superheavy nuclei.

All superheavy element discovery measurement to date used heavy-ion fusion reactions [18].

1.2 Heavy-Ion Fusion Reactions

A heavy-ion fusion reaction is a general term for any reaction between two nuclei larger than an alpha particle. The mechanism for heavy-ion fusion reactions is illustrated in Figure. 1.1 where the arrows indicate the progression of the example reaction with time. The heavy-ion fusion reaction mechanism can proceed through several channels. The evaporation residue production channel (needed for superheavy element production) is segmented into three primary stages. First, the projectile and target must overcome the interaction barrier and mutually capture to form a dinuclear system. Second, the dinuclear system must fully equilibrate in all degrees of freedom to form a fully fused compound nucleus. Historically, this was referred to as possessing the “extra push energy” [30]. Third, the compound nucleus must survive against fission and decay by light particle emission to form an evaporation residue. The reaction channel leading to the production of an evaporation residue is shown as the straight, horizontal path in Figure 1.1.

Two other potential outcomes from a heavy-ion fusion reaction are depicted in Figure 1.1. 1) The system can follow the quasifission channel by separating before a fully fused compound system is formed. 2) After compound nucleus formation the system could fission through a channel called fusion-fission. The cross section for the formation of an evaporation residue can be formally described as follows,

$$\sigma_{\text{ER}} = \sum_{J=0}^{\infty} \sigma_{\text{cap}}(E, J) P_{\text{CN}} W_{\text{Sur}}(E, J), \quad (1.1)$$

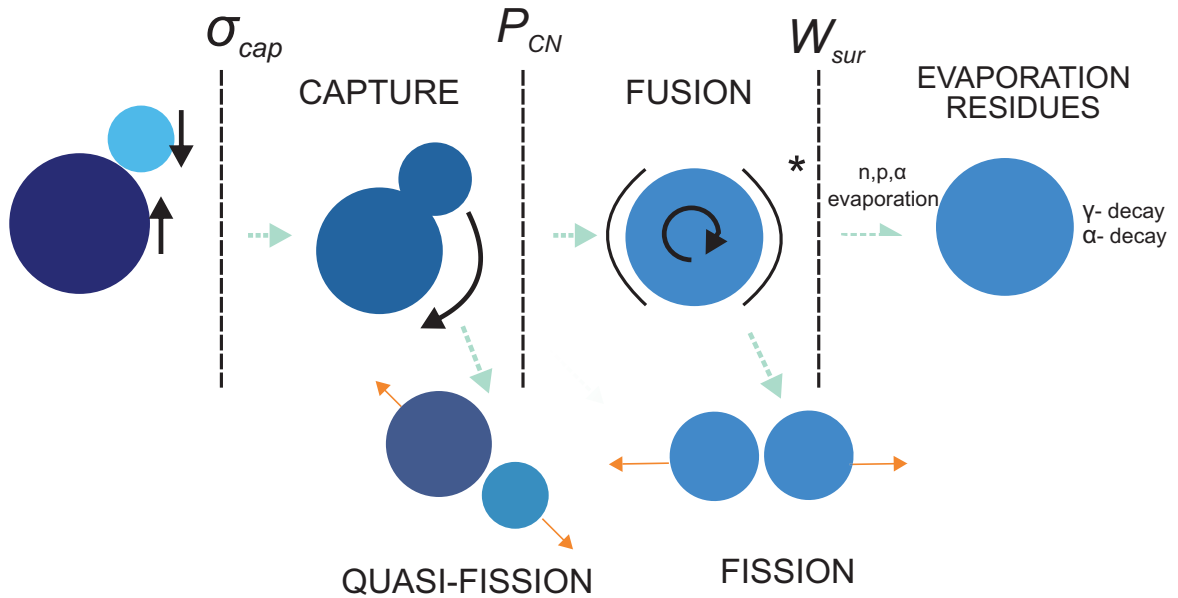


Figure 1.1: Illustration of an example heavy-ion fusion reaction showing various reaction channels. Key points in the reaction path are emphasized by the dashed lines. The arrows indicate the progression of the reaction with time.

where σ_{cap} is the capture cross section, P_{CN} is the probability of forming a compound nucleus, and W_{sur} is the survival probability of the compound nucleus against fission. [29]

In the following sections, the three primary stages of the formation of an evaporation residue (capture, compound nucleus formation, and survival against fission) are discussed. The probability of forming a compound nucleus is the primary focus of this work, so capture and survival are briefly introduced, then a more detailed description of compound nucleus formation follows.

1.2.1 Capture, σ_{cap}

The capture cross section for a heavy-ion reaction can be described reasonably well by the classical, geometric cross section with the sharp cutoff limit [31]

$$\sigma_{\text{cap}} = \pi\lambda^2 \sum_{l=0}^{l_{\text{max}}} (2l + 1), \quad (1.2)$$

where λ is the de Broglie wavelength of the incident particle, l is the angular momentum resulting from the collision [29]. The sharp cutoff limit assumes that there is some angular momentum (l_{max}) above which the capture cross section goes to zero. Capture cross sections for heavy-ion collisions are generally on the order of 10 to 100 mb [29]. Three of the primary channels available at this stage of a heavy-ion reaction are depicted in Figure 1.2. If the systems does not possess enough energy or has too large of an impact parameter (discussed in Section 1.2.1.2) then a dinuclear system will not form and the system will elastically scatter as illustrated in Panel A of Figure 1.2. Panel B depicts an example of a deep inelastic scattering reaction where the nuclei are close enough to exchange a few nucleons but full energy dissipation does not occur. If the system does overcome the capture barrier, then a dinuclear system is formed as depicted in Panel C.

1.2.1.1 Angular Momentum

From the geometric cross section in eq. 1.2 it is clear that angular momentum plays an important role in capture. The angular momentum introduced into the dinuclear systems by the collision is an indication of the types of reaction channels available [32]. A plot of the cross section (σ) is shown in Figure 1.3 as a function of angular momentum, which is calculated as $\sigma = \pi\lambda^2(2l + 1)$. The possible reactions at a given angular momentum are indicated

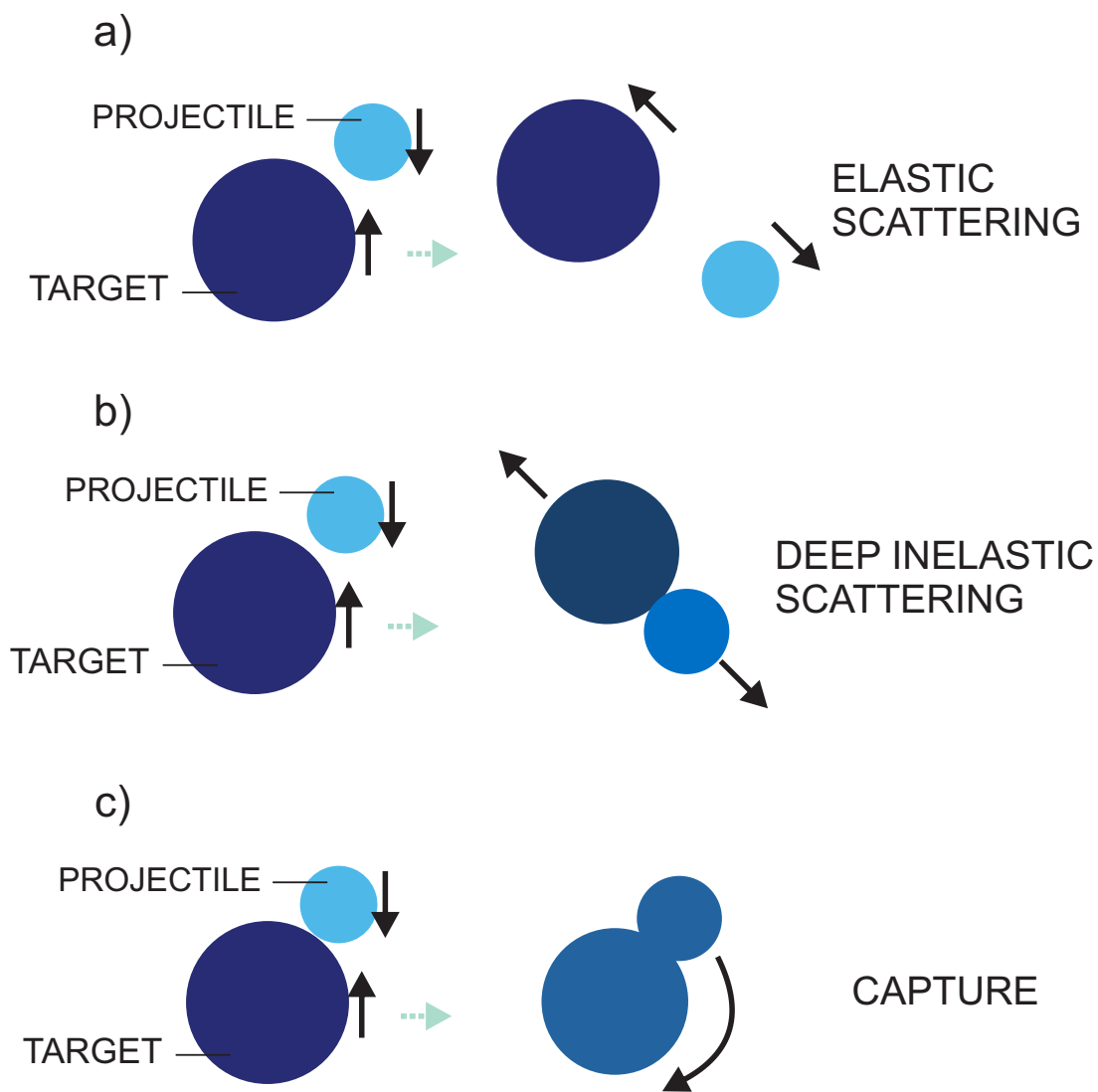


Figure 1.2: Illustration of three possible reaction outcomes from a heavy-ion reaction. Panel A depicts elastic scattering, Panel B depicts deep inelastic scattering, and Panel C depicts capture.

in Figure 1.3. It is important to note that this picture will be reaction dependent and these are all approximate and relative values. Also, there will be significant overlap between these types of reactions. There are four important angular momentum values indicated below the x axis. The first is l_{\max} , this is the maximum angular momentum value at which contact between the projectile and target can occur. At angular momenta larger than l_{\max} elastic scattering and Coulomb excitation reactions occur. At angular momentum values just below l_{\max} quasielastic reactions and direct reactions, like one nucleon transfer reactions, occur. Below l_{crit} compound nucleus formation becomes available. At angular momenta slightly above l_{crit} , fission-like reactions take place. These can be multinucleon transfer reactions, quasifission, or fast-fission type reactions. This region near l_{crit} will be the focus of the present work. In Figure 1.3, l_{D} indicates the threshold where the direct reaction channel opens and l_{f} indicates the threshold angular momenta value where fusion-like reaction channels open. In principle, all of these reaction types could be separated by various threshold angular momenta values. In practice, the boundaries of these regions are difficult to determine.

1.2.1.2 Impact Parameter

In experimental nuclear reactions it can be more straightforward to think of the reaction in terms of the impact parameter rather than the angular momentum. Impact parameter, b , is defined as the distance of closest approach between two nuclei in a collision. Impact parameter is related to angular momentum by $b = l\lambda$. Note that l is quantized while b is not. Thus, each value of l will correspond to a range in b . Head on collisions, where the two nuclei collide along their respective nuclear symmetry axes, are defined as $b=0$. Two cartoon depictions of impact parameter are depicted in Figure 1.4, in Panel A the collision

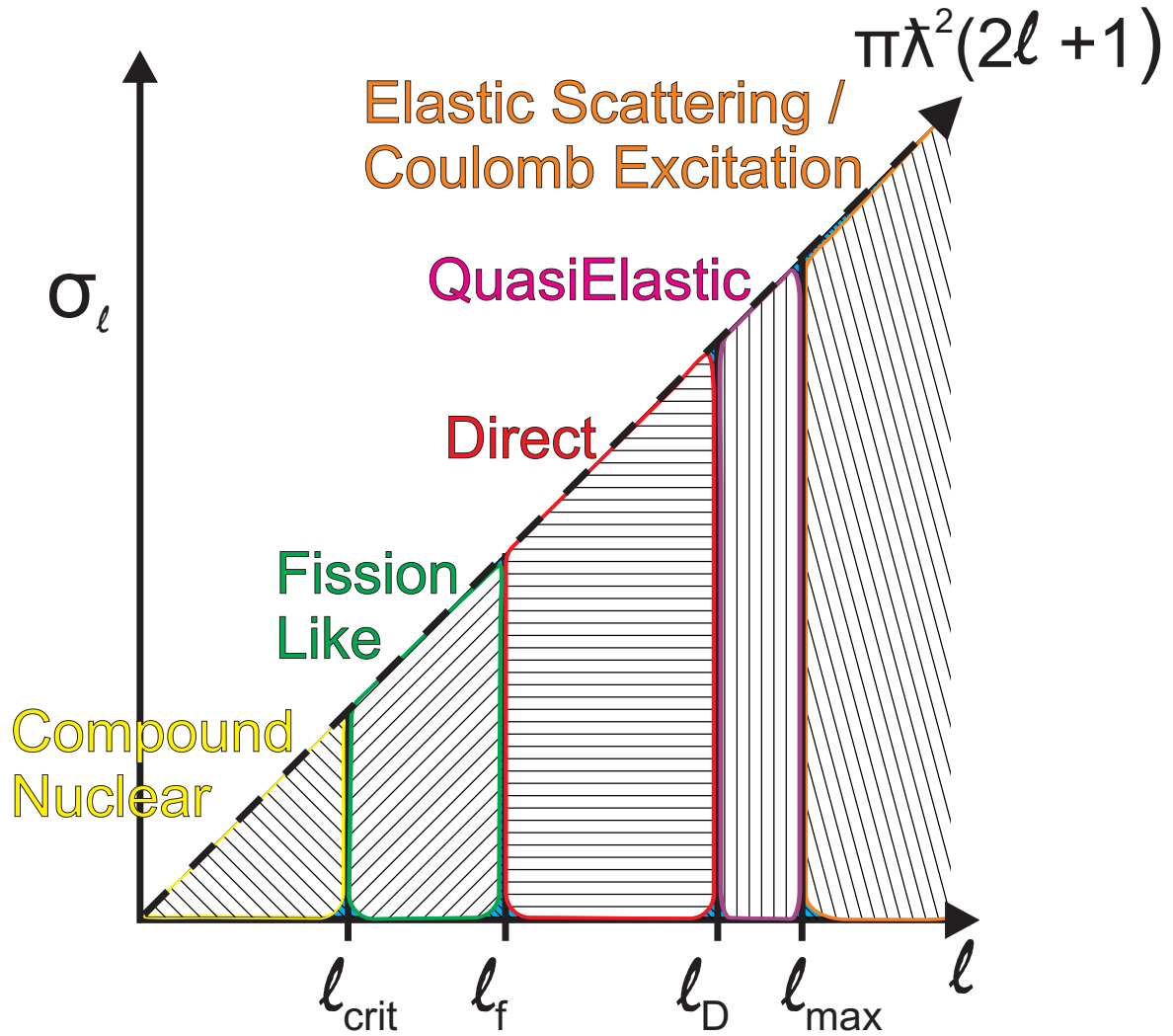


Figure 1.3: Illustration of the cross section of a heavy-ion reaction as a function of angular momentum. The black, dashed line represents the line $\sigma = \pi\lambda^2(2l + 1)$. The various hashed regions indicate the various angular momentum values where different processes are prominent. The most prominent type of reaction in each angular momentum region is indicated. Four different angular momentum values are called out (l_{crit} , l_f , l_D , and l_{max}). See text for the definition of each of the indicated angular momentum values. Adapted from [32]

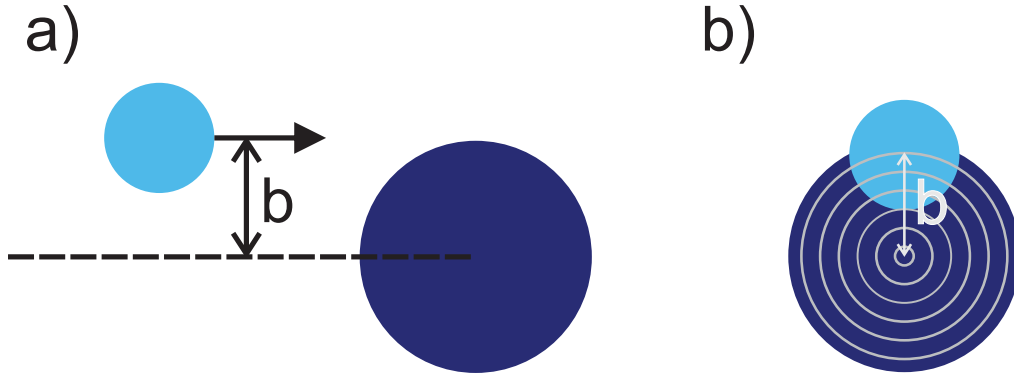


Figure 1.4: Cartoon example of the definition of impact parameter. Panel A shows a side view of a heavy-ion collision. Panel B shows a beam view of a collision. As presented in the cartoon, the dark blue sphere is the target and the light blue sphere is the projectile.

is viewed from the side. In this example reaction in the frame of the cartoon, the center of the projectile is above that of the target resulting in a positive impact parameter. In Panel B the collision is shown along the beam axis upstream of the collision and once again it is apparent that the collision would take place at an impact parameter greater than 0. The white concentric circle in Panel B represent that various l rings.

1.2.1.3 Bass Barrier

Another important entrance channel property is the interaction barrier assumed for the system. The interaction barrier used in the present work is the Bass Barrier [33], which is used throughout the literature in heavy-ion fusion reactions. The Bass barrier uses a simple, classical two-body model to describe fusion [34, 35]. The nuclear interaction parameters were then calculated from a fit of the model to experimental fusion excitation functions [9]

where the reaction cross section is determined as

$$\sigma_R = \pi R_{\text{int}}^2 \left(1 - \frac{V(R_{\text{int}})}{E_{\text{c.m.}}} \right). \quad (1.3)$$

The critical radius, R_{int} , for fusion used in this approach is the half-density radius, where $R = aA^{1/3} - b^2(aA^{1/3})^{-1}$ [9]. Previous work found the best fit to the data when $a = 1.16$ fm and $b^2/a = 1.39$ fm [9, 33]. The Bass interaction used is defined as

$$V(R_{\text{int}}) = 1.44 \frac{Z_1 Z_2}{R_{\text{int}}} - b \frac{R_1 R_2}{R_1 + R_2} \quad (1.4)$$

where b is approximately 1 MeV/fm [9].

1.2.2 Survival against Fission, W_{sur}

Like the capture process, survival against fission has been thoroughly studied and can be reasonably well calculated. The survival probability can be calculated as

$$W_{\text{sur}} = P_{\text{xn}}(E_{\text{CN}}^*) \prod_{i=1}^{i_{\text{max}}=x} \left(\frac{\Gamma_n}{\Gamma_n + \Gamma_f} \right)_{i,E} \quad (1.5)$$

where i is the number of neutrons emitted, P_{xn} is the probability of emitting exactly x neutrons, E_{CN}^* is excitation energy of the compound nucleus, and $\left(\frac{\Gamma_n}{\Gamma_n + \Gamma_f} \right)_{i,E}$ is the likelihood of emitting a neutron compared to the fission width. If the system de-excites by emitting small particles, like neutron, protons, and alphas, the remaining nucleus is called an evaporation residue. In superheavy element formation, the survival probability against fission is small, on the order of pb [36]. Most reactions follow either the fusion-fission or quasifission channels.

Fusion-fission occurs when the system reaches full equilibration of all degrees of freedom and then the excited compound nucleus undergoes fission, where it separates into two symmetric fragments.

1.2.2.1 Liquid Drop Model

The nuclei involved in heavy-ion fusion reactions are considered in the context of the Liquid Drop Model of the nucleus. In this model, the nucleus is approximated as an incompressible, uniformly charged liquid drop [37]. The binding energy (B_{tot}) of a nucleus can be described by the semi empirical mass equation

$$B_{tot} = a_v A - a_s A^{2/3} - a_C \frac{Z^2}{A^{1/3}} - a_a \frac{(A - 2Z)^2}{A} \pm \delta \quad (1.6)$$

where A is the mass of the nucleus and Z is the charge. The coefficients (a_i) correspond to various components of the binding energy. The first term is the volume term. The second term is the surface term and corrects the binding energy for the energy lost due to the reduced number of interactions between surface nuclei. The third term is the Coulomb term and accounts for the change in binding energy due to the Coulomb repulsion between the protons in the nucleus. The last term is the asymmetry term and accounts for the change in binding energy associated with moving away from $N = Z$. Finally, the δ is the pairing correction. The two terms associated with fission (or quasifission) of a nucleus are the surface and Coulomb terms. During fission the nucleus deforms which results in a change in energy because the surface area of the system increases. Simultaneously, the elongation of the systems means that the nucleons are on average further apart which reduces the Coulomb repulsion between the protons. A similar change in energy applies to systems involved in

quasifission.

This change in energy can be described by $\Delta E = \Delta E_s + \Delta E_C$, where ΔE_s and ΔE_C are the change in the surface and Coulomb energies, respectively. When the deformation of the system is small the surface and Coulomb energies can be determined from

$$E_s = E_s^0 \left(1 + \frac{2}{5} \alpha_2^2 \right) \quad (1.7)$$

$$E_C = E_C^0 \left(1 - \frac{1}{5} \alpha_2^2 \right) \quad (1.8)$$

where E_s^0 and E_C^0 are the surface and Coulomb energies for a spherical nucleus and α_2^2 is the quadrupole distortion parameter. A nucleus becomes unstable against fission when ΔE_s and ΔE_C are equal ($E_s - E_s^0 = E_C^0 - E_C$). From the definitions in eqs. 1.7 and 1.8 it can be shown that ΔE_C and ΔE_s are equal when

$$\frac{E_C^0}{2E_s^0} = 1. \quad (1.9)$$

The ratio in eq. 1.9 is termed the fissility parameter and expresses the fissionability of a nucleus as a ratio of the Coulomb energy of a charged sphere to two times the surface energy of a sphere. Now, the Coulomb energy of a charged sphere can be approximated as

$$E_C^0 = \frac{3}{5} \frac{Z^2 e^2}{R_0 A^{1/3}} = \left(a_C \frac{Z^2}{A^{1/3}} \right) \quad (1.10)$$

where R_0 is the radius of a spherical nucleus, and a_C is the coefficient for the Coulomb term

in eq. 1.6 defined as $a_C = 3e^2/5R_0$. The surface energy of a sphere can be approximated as

$$E_s^0 = 4\pi R_0^2 S A^{(2/3)} = a_s A^{(2/3)} \quad (1.11)$$

where S is the surface tension per unit area and the coefficient for the surface energy (a_s) in eq. 1.6 is defined as $a_s = 4\pi R_0^2 S$. By substituting these approximations into eq. 1.9 the fissility parameter (χ) can be described by

$$\chi = \left(\frac{a_C}{2a_s} \right) \left(\frac{Z^2}{A} \right). \quad (1.12)$$

The ratio of $(2a_s/a_C)$ is defined as $(Z^2/A)_{\text{critical}}$. Previous work has concluded that the fissility of a system has an important influence on the dominate reaction channel in heavy-ion fusion reactions.

1.2.3 Probability of forming a Compound Nucleus, P_{CN}

If the system reacts at low enough angular momentum and a dinuclear system is formed then the next stage of a heavy-ion fusion reaction involves equilibration of all degrees of freedom as the dinuclear system fuses to form a compound nucleus. The least understood portion of the heavy-ion fusion reaction mechanism is the probability of forming a compound nucleus P_{CN} . Predictions for P_{CN} can vary by 1 to 2 orders of magnitude [29]. If the systems separates before equilibrating in all degrees of freedom then it is said to have undergone quasifission.

1.2.3.1 Quasifission

Quasifission, which occurs in heavy-ion fusion reactions of large systems, causes the greatest uncertainty in predictions of P_{CN} . Previous work has shown that quasifission becomes prominent in systems with charge products, $Z_p Z_t$, greater than 1600 [38], though it has been seen in systems with $Z_p Z_t$ as low as 800 [7]. The charge product is often used to characterize these types of reactions because it gives an indication of the Coulomb potential between the projectile and target.

1.3 Experimental Signatures of Quasifission

In many medium mass heavy-ion fusion reactions the evaporation residue cross section is small. After capture most systems follow the fusion-fission or quasifission reaction channels. Therefore, the number of fusion-fission events from a reaction can be assumed to be equivalent to the number of events that formed a compound nucleus. Recalling Figure 1.1, the number of fusion-fission events compared to the total number of quasifission and fusion-fission events provides a means of determining the probability of forming a compound nucleus, P_{CN} , for the system. All of the signatures of quasifission discussed in this section use a comparison with fusion-fission to deduce information about the P_{CN} for the system. Previous work has concluded that there are three signatures of quasifission that are useful in distinguishing between fusion-fission and quasifission: a broadening of the mass distribution, an enhancement of the anisotropy in the angular distribution, and a correlation between mass and angle in the mass angle distribution [39, 40]. Each of these signatures will be discussed in detail in the following sections.

1.3.1 Mass Distributions

In many experiments designed to study fusion-fission and quasifission competition, the two exit channel fragments are detected and then their relative or absolute masses are determined [41, 42, 43, 44, 39, 45, 46]. Mass distributions provide a summarized overview of the mass information observed in the measurement. Throughout the literature the mass information in a mass distribution is presented in one of two forms: the absolute mass of the fragments (A_i) or the mass ratios of the two fragments ($M_{R,i}$) [41, 42, 43, 44, 39, 45, 46]. In the present work the mass ratio will be used and is defined as

$$M_{R,1} = \frac{A_1}{A_1 + A_2} \quad (1.13)$$

where A_i is the mass of one of the binary fragments.

All possible exit channels from a heavy-ion reaction contribute to the observed mass distribution and certain signatures can be used to identify the exit channels. A cartoon example of a mass distribution for a reaction where the entrance channel nuclei had mass ratios of 0.25 and 0.75 is depicted in Figure 1.5. The x axis shows the approximate mass ratios. Normally, the y axis of a mass distribution shows counts, but is ignored for this discussion. Various example exit channel pairs are shown in the distribution. The light fragments are shown above the heavy fragments for clarity alone. In a mass distribution the exit channel fragments from elastic scattering events will be observed at or near to the mass ratios of the entrance channel. In the example mass distribution in Figure 1.5 scattering events are indicated by “S”. The exit channel fragments from deep inelastic scattering and few nucleon transfer reactions will be observed at mass ratios very near to those of elastic scattering events, still at the positions labeled “S” in Figure 1.5. The exit channel fragments

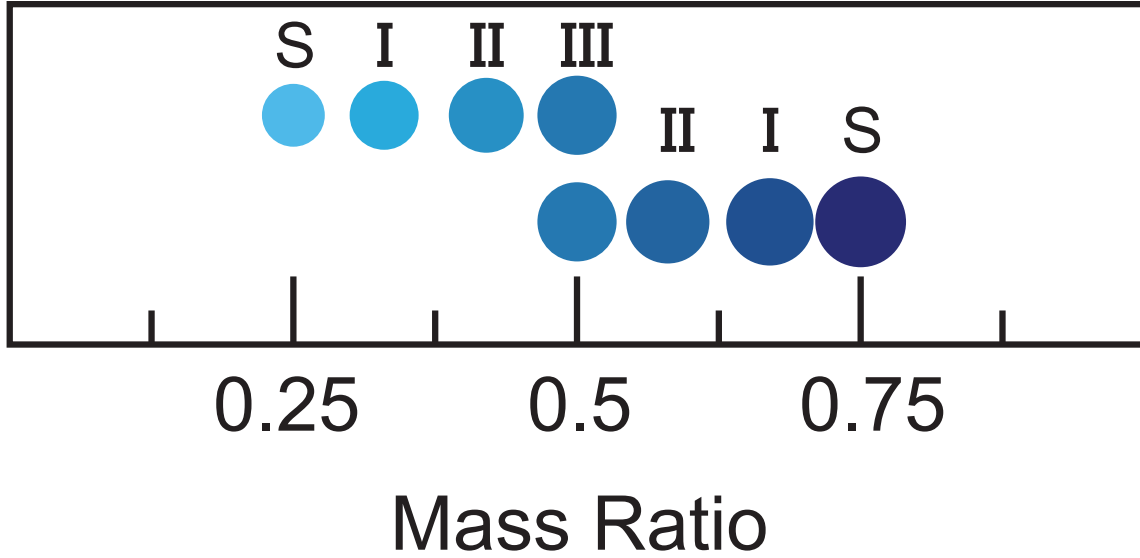


Figure 1.5: Illustration of a mass distribution. The various circles indicate the exit channel fragments expected at various mass ratios. See text for explanation.

from fusion-fission reactions, where full mass equilibration is reached, will be approximately symmetric in mass at the energies considered in this work [46] and are indicated by “III” in Figure 1.5.

Now, the fragments at the mass ratios regions indicated by either “I” or “II” result primarily from non mass equilibrated reactions, like quasifission. In quasifission reactions, the dinuclear systems interact long enough for significant mass transfer to occur, but may not reach full mass equilibration. Therefore quasifission fragments populate the region of a mass distribution between the entrance channel mass ratios and the symmetric mass ratios. Additionally, it is possible for quasifission reactions to results in fragments with mass ratios of 0.5 so mass distributions for quasifission and fusion-fission reactions can overlap in that region.

Events from quasifission reactions at mass ratios like those indicated by “I” or “II” provide

an observable signature of quasifission in a heavy-ion reaction measurements. In a heavy-ion reaction where no quasifission occurred, there would generally be three peaks expected in the mass distribution. Two occur at the mass ratios of the projectile and target from scattering reactions. The third one is observed at symmetric mass ratios from fusion-fission reactions. When quasifission is present, the mass distribution is also populated in between these peaks. This is referred to as a broadening of the mass distribution because the narrow peak at symmetric mass ratios is broadened by the inclusion of quasifission events. It is necessary to note, however, that in the extreme case where short time scale quasifission dominates, the elastic peaks will appear to broaden towards symmetric mass ratios and result in a minimum in the mass distribution at mass ratios of 0.5.

The mass distribution previously measured by Wakhle [47] for $^{12}\text{C} + ^{208}\text{Pb}$ at $E_{\text{lab}} = 66.0$ MeV is shown in Figure 1.6. The high mass asymmetry (0.89) and low charge product (492) of this system indicate that quasifission will not be a prominent exit channel in this system. P_{CN} should be one and all of the products observed in the fission-like region should come from fusion-fission. A peak observed in the mass distribution in Figure 1.6 has a FWHM of $0.12 M_{\text{R}}$ units and is considered “narrow”. Only one peak is observed because the elastic scattering events were outside the acceptance of this measurement. For comparison, the mass distribution for $^{48}\text{Ti} + ^{192}\text{Os}$ at $E_{\text{lab}} = 259.9$ MeV previously measured by Lin *et al.* [46] is shown in Figure 1.7. The $^{48}\text{Ti} + ^{192}\text{Os}$ system has a charge product of 1672 and a mass asymmetry of 0.6, so quasifission is expected to be a strong exit channel in this system. The mass distribution in the fission-like region ($0.35 < M_{\text{R}} < 0.65$) has a FWHM of $0.31 M_{\text{R}}$ units and is considered broadened.

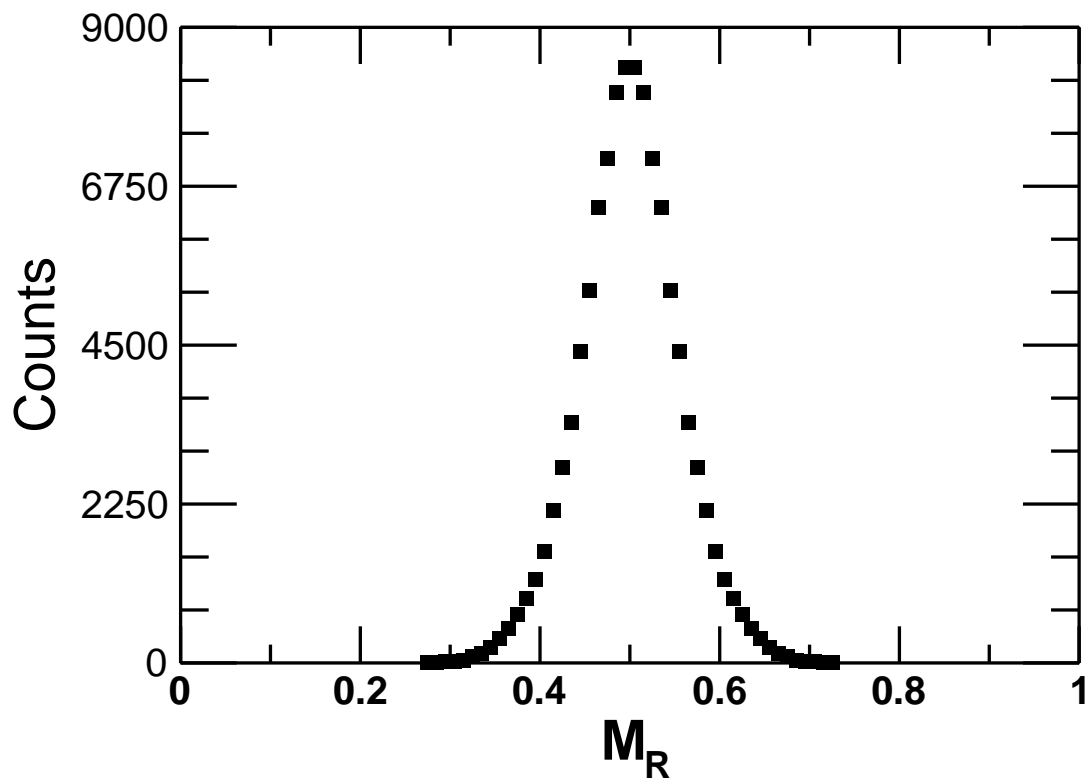


Figure 1.6: Mass distribution deduced from the reaction of $^{12}\text{C} + ^{208}\text{Pb}$ at $E_{\text{lab}} = 66.0$ MeV [47].

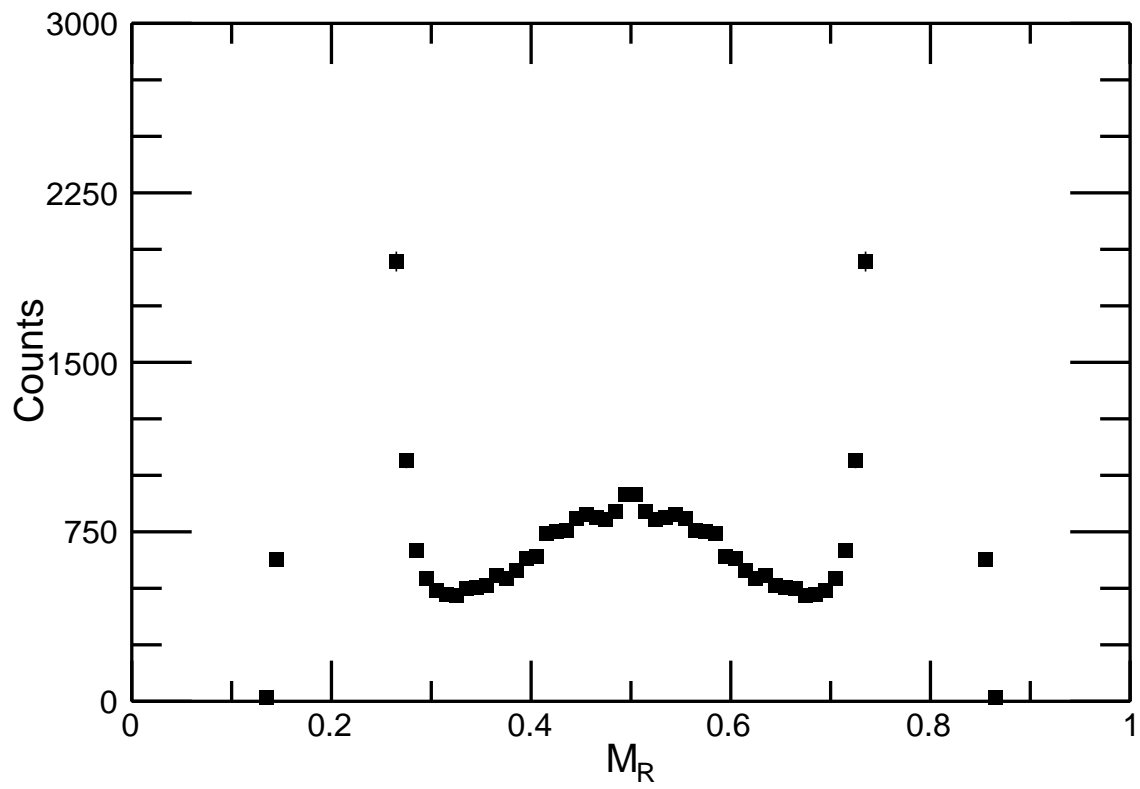


Figure 1.7: Mass distribution deduced from the reaction of $^{48}\text{Ti} + ^{192}\text{Os}$ at $E_{\text{lab}} = 259.9$ MeV [46].

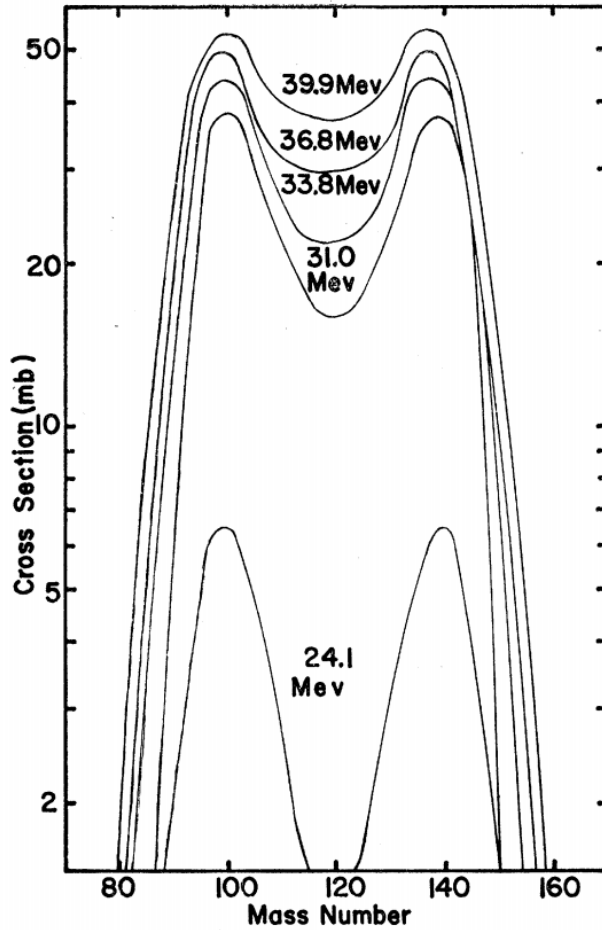


Figure 1.8: Mass distributions reported in [48] from the reaction of helium and uranium-233. Reprinted figure with permission from [48] Copyright (1961) by the American Physical Society. <http://dx.doi.org/10.1103/PhysRev.121.1415>

1.3.1.1 Excitation Energy and Fusion-Fission

It is important to note that the mass distribution of a fissioning system is highly dependent of excitation energy. A series of mass distributions from the reaction of helium projectiles on uranium-233 are shown in Figure 1.8 as reported in [48]. At the lowest energies, asymmetric fission dominates, but as the energy increases symmetric fission becomes more prominent [49, 50, 51]. At the relatively high excitation used in the present work and in the previous work at ANU ($E_{CN}^* \sim 50$ MeV) shell effects are minimized and fragments from fusion-fission reactions are focused at symmetric mass ratios.

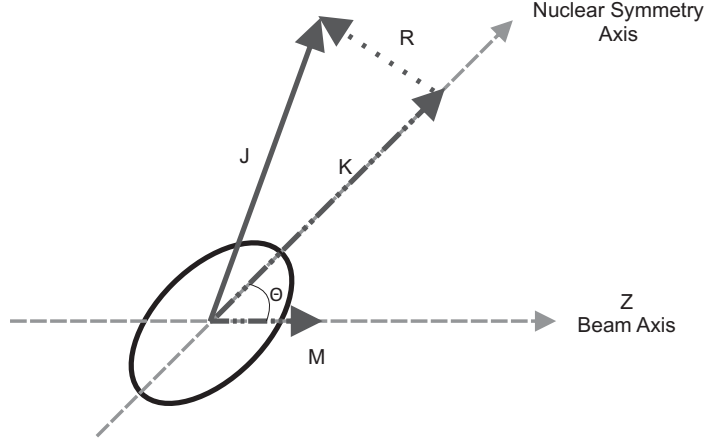


Figure 1.9: Schematic image of angular momentum coupling coordinate system for a deformed nucleus. Adapted from [51]

1.3.2 Angular Distributions

The angular distributions from a heavy-ion fusion reaction can be considered in the terms of the transition state model for fission of a compound nucleus. The probability of emitting fission fragments from a particular state with the quantum numbers J , M , and K as a function of angle is described by [52],

$$P_{M,K}^J(\theta) = (2J + 1) \frac{2\pi R^2 \sin\theta d\theta}{4\pi R^2} |d_{M,K}^J(\theta)|^2 \quad (1.14)$$

where J is the total angular momentum, M is the projection of J along the beam axis, and K is the projection of J along the nuclear symmetry axis [52]. The $d_{M,K}^J(\theta)$ functions are the wave functions of a symmetric top for a given J , M , and K [52]. The angular distribution ($W_{M,K}^J(\theta)$) is obtained by dividing $P_{M,K}^J(\theta)$ by $\sin\theta$.

A nucleus prior to fission with quantum numbers J , M , and K is illustrated in Figure 1.9 and defines the coordinate system. In the transition state model, the fission fragments are

assumed to be emitted along the nuclear symmetry axis, in the K direction. Consider the extreme case where J is perpendicular to the beam axis. Then, the possible directions along which the fragments may be emitted are distributed along the surface of a sphere and the angular distribution can be approximated by the function $1/\sin\theta$. Previous work has shown that this approximation holds for all but the most extreme angles for fusion-fission angular distributions [53, 54, 55]. Much work has been done to extend the use of the transition state model understanding of the angular distribution to systems where quasifission occurs [54]. This is a difficult task, but one can leverage the fact that the transition state model relies on the assumption that the fissioning nucleus has equilibrated, which is not the case in quasifission [54]. Therefore, a deviation in the angular distribution from what would be expected in the transition state model can be taken as a signature of quasifission [54].

1.3.3 Mass-Angle Distributions

If mass and angle information is deduced for fission-like (fusion-fission and quasifission) fragments, then a two dimension mass angle distribution can be generated. Mass-angle distributions (MAD) are a useful tool in studying reaction dynamics of heavy-ion fusion reactions [4, 56, 40]. MADs generally relate the center-of-mass angles as a function of the corresponding mass ratio of an observed fragment. As discussed above, fission fragments will be concentrated at symmetric mass ratios and be isotropic in the center-of-mass frame. Therefore, a fusion-fission MAD will have very distinct appearance: a band of events evenly distributed in angle will be observed at symmetric mass ratios. An example of a fusion-fission MAD previously deduced for $^{12}\text{C} + ^{208}\text{Pb}$ [47] is shown in Figure 1.10, where the fusion-fission events fall as described above. Now, if quasifission is present, the appearance of the MAD changes. An example of the deduced MAD for $^{48}\text{Ti} + ^{192}\text{Os}$ [46] is shown

in Figure 1.11. As discussed in Section 1.3.1 quasifission is expected in this system and changes the appearance of the MAD. The groups of events near $M_R = 0.2$ and $M_R = 0.8$ are from elastic scattering events. The events in the fission-like region are no longer isotropic or concentrated at symmetric mass ratios. In fact, a correlation between mass and angle is observed in MADs where quasifission is present. This correlation is highlighted by the dashed, grey line in Figure 1.11.

This correlation is described in Figure 1.12. In Reaction I, the projectile and target have a large impact parameter. They form a dinuclear system that only rotates through a few degrees before separating. As a result, one fragment is still similar in mass to the projectile and the other fragment is still similar in mass to the target nucleus. Events similar to this case will populate the mass distributions in the regions indicated by I in Figure 1.5.

In the second case, Reaction II, the reaction takes place at a smaller impact parameter compared to Reaction I. The dinuclear system rotates more than 90° but less than 180° before separating. The longer contact time results in more mass exchange relative to Reaction I, but the system is still not fully mass equilibrated. As shown in Figure 1.5, these systems are at more symmetric mass ratios at II.

In the third case, that with the smallest impact parameter, the dinuclear system rotates beyond 180° . The contact time is long enough for significant of mass exchange and it is no longer possible to distinguish between the projectile-like and target-like fragments. These long-timescale quasifission events overlap with the fusion-fission events in the mass distribution, making them difficult to distinguish. While the characteristics of the MADs are similar for long-time scale quasifission and fusion-fission, both reaction channels can contribute to the final reaction products.

Quasifission reactions, like Reactions I and II in Figure 1.12, cause the broadening of the

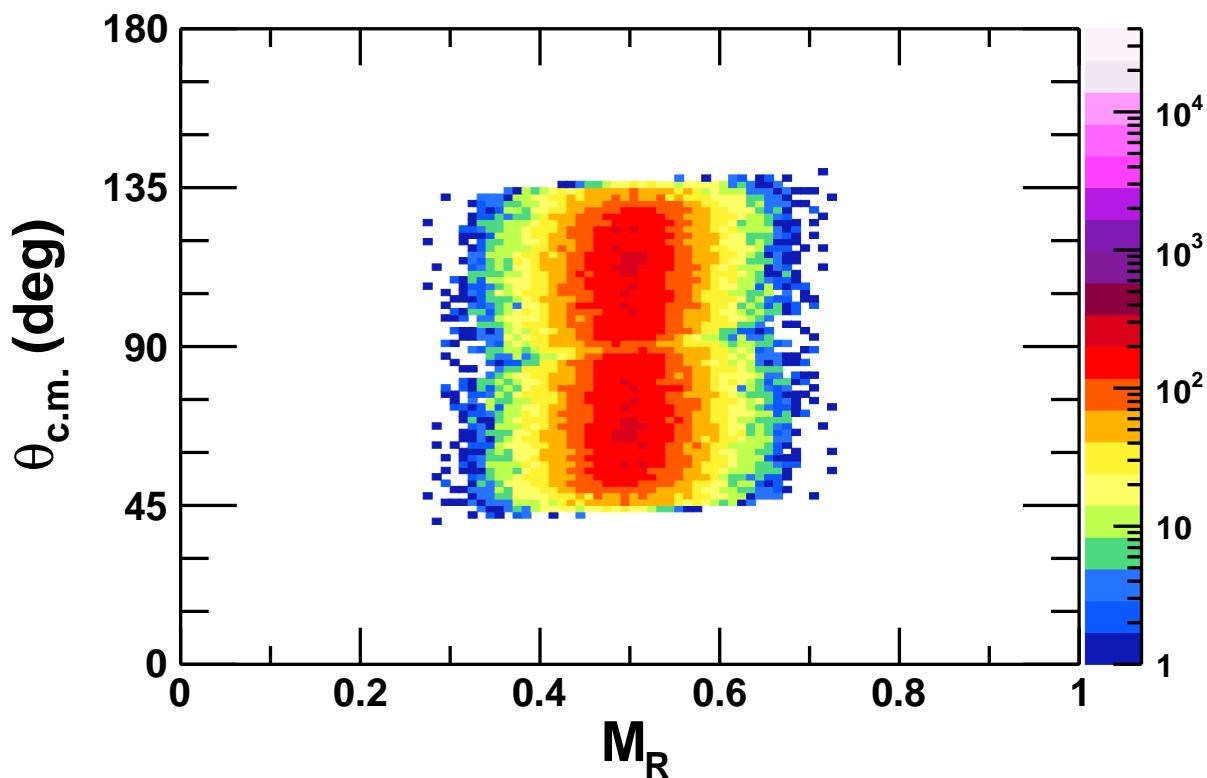


Figure 1.10: The mass angle distribution previously deduced from the reaction of $^{12}\text{C} + ^{208}\text{Pb}$ at $E_{\text{lab}} = 66.0$ MeV [47].

mass distribution relative to pure fusion-fission. As depicted in Figure 1.12, mass exchange, angle of rotation, and contact time are all related. The longer the system is in contact, the more opportunity there is for mass exchange.

1.3.3.1 Types of Mass Angle Distributions

Previous work by the reaction dynamics group at ANU has shown that medium mass heavy-ion fusion reactions can be categorized into three types by features observed in 42 MADs [40]. A map of the MADs for the 42 systems is shown in Figure 1.13. The projectile used is shown on the x-axis, the formed compound system is shown on the y-axis, and the diagonal lines indicate the target used in the reaction.

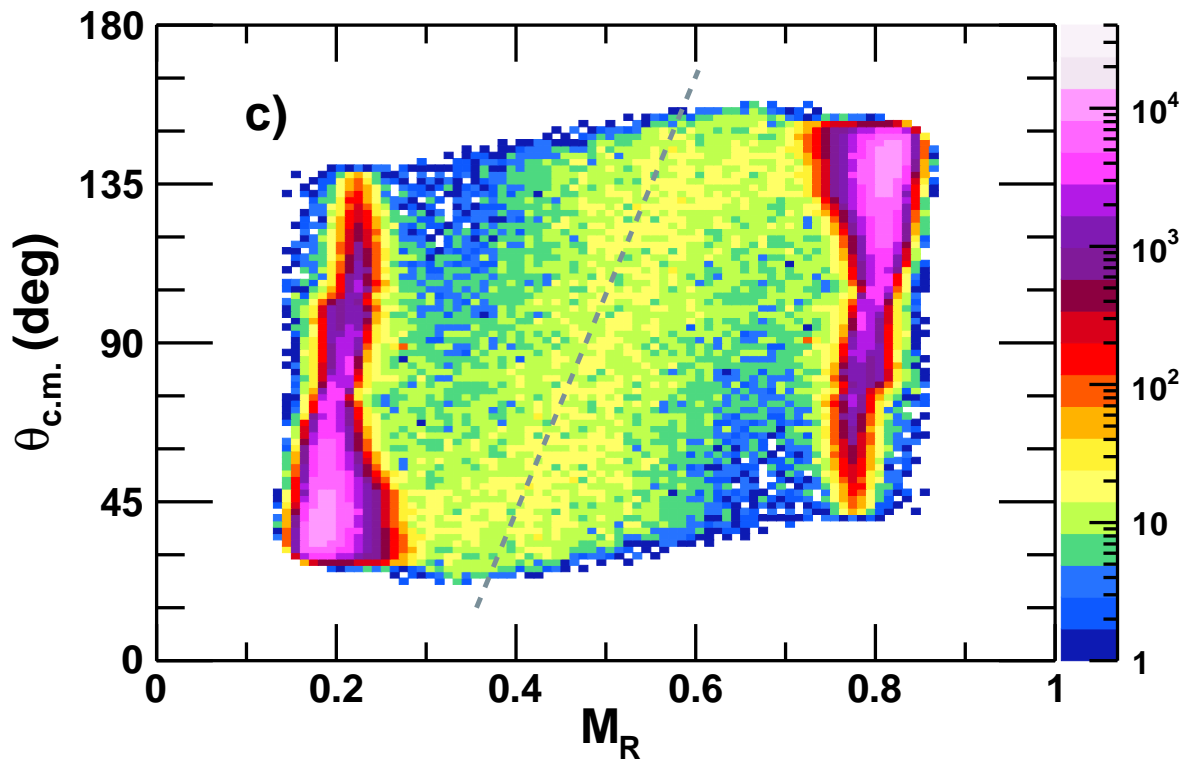


Figure 1.11: The mass angle distribution deduced from the reaction of $^{48}\text{Ti} + ^{192}\text{Os}$ at $E_{\text{lab}} = 259.9$ MeV [46]. The dashed, grey line is included to highlight the correlation between mass and angle.

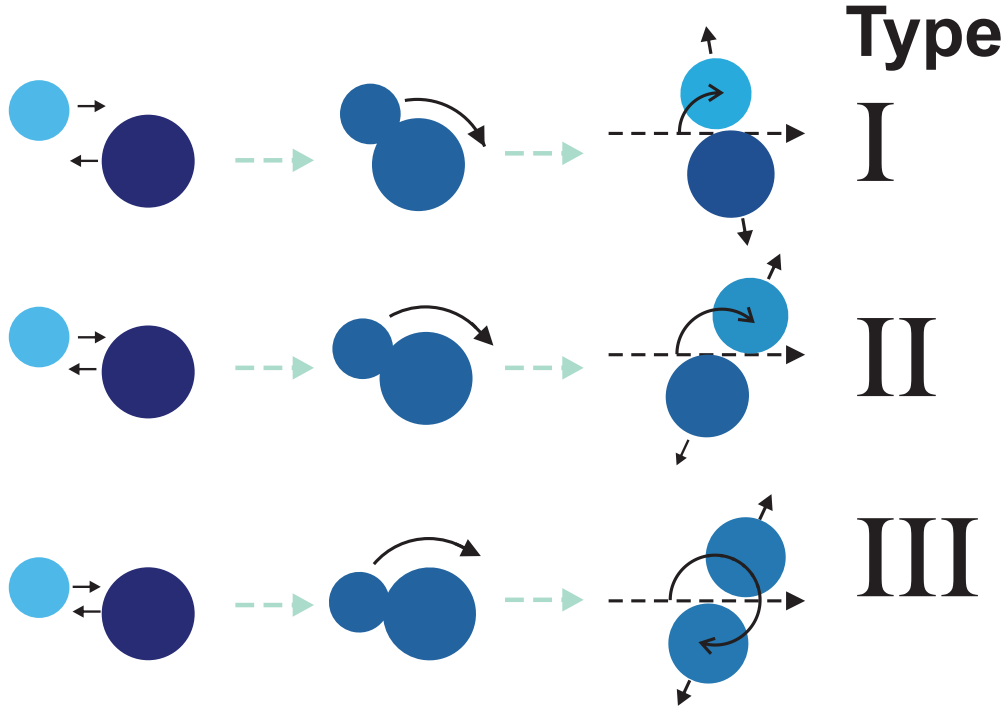


Figure 1.12: Three example quasifission reactions. Illustrating the influence of impact parameter of and angle of rotation of the mass and angle of the emitted fragments.

Du Rietz *et al.* [40] identified three types of MADs among these reactions. Examples of the three types were highlighted by Du Rietz *et al.* as shown in Figure 1.14. The types are correlated with the “Reactions” discussed above and shown in Figure 1.12. Extremely short timescale quasifission is observed in the MADs for Type I systems. This type is characterized by a minimum in the mass distribution at $M_R = 0.5$. In these systems, separation occurs quickly and very little mass transfer occurs. The MAD and mass distribution deduced from the reaction of $^{64}\text{Ni} + ^{170}\text{Er}$ are shown in Panels A and D in Figure 1.14 as an example of a Type I system. Medium length timescale quasifission is observed in the MADs of Type II systems. These systems are characterized by a correlation between mass and angle in the fission-like region of the MAD and a maximum in the mass distribution at $M_R = 0.5$. The MAD and mass distribution deduced from the reaction of $^{48}\text{Ti} + ^{186}\text{W}$ are shown in Panels B and E in Figure 1.14 as an example of a Type II system. Type III systems undergo long

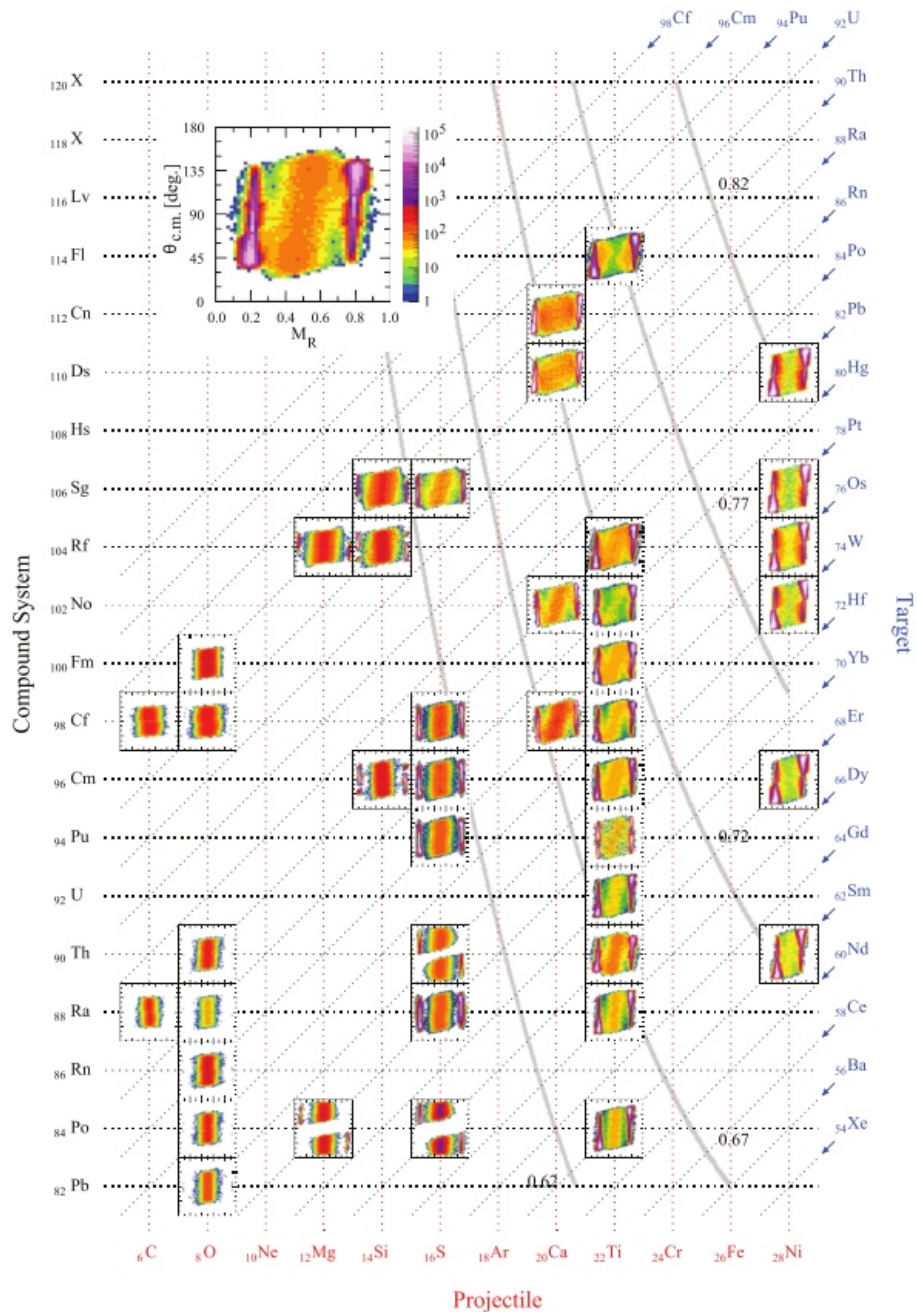


Figure 1.13: Plot of the 42 MADs reported in [40]. In the top left corner, the MAD deduced from the measurement of $^{48}\text{Ti} + ^{170}\text{Er}$ at $E_{\text{lab}} = 225.0$ MeV is enlarged to highlight the axis labels. Systems that fall along the same vertical, red, dashed- or diagonal, blue, dashed- lines were formed with the same projectile or target, respectively. Systems along the same horizontal, black, dashed lines formed the same compound nucleus. Reprinted figure with permission from [40] Copyright (2013) by the American Physical Society. <http://dx.doi.org/10.1103/PhysRevC.88.054618>

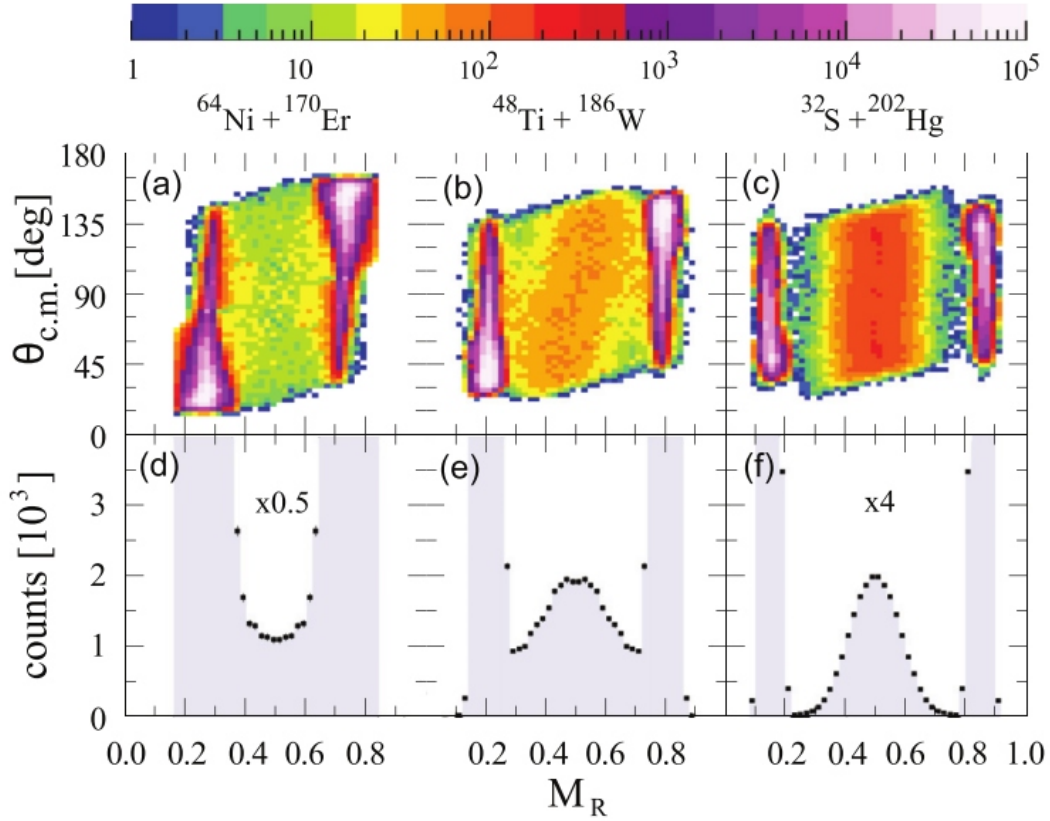


Figure 1.14: MADs representative of Types I, II, III as identified by Du Rietz *et al.* [40] are shown in Panels A, B, and C, respectively. The corresponding mass distributions are shown in Panels D, E, and F. Reprinted figure with permission from [40] Copyright (2013) by the American Physical Society. <http://dx.doi.org/10.1103/PhysRevC.88.054618>

timescale quasifission. The MADs for these systems are difficult to distinguish from those of pure fusion-fission. The MAD and mass distribution deduced from the reaction of $^{32}\text{S} + ^{202}\text{Hg}$ are shown in Panels C and F in Figure 1.14 as an example of a Type III system.

A distinction between the three types was observed when the charge of the compound nucleus was plotted as a function of charge product ($Z_1 Z_2$) [40] as shown in Figure 1.15. The boundary between Types I and II occurred along a line from $(Z_{\text{CN}}, Z_1 Z_2)$ of (80,1450) to (120, 1150) (indicated by the solid, blue line in Figure 1.15). The boundary between Types II and III was observed along a line from $(Z_{\text{CN}}, Z_1 Z_2)$ of (80,2000) to (120, 1700) (indicated

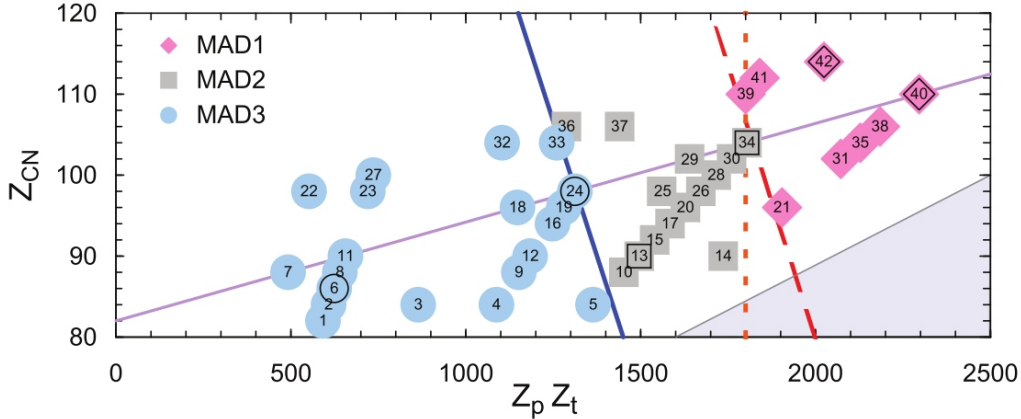


Figure 1.15: Z_{CN} as a function of $Z_p Z_t$ for the 42 reactions included in [40]. The identified boundaries between the Types of MADs are indicated by the solid, blue-and long-dashed, red-lines. Reprinted figure with permission from [40] Copyright (2013) by the American Physical Society. <http://dx.doi.org/10.1103/PhysRevC.88.054618>

by the long-dashed, red line in Figure 1.15). Systems of particular interest are those that fall along the lines between two of these types because they may provide insight into the change in the reaction dynamics.

1.3.4 Entrance Channel Energy and Quasifission

The entrance channel center-of-mass energy ($E_{c.m.}$) is an important factor in nuclear reactions, and in particular quasifission and fusion-fission competition. First, the $E_{c.m.}$ of the reaction is directly related to the compound nuclear excitation energy (E_{CN}^*), since E_{CN}^* is simply the sum of $E_{c.m.}$ and the Q value for fusion (Q_{fus}). Shell effects are known to play a large role in reaction dynamics at E_{CN}^* less than ≈ 20 MeV [57, 51]. Second, entrance channel deformation has been shown [58, 59, 41, 39, 60, 61, 62, 63, 64, 65] to hinder fusion in heavy-ion reactions at $E_{c.m.}$ near the interaction barrier (V_B) [9], where the relative orientation of deformed nuclei can significantly change the potential.

1.4 Heavy-Ion Fusion Reactions with Neutron-rich Rare Isotope Beams

Heavy-ion fusion reactions with neutron-rich, radioactive medium mass ($8 < z < 50$) projectiles are thus far fairly unexplored. Previously, there have been only three published results [66, 67, 68]. With the next generation rare isotope facilities, there will be opportunities to understand how the heavy-ion fusion reaction mechanism is affected by the use of neutron-rich, radioactive beams. In general, an increase in neutron-richness leads to an increase in the experimentally observed evaporation residue cross section [25, 69, 70]. However, the impact of increased neutron-richness on the probability of forming a fully-fused compound nucleus is still disputed.

Much previous work has been done to explore the interplay between quasifission and neutron-richness [71, 72, 73, 74, 75, 76, 77, 30, 78, 79, 80, 81]. However, these works led to conflicting conclusions. Some works concluded that the probability of forming a compound nucleus increases with increasing neutron-richness [74, 72], while others observed a decrease in P_{CN} with increasing neutron-richness [75, 73]. One challenge in all these works was that the final results required a theoretical model of the reaction dynamics to determine P_{CN} [71, 30, 72, 77, 78, 78]. Since model predictions of P_{CN} can vary significantly, the choice of model greatly affects the results of these works. In the present work, the change in quasifission with increasing neutron-richness was explored in a systematic, model independent way.

1.5 Organization of Dissertation

In this chapter the motivation for this work was discussed, including the effect of quasifission on superheavy element production and the need to understand the impact of increasing neutron-richness on quasifission for future SHE research. In Chapter 2 the Australia National University (ANU) Heavy-Ion Accelerator facility and the measurements that were performed are described. Then, the technique used to determine the mass ratios and center-of-mass angles of the reaction products is described Chapter 3. In Chapter 4, the mass distributions, angular distributions, and mass-angle distributions deduced for a series of Cr + W reactions at two different reaction energies are presented. Chapter 5 provides a discussion of the results. Finally, Chapter 6 gives some general conclusions from the work presented here.

Chapter 2

Experimental Details

The effect of neutron-richness on heavy-ion reaction dynamics can be studied by deducing mass and angular distributions for reactions between different isotopes of a given pair of elements. In this approach, the effect of neutron-richness can be isolated from the effects of other variables that are known to influence quasifission: compound nuclear fissility [71, 30], mass asymmetry [7], magicity [82, 83], deformation [60, 46, 63], and charge product [40]. The design of the experiment carried out as part of this work, including a justification for the systems and energies that were selected and a description of the experimental equipment, is discussed in this chapter.

2.1 System Selection

For the present work, chromium (Cr, $Z=24$) was selected as the projectile and tungsten (W, $Z=74$) was selected as the target. The results from the Cr + W, medium mass system provide relevant information important for future medium mass measurements with radioactive ion beams that will be available at next generation facilities. Only even-even isotopes of Cr and W were considered here to minimize pairing effects. Table 2.1 lists the natural abundances and half-lives of all isotopes used in the present work. There are two stable and one very long-lived, even isotopes of Cr: 54, 52, and 50, respectively. Natural chromium was used as the source material for the measurements involving ^{52}Cr because it is the most abundant

isotope. Isotopically-enriched samples of $^{50,54}\text{Cr}$ were obtained from Isoflex with 97.4% and 99.20% purity, respectively, for the measurements with these isotopes. W has one very long-lived and three stable, even isotopes: 180, 182, 184, and 186, respectively. Isotopically-enriched targets of each W isotope were prepared at Argonne National Laboratory and the preparation of the targets is described in [84]. Each W target was backed with carbon to support the thin deposit of the heavy element. Table 2.2 contains a list of W and C thicknesses for each target.

In the series of Cr + W reactions considered in the present work the following items need consideration: (a) Only one isotope, ^{52}Cr , has a closed nuclear shell ($N = 28$); (b) The Cr + W reactions have the same entrance channel charge product, of course ($Z_p Z_t = 1776$); (c) The W isotopes are all significantly deformed, but with similar values of β_2 in the range of 0.23-0.26; and (d) A large range in neutron number was available between the Cr + W systems because of the many available isotopes. The most neutron-deficient reaction ($^{52}\text{Cr} + ^{180}\text{W} \rightarrow ^{230}\text{Cf}$) and the most neutron-rich combination ($^{54}\text{Cr} + ^{186}\text{W} \rightarrow ^{240}\text{Cf}$) differ by 10 neutrons. The combination of a wide range in neutron number in the compound nucleus with limited variation in magicity, $Z_p Z_t$, and deformation makes Cr + W an ideal system for exploring the effect of neutron-richness on quasifission in medium mass reactions. Additionally, with a charge product of 1776 and compound nucleus charge of 98, the chromium and tungsten system falls on the boundary determined by Du Rietz *et al.* [40] between Type II and III systems as discussed in Section 1.3.3.1.

2.1.1 Two Energy Regimes

As discussed in Section 1.3.4 the entrance channel energy of the reaction plays a key role in quasifission and fusion-fission competition. The excitation energy of the compound nucleus

Table 2.1: Chromium and tungsten isotopic information including percent abundances (half-lives), β_2 values, and any magic numbers in the nucleus.

Isotope	Percent Abundance (half-life) [85]	β_2 [86]	Magic Number
^{50}Cr	4.345 % ($\geq 1.3 \times 10^{18}$ y)	0.0	No
^{52}Cr	83.789%	0.0	Yes, N=28
^{54}Cr	2.365 %	0.0	No
^{180}W	0.12 % ($\geq 6.6 \times 10^{17}$ y)	0.258	No
^{182}W	26.50 %	0.259	No
^{184}W	30.64 %	0.24	No
^{186}W	28.43 %	0.23	No

Table 2.2: Tungsten target and carbon backing thickness, and reaction [84]

Isotope	Thickness ($\mu\text{g cm}^{-1}$)	Carbon Backing ($\mu\text{g cm}^{-1}$)	Projectile and E_{Lab} (MeV)
^{180}W	48	60	^{50}Cr , 284.6; ^{50}Cr , 268.3; ^{52}Cr , 285.0; ^{52}Cr , 276.0
^{180}W	46	60	^{54}Cr , 280.0
^{182}W	97	80	^{54}Cr , 284.4; ^{50}Cr , 277.2
^{184}W	64	40	^{52}Cr , 282.3; ^{52}Cr , 269.0; ^{54}Cr , 283.1; ^{50}Cr , 274.0
^{186}W	43	40	^{50}Cr , 280.4; ^{50}Cr , 255.5; ^{54}Cr , 281.7; ^{54}Cr , 270.3

and the ratio of the center-of-mass energy to the interaction both effect the quasifission reaction channel [57, 51, 58, 59, 41, 39, 60, 61, 62, 63, 64, 65]. To help disentangle these two effects, each reaction system was measured at two $E_{c.m.}$ values: $E_{c.m.} / V_B = 1.13$ and $E_{CN}^* = 52.0$ MeV. The constant fraction above the Coulomb barrier of $E_{c.m.} / V_B = 1.13$ has been shown to be high enough above the barrier that deformation effects should be minimal [46]. The constant compound nuclear excitation energy of $E_{CN}^* = 52.0$ MeV is comparable to hot fusion reactions, where three to four neutrons are evaporated from very heavy compound nuclei in attempts to form new elements. Additionally, $E_{CN}^* = 52.0$ MeV is sufficiently higher than the 20 MeV generally required to minimize shell effects in the dinuclear system. By studying these systems in both energy regimes, the effect of neutron-richness can be explored independent of the energy effects. The energetics of the set of reactions to meet the $E_{c.m.}$ requirements are given in Table 2.3.

2.1.2 Cr + W Systems

Eight Cr + W systems were measured in the two different energies regimes at the Australia National University (ANU) Heavy Ion Accelerator Facility. The Heavy Ion Accelerator Facility at ANU provided an ideal location for the series of Cr + W measurements since a large number of systematic studies of heavy-ion fusion reactions have previously been completed at the Heavy-Ion Accelerator Facility by the reaction dynamics group at ANU, led by Dr. David Hinde. The present work benefited from the previous experience of the local group, and the well-established detector systems for heavy-ion fusion studies [41, 39, 87, 60, 39, 40, 65, 64, 7, 83]. The CUBE detector [41, 40] (see Figure 2.3) was specifically designed to measure mass and angle distributions of fission fragments from heavy-ion induced reactions. The CUBE is composed of two large area, position sensitive multiwire proportional

counters (MWPC) and resides in a vacuum chamber on a dedicated beam line downstream of the 14 UD tandem accelerator and the Superconducting Linear Accelerator (LINAC). The ANU facility provided beams (10^9 – 10^{10} pps) of the Cr isotopes at the energies listed in Table 2.3 during the course of about one week. To demonstrate that this work can explore the probability of forming the compound nucleus, it is important to exclude the effects of the capture cross section or the evaporation residue cross section. The capture cross section and l_{crit} were calculated using the PACE4 code in Lise++ [88] and are listed in Table 2.4. As these quantities are energy dependent, Table 2.4 is separated into two sections based on the entrance channel energy. PACE4 also calculated an evaporation residue cross section of 0 mb for each Cr + W system. The values of l_{max} was also calculated for each system as

$$l_{\text{max}} = \sqrt{\frac{\sigma_{\text{cap}}}{\pi\lambda^2}} + 1 \quad (2.1)$$

and are listed in Table 2.4. The remainder of this chapter describes the equipment used to measure the mass and angle distributions for the Cr + W reactions.

2.2 The ANU Heavy-Ion Accelerator Facility

The ANU Heavy Ion Accelerator Facility consists of a 14 UD Pelletron tandem accelerator and a superconducting LINAC, shown schematically in Figures 2.1 and 2.2, respectively. The following sections describe each of the primary components of the present measurements: ion source, tandem accelerator, superconducting LINAC, CUBE detector system, and data acquisition.

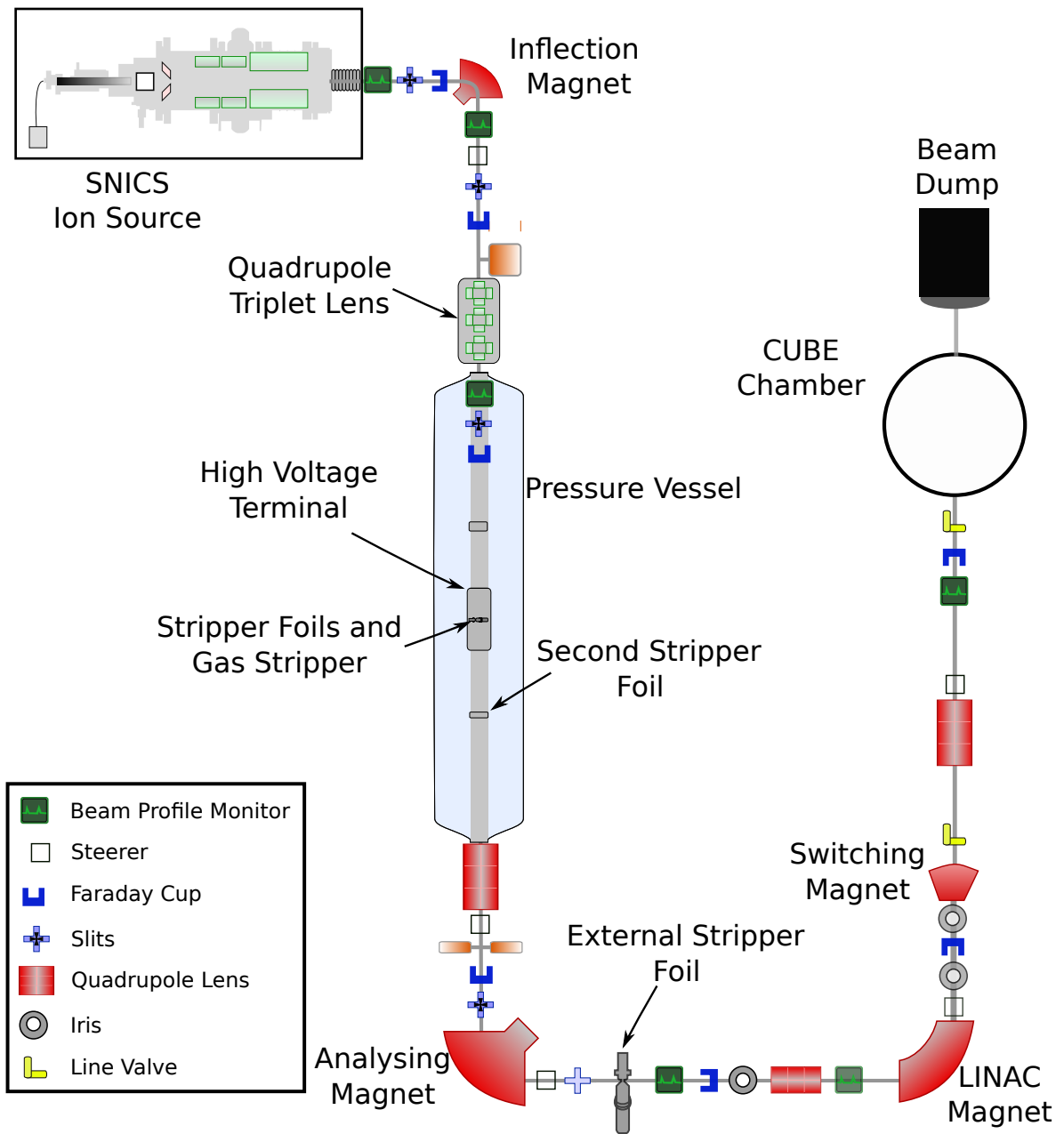


Figure 2.1: Schematic diagram of the ANU heavy-ion accelerator facility. The ion source is shown at the top (more detail in Figure 2.3). The 14UD Pelletron Tandem accelerator is in the center, followed by an analysing magnet and the connection to the CUBE beam line. Only the LINAC magnet is indicated here and a schematic diagram of the complete LINAC is shown in Figure 2.2

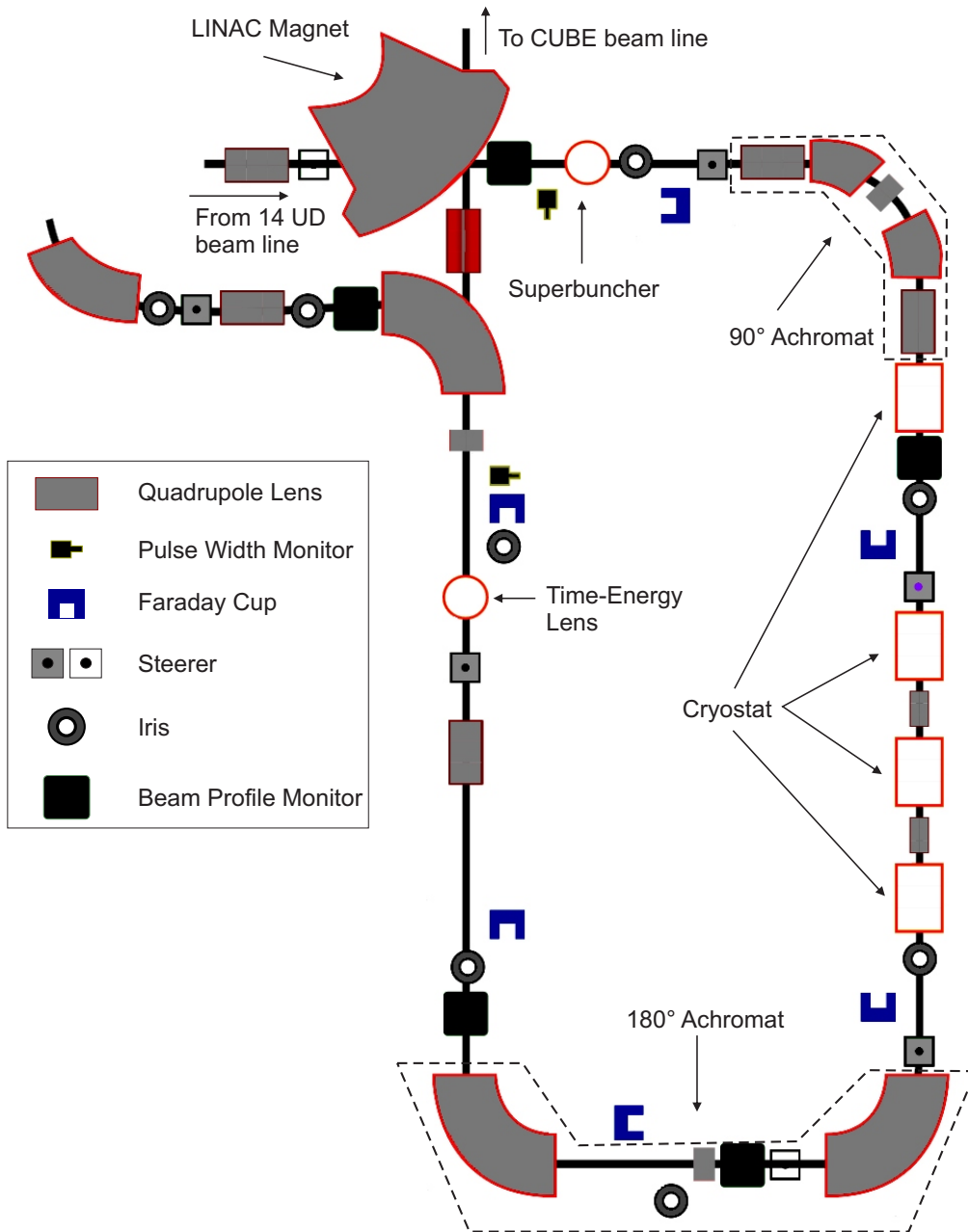


Figure 2.2: Schematic diagram of the ANU LINAC. The cryostats are depicted as well as many beam line components including the two achromats and the pre and post bunchers.

Table 2.3: Cr + W systems, compound nuclei, relative change in neutrons (ΔN), fusion Q value (Q_{fus}), Bass interaction barrier (V_B) [9], $E_{\text{c.m.}}$ for both energy regimes

Reaction	ΔN	Q_{fus} (MeV)	V_B (MeV)	$E_{\text{c.m.}}/ V_B = 1.13$		$E_{\text{CN}}^* = 52.0 \text{ MeV}$	
				$E_{\text{c.m.}}$ (MeV)	E_{CN}^* (MeV)	$E_{\text{c.m.}}$ (MeV)	$E_{\text{c.m.}} / V_B$
$^{50}\text{Cr} + ^{180}\text{W} \rightarrow ^{230}\text{Cf}$	0	-158.0	196.95	222.6	64.6	210.0	1.07
$^{50}\text{Cr} + ^{186}\text{W} \rightarrow ^{236}\text{Cf}$	6	-149.3	195.59	221.0	71.7	201.4	1.03
$^{52}\text{Cr} + ^{180}\text{W} \rightarrow ^{232}\text{Cf}$	2	-162.1	195.75	221.2	59.1	214.1	1.09
$^{52}\text{Cr} + ^{184}\text{W} \rightarrow ^{236}\text{Cf}$	6	-157.7	194.80	220.1	62.4	209.7	1.08
$^{54}\text{Cr} + ^{180}\text{W} \rightarrow ^{234}\text{Cf}$	4	-163.1	194.56	219.8	56.7	215.4	1.11
$^{54}\text{Cr} + ^{182}\text{W} \rightarrow ^{236}\text{Cf}$	6	-161.8	194.12	219.3	57.6	213.8	1.10
$^{54}\text{Cr} + ^{184}\text{W} \rightarrow ^{238}\text{Cf}$	8	-159.8	193.67	218.9	59.0	211.8	1.09
$^{54}\text{Cr} + ^{186}\text{W} \rightarrow ^{240}\text{Cf}$	10	-157.5	193.22	218.3	73.1	207.5	1.08

2.2.1 Ion Source

The ion source used for the present work was a National Electrostatics Corporation (NEC) source of negative ions produced by cesium sputtering (SNICS) of the solid chromium material. The source is located at the top of the 14UD tower [89]. A schematic diagram of the source is shown in Figure 2.3. The active volume of the source is a chamber filled with cesium vapor. The cesium vapor is produced by liquifying Cs at 100 to 120°C in a reservoir that is separated from the chamber. The Cs is allowed to pass into the active volume of the source through a delivery tube that is held at 200°C. The solid Cr metal was placed in a vial in the cathode at the end of the active volume of the source. Recall that three different source materials were used for these experiments: $^{nat,50,54}\text{Cr}$. In the middle of the source, there are two ionizers for the cesium. Each ionizer has a tungsten ionizing surface heated to 1000°C. When Cs atoms come into contact with the ionizer they lose an electron because the tungsten has a higher electron affinity than cesium. Positively-charged Cs ions

Table 2.4: Cr + W systems, compound nuclei, relative change in neutrons (ΔN), $E_{\text{c.m.}}$, E_{CN}^* , interaction cross section (mb) [88], l_{max} , and l_{crit} [88] for both energy regimes

Reaction	ΔN	$E_{\text{c.m.}}$ (MeV)	E_{CN}^* (MeV)	σ_{cap} (mb)	l_{max}	l_{crit}
$E_{\text{c.m.}}/V_{\text{B}} = 1.13$						
$^{50}\text{Cr} + ^{180}\text{W} \rightarrow ^{230}\text{Cf}$	0	222.6	64.6	629.0	90	81
$^{50}\text{Cr} + ^{186}\text{W} \rightarrow ^{236}\text{Cf}$	6	221.0	71.7	628.9	90	82
$^{52}\text{Cr} + ^{180}\text{W} \rightarrow ^{232}\text{Cf}$	2	221.2	59.1	626.4	91	83
$^{52}\text{Cr} + ^{184}\text{W} \rightarrow ^{236}\text{Cf}$	6	220.1	62.4	625.3	91	83
$^{54}\text{Cr} + ^{180}\text{W} \rightarrow ^{234}\text{Cf}$	4	219.8	56.7	623.1	92	84
$^{54}\text{Cr} + ^{182}\text{W} \rightarrow ^{236}\text{Cf}$	6	219.3	57.6	623.3	92	85
$^{54}\text{Cr} + ^{184}\text{W} \rightarrow ^{238}\text{Cf}$	8	218.9	59.0	623.2	92	85
$^{54}\text{Cr} + ^{186}\text{W} \rightarrow ^{240}\text{Cf}$	10	218.3	60.85	622.7	92	85
$E_{\text{CN}}^* = 52.0 \text{ MeV}$						
$^{50}\text{Cr} + ^{180}\text{W} \rightarrow ^{230}\text{Cf}$	0	210.0	52.0	365.3	67	58
$^{50}\text{Cr} + ^{186}\text{W} \rightarrow ^{236}\text{Cf}$	6	201.4	52.0	166.6	44	39
$^{52}\text{Cr} + ^{180}\text{W} \rightarrow ^{232}\text{Cf}$	2	214.1	52.0	452.0	76	71
$^{52}\text{Cr} + ^{184}\text{W} \rightarrow ^{236}\text{Cf}$	6	209.7	52.0	403.4	72	64
$^{54}\text{Cr} + ^{180}\text{W} \rightarrow ^{234}\text{Cf}$	4	215.4	52.3	536.6	85	76
$^{54}\text{Cr} + ^{182}\text{W} \rightarrow ^{236}\text{Cf}$	6	213.8	52.0	491.8	81	75
$^{54}\text{Cr} + ^{184}\text{W} \rightarrow ^{238}\text{Cf}$	8	211.8	52.0	445.5	76	72
$^{54}\text{Cr} + ^{186}\text{W} \rightarrow ^{240}\text{Cf}$	10	207.5	52.0	397.6	72	69

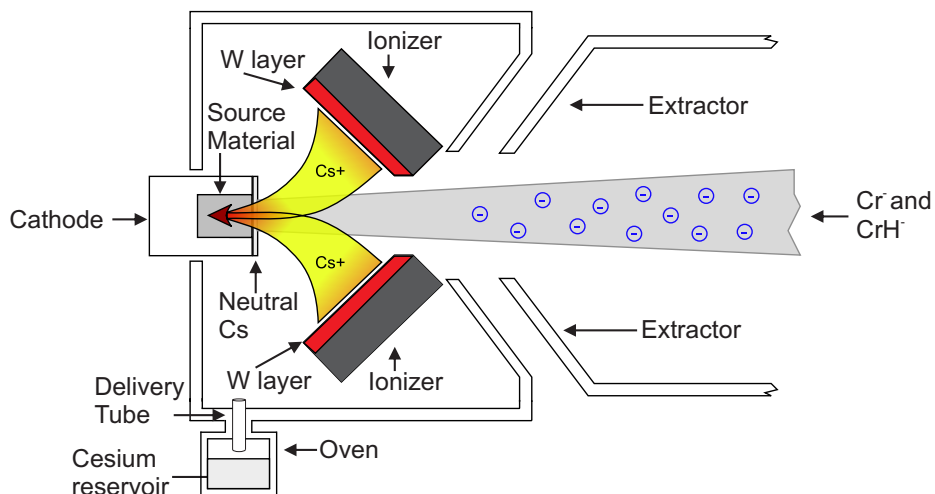


Figure 2.3: Schematic diagram of the operation of the SNICS showing the active volume of the source, the ionizers, the cathode, the path of ionized Cs and the path of sputtered sample material.

are then drawn towards the Cr by a 5kV charge on the cathode, as depicted in Figure 2.3. The cathode is cooled to 20°C so a layer of condensed Cs atoms forms on the surface of the cathode and serves as a source of e^- for the production of negative ions of the source material. The ionized Cs sputters the source material on impact and some negative chromium ions are formed by electron transfer from the neutral cesium.

The Cr ions were extracted as molecular ions because of their electron affinity [90]. Cr hydrides were produced by introducing ammonia gas into the ion source volume near the cathode. The negative hydride ions were repelled by the 5-kV charge of the cathode and accelerated out of the ion source.

After the CrH⁻ molecular ions were extracted from the source, they were accelerated by a 150 kV potential difference. Next, a 90° inflection magnet was used to separate the various components of the beam from the ion source. The magnetic field (B) needed to select the

mass to charge ratio of the ion to be accelerated can be calculated from the expression:

$$B_{\rho} = \frac{\sqrt{2mE}}{q} \quad (2.2)$$

where m is the mass of the ion of interest, E is the kinetic energy of the ions after the 150 kV acceleration, ρ is the radius of the ions through the magnet, and q is the charge state of the ion of interest. For example, selection of $^{50}\text{CrH}^{-}$ beam from the ion source under these conditions would require

$$B_{\rho} = \frac{\sqrt{2 * 50.954\text{amu} * 931.5\text{MeV}/c^2\text{amu} * .150\text{MeV}}}{1.602 * 10^{-19}\text{Coul}} = 0.398\text{Tm} \quad (2.3)$$

2.2.2 14 UD Pelletron

NEC also made the 14 UD Tandem Van de Graff accelerator [91, 92, 93] that is the primary accelerator at the facility. The operating principles of the accelerator were described in detail in Refs. [94, 95]. Negatively-charged ions from the ion source are accelerated by a large positive electrostatic potential to the terminal; there they are stripped of some electrons and accelerated away from the terminal. The maximum terminal voltage available from the 14UD accelerator is 15.5 million volts [93]. In the case of the 14 UD tandem accelerator, the positively-charged terminal in the center of the accelerating tube is charged by a three chain Pelletron charging system [92], composed of cylindrical metal pellets separated by insulating nylon links. Each pellet is positively charged through inductive charge transfer at the bottom of the accelerator tube to provide a net positive charge to the pellet, which is then moved to the terminal by a motor and pulley system. At the terminal, each metal pellet is brought in contact with the terminal and the positive charge becomes distributed

on the whole terminal. The accelerator tube is filled with sulfur hexafluoride gas (SF_6) at 6 bar to minimize electrostatic discharges.

In the first step of acceleration in the 14 UD tandem, negative ions are accelerated from ground potential to the positively charged terminal of voltage V_T . This stage of acceleration provides an energy gain of $\mu(eV_T)$, where μe is the electronic charge of the ion and is $1e$ for the ions out of the SNICS source (e is the charge of the electron).

Inside the terminal, the ions pass through a $4 \mu\text{g cm}^{-2}$ carbon stripper foil to break up the CrH^- and remove some electrons [96] from the metal atom. The new charge q state of the ions can be calculated from the empirical expression [97, 98]

$$q = Z \left[1 + Z^{3/4} \left(3.86 \frac{E}{A} \right)^{-1.67} \right]^{-0.6}, \quad (2.4)$$

where E is the kinetic energy of the atom, A is the mass number, and Z is the atomic number. For example in the present case, ^{50}Cr at 14.4 MeV, one would expect $q = 5+$. The positively-charged ions are then accelerated back to ground potential for an energy gain of $q_i V_T$ for ions of charge state q_i . In total, the energy gained in the two stages of acceleration can be calculated as

$$E = q_i V_T + V_T + 0.150 \text{MeV} - \frac{dE}{dx} \quad (2.5)$$

After acceleration, the desired beam is selected by a high resolution 90° analyzing magnet based on the charge to mass ratio. Notice that the energies required for this experiment were larger than those that the 14UD accelerator could provide, so the superconducting LINAC booster was used as well. For example in the measurement of the $\text{Cr} + \text{W}$ reaction, the maximum energy available from the tandem was 273 MeV in the lab frame. In the center-

of-mass frame for the $^{50}\text{Cr} + ^{180}\text{W}$ this is about 214 MeV and is lower than the energies listed in Table 2.3.

2.2.3 Superconducting LINAC

The beam from the tandem is continuous in time. A LINAC, on the other hand, only works with pulsed beams. Before injection into the LINAC, the beam from the tandem is bunched into 100 ps FWHM buckets by a Superbuncher Quarter Wave Resonator. The LINAC consists of 12 Applied Superconducting Incorporated Split Loop Resonators in four cryostats as indicated in Figure 2.2. The 12 resonators work together to provide a 6 MeV/q energy gain. After acceleration, the beam is rebunched to minimize spread at the target. The beam line uses a 180° achromatic section and then the CUBE beam line as shown in Figure 2.2.

2.3 The CUBE Detector System

The CUBE detector system has served as the primary detector for reaction dynamics experiments at ANU [40, 41]. The device is housed in a vacuum chamber that is maintained at $\sim 2 \times 10^{-5}$ Torr during operation. The CUBE consists of two MWPCs with an active area of $28 \times 36 \text{ cm}^2$ each. Each MWPC provides a position and timing measurement, so that the mass ratio and center of mass angle for fragments can be deduced by using the kinematic coincidence method [41], described in the Section 3.4. The Front MWPC covered lab angles between $5^\circ < \theta_{\text{lab}} < 80^\circ$ and the Back MWPC covered lab angles between $50^\circ < \theta_{\text{lab}} < 125^\circ$ during the present work. In Φ , the Front and Back MWPCs were centered at $\Phi_{\text{lab}} = 0^\circ$ and $\Phi_{\text{lab}} = 180^\circ$, respectively. The front wire plane of each MWPC was 18 cm from the center

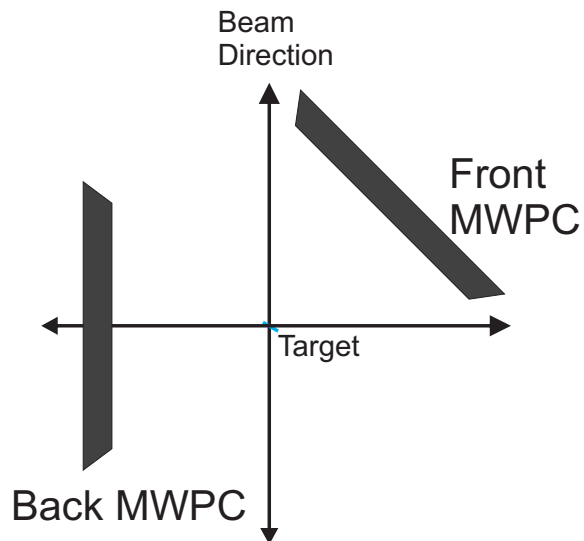


Figure 2.4: Schematic scale diagram of the layout of the detectors inside the CUBE detector system as viewed from above. One monitor detector is above the beam path and the other is below, see text.

of the target. These positions were selected to provide optimal coverage of the folding angles for fission-like fragments emitted perpendicular to the plane of the target in these reactions. A schematic drawing of detectors that make up the device is shown in Figure 2.4.

The CUBE target ladder can hold seven 1.9 mm diameter targets in addition to one tuning aperture and was mounted in the center of the chamber as shown in Figure 2.5. The W targets were rotated 30° with respect to the beam axis as shown in Figure 2.4. Two silicon surface barrier detectors were used to measure Rutherford scattering along the beam direction. They are highlighted by the red circles in Figure 2.5. The Si monitor mount provides three options for the placement as shown in Figure 2.5. For the present work, they were placed 18 cm behind the target at $\theta_{\text{lab}} = 22.5^\circ$ and $\Phi_{\text{lab}} = 90^\circ$ and 270° .

2.3.1 MWPCs

MWPCs utilize the ionization created by charged particles passing through a gas to provide a measure of the time and position of that particle [99, 100, 101]. A rendering of the design of the two MWPCs inside the CUBE chamber is shown in Figure 2.5. MWPCs, like other proportional counters, rely on charge multiplication in the gas (called a Townsend avalanche) to amplify the electrons from the primary ionization produced by the interaction of the charged particle with the gas [102]. In a Townsend Avalanche, electrons are accelerated by a strong electric field over a distance of one mean-free path and gain enough energy to cause additional ionization [102]. This process is repeated until the electrons are collected on the anode. MWPCs are similar to other proportional counters with anode wires. Thin wires are used so that electrons that are far from the anode will find that the electric field is fairly uniform, but when the electrons approach the anode wire they encounter a steeply rising electric field. Therefore, the electrons are accelerated towards the nearest wire and the avalanches produced near an individual wire induce large signals on the wire and give a position resolution based on the spacing of the wires and the time delay of the signals [102].

2.3.2 Structure of the CUBE MWPCs

In a CUBE MWPC, the layer of the detector nearest to the target was a $0.9\mu\text{m}$ thick Mylar pressure window (to reduce diffusion of the gas through the window) and was coated with copper to limit charge build up on the Mylar. The pressure window thus defined the gaseous volume of the detector. Each detector was filled with propane gas to a pressure of 3.5 Torr relative to the chamber. Each pressure window was retained by four vertical and three horizontal 0.45 mm diameter stainless steel wires to mitigate the bowing of the foil due to

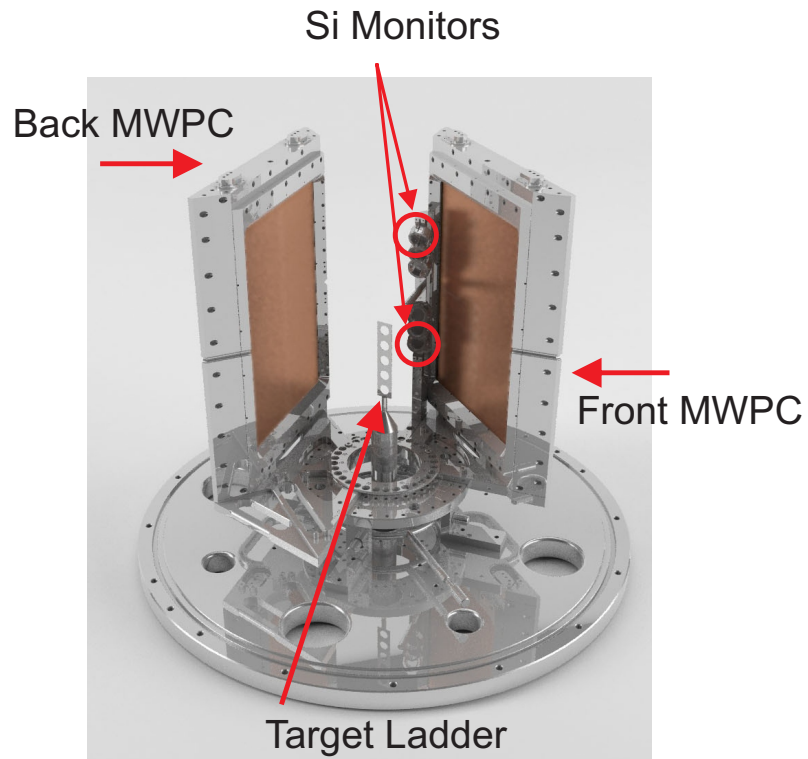


Figure 2.5: Rendering of the CUBE detector setup as used in the present work. The Front and Back MWPCs, the beam direction, the target ladder support, and the two Si monitor detectors are indicated.

the pressure differential. Inside each MWPC are two orthogonal anode wire planes composed of gold-coated tungsten wires, $20\mu\text{m}$ in diameter and spaced at 1 mm intervals. The vertical plane was made up of 357 wires and the horizontal had 284 wires to provide two dimensional position sensitivity. Signals from the anode wires were read out using 10-tap passive delay chips that were connected in series. Each anode wire was connected to a 1 ns tap of a delay chip. The two anode planes were 6 mm apart and separated by a central cathode foil (3 mm from each anode). The cathode was a $0.9\ \mu\text{m}$ thick Mylar foil that had $40\ \mu\ \text{gcm}^{-2}$ of Au on each side. The gold was segmented into 4 quadrants on each side to limit the capacitance of the foil. The cathode was charged to -490 V during this experiment. The back plane of the detector was a solid plate that held the time delay lines.

A fragment observed in the one of the MWPCs produces an energy signal that travels through the time delay lines. The relative time difference between the signals at each end of the delay line cables provides a measurement of the position at which the event occurred. Each time delay signals was sent into a 11-bit Silena 7423 UHS analog-to-digital converter. The position resolution was limited by the 1 mm radius of the beam spot on the target [103]. The position and timing information recorded from the CUBE was then used to provide mass and angle information for each event as described in the next chapter.

Chapter 3

Data Analysis Techniques

This chapter describes the techniques used to determine the mass ratios and center-of-mass angles from the timing and position signals observed for coincident two-body events in the CUBE detector setup. The coordinate systems used in the present work are described. The calibration of the position and timing signals observed in the MWPCs in the present work are discussed. The kinematic coincidence method [4] was used to determine the velocity vectors for each detected fragment from the position and timing signals and is described in Section 3.4. A C++ based program using the Root Data Analysis Framework [104], developed by the reaction dynamics group at ANU for CUBE measurements, called Dagui, was used for the analysis.

3.1 Coordinate System Definition

In this section, the coordinate systems used in the present work are defined. Each MWPC has a coordinate system defined within its active detection area as illustrated in Figure 3.1. The shorter length was parallel to the beam axis during the measurements and defined as the x dimension. The longer dimension was perpendicular to the beam direction and defined as the y dimension. The coordinates in units of mm of the center of each edge are indicated. Note that there is an offset between the electronic center and the physical center of the detectors. In the present work, the center of the detector refers to the electronic center,

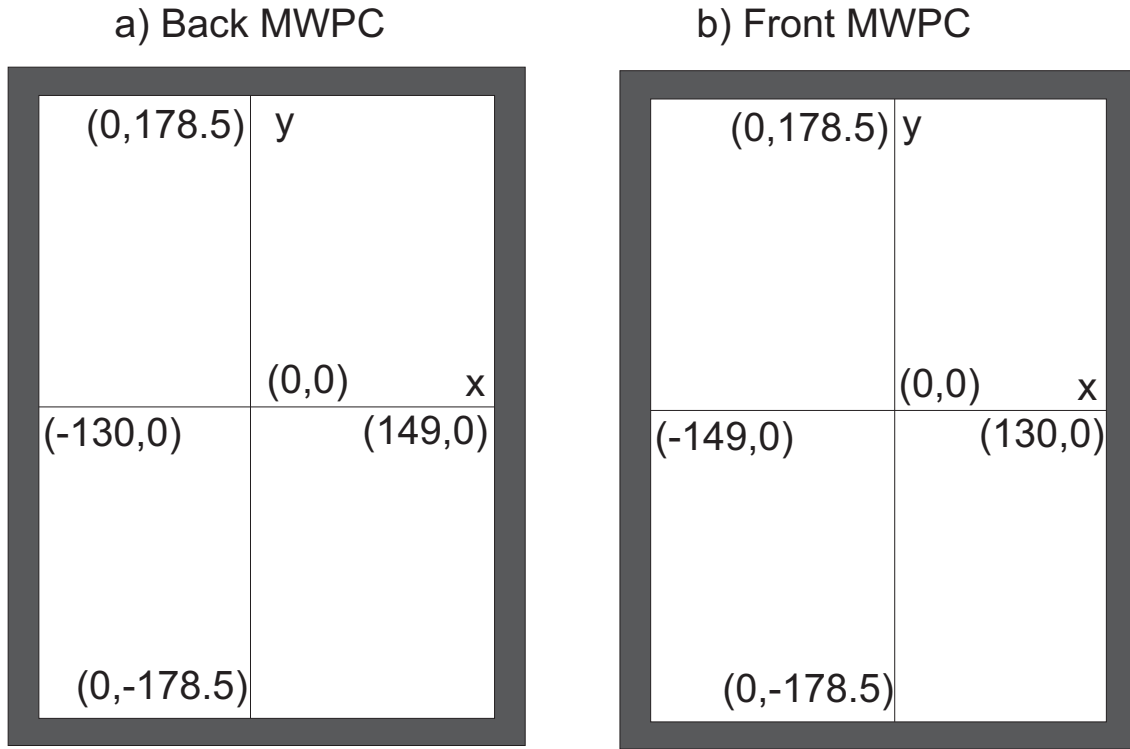


Figure 3.1: Schematic scale diagram of the individual MWPC coordinate systems used in the present work. The gray borders represent the MWPC support structure and the white inner regions represent the active area of the MWPCs. The four position quadrants of the MWPCs cathodes are indicated. The coordinates at the center of the detector and the center of each edge of the active area are indicated in units of mm.

defined as $(0,0)$ in mm in the (x, y) plane.

The two MWPCs are included within the full CUBE detector setup Cartesian coordinate system as shown to scale in Figure 3.2. Note that the shapes representing the target are to scale with the size of a target frame to make them more visible in the diagram. The center of CUBE Cartesian coordinate system, where $(X, Y, Z) = (0,0,0)$, is defined at the center of the target. The Z dimension is defined along the beam axis. The X dimension is defined perpendicular to the beam axis and through the center of the Back MWPC. The Y dimension is defined perpendicular to the X and Z dimensions. A scale diagram of the $(X, 0, Z)$ plane in the CUBE detector setup is shown in Panel A of Figure 3.2 from a top

down view. The $(X, 0, Z)$ plane is defined between the center of the target and the centers of the MWPCs. Panel B shows a scale diagram of the $(X, Y, 0)$ plane in the CUBE setup from the point of view of the beam upstream of the target. The $(X, Y, 0)$ plane is defined between the center of the target and the center Back MWPC, normal to the beam direction. In Figure 3.2, the (X, Y, Z) coordinates at the centers of the two MWPCs are indicated. This coordinate system can then be converted to the spherical coordinate system illustrated in Figure 3.3.

The same schematic diagrams of the CUBE detector setup are illustrated in Panels A and B in Figure 3.3 as in Figure 3.2. The θ and ϕ definitions were selected to be consistent with previous measurements from the CUBE detector setup. In the present work, θ is defined in the plane between the center of the target and the centers of the MWPCs as illustrated in Panel B in Figure 3.3. $\theta = 0^\circ$ is defined at the beam axis downstream of the target, $\theta = 180^\circ$ is defined at the beam axis upstream of the target and θ is always defined between 0° and 180° . Φ is defined along a circle centered on the beam axis in any plane normal to the direction of the beam, like the example illustrated in Panel B in Figure 3.3. $\Phi = 0^\circ$ at the center of the Front MWPC and as $\Phi = 180^\circ$ at the center of the Back MWPC. Φ is defined to be between 0° and 180° above the beam axis and between 180° and 360° below the beam axis. The radius, r , is defined as the distance from the center of the target to a given position within the CUBE setup. The center of each MPWC was 180 mm from the center of the target. The spherical coordinates at the center of the two MWPCs are indicated in Figure 3.3. Table 3.1 lists the coordinates corresponding to the center of the detector active area and the center of each edge of the detectors in the three coordinate system.

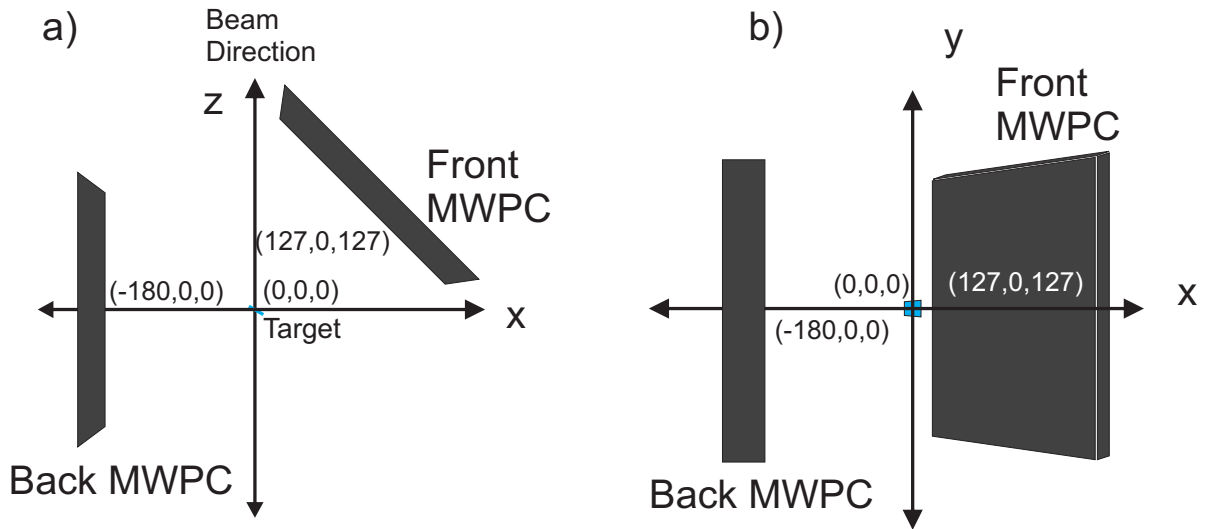


Figure 3.2: Schematic scale diagram of the Cartesian coordinate system used in the present work in relation to the CUBE detector setup. Panel A shows a diagram of the CUBE detectors setup from above illustrating the $(X, 0, Z)$ plane. Panel B shows a diagram of the CUBE detector setup from the beam axis upstream of the target illustrating the $(X, Y, 0)$ plane. The coordinates at the center of the CUBE and at the center of the two MWPCs are indicated.

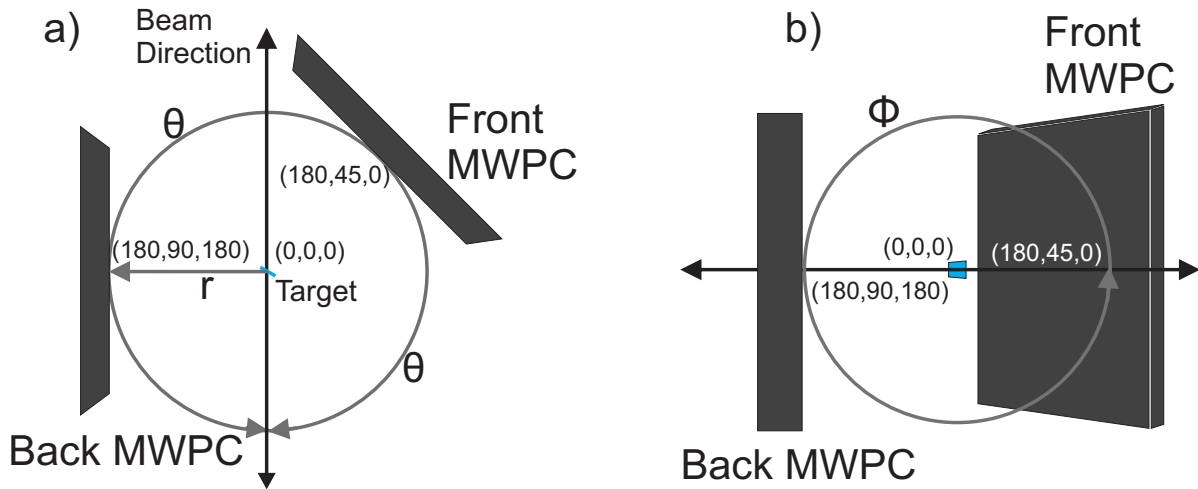


Figure 3.3: Schematic scale diagram of the spherical coordinate system used in the present work in relation to the CUBE detector setup. Panel A shows a diagram of the CUBE detector setup from above. The definitions of θ and r are indicated. Panel B shows a view from the beam axis upstream of the CUBE and the definition of Φ is indicated. The coordinates at the center of the CUBE and at the center of the two MWPCs are indicated.

Table 3.1: Coordinates in each of the three systems defined in this work for the center and four positions around the edge of the two MWPCs. The edge positions listed are at the center of the edges of the top, bottom, left, and right sides of the active area of the two MWPCs. In the Cartesian systems and in r in the spherical system the values are give in mm. In the spherical coordinate system the values θ and Φ are given in degrees.

		Detector Coordinates	CUBE Coordinates	Spherical Coordinates
		(x, y)	(X, Y, Z)	(r, θ, Φ)
	Center	(0,0)	(-180,0,0)	(180,90,180)
Back	Top	(0,17.5)	(-180, 177, 10)	(253, 90, 135)
MWPC	Right	(14,0)	(-180, 0, 150)	(235, 50, 180)
	Bottom	(0,-17.5)	(-180, -163, 10)	(243, 90, -135)
	Left	(-14,0)	(-180, 0, -130)	(222, 125, 180)
	Center	(0,0)	(127,0,127)	(180,45,0)
Front	Top	(0,17.5)	(120, 175, 134)	(251, 45, 45)
MWPC	Right	(14,0)	(219, 0, 36)	(222, 80, 0)
	Bottom	(0,-17.5)	(120, -175, 134)	(253, 45, 315)
	Left	(-14,0)	(22, 0, 232)	(234, 5, 0)

3.2 Position Information

The following sections describe the process for calibrating the MWPCs and converting among the coordinate systems. As discussed in Section 2.3, each fragment observed in an MWPC during a CUBE measurement results in a position signal. The reaction of $^{50}\text{Cr} + ^{180}\text{W}$ at $E_{\text{Lab}} = 284.0$ MeV is used throughout the discussion as an example. This process was applied consistently to the whole data set to obtain the results for each reaction presented in this work.

3.2.1 Position Calibrations

The edges of the active area of the MWPCs were determined to calibrate the observed position information to the coordinate systems defined in Section 3.1. During the experiment,

a calibration measurement was carried out in which the entire active area of the Back MWPC was illuminated. In this calibration measurement, ^{50}Cr was reacted with ^{184}W at $E_{\text{Lab}} = 186.0$ MeV. At this energy, the reaction of $^{50}\text{Cr} + ^{184}\text{W}$ was well below the interaction barrier so only elastic scattering occurred. The data acquisition system was run in “singles mode” where only an event in the Back MWPC was required to trigger the data acquisition system. This allowed for the collection of individual events across the entire active area of the detector. The signal amplitudes from the adc were then normalized to the physical edges of the detector to provide a linear transformation to position.

The position spectra recorded during the calibration measurement are shown in Figure 3.4. The edges of the Back MWPC were determined from the spectra shown in Panels A and B of Figure 3.4 by the sharp cutoffs in the position distributions. The active area edges can be observed in Panel A of Figure 3.4 in the x dimension at channel numbers 215 and 915 in x. The active area edge can be observed in Panel B of Figure 3.4 in the y dimension at channel numbers 358 and 795. These values are consistent with previous CUBE measurements. In the Front MWPC, the edges of the active area were less clear. The position distributions in the x and y dimensions measured in the Front MWPC are shown in Panel C and D, respectively, in Figure 3.4. The edges were determined to be at channel numbers 240 and 1050 in the x dimension and 142 and 1020 in the y dimension based on previous measurements with full illumination of the front MWPC. The channel numbers considered to be the edge of the two detector active areas are listed in Table 3.2 with the corresponding position in mm defined for the detector coordinate system.

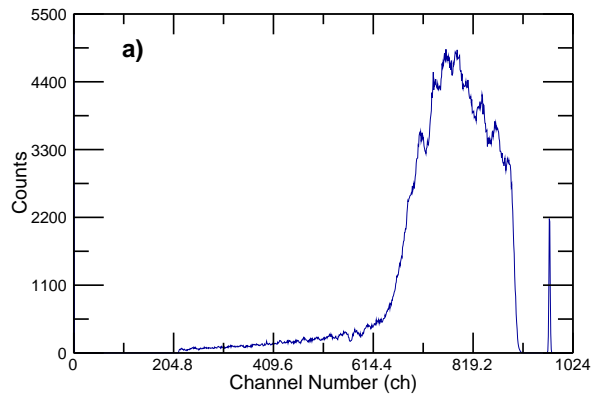
There are additional points of interest in the four spectra shown in Figure 3.4. In the Back MWPC a time delay module was not functioning correctly and caused a group of events to be observed at lower channel numbers than they should have been. In Panel B of

Table 3.2: The experimentally determined positions in channel numbers and the defined positions in mm for the edges of the active area of the Front and Back MWPCs.

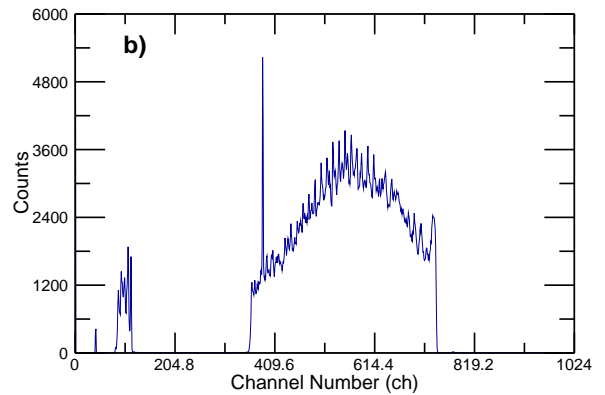
Position	Back MWPC		Front MWPC	
	Channel Number	mm	Channel Number	mm
X Left	215	-130.0	240	-149.0
X Right	910	149.0	1050	130.0
Y Top	358	178.5	142	178.5
Y Bottom	795	-178.5	1020	-178.5

Figure 3.4, these events can be observed around channel number 100. Also, a pulser signal was introduced to the data acquisition system for each detector and can be observed in the spectra. In the Back MWPC (Panels A and B of Figure 3.4), the pulser signals were observed around channels numbers $x = 976$ and $y = 385$. In the Front MWPC (Panels C and D of Figure 3.4), the pulser signals were observed around channels numbers $x = 256$ and $y = 1069$.

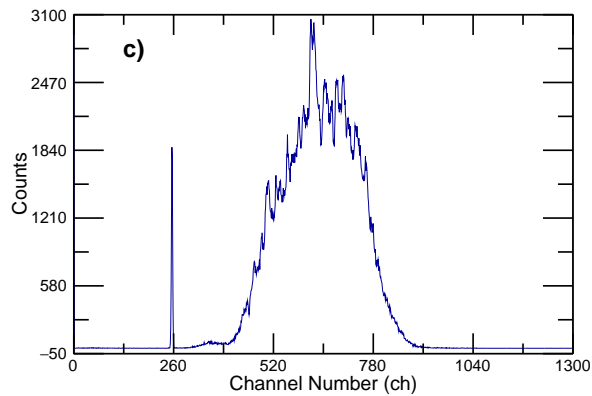
The two dimensional position spectra for the Back and Front MWPCs are shown in Figures 3.5 and 3.6, respectively, to demonstrate the gates that were applied to the data set in the present work. Erroneous events can result from edge effects, noise in the MWPCs, and data conversion errors. Additional erroneous events include those misplaced by the time delay module that was not functioning correctly in the Back MWPC. These events were removed from the data set by gates represented by the solid, black rectangles in Panel A of Figures 3.5 and 3.6 for $^{50}\text{Cr} + ^{180}\text{W}$ at $E_{\text{Lab}} = 284.0$ MeV. The two dimensional position distributions observed in the Back and Front MWPCs are shown in Panel B in Figures 3.5 and 3.6, respectively, after the gates were applied. Note that the variation of the intensity is clearly visible in the gated spectra shown in Panel B of Figures 3.5 and 3.6. The intense regions result from the limited angular coverage of the two MWPCs in the center-of-mass



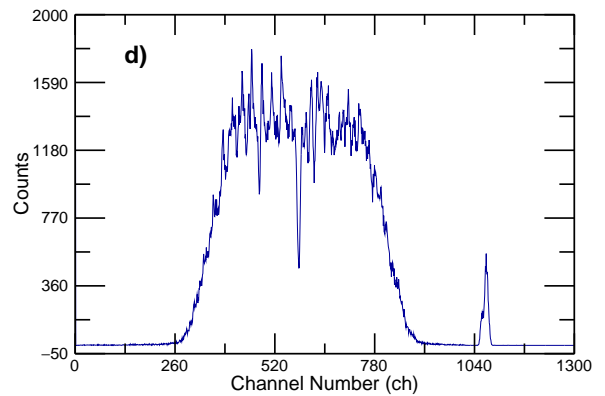
Back MWPC X Position Distribution



Back MWPC Y Position Distribution



Front MWPC X position Distribution



Front MWPC Y position Distribution

Figure 3.4: Position distributions in the x and y dimensions in channel number observed from the calibration measurement of $^{50}\text{Cr} + ^{184}\text{W}$ at $E_{\text{Lab}} = 186.0$ MeV that was used to determine the detector edges in Front and Back detectors. Panels A and B correspond to the x and y position distributions for the Back MWPC and Panels C and D correspond to the x and y position distributions for the Front MWPC.

frame. The forward focusing effect resulting from the momentum of the compound nucleus causes the non-rectangular shape observed in the position spectra from the Front MWPC. An additional feature of note in the Front MWPC position spectra is the angled lines which likely result from an ambiguity in the position determination at positions where the x position equals the y position. This effect could be corrected if a third position sensitive layer was added to the detector to remove this ambiguity. Additionally, noise in the spectra comes from RF signals picked up by the pre-amplifiers. The effect of this noise is small and only caused about a 1 mm modulation in the position signals. The wires of the MWPC can be seen in the position spectra as well. In the center of both detectors in the Y dimension there is a large dip in the position spectra at Y equals 0. This is due to the placement of a pressure window support wire in the center of the detector.

The calibration parameters for the detector edges allowed for the conversion from channel number to millimeters. For the linear transformation from channel number to mm in the x dimension the slope was calculated as

$$\text{Slope}_x = \frac{x\text{Left}(\text{mm}) - x\text{Right}(\text{mm})}{x\text{Left}(\text{ch}) - x\text{Right}(\text{ch})} \quad (3.1)$$

where $x\text{Left}(\text{mm})$ and $x\text{Right}(\text{mm})$ are the known positions of the detector edges in mm, and $x\text{Left}(\text{ch})$ and $x\text{Right}(\text{ch})$ are the channel numbers determined to be the edge of the detectors. The intercept was determined from the same information as

$$\text{Intercept}_x = \frac{x\text{Right}(\text{mm}) * x\text{Left}(\text{ch}) - x\text{Left}(\text{mm}) * x\text{Right}(\text{ch})}{x\text{Left}(\text{ch}) - x\text{Right}(\text{ch})}. \quad (3.2)$$

The slope and intercept in the y dimension were determined in the same manner using the

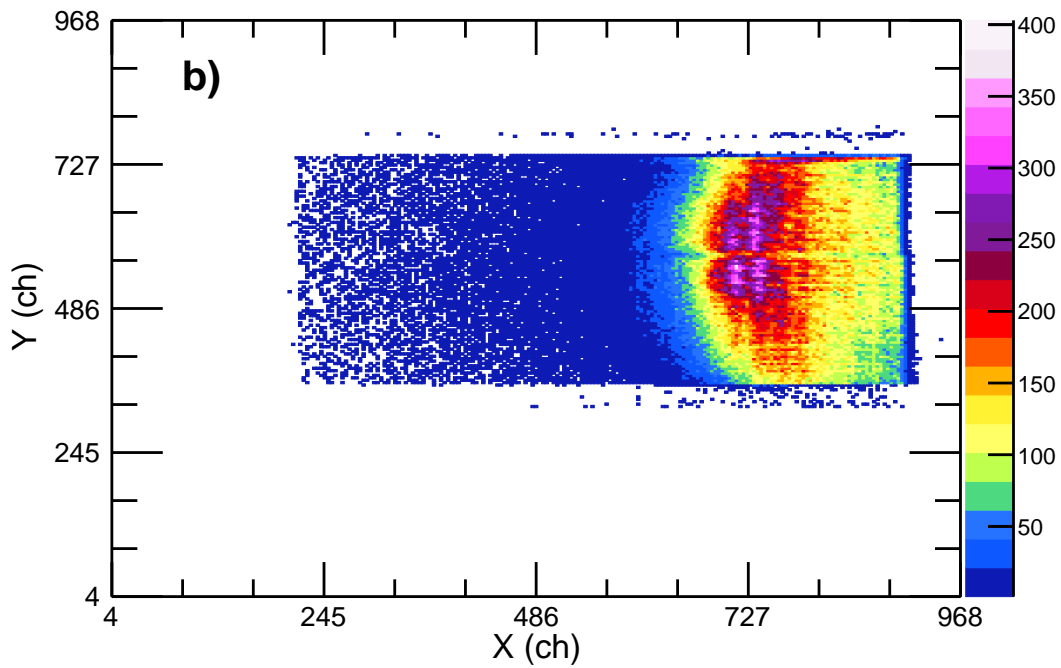
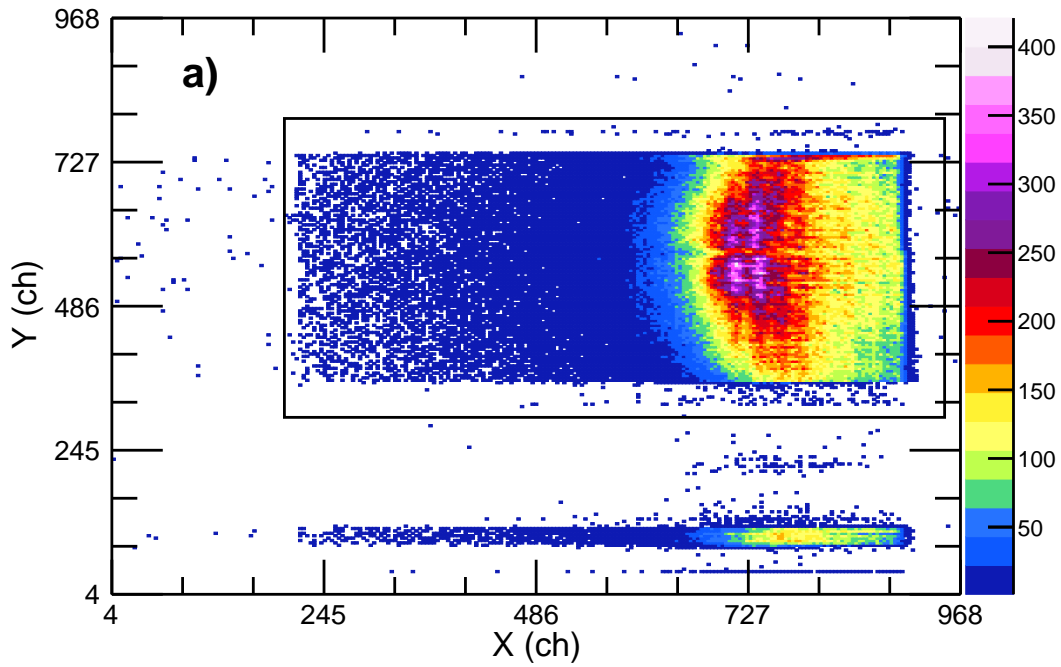


Figure 3.5: Two dimensional position spectra for the Back MWPC. Panel A shows the raw position information and the solid black rectangle reflects the gate applied to the data sets. Panel B shows the position spectra after the gate was applied. Both are for $^{50}\text{Cr} + ^{180}\text{W}$ at $E_{\text{Lab}} = 284.0$ MeV as an example.

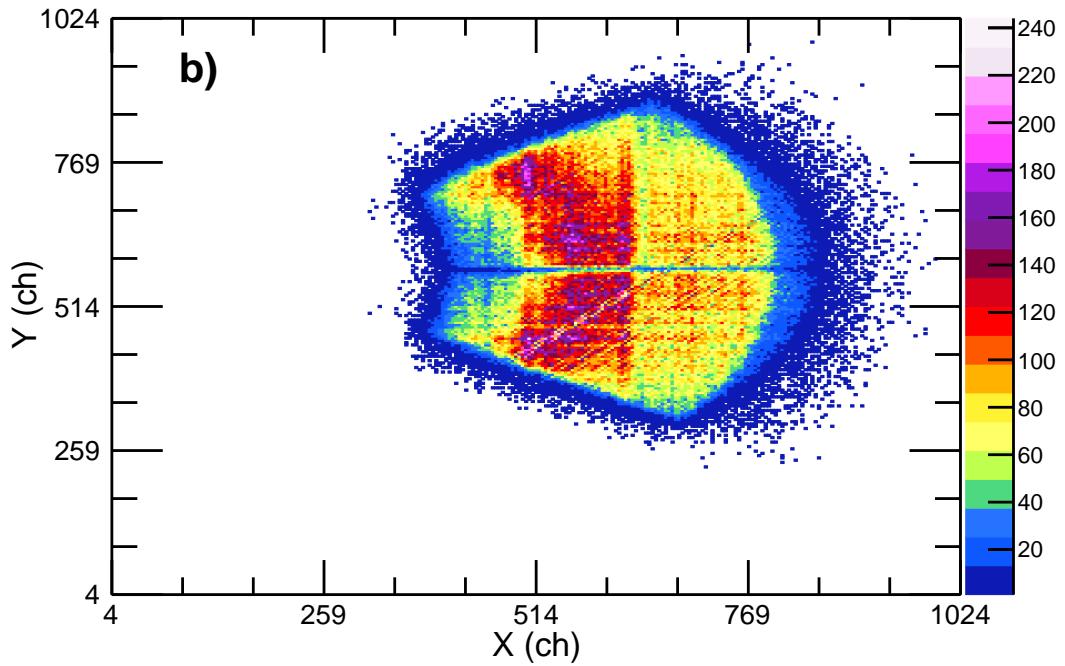
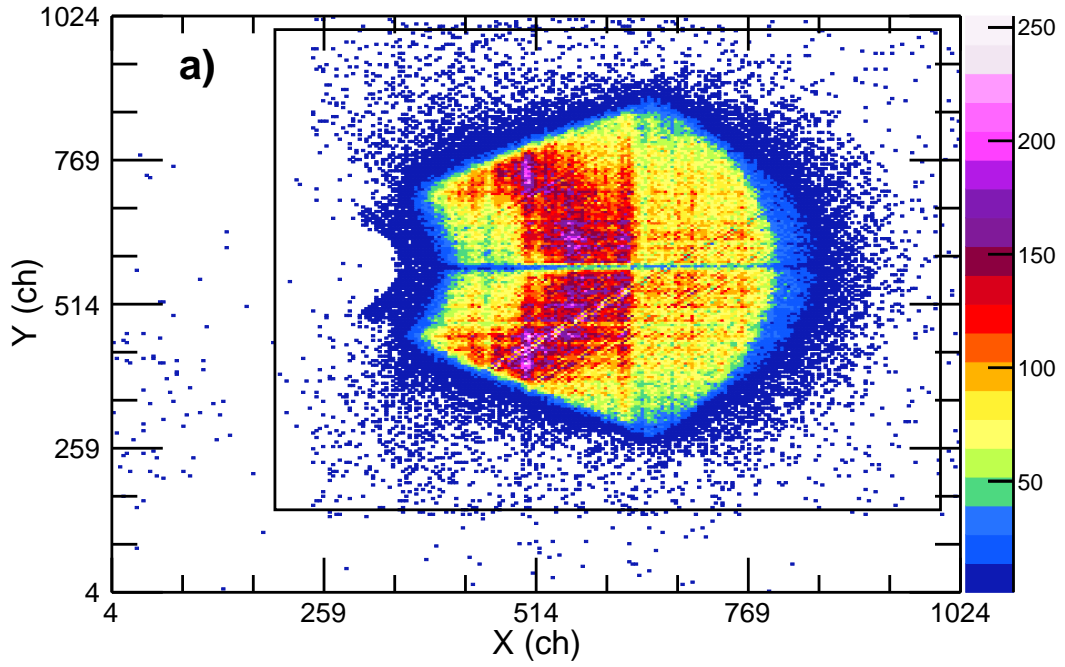


Figure 3.6: Two dimensional position spectra for the Front MWPC. Panel A shows the raw position information and the solid black rectangle reflects the gate applied to the data sets. Panel B shows the position spectra after the gate was applied. Both are for $^{50}\text{Cr} + ^{180}\text{W}$ at $E_{\text{Lab}} = 284.0$ MeV as an example.

Table 3.3: Slopes and Intercepts determined for the linear conversion from channel number to millimeters for the MWPCs.

	Detector 0		Detector 1	
Dimension	Slope (mm / ch)	Intercept (mm)	Slope (mm / ch)	Intercept (mm)
x	0.401	-216.3	0.344	-231.7
y	-0.817	471.0	-0.407	236.2

channel numbers and known detector edges in the y dimension. The slope and intercept values in x and y for the MWPCs are listed in Table 3.3.

From the slope and intercept values each position could be determined in mm as

$$\text{Position}_{x/y}(\text{mm}) = \text{Slope}_{x/y}(\text{mm}/\text{ch}) * \text{Position}_{x/y}(\text{ch}) + \text{Intercept}_{x/y}(\text{mm}) \quad (3.3)$$

where each variable corresponds to the appropriate x or y dimension value. The position signals in mm for $^{50}\text{Cr} + ^{180}\text{W}$ at $E_{\text{Lab}} = 284.0$ MeV in the Back and Front MWPCs are shown in Panels A and B of Figures 3.7, respectively.

3.2.2 Transformation Among the Coordinate Systems

One of the primary quantities of interest in the present work is the center-of-mass angle at which the fragments were emitted. To determine this angle, the (x, y) position information observed in the MWPCs needed to be transformed to the full CUBE setup Cartesian coordinate system and then transformed to spherical coordinates. This section describes the process used in the present work to transform the two dimensional detector position signals to the full CUBE system coordinates. As discussed in Section 3.1, the center of each MWPC was defined in both Cartesian and spherical coordinates, thus all other positions observed in the MWPCs were determined relative to the center of the detector. All positions in the

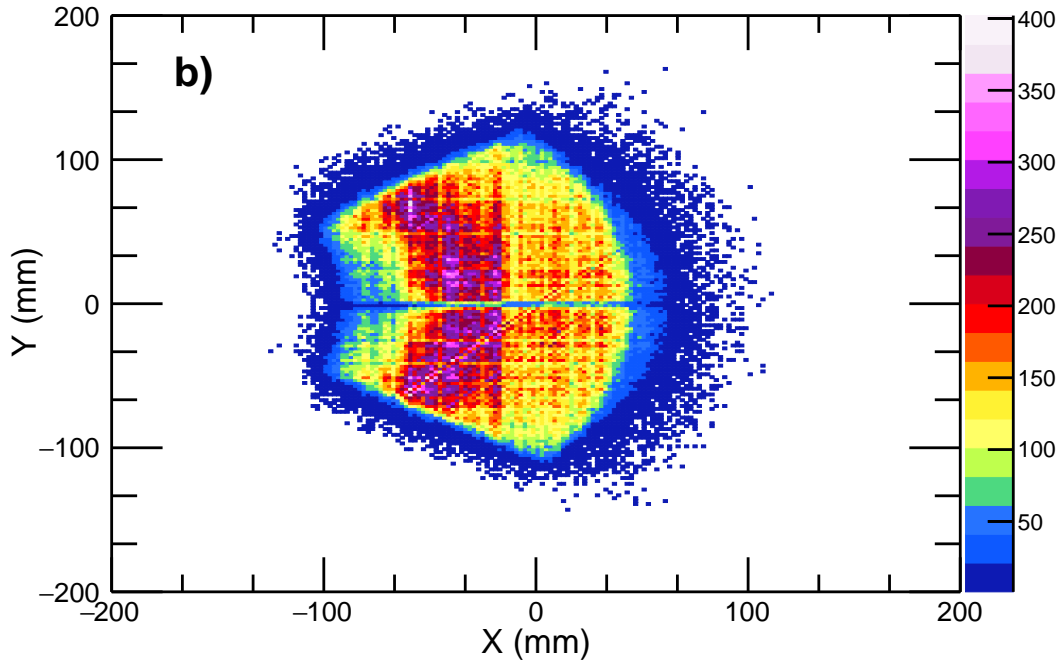
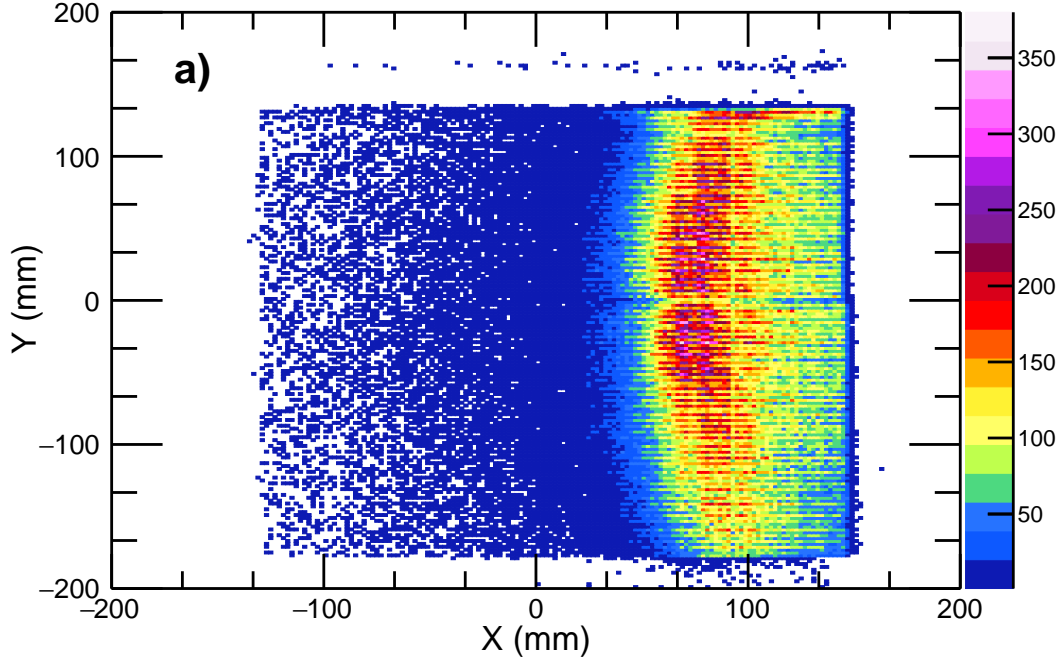


Figure 3.7: Two dimensional position spectra following the conversion from channel number to mm for the Back (A) and Front (B) MWPCs observed during the measurement of $^{50}\text{Cr} + ^{180}\text{W}$ at $E_{\text{Lab}} = 284.0$ MeV as an example.

CUBE coordinate system were initially determined in channel numbers. The Y coordinate in the CUBE Cartesian coordinate system was determined from the center of the detector (Y_{center}) in the CUBE Cartesian coordinate system, defined as zero, and the channel number of a given event (y_{event}) in the MWPC coordinate systems as

$$Y(\text{ch}) = Y_{\text{center}}(\text{ch}) + y_{\text{event}}(\text{ch}) \quad (3.4)$$

The X value in the CUBE Cartesian coordinate system was determined from the X and θ values defined at the center of the detector in the CUBE Cartesian coordinate system and the x position observed for the event (x_{event}) in channel numbers as

$$X(\text{ch}) = X_{\text{center}}(\text{ch}) + x_{\text{event}}(\text{ch}) * \cos(\theta_{\text{center},i}). \quad (3.5)$$

Finally, the Z value in the CUBE Cartesian coordinate system was determined from the Z and θ values defined at the center of the detector in the CUBE Cartesian coordinate system and the x position observed for the event (x_{event}) in channel numbers as

$$Z(\text{ch}) = Z_{\text{center}}(\text{ch}) + x_{\text{event}}(\text{ch}) * \sin(\theta_{\text{center},i}). \quad (3.6)$$

After (X, Y, Z) positions were determined a simple Cartesian to spherical coordinates transformation was used to determine the spherical coordinates for an observed event. The conversion from Cartesian to spherical coordinates was done by using the root TVector3 class [104]. The angular coverage (Φ as a function of θ) of the Back and Front MWPCs are shown in Panels A and B in Figure 3.8, respectively, for events recorded in “singles mode” from the calibration measurement of $^{50}\text{Cr} + ^{184}\text{W}$ at $E_{\text{Lab}} = 186.0$ MeV.

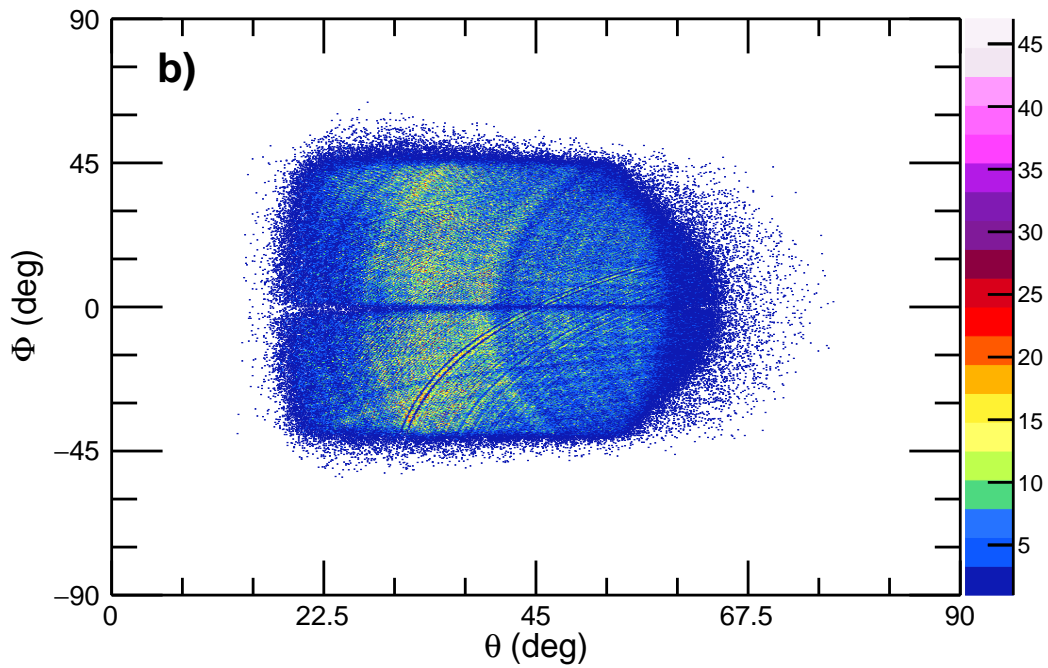
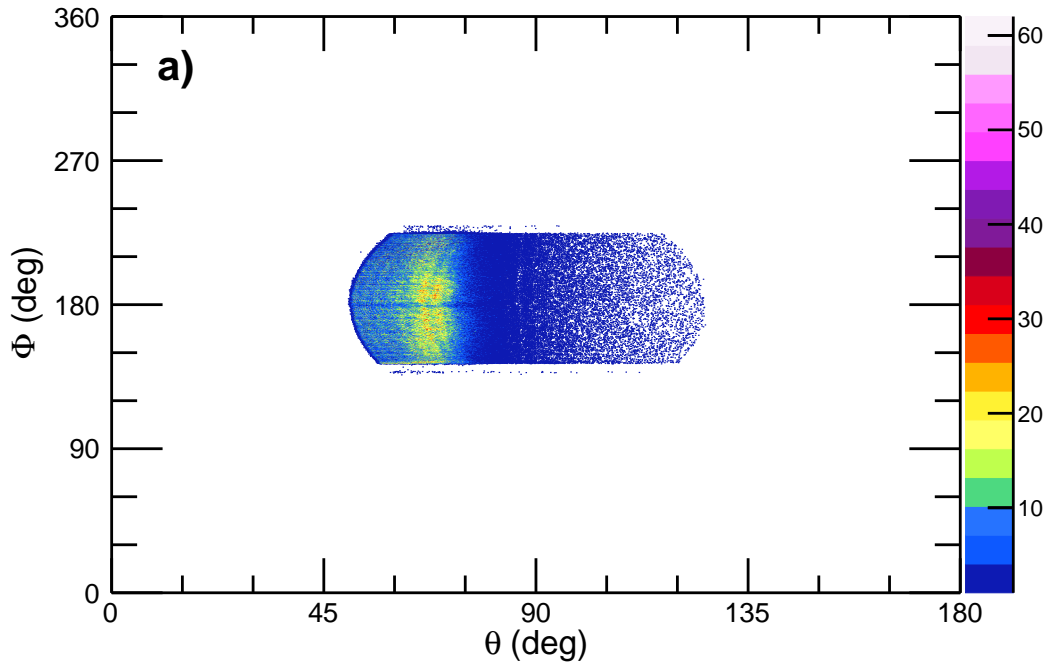


Figure 3.8: Angular coverage of the Back (a) and Front (b) MWPCs shown as θ_{Lab} on the x-axis and Φ on the y-axis from the measurement of $^{50}\text{Cr} + ^{180}\text{W}$ at $E_{\text{Lab}} = 284.0$ MeV.

3.3 Timing Information

In addition to the position information discussed above, a timing signal was also recorded for events observed in the CUBE MWPCs. The raw, uncalibrated time distribution of the coincident timing signals observed in the measurement of $^{50}\text{Cr} + ^{180}\text{W}$ at $E_{\text{Lab}} = 284.0$ MeV for the two MWPCs is shown in Panel A in Figure 3.9. The solid black polygon in Panel A in Figure 3.9 represents the gate applied to the data set to remove events incorrectly associated with a beam pulse. Events outside of the gated region are due to events from neighboring beam bunches from the beam chopper. The double peak in the elastic scattering events in the Back MWPC (time_0) results from a time offset between the quadrants in the y dimension. The coincident time signals following conversion from channel number to ns are shown in Panel B in Figure 3.9. To convert the signals from channel number to ns, a calibration of the time to analog conversion (TAC) was done with an Ortec 462 Time Calibrator to determine the channel number to ns calibration for the MWPCs. The time calibrator was set up to produce pulses spaced by 10 ns and the time spectra observed during this calibration measurement are shown in Figure 3.10. Each peak corresponds to a pulse from the time calibrator. The center of each peak was determined and the average spacing between each peak provided the channel number to ns conversion. In the Back MWPC, the mean spacing was 66 channels and the time slope was 0.1516 ns/ch. In the Front MWPC, the mean spacing was 113 channels and the time slope was 0.088 ns/ch. The larger spacing in the Front MWPC TAC calibration timing spectra compared to the spacing in the Back MWPC TAC calibration timing spectra was due to a variation in the settings between the two detectors.

An example illustration of the timing structure of the 14 UD Tandem Accelerator and

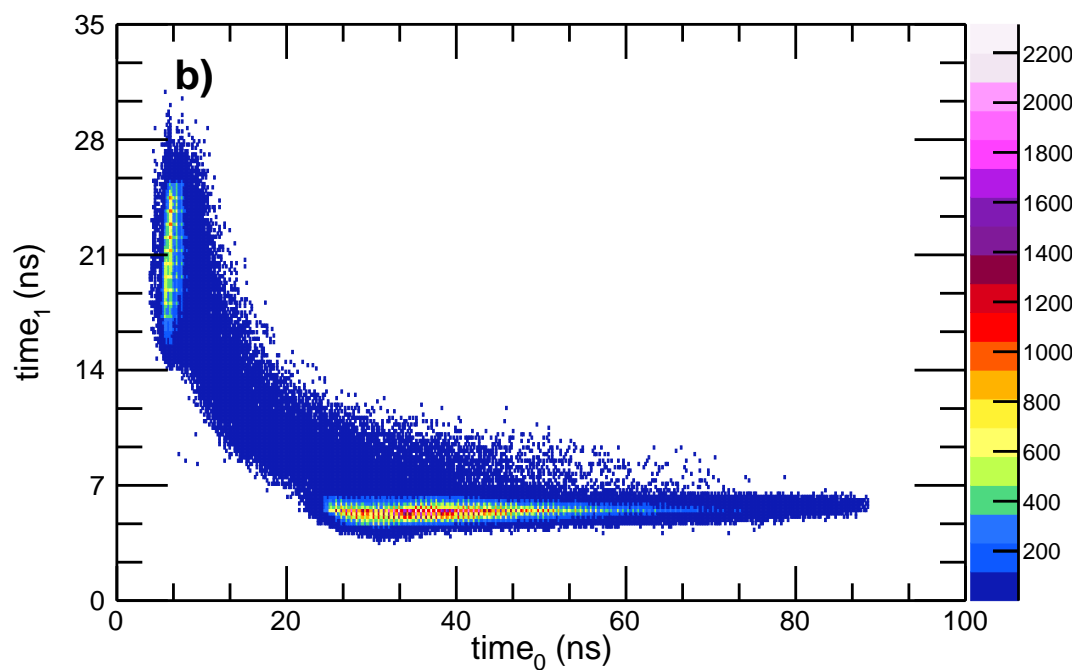
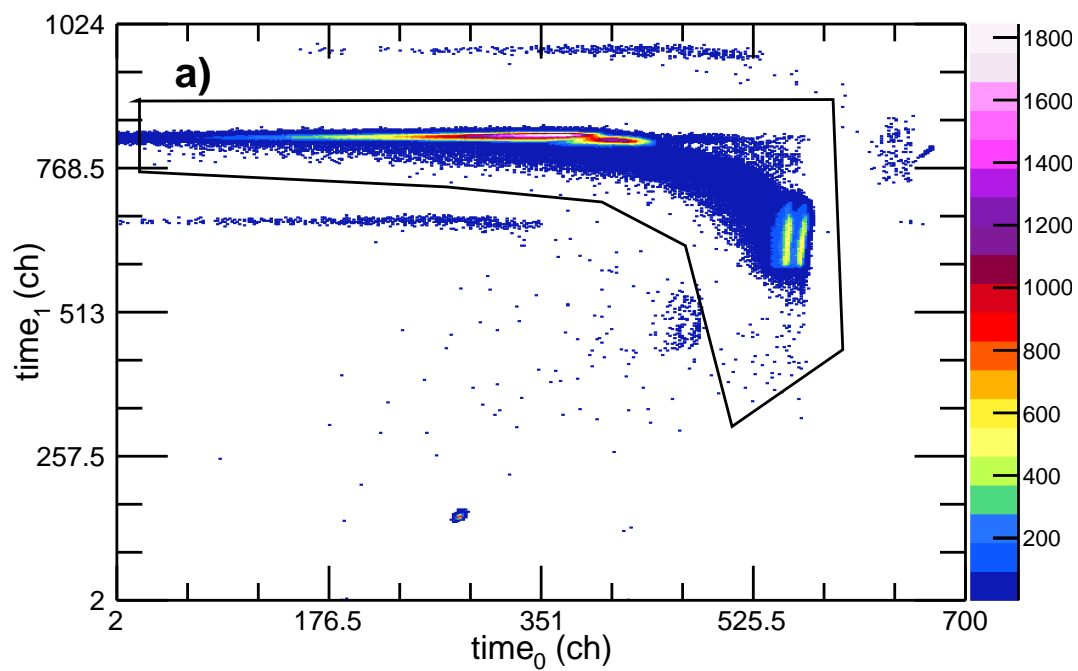


Figure 3.9: Panel A shows the raw timing signals observed for coincident fragments in the Front (x-axis) and Back (y-axis) MWPCs from the measurement of $^{50}\text{Cr} + ^{180}\text{W}$ at $E_{\text{Lab}} = 284.0$ MeV. Panel B shows the observed timing signals following conversion to ns. See text for details on this conversion.

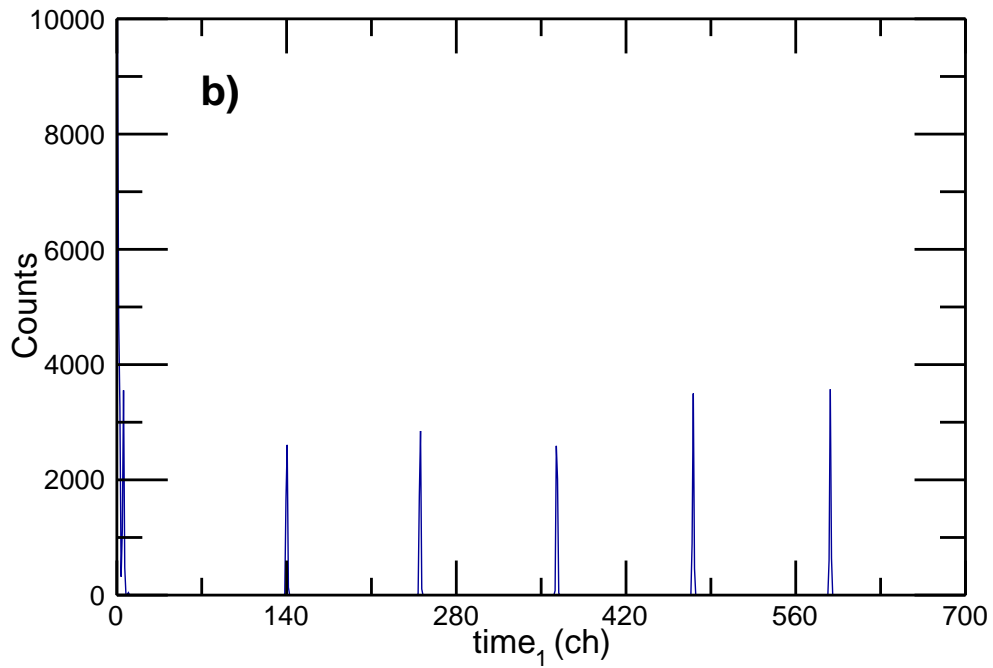
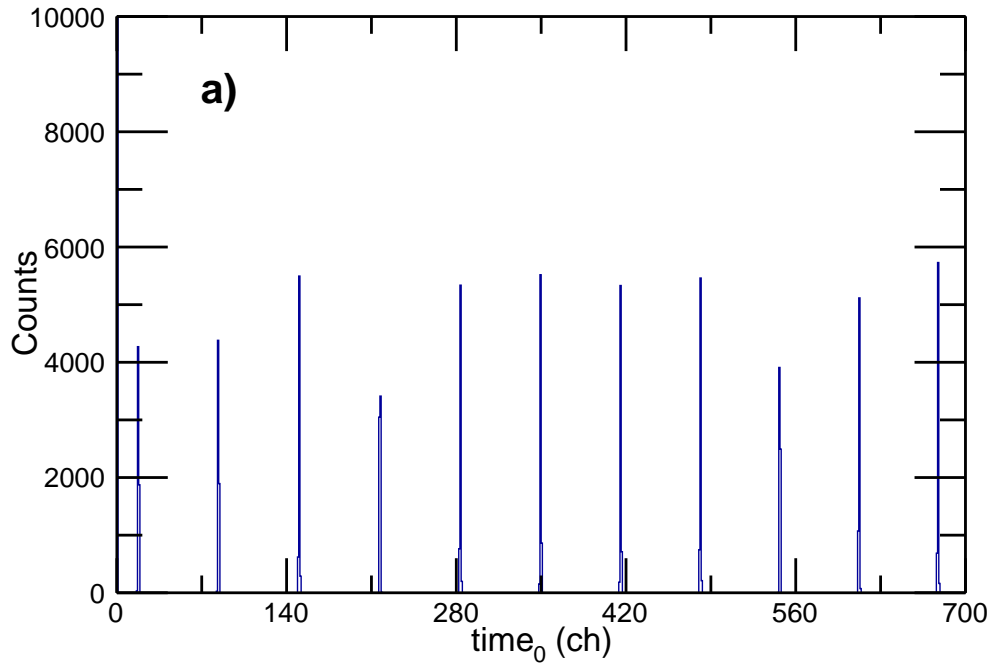


Figure 3.10: Time spectra in channel numbers observed in the Back (A) and Front (B) MWPCs from the TAC calibrations with 10 ns pulses.

CUBE setup at ANU is shown in Figure 3.11. The length of the flight path from the accelerator to the target and the target to the detectors were well known and constant. An example of two RF pulses is illustrated in Panel A of Figure 3.11. In the present work, the RF signal from the accelerator was utilized as a reference time signal and was pulsed at intervals of 106.7 ns. An example timing signal observed in the Back MWPC, which was used as the “start” signal for the data acquisition, is shown in Panel B of Figure 3.11. An example signal observed in the Front MWPC, which was used as the “stop” signal, is illustrated in Panel C of Figure 3.11. For these example signals in the MWPCs, the left most RF pulse would be the reference time, and the right most pulse corresponds to the next beam pulse. The time difference between the observed time signal in the Back detector and the reference RF signal corresponds to the transmission time through the accelerator and beam line to the target and then from the target to the detector (t_0). The time difference between the observed signals in the Back and Front MWPCs is the electronic delay time (δ_t).

The electronic delay time (δ_t) between the Back and Front MPWC timing signals depends on the cable lengths and the transmission times of the electronics signals of the MWPCs. Small variations in time may be caused by temperature drifts of the electronics system. δ_t was optimized by requiring that the binary fragments were symmetric about a line at mass ratio equal to 0.5. The transmission time (t_0) depends on the beam species and energy. t_0 was optimized by requiring that only binary events were included.

For the MWPCs, the final calibrated times were calculated as

$$T(\text{Back})_{\text{Calibrated}} = -\text{TimeSlope} * T(\text{Back})_{\text{Raw}} + t_0 \quad (3.7)$$

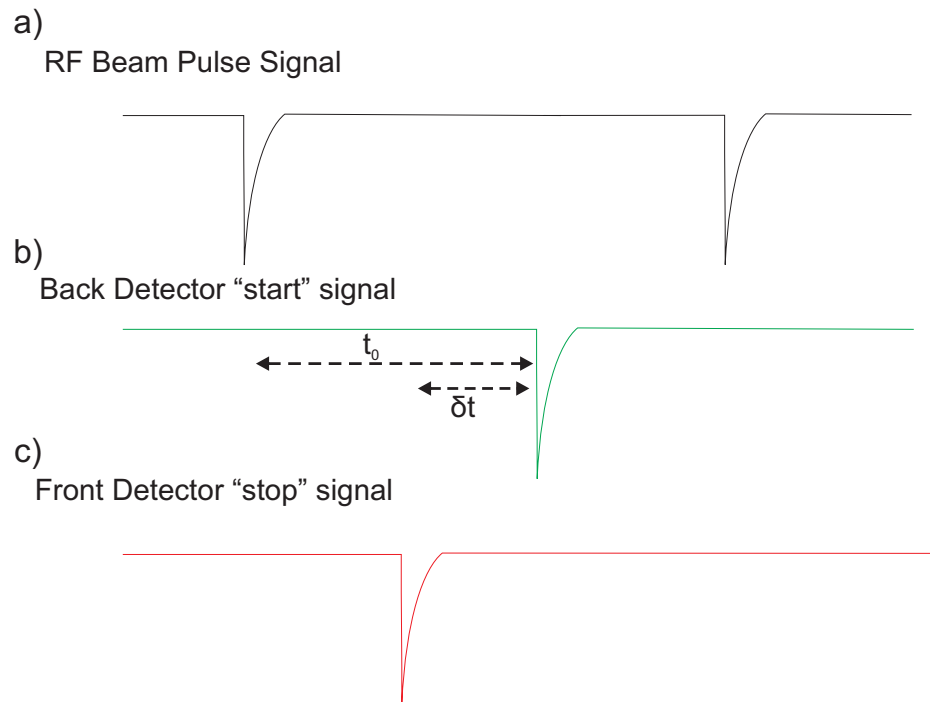


Figure 3.11: Illustration of an example set of timing signals including, RF signals in the top panel, a timing signal from the Back MWPC in the middle panel, and a timing signal from the Front MWPC in the bottom panel. t_0 and δt are the time parameters used in the CUBE calibration. See text for discussion.

$$T(\text{Front})_{\text{Calibrated}} = -\text{TimeSlope} * T(\text{Front})_{\text{Raw}} + t_0 + \delta_t \quad (3.8)$$

After the position and timing signals were calibrated they were used to determine the velocity vectors needed in the kinematic coincidence method.

3.4 Kinematic Coincidence Method

The well-established kinematic coincidence method [41, 4] is a technique used to determine the mass ratios of coincident fragments and has been applied extensively to fission and fission-like reactions [4, 41, 5, 87, 46, 40, 105, 106, 64, 65]. In the kinematic coincidence method, the measured position and timing signals are used to determine the laboratory frame velocity vectors for a pair of coincident fragments. The velocity vectors are then converted into the center-of-mass frame and used to determine the M_R of each fragment. The kinematic coincidence method relies on the assumption of binary reaction kinematics to ensure that the mass ratios can be determined from the center-of-mass velocity vectors. Two tests were performed to ensure that this assumption was valid for the data set in the present work and are discussed in Section 3.5.1.

In the kinematic coincidence method, the two emitted fragments are characterized by their velocity vectors. An example of an event observed in the present work is illustrated in Figure 3.12 and the pertinent vectors are indicated. Following separation, each fragment will have a three dimensional velocity vector in the lab frame ($v_{3D,i,\text{lab}}$). Additionally, the motion of the fragments can be considered in the center-of-mass frame, with the three dimensional velocity vectors $V_{3D,i,c.m.}$. The lab frame and center-of-mass frame velocity vectors can be projected onto the $(X, 0, Z)$ plane as defined in the CUBE Cartesian coordinate system in

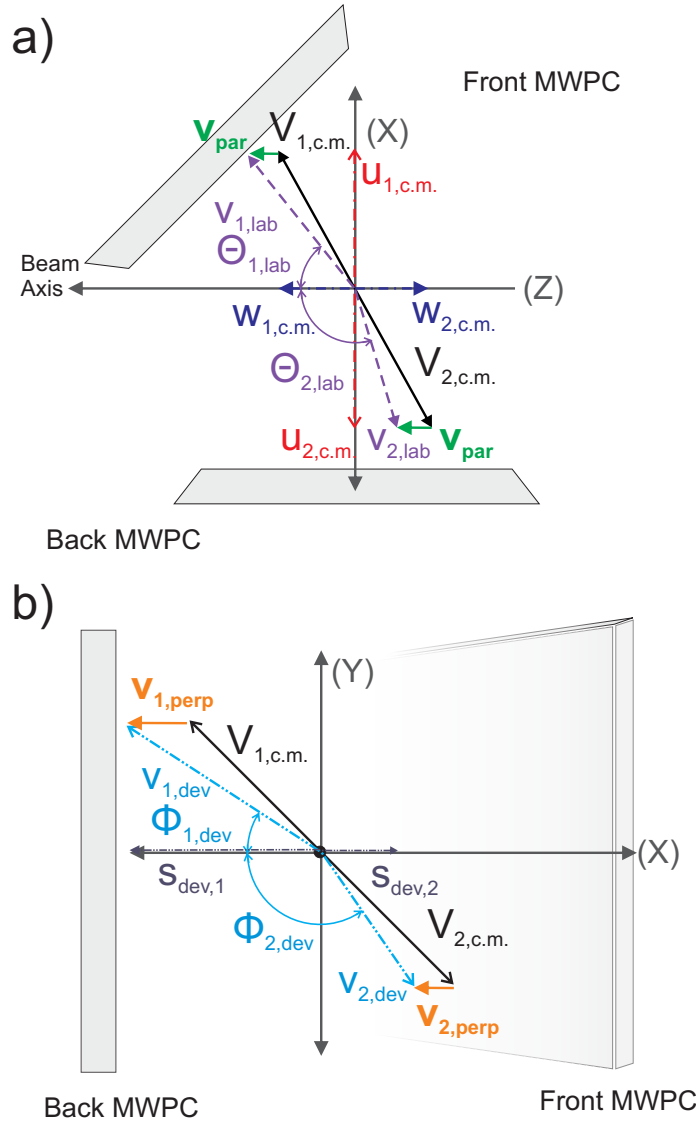


Figure 3.12: Illustration of the primary vectors considered in the kinematic coincidence method for two emitted fragments. Panel A shows the projection of one possible combination of vectors on to a plane $(X, 0, Z)$ along the beam axis. The Z-axis represents the beam axis. The solid, black vectors represent a possible set of $V_{i,c.m.}$ for two fragments i . The dashed, purple vectors represent one possible set of $v_{i,lab}$. As an example, the two components of the two $V_{i,c.m.}$ are shown. The dotdashed, red vectors represent $u_{i,c.m.}$ and the dotdashed, blue vectors represent $w_{i,c.m.}$. $\theta_{i,lab}$ is shown as an example of the definition of θ . Panel B shows a projection of one possible combination of velocity vectors on to a plane $(X, Y, 0)$ perpendicular to the beam axis. The dashed, black vectors represent one possible combination of $V_{i,c.m.}$ for fragments i . The dotdashed, sky blue vectors represent possible $V_{i,dev}$. The projection of each $V_{i,dev}$ on the z-axis is represented by the dotdashed, dark purple vectors (shown just off the z axis for clarity). The solid, orange vectors represent v_{perp} , which should be zero in binary kinematics. $\phi_{i,dev}$ are also indicated.

Table 3.4: Component definitions for the projections $v_{i,\text{lab}}$ along the X and Z axes in the $(X, 0, Z)$ plane and along the X axis in the $(X, Y, 0)$ plane. The components in the $(X, 0, Z)$ plane are defined relative to θ , while X_Φ is defined in the $(X, Y, 0)$ plane relative to Φ . See text for full descriptions of planes and angles.

	$v_{i,\text{lab}}$	$V_{i,\text{c.m.}}$
X_θ component	$w_{i,\text{lab}} = v_{i,\text{lab}} \cos \theta_{i,\text{lab}}$	$w_{i,\text{c.m.}} = V_{i,\text{c.m.}} \cos \theta_{i,\text{c.m.}}$
Y component	$u_{i,\text{lab}} = v_{i,\text{lab}} \sin \theta_{i,\text{lab}}$	$u_{i,\text{c.m.}} = V_{i,\text{c.m.}} \sin \theta_{i,\text{c.m.}}$
X_Φ component	$s_{i,\text{lab}} = v_{i,\text{lab}} \sin \Phi_{i,\text{lab}}$	$s_{i,\text{c.m.}} = V_{i,\text{c.m.}} \sin \Phi_{i,\text{c.m.}}$

Section 3.1. The $(X, 0, Z)$ plane is illustrated in Panel A of Figure 3.12 where the lab frame and center-of-mass frame vector projections are indicated by $v_{i,\text{lab}}$ and $V_{i,\text{c.m.}}$, respectively. Each projected vector can be decomposed into its components along the X and Z axes. The components of the center-of-mass frame vector projection are illustrated in Panel A of Figure 3.12, as an example. The component in the Z dimension is indicated by u and the component in the X dimension is indicated by w . The definitions for the components are listed in Table 3.4. In Panel A of Figure 3.12 the angle θ at which the fragments were emitted in the laboratory frame is represented by the curved, purple arrows. Additionally, in Panel A of Figure 3.12 the vector representing the conversion from $V_{i,\text{c.m.}}$ to $v_{i,\text{lab}}$ is indicated by the green arrow and labeled v_{par} . v_{par} represents the velocity of the compound system in the direction parallel to the beam.

An example event viewed from upstream of the target is illustrated in Panel B in Figure 3.12 in the $(X, Y, 0)$ plane, as defined in Section 3.1. The two dashed, black vectors ($V_{i,\text{c.m.}}$) represent the velocity vectors projections of the two fragments onto the $(X, Y, 0)$ plane in the center-of-mass frame. The projectile beam should have no momentum in this plane, so the projections of $v_{i,\text{lab}}$ and $V_{i,\text{c.m.}}$ should be equivalent. Further, conservation of momentum requires that the two nuclei be emitted back to back with $\phi_1 - \phi_2 = 180^\circ$

in the center-of-mass frame. This is true of two-body, full momentum transfer events and is required for the assumptions of the kinematic coincidence method to hold. This will not be observed if light particle (alpha, neutron, or proton) emission or transfer-induced fission occur in a specific event but only on average for an ensemble of events. Such processes would result in the observed $v_{i,\text{lab}}$ not being equivalent to $V_{i,\text{c.m.}}$ in the $(X, Y, 0)$ plane. The dot-dashed, light blue vectors ($V_{\text{dev},i}$) represent the velocity vectors of the fragment observed in the lab frame after an event like light particle emission that would alter the velocity of the fragments. In Panel B of Figure 3.12 the angle Φ_i at which the fragments were emitted is represented by the light blue, curved arrows. The dot-dashed, purple vectors labeled $s_{\text{dev},i}$ represent the component of $V_{\text{dev},i}$ along the X axis determined with respect to Φ_i . The mathematical definition of $s_{\text{dev},i}$ is included in Table 3.4. The deviation between $V_{i,\text{c.m.}}$ and $V_{\text{dev},i}$ is represented by the orange vectors labeled v_{perp} and encompasses the velocity perpendicular to the beam direction.

Both v_{perp} and v_{par} are used to ensure that the events included in the data set were two body events. v_{perp} can be calculated from the z components of V_{dev} from each fragment as

$$v_{\text{perp}} = \frac{s_{\text{dev},1}s_{\text{dev},2}\sin\Phi_{12}}{\sqrt{s_{\text{dev},1}^2 + s_{\text{dev},2}^2 - 2s_{\text{dev},1}s_{\text{dev},2}\cos\Phi_{12}}}. \quad (3.9)$$

where $\Phi_{1,2}$ is $\phi_1 - \phi_2$. It is clear that when the two fragments are emitted back to back ($\Phi_{12} = 180^\circ$) v_{perp} will be zero.

When v_{perp} is zero, then all of the compound nuclear momentum is accounted for in v_{par} and $V_{1,\text{c.m.}}$ will be equivalent to $V_{2,\text{c.m.}}$. A ratio of the $V_{i,\text{c.m.}}$ components and v_{par} can then be written as

$$\frac{u_{1,\text{c.m.}}}{w_{1,\text{c.m.}} - v_{\text{par}}} = -\frac{u_{2,\text{c.m.}}}{w_{2,\text{c.m.}} - v_{\text{par}}} \quad (3.10)$$

The minus signs results from the fact that u will only be positive, while w can be positive or negative. When eq. 3.10 is solved for v_{par} using the component definitions in Table 3.4 and the trigonometric angle addition rule, the following equation results,

$$v_{\text{par}} = \frac{u_1 w_2 + u_2 w_1}{u_1 + u_2} = \frac{v_1 v_2 \sin(\theta_1 + \theta_2)}{v_1 \sin\theta_1 + v_2 \sin\theta_2} \quad (3.11)$$

where all components are relative to the center-of-mass frame velocity vectors. When v_{perp} is zero, then v_{par} should be equivalent to the compound nucleus velocity (v_{CN}), which can be calculated as

$$v_{\text{CN}} = 1.389 \sqrt{\frac{E_{\text{Lab}}}{A_{\text{p}}}} \frac{A_{\text{p}}}{A_{\text{p}} + A_{\text{T}}} \text{ (cm/ns)}. \quad (3.12)$$

where E_{Lab} is the incident beam energy in the lab frame in MeV and A_{p} and A_{T} are the masses of the projectile and target, respectively.

3.5 Velocity Determination

In the present work, the lab frame velocities were determined from the observed position and timing signals as

$$v_{i,\text{lab}} = \frac{r}{T_{\text{Calibrated}}} \quad (3.13)$$

where r is the magnitude of the position vector in spherical coordinates in mm, and time is the final time in ns. Each $v_{i,\text{lab}}$ was converted to the center-of-mass frame by

$$V_{i,c.m.} = \sqrt{v_{i,\text{lab}}^2 + v_{\text{CN}}^2 - 2 * v_{i,\text{lab}} * v_{\text{CN}} * \cos(\theta)}. \quad (3.14)$$

3.5.1 Using Φ to demonstrate v_{perp} is zero

As discussed in Section 3.4, the kinematic coincidence method relies on the assumption that v_{perp} be zero. This assumption should be valid in the present work because the systems were measured at center-of-mass energies well below the fission barriers for the W targets and one expects only two massive fragments in the exit channel. Therefore, three-body events arising from transfer induced fission of the target should be rare.

To appropriately use the kinematic coincidence method all events violating the assumption of binary kinematics were removed from the data set. This was done by removing events from the data set where v_{perp} was not zero and v_{par} did not equal v_{CN} . The v_{perp} values are shown in Panel A in Figure 3.13 as a function of $v_{\text{par}}-v_{\text{CN}}$ determined for the events observed during the measurement of $^{50}\text{Cr} + ^{186}\text{W}$ at $E_{\text{Lab}} = 284.0$ MeV. The group of events with $v_{\text{par}}-v_{\text{CN}}$ between 10 and 15 mm/ns come from reactions with the carbon backing on the target. Light particle emission will occur after the two fragments separate. This causes the wide spread in the events centered at zero in Panel A of Figure 3.13. The gate applied to the data was a circle with a radius of 1 mm/ns and is represented by the black circle in Figure 3.13. The 1 cm/ns gate was selected so that the three body events were removed without effecting the two body events throughout the data set. As a result of the gate applied to the data only events where the effects of light particle emission averaged to zero are included in the data set. As discussed in Section 3.4 for binary events, $v_{\text{par}}-v_{\text{CN}}$ must equal zero and v_{perp} must equal zero [41]. The values of v_{perp} are shown in Panel B in Figure 3.13 as a function $v_{\text{par}}-v_{\text{CN}}$ after the gate was applied to the data set. The distribution is now centered on v_{perp} of zero in the y dimension, and $v_{\text{par}}-v_{\text{CN}}$ of zero in the x dimension. Note that even prior to applying the gate the distribution is strongly peaked at v_{perp} of zero and

$v_{\text{par}}-v_{\text{CN}}$ of one, indicating that the two-body reactions are the dominant exit channel.

v_{perp} will be zero when the two fragments are emitted at 180° in the center-of-mass frame. To reiterate that v_{perp} can be assumed to be zero in the present work, the difference between Φ_1 and Φ_2 is shown in Figure 3.14 for $^{50}\text{Cr} + ^{180}\text{W}$ at $E_{\text{Lab}} = 284.0$ MeV. The two fragments are emitted 180° apart, thus the use of the kinematic coincidence method is justified in the present work.

3.5.2 Calculating M_R

One of the primary deduced quantities from CUBE measurements is the mass ratio of a fragment, defined as $M_{R,1} = \frac{A_1}{A_1+A_2}$, where A_i is the mass of one of the fragments detected in coincidence. The kinematic coincidence method is used to determine the mass ratios from the center-of-mass velocity vectors using conservation of momentum. In the center-of-mass frame, the momentum of the two fragments is equal ($p_1 = p_2$) and $A_T = A_1 + A_2$. Using these relations and the definition of momentum, the mass ratio of a fragment can be determined from the velocities as

$$p_1 = p_2 \quad (3.15)$$

$$A_1 V_{1,c.m.} = A_2 V_{2,c.m.} \quad (3.16)$$

$$(A_T - A_2) V_{1,c.m.} = A_2 V_{2,c.m.} \quad (3.17)$$

$$A_T V_{1,c.m.} - A_2 V_{1,c.m.} = A_2 V_{2,c.m.} \quad (3.18)$$

$$A_T V_{1,c.m.} = A_2 V_{2,c.m.} + A_2 V_{1,c.m.} \quad (3.19)$$

$$A_T V_{1,c.m.} = A_2 (V_{2,c.m.} + V_{1,c.m.}) \quad (3.20)$$

$$\frac{V_{1,c.m.}}{V_{2,c.m.} + V_{1,c.m.}} = \frac{A_2}{A_T} = M_R \quad (3.21)$$

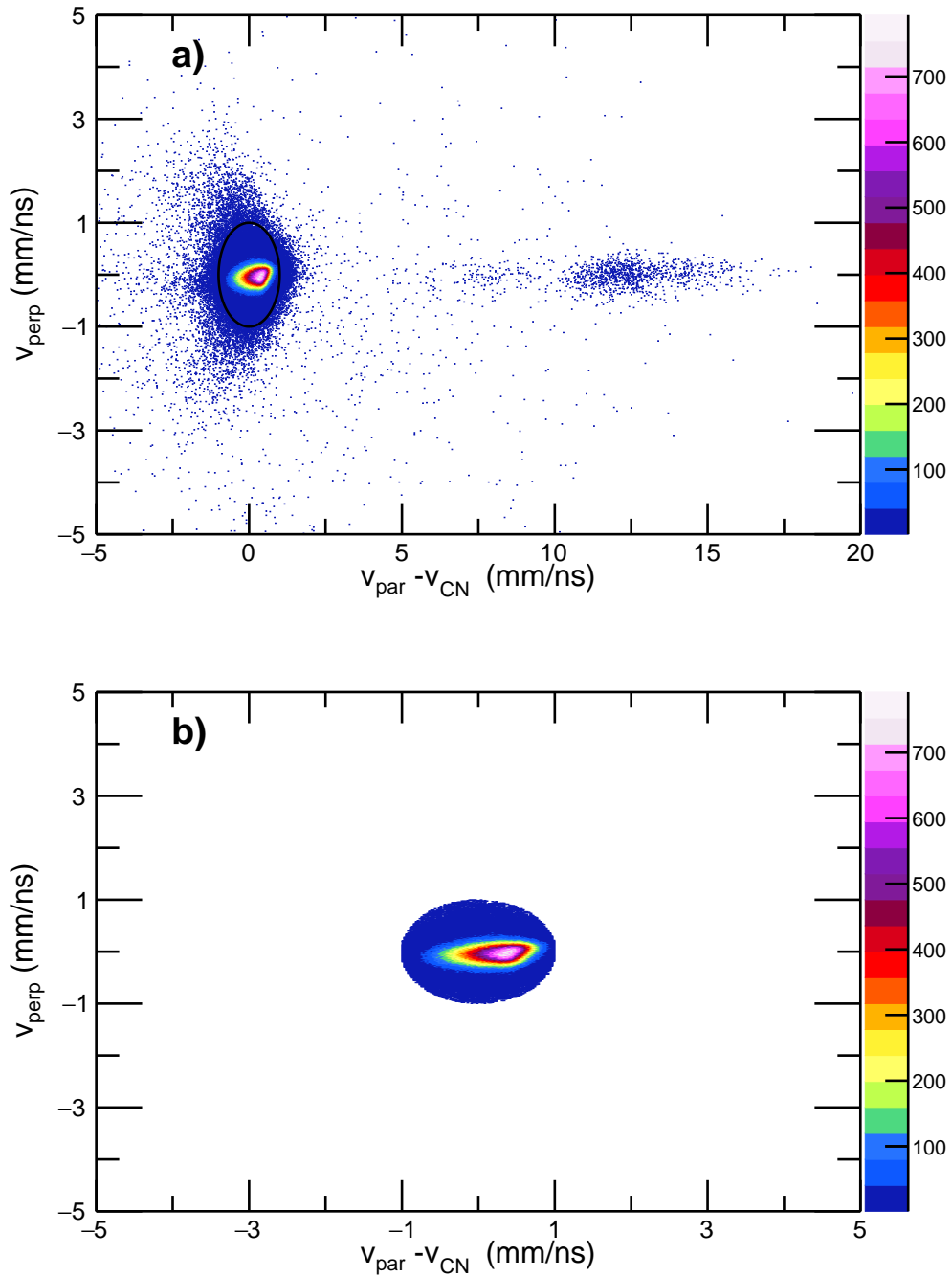


Figure 3.13: Perpendicular velocity determined for $^{50}\text{Cr} + ^{180}\text{W}$ at $E_{\text{Lab}} = 284.0$ MeV as a function of the difference between v_{par} and v_{CN} . The solid, black circle in Panel A represents the gate applied to the data set and has a 1 mm/ns radius. Panel A shows the distribution before the gate was applied. Panel B shows the distribution after the gate was applied to the data set.

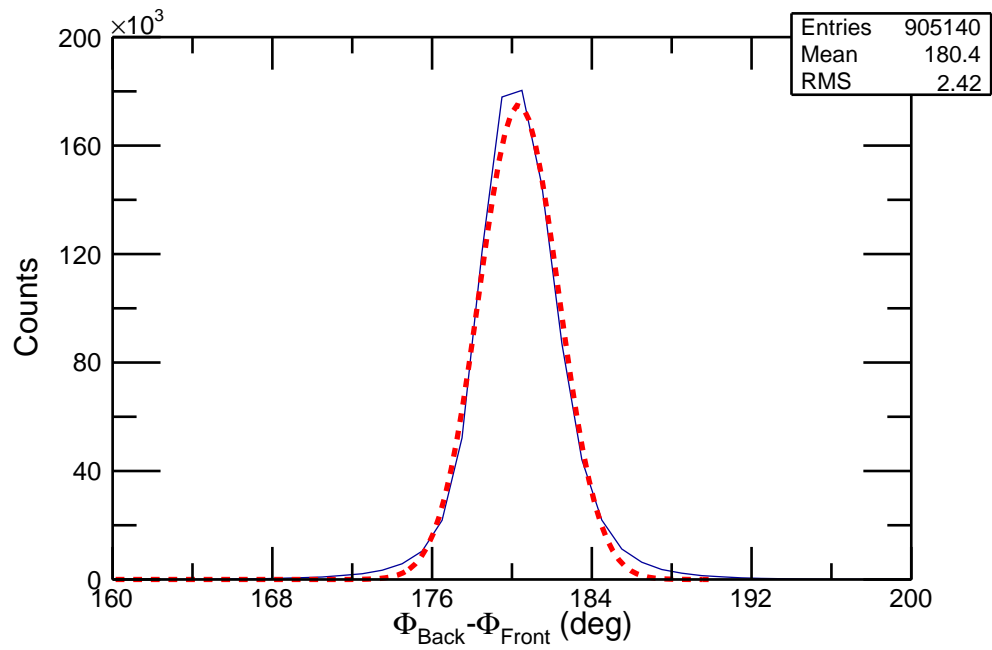


Figure 3.14: The number of counts observed for $^{50}\text{Cr} + ^{180}\text{W}$ at $E_{\text{Lab}} = 284.0$ MeV shown as a function of the difference between the determined values of Φ from the Back detector and the Front detector for gated coincident events. The data is represented as the solid blue line and shows a strong peak at a Φ difference of 180° . A Gaussian function fitted to the data is shown as the dashed, red line and the box in the upper right corner provides the means and RMS from the fit.

where A_i is the mass of fragment i and $V_{i,c.m.}$ is the total velocity vector in the center-of-mass frame for fragment i .

3.5.3 Energy Calculation

The deduced velocity vectors were corrected for energy loss of the projectile in the target and target backing material and for the energy loss of the fragment exiting the target by estimating the energy loss relative to the energy loss of an alpha particle in the same material [102].

To determine the estimated energy loss, an initial energy $E_{int,Lab}$ of the emitted fragment was determined as

$$E_{int,Lab} = 0.00518 * M_R * (A_P + A_T) * v_{lab}^2 \quad (3.22)$$

then v_{lab} of the emitted fragment was recalculated with the new energy values as

$$v_{lab} = 13.89 \sqrt{\frac{E_{new,Lab}}{M_R * (A_P + A_T)}} \text{ (mm/ns)}. \quad (3.23)$$

This process was iterated until the change in E_{lab} was less than 10 keV. Then, the center-of-mass velocities were determined with eq. 3.14 with the v_{lab} corrected for energy loss in the target.

Additionally, the energy of each emitted fragments was determined. The energy was estimated as

$$E_{frag,i} = M_{R,i} * (A_P + A_T) * V_{lab}^2 \quad (3.24)$$

It is important to note that the CUBE detector setup was optimized for position and time measurements, not for measuring the energy of the emitted fragments. Additionally, the

CUBE detector setup was optimized for mass ratio determination and does not account for neutron loss, which could change the mass and therefore the total energy. Thus, this is only an approximation. Further corrections would be necessary to accurately determine the energy of the fragments.

3.5.4 Total Kinetic Energy Gates

The sum of the $E_{\text{frag},i}$ values for two coincident fragments is the total kinetic energy of the system. The ratio of the deduced total kinetic energy to a theoretical total kinetic energy is shown in Figure 3.15. Where the theoretical total kinetic energy for fission fragments is calculated using Viola systematics [107, 108]

$$TKE = 0.11897Z^2/A^{1/3} + 7.3\text{MeV}, \quad (3.25)$$

where Z and A refer to the compound nucleus [108]. The deduced total kinetic energy ($E_{\text{frag},1} + E_{\text{frag},2}$) for fission events should be equivalent to that given by eq. 3.25. The total kinetic energy calculated with Viola systematics for the $^{50}\text{Cr} + ^{180}\text{W}$ system is 193.8 MeV. The intense groups at $M_R = 0.2$ and 0.8 in Figure 3.15 are scattering events. The band of events between $M_R = 0.35$ and 0.65 with a total kinetic energy ratio of approximately one are fission-like events. As observed in Figure 3.15 the tail of the heavy scattering events includes events at M_R values near to the range of the fission-like events. The scattering events in that region were removed from the data set by a gate represented by the black polygon shown in Panel A of Figure 3.15. The distribution after the gate was applied to the data is shown in Panel B of Figure 3.15.

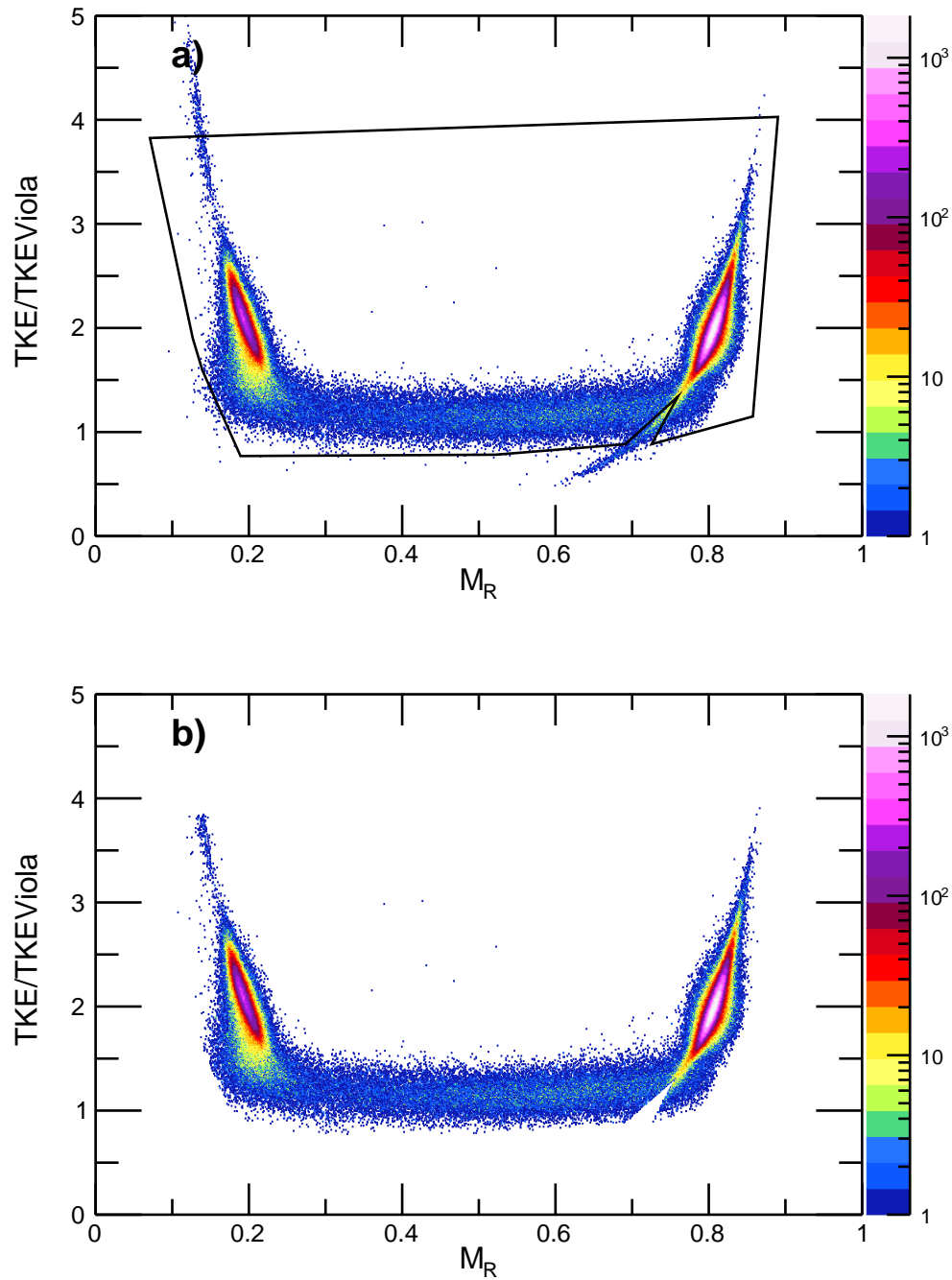


Figure 3.15: Ratio of the deduced total kinetic energy from binary fragments to the total kinetic energy calculated for fission fragments for $^{50}\text{Cr} + ^{180}\text{W}$ at $E_{\text{Lab}} = 284.0$ MeV shown as a function the determined mass ratios. The solid, black polygon in Panel A represents the gates used to remove scattering events with mass ratios in the fission-like region. Panel A shows the distribution before the gate was applied. Panel B shows the distribution after the gate was applied.

3.5.5 Determination of M_R and $\theta_{c.m.}$

After accounting for energy loss in the target, the fragment velocities were used to determine the final mass ratios and center-of-mass angles. The mass ratios were determined from the center-of-mass velocities as

$$M_{R,i} = \frac{V_{c.m.,j}}{V_{c.m.,i} + V_{c.m.,j}} \quad (3.26)$$

where i corresponds to the fragment for which the mass ratio was determined, and j corresponds to the coincident fragment. The second quantity of interest in the present work is $\theta_{c.m.}$, which was determined from the components of the center-of-mass velocity vectors and v_{cn} as

$$\theta_{c.m.} = \tan\left(\frac{u_i}{w_i - v_{cn}}\right) \quad (3.27)$$

The chapter has discussed the full set of calibrations and gates applied to the data set in the present work. The resulting mass ratios and $\theta_{c.m.}$ determined for the coincident fragments observed in the present work will be discussed in Chapter 4.

Chapter 4

Results

This chapter presents the results of the Cr+W measurements performed at the Australia National University in November 2013. Mass distributions, angular distributions, and mass-angle distributions (MAD) were deduced for each of the eight reactions measured in the present work at both $E_{c.m.}/V_B = 1.13$ and $E_{CN}^* = 52.0$ MeV. The techniques for fitting each mass distribution to determine the width and the details of the calculation of the theoretical predictions for pure fusion-fission mass distributions are discussed. This chapter also describes the method for determining the angular distributions for each system in the present work.

4.1 Cr + W: $E_{c.m.}/V_B = 1.13$

This section presents the MADs, mass distributions, and angular distributions generated for the series of systems measured at $E_{c.m.}/V_B = 1.13$ in the present work.

4.1.1 Mass-Angle Distributions

As discussed in Section 1.3.3, MADs have been used extensively in studies of reaction dynamics [40, 39, 87]. MADs are a histogram of the $\theta_{c.m.}$ as a function of the determined mass ratios, which constitutes the full data set of the present work. A MAD was generated for each of the two MWPCs in the present work. The MADs generated from events in the Back

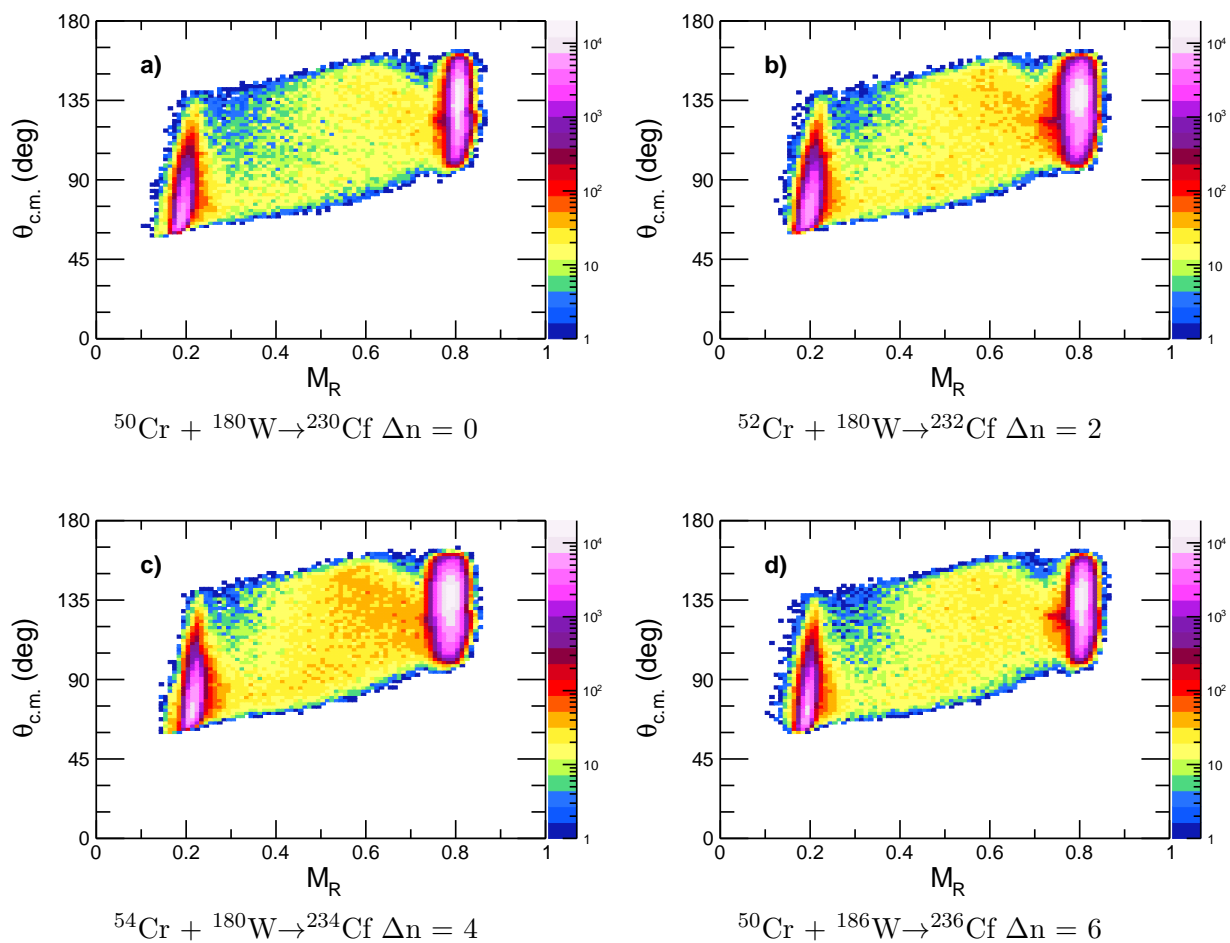
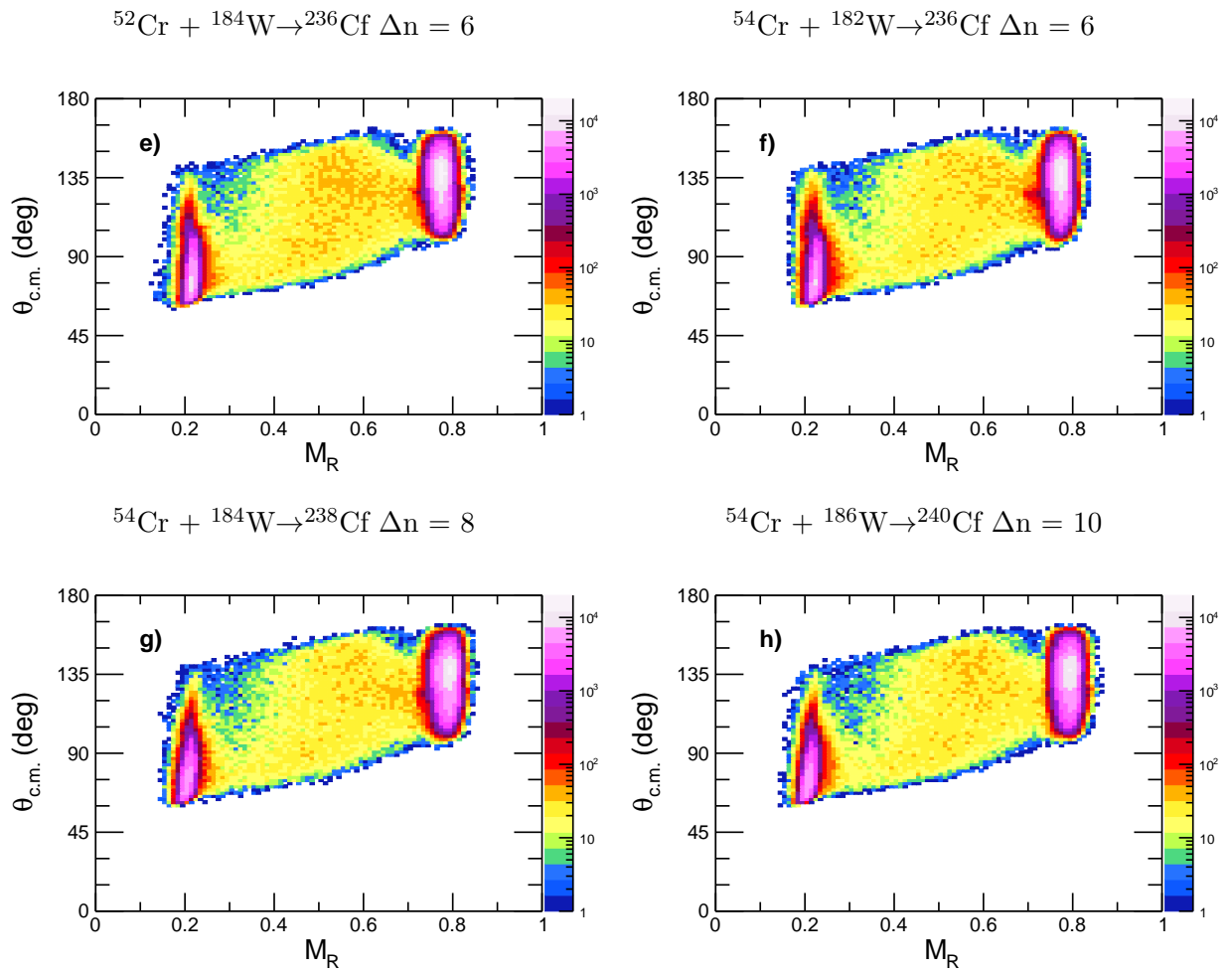


Figure 4.1: Unsymmetrized MADs of the eight Cr + W reactions in the Back MWPC at $E_{c.m.}/V_B = 1.13$. Δn is the change in the number of neutrons in the compound nucleus relative to $^{50}\text{Cr} + ^{180}\text{W}$, where $N = 132$.

MWPC for each system studied in the present work are shown in Figure 4.1. Coincidence between two observed fragments in each detector was required for each event recorded in the present work. The complementary MADs observed by the Front MWPC for the systems measured in the present work are shown in Figure 4.2. These MADs are obtained directly from the MWPCs and are referred to as “unsymmetrized.” As the term implies, the MADs can also be shown in a symmetrized fashion. The following section briefly discusses symmetrization.

Figure 4.1: (cont'd)



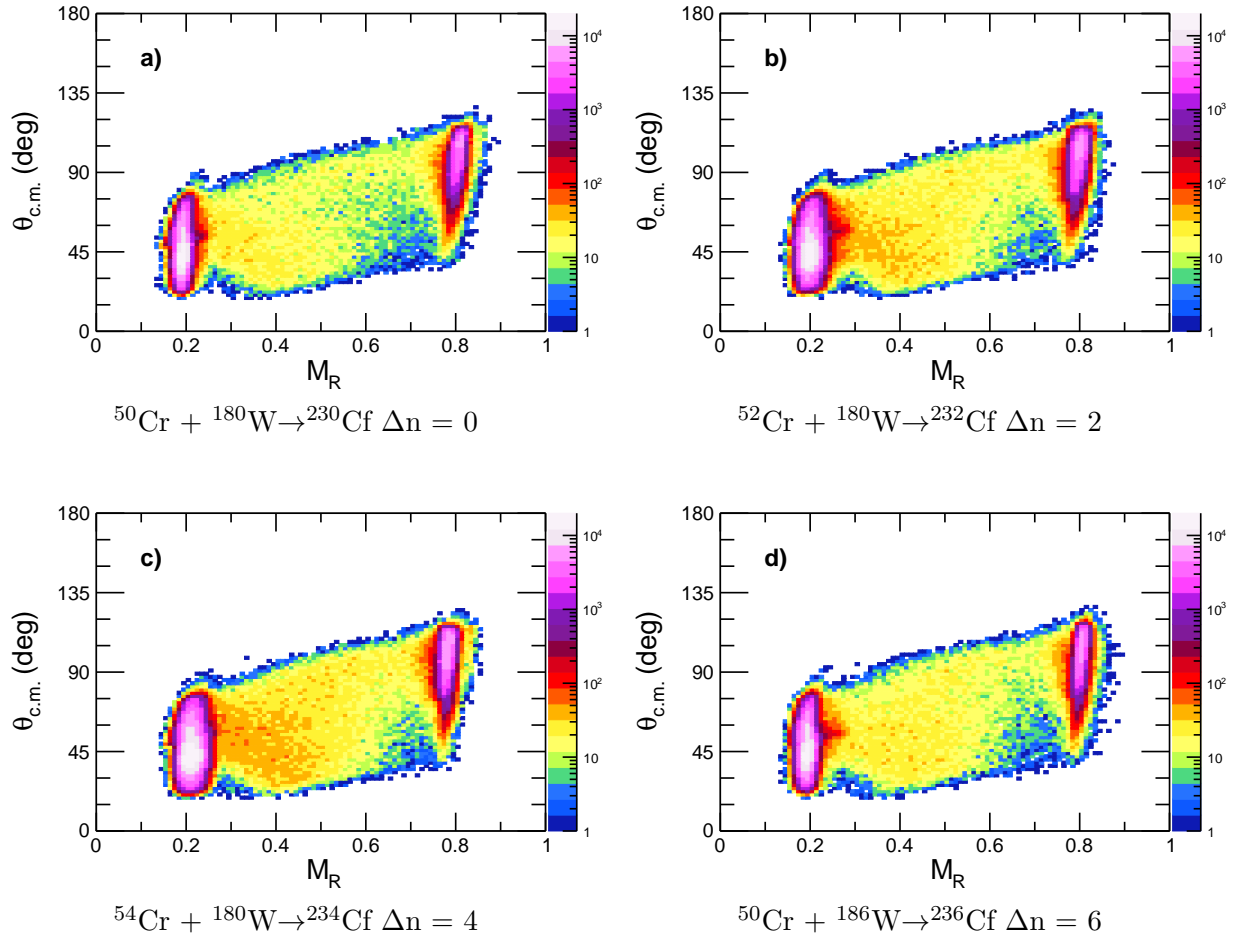
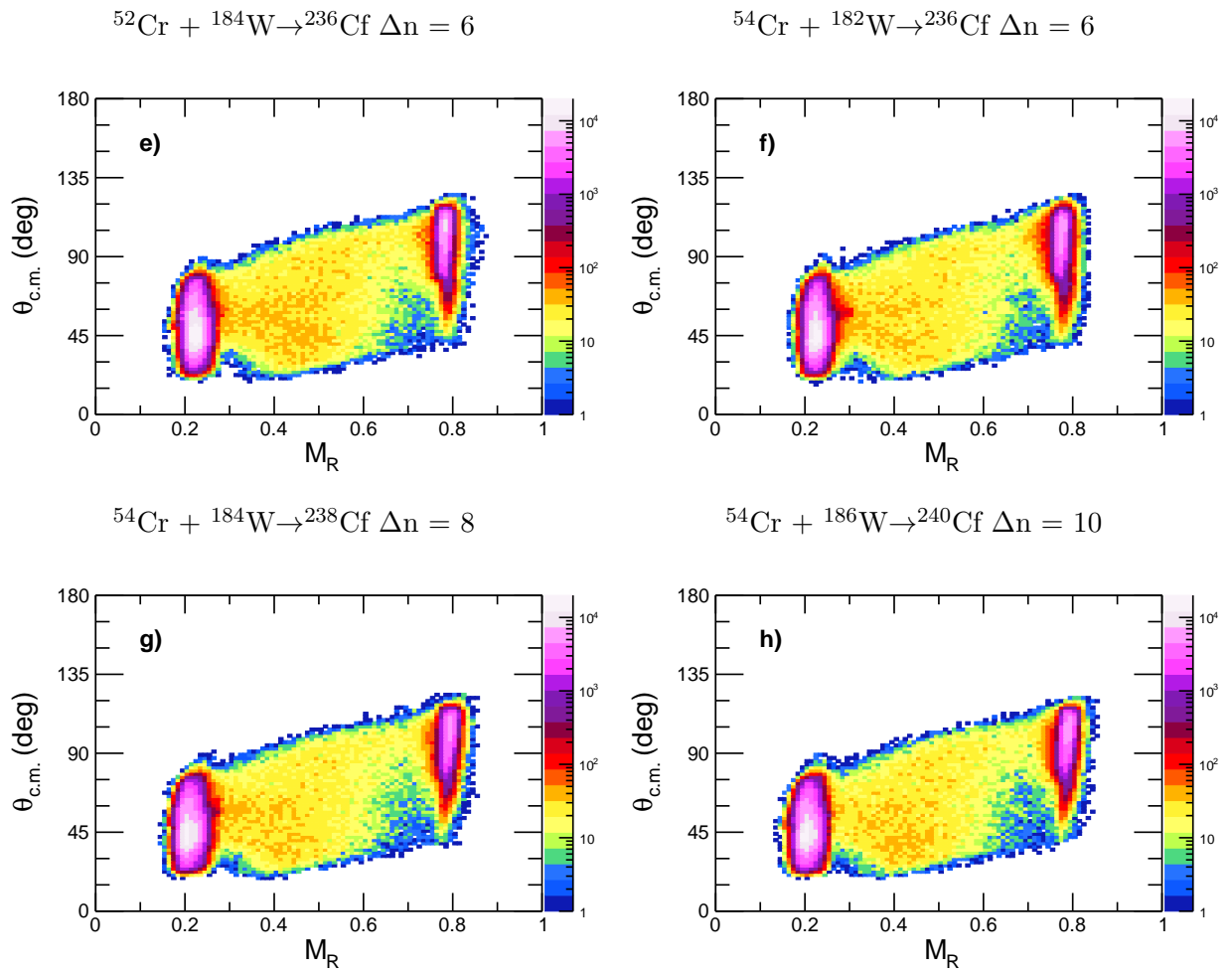


Figure 4.2: Unsymmetrized MADs generated for the Cr + W reactions in the Front MWPC at $E_{\text{c.m.}}/V_{\text{B}} = 1.13$. Δn is the change in the number of neutrons in the compound nucleus relative to the lightest system, $^{50}\text{Cr} + ^{180}\text{W}$, where $N = 132$.

Figure 4.2: (cont'd)



4.1.1.1 Symmetrization

Often in heavy-ion fusion reaction studies MADs are symmetrized. This means that for half of the events shown in the MAD the mass ratio and $\theta_{\text{c.m.}}$ were determined based on the assumption that for binary events detected in coincidence, any fragment detected at θ_1 , $M_{\text{R},1}$ will have a partner at $180 - \theta_1$, $1 - M_{\text{R},1}$ in the center-of-mass frame. An important consideration when looking at MADs though is that the angular dimension is generally considered from $0^\circ \leq \theta_{\text{c.m.}} \leq 180^\circ$ on both sides of the beam axis, as shown in Panel A of Figure 3.3. If θ were to be shown as 360° , then a more expanded MAD could be plotted like the cartoon MAD in Figure 4.3 Panel A. This illustration of a MAD depicts the mass and angle trajectories of an example reaction as a function of contact time. One possible correlation between $\theta_{\text{c.m.}}$ and M_{R} for the light fragment is depicted by the dotdashed, blue lines and the corresponding correlation between $\theta_{\text{c.m.}}$ and M_{R} for the heavy fragment is depicted by the dashed, red lines. At 45 degree increments, illustrations of the separating system are shown. For example, a light fragment observed at $\theta_{\text{c.m.}}$ of 135° corresponds to a heavy fragment observed at $\theta_{\text{c.m.}}$ of -45° . To move between this expanded MAD and the generally used MADs, the negative angles are reflective at 0° , to produce MADs like the one shown in Figure 4.3 Panel B. Now, a light fragment observed at $\theta_{\text{c.m.}}$ of 135° corresponds to a heavy fragment observed at $\theta_{\text{c.m.}}$ of 45° . This distinction is important to keep in mind when considering MADs. The two fragments are emitted 180° apart, but are depicted at θ_1 and $180 - \theta_1$.

Symmetrized MADs are used throughout the literature to study fusion-fission and quasi-fission competition in heavy-ion reactions. In order to be consistent with the literature, the MADs in the present work were also symmetrized. The symmetrized MADs shown here

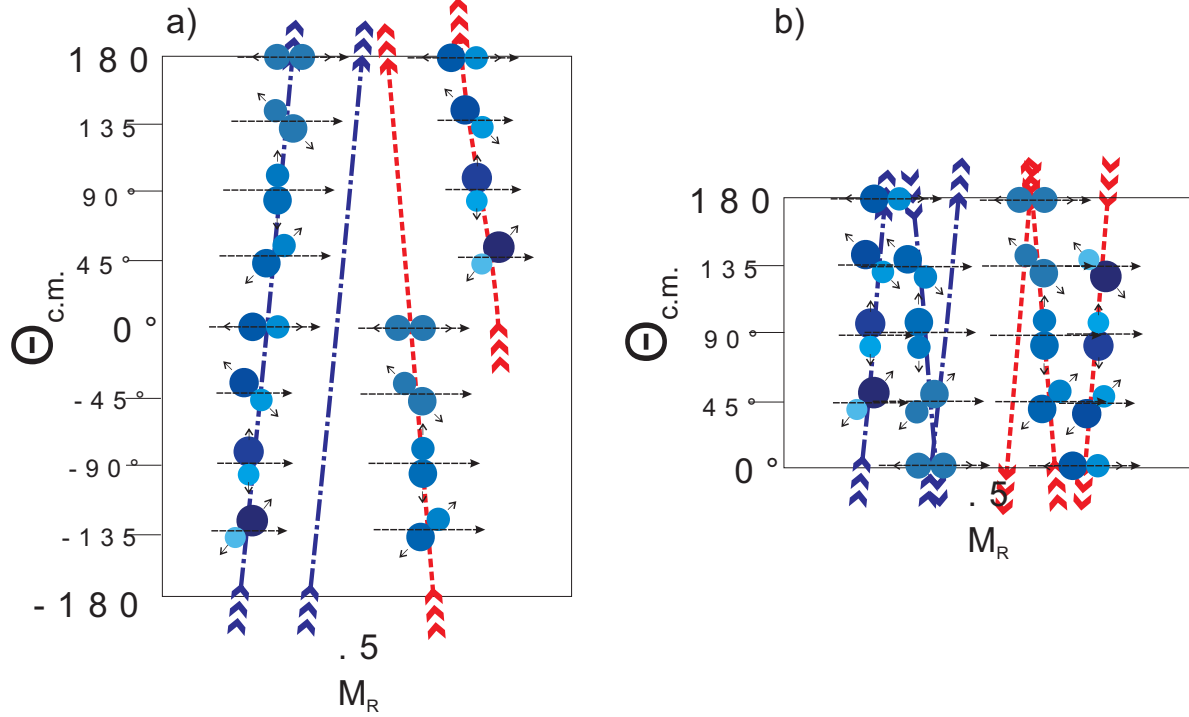


Figure 4.3: Evolution of a mass angle distribution through various separation angles. Panel A shows the full 360 degree coverage. Panel B shows a symmetrized MAD with a 0-180 degree scale in θ .

were generated from the Back MWPC MADs. For each event in the Back MWPC MAD a corresponding event was placed at $180 - \theta_1$ and $1 - M_{R,1}$.

4.1.1.2 Symmetrized MADs for Cr + W systems

There are three key regions in a MAD: the first is the intense region of products near the mass ratio of the projectile (≈ 0.2 in the present work). The second is the complementary cluster of products near the mass ratio of the target (≈ 0.8 in the present work). Together, the events in these regions constitute the largest fraction of scattering events detected in the multi-wire proportional counters (MWPC) during the measurements. The third region contains the fission-like events at central mass ratios and is the focus of the present work. The fission-like region is taken to be between mass ratios of 0.35 and 0.65 in the present work and

is indicated by the solid, black rectangle in Figure 4.4. This region was selected because it consistently excludes the elastic events throughout the data set. Previous work has concluded that a correlation between mass ratio and angle in the fission-like region of a symmetrized MAD (as opposed to a constant angle and mass ratio) is one indication of the presence of quasifission [5, 4]. A mass-angle correlation was observed in each experimental MAD in the present work at $E_{c.m.}/V_B = 1.13$ in the central fission-like region, indicating the presence of quasifission. The MAD generated from the reaction of $^{50}\text{Cr} + ^{180}\text{W}$ at $E_{\text{lab}} = 284.6$ MeV is shown in Figure 4.4. The observed correlation is highlighted by the three regions indicated in Figures 4.4 and 4.5. The solid, black rectangle encompasses events from $M_R = 0.35 - 0.65$ and spans the angular coverage of the detectors to highlight the region where fission-like fragments are expected. One region of note is centered at $M_R \sim 0.4$ and $\theta_{c.m.} \approx 45^\circ$. The second complementary region is centered at $M_R \sim 0.6$ and between $\theta_{c.m.} \approx 135^\circ$. Events with this combination of mass ratios and $\theta_{c.m.}$ can likely be attributed to quasifission due to relatively small angular deflection from the grazing angle and indicates a short contact time for the dinuclear system. These regions indicate that the heavy fragments ($M_R > 0.5$) were preferentially emitted at backward angles ($\theta_{c.m.} > 90^\circ$), while the light fragments ($M_R < 0.5$) were preferentially emitted at forward angles ($\theta_{c.m.} < 90^\circ$), which is termed a mass-angle correlation. For example, note that the light fragments are preferentially detected in the Front Detector (Figure 4.2) at small $\theta_{c.m.}$ and M_R , while the heavy fragments are observed in the Back MWPC (Figure 4.1). Only in the symmetrized figures are they both present (Figure 4.6). The mass distribution generated from the reaction of $^{54}\text{Cr} + ^{186}\text{W}$ at $E_{\text{lab}} = 287.6$ MeV, Figure 4.5, shows that the regions at asymmetric mass ratios are less enhanced relative to the mass symmetric region in Figure 4.4. The enhancement of the symmetric mass ratio events relative to the asymmetric mass ratio events indicates that less

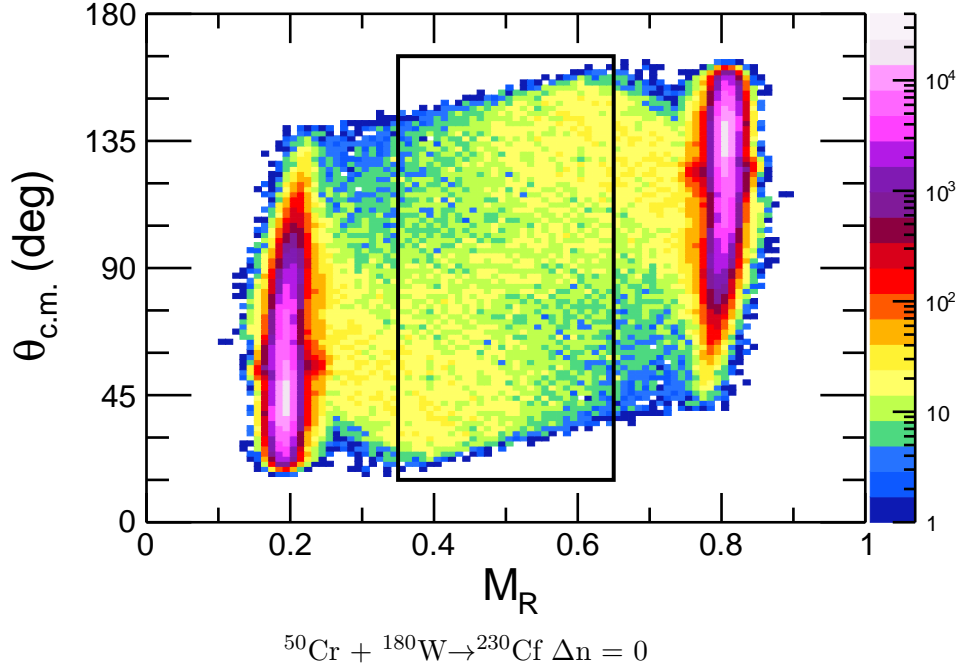


Figure 4.4: The mass angle distribution, where $\theta_{\text{c.m.}}$ is shown as a function of mass ratio, for coincident events from the reaction of ${}^{50}\text{Cr} + {}^{180}\text{W}$ at $E_{\text{lab}} = 284.6$ MeV. The solid, black rectangle highlights the mass symmetric region ($M_{\text{R}} = 0.35 - 0.65$) across the full angular coverage of the symmetrized MAD. See text for discussion. Δn is the change in the number of neutrons in the compound nucleus relative to the lightest system, ${}^{50}\text{Cr} + {}^{180}\text{W}$, where $N = 132$.

of the reaction flux is lost to quasifission in the reaction with the largest neutron number.

The six other MADs generated from the Cr + W systems at $E_{\text{c.m.}}/V_{\text{B}} = 1.13$ are shown in Figure 4.6. All axis scales and labels are the same in Figures 4.6 as those in Figure 4.4 and 4.5. Notice that in each MAD in the present work a mass angle correlation was observed. The change in the angular correlation with increasing neutron-richness will be addressed quantitatively in the mass distributions and is discussed in Section 4.1.2 below.

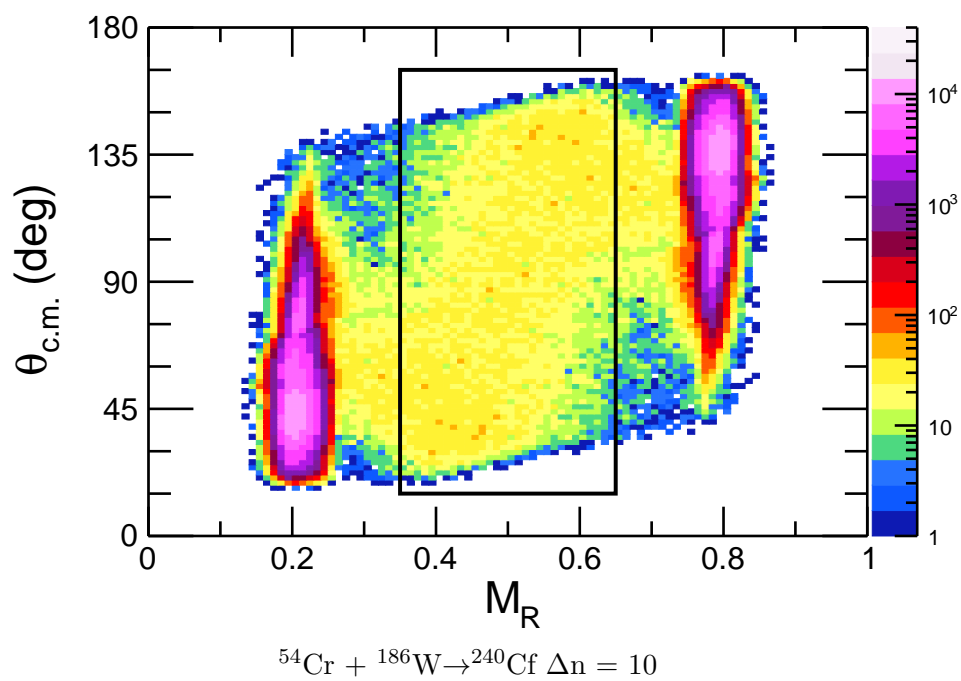


Figure 4.5: The symmetrized MAD from the reaction of $^{54}\text{Cr} + ^{186}\text{W}$ at $E_{\text{lab}} = 281.7$ MeV. As in Figure 4.4, the solid, black rectangle was drawn to highlight the region of mass symmetric events between $M_R = 0.35 - 0.65$ across the angular coverage of the MWPCs.

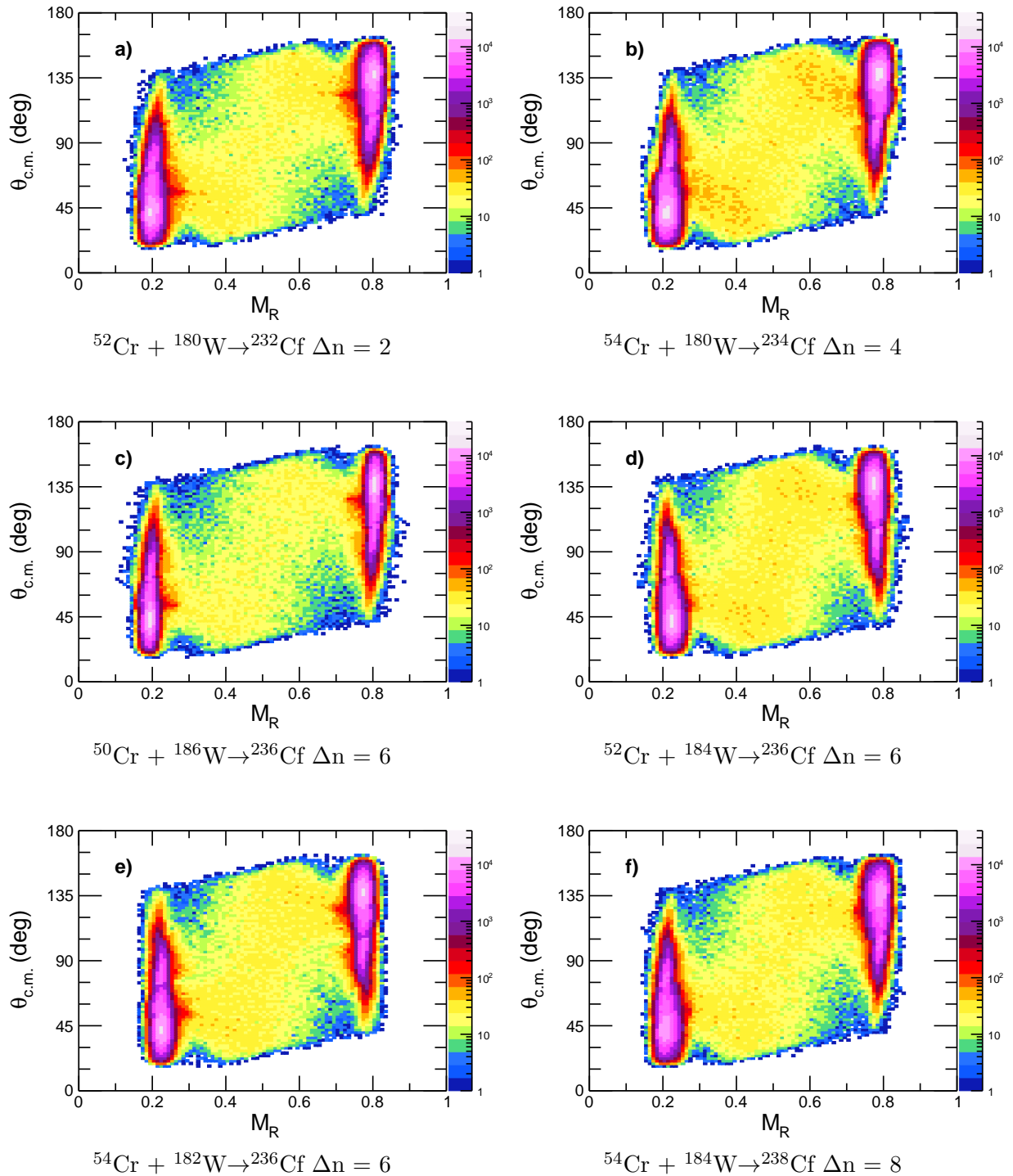


Figure 4.6: Symmetrized MADs of the remaining six Cr + W reactions at $E_{c.m.}/V_B = 1.13$. Δn is the change in the number of neutrons in the compound nucleus relative to $^{50}\text{Cr} + ^{180}\text{W}$, where $N = 132$.

4.1.2 Mass Distributions

The mass distributions from the symmetrized MADs for the eight Cr + W reactions measured at $E_{c.m.}/V_B = 1.13$ are shown in Figure 4.7. Each mass distribution is a simple projection of the corresponding symmetrized MAD onto M_R . The entire angular range was included in the mass distributions. The large peaks at $M_R = 0.2$ and 0.8 are the quasielastic scattering events with mass ratios similar to that of Cr to W in the entrance channel. The scattering peaks extend above the range presented in Figure 4.7, as the y-axis range was selected to clearly see the shape of the distribution in the fission-like region. The mass distributions have a maximum at mass ratios of 0.5 and a seemingly broad peak, which indicates that they are likely Type II systems according to the distinction discussed in Section 1.3.3.1 [40].

4.1.2.1 Determination of Mass Width from Mass Distribution

The mass-angle correlation in the MADs provided a qualitative means of comparing the reaction dynamics of the systems, however, it is useful to have a quantitative means of comparison. Therefore, the width of the mass distribution in the fission-like region was obtained. As discussed previously (1.3.1) a narrow mass distribution, similar to that obtained in low energy fission, indicates fusion-fission while a broad mass distribution is commonly considered to be an indication of the presence of quasifission.

In fusion-fission, since equilibrium is reached in the mass degree of freedom, the most probable fission fragments have a symmetric mass ratio. This results in a concentration of fragments with mass ratios near $M_R = 0.5$ and thus a sharp peak in the mass distribution. The width of the mass peak is indicative of the excitation energy of the fissioning system. However, in quasifission the dinuclear system separates before reaching full equilibrium, including in the mass degree of freedom. Larger impact parameter collisions with higher

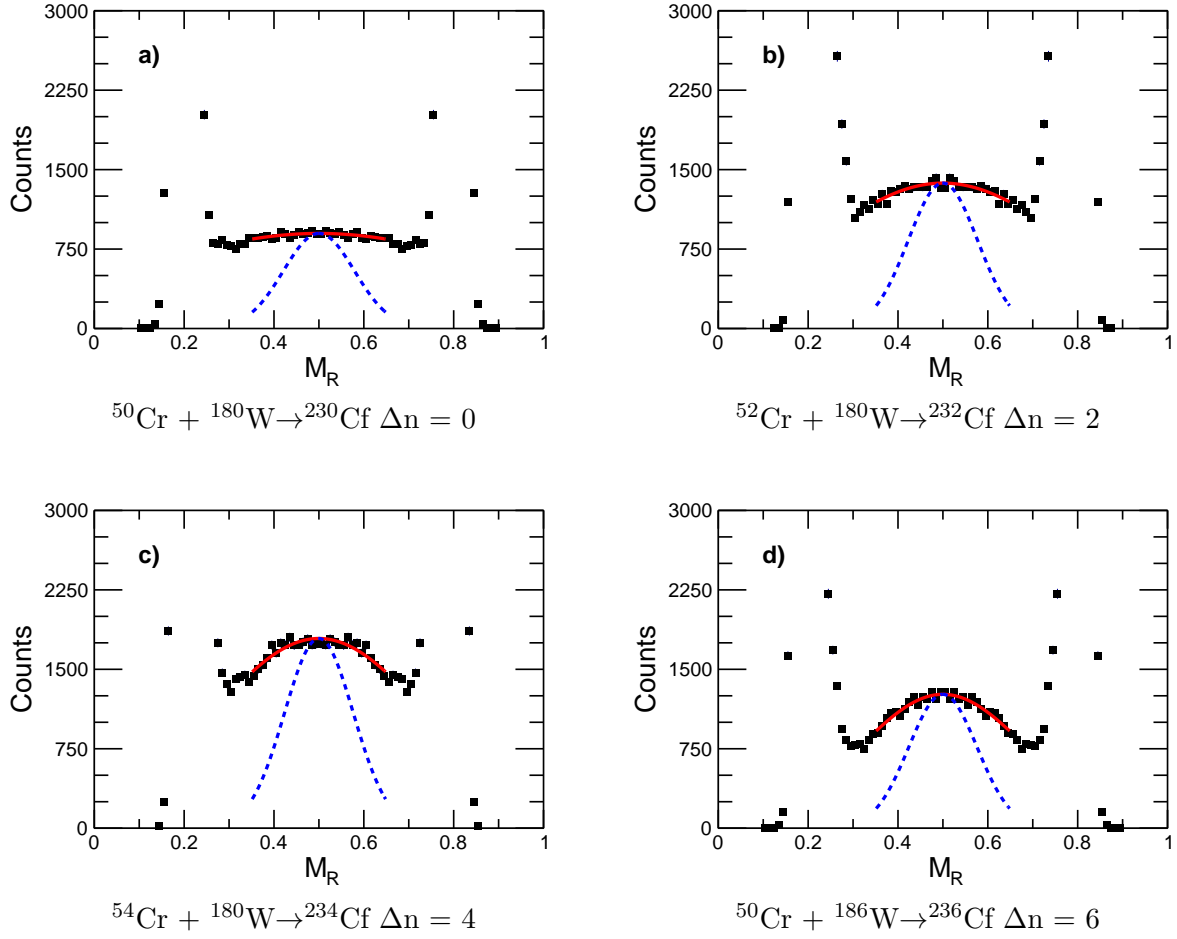
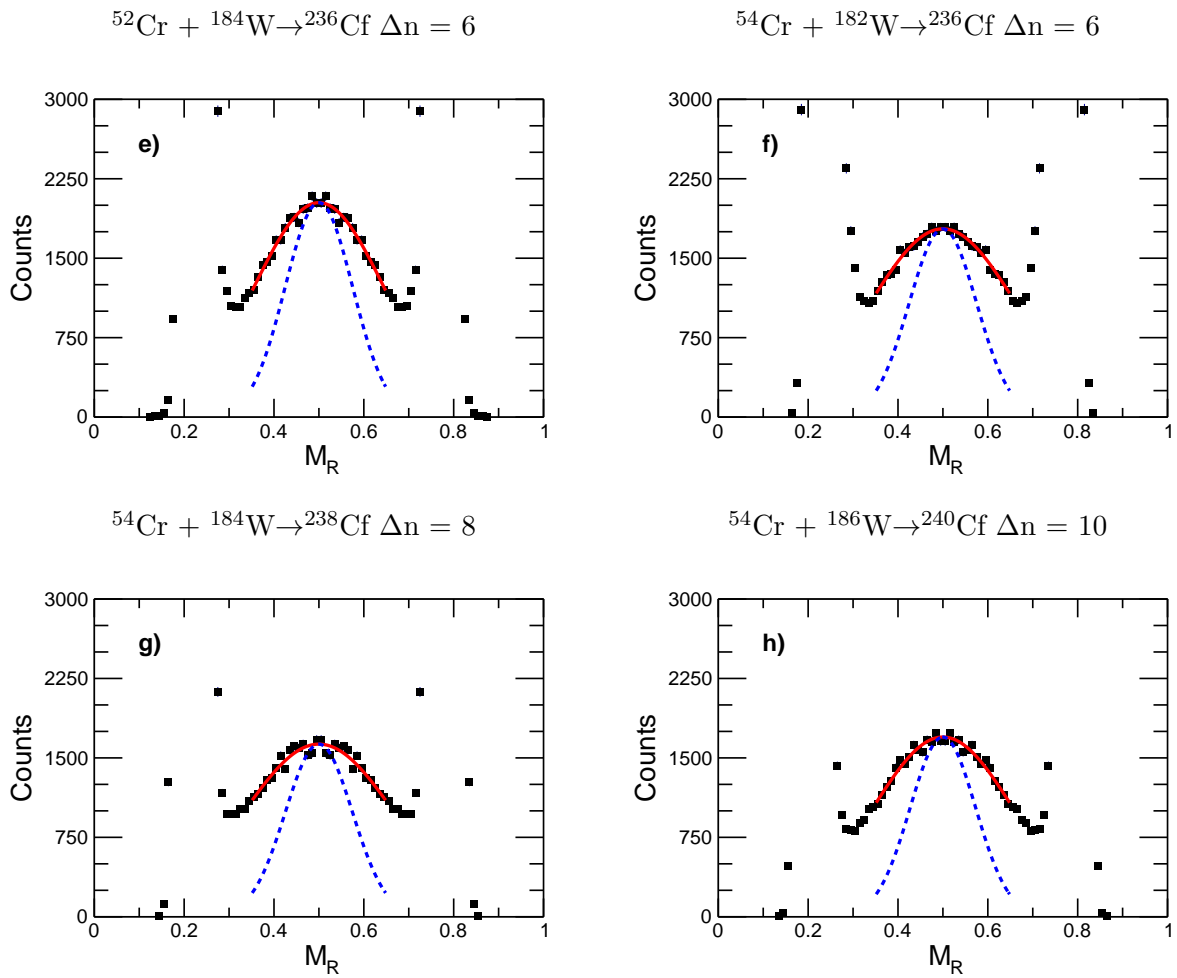


Figure 4.7: Mass distributions for all eight Cr + W systems from the present work at $E_{c.m.}/V_B = 1.13$. The solid red line represent a Gaussian fitted to the data. The dashed blue line represents a Gaussian function with the widths calculated from a statistical approximations for pure Fusion-fission. This Gaussian function has been normalized to the peak of the experimental mass distribution. Δn is the change in the number of neutrons in the compound nucleus relative to $^{50}\text{Cr} + ^{180}\text{W}$, where $N = 132$.

Figure 4.7: (cont'd)



orbital angular momentum result in re-separation of the dinuclear system on a shorter time scale, before full mass transfer has occurred. This results in fission-like fragments with a range of mass ratios, thus broadening the mass distribution for the system relative to the mass distribution of a system without quasifission.

In order to determine the width of the mass distributions, each experimental mass distribution was fitted with a Gaussian function centered on $M_R = 0.5$. It is important to note that the distributions are not expected to be purely Gaussian [43] However, they were similar enough to a Gaussian distribution in shape that they could be fit with a Gaussian function as a means of extracting the width of the experimental distributions. The mass distributions were only fitted between the mass ratios of 0.35 and 0.65 to uniformly exclude elastic and deep-inelastic scattering events. The resulting Gaussian functions are shown as the solid, red line in each panel of Figure 4.7. The width of the distribution was multiplied by A_{CN} to give the mass width (σ_{exp}). The mass distribution widths for each system are listed in Table 4.4. The uncertainty on the width of the Gaussian function fitted to the data was determined from a chi-squared minimization and is listed in Table 4.4. Each experimental width can be compared with a statistical approximation of pure fusion-fission (σ_{ff}) to account for any small changes resulting from the subtle differences among the systems. A method to calculate the expected width for fusion-fission is presented in the next section.

4.1.2.2 Statistical Approximation of Pure Fusion-Fission

The width of the fission mass distribution, σ_{ff} , from pure fusion-fission can be estimated by the statistical approximation

$$\sigma_{\text{ff}}^2 = \frac{T}{k} = \frac{1}{k} \sqrt{\frac{E_{\text{sci}}^*}{a}}, \quad (4.1)$$

where T is the nuclear temperature at the scission point [5, 46], k is the stiffness parameter, 0.0048MeV/u^2 , E_{sci}^* is the excitation energy of the compound nucleus at the scission point, and a is the level density parameter defined as $a = A/8.5\text{MeV}^{-1}$. Lin et al. suggest that the nuclear excitation energy at scission can be calculated as

$$E_{\text{sci}}^* = E^* + Q_{\text{sym}} - \text{TKE} - \langle E_{\text{pre}}^{\text{sci}} \rangle - E_{\text{rot}}^{\text{sci}} - E_{\text{def}}. \quad (4.2)$$

where Q_{sym} is the Q value for symmetric fission of the compound nucleus, TKE is the total kinetic energy released in fission from the Viola systematics [108] (See eq. 3.25). The average energy carried away by prescission neutron emission $\langle E_{\text{pre}}^{\text{sci}} \rangle$ is estimated from the neutron multiplicity ($\langle \nu_{\text{pre}} \rangle$) scaled by the energy removed by each neutron emitted, $\langle E_{\text{npre}} \rangle$. The neutron multiplicity was estimated as in [109] where

$$\langle \nu_{\text{pre}} \rangle = 1.98 - 0.0133A_{\text{CN}} - 0.0376E^* + 0.00042A_{\text{CN}}E^*. \quad (4.3)$$

The average energy removed by each emitted neutron was estimated in the same manner as [110] where $\langle E_{\text{npre}} \rangle = \langle E_{\text{n}} \rangle + \langle B_{\text{n}} \rangle$, with $\langle B_{\text{n}} \rangle$ is the average neutron binding energy, 8.027 MeV, $\langle E_{\text{n}} \rangle = 2.0 * T_{\text{n}}$ and $T_{\text{n}} = \sqrt{E^*/a}$. The deformation energy (E_{def}) was set to 12 MeV because it is a commonly used value in actinide fission [5]. The rotational energy at scission $E_{\text{rot}}^{\text{sci}}$ was calculated as described in [109], where $E_{\text{rot}}^{\text{sci}} = (E_{\text{rot}}^0 / 4.3) + (T / 2.0)$. E_{rot}^0 was defined as $E_{\text{rot}}^0 = 34.54 l^2 / A_{\text{CN}}^2$, where l is the average entrance channel angular momentum. An average l value of $25.19 \hbar$ for the Cr+W systems was calculated from CCFULL [111, 112]. $E_{\text{rot}}^{\text{sci}}$ and T had to be calculated iteratively so for each system convergence was defined as a change in $E_{\text{x}}^{\text{sci}} \leq 0.001$ and was reached after two iterations. The calculated σ_{ff} are listed in

Table 4.1: Calculated values used in the determination of E_{sci}^* .

System	E^* (MeV)	Q_{sym} (MeV)	TKE (MeV)	$E_{\text{pre}}^{\text{sci}}$ (MeV)	$E_{\text{rot}}^{\text{sci}}$ (MeV)	E_{def} (MeV)	E_{sci}^* (MeV)
$^{50}\text{Cr} + ^{180}\text{W}$	64.3	236.1	187.3	31.2	1.48	12	68.2
$^{50}\text{Cr} + ^{186}\text{W}$	71.4	231.5	185.9	37.7	1.43	12	65.7
$^{52}\text{Cr} + ^{180}\text{W}$	59.0	233.5	186.9	27.6	1.45	12	64.6
$^{52}\text{Cr} + ^{184}\text{W}$	62.2	231.5	185.9	30.4	1.42	12	63.8
$^{54}\text{Cr} + ^{180}\text{W}$	56.9	234.9	186.4	26.2	1.44	12	65.7
$^{54}\text{Cr} + ^{182}\text{W}$	57.2	231.5	185.9	26.6	1.41	12	62.7
$^{54}\text{Cr} + ^{184}\text{W}$	59.0	232.4	185.5	28.2	1.41	12	64.3
$^{54}\text{Cr} + ^{186}\text{W}$	61.1	228.5	185.0	29.6	1.38	12	61.05

Table 4.4.

A Gaussian function with its width set to the calculated width for pure fusion-fission for each system is shown as the dashed blue line for each respective mass distribution in Figure 4.7. Each theoretical Gaussian function was centered at $M_{\text{R}} = 0.5$ and normalized to the experimental data point at $M_{\text{R}} = 0.5$. It was not expected that pure fusion-fission would account for the full experimental mass distribution at symmetric mass ratios. The contribution to the mass distribution for pure fusion-fission would likely be smaller. Even normalized to the experimental data, it is clear that the pure fusion-fission width under estimates the experimental mass distribution. The additional contribution to the mass distribution must come from other processes and quasifission is the most likely cause of this deviation from pure fusion-fission.

The absolute height of the mass distribution for pure fusion-fission could not be determined from the experimental data, so only an upper limit of P_{CN} is reported in the present work. The upper limit of the probability of forming a compound nucleus P_{CN} for each

Table 4.2: Calculated values used in the determination of $E_{\text{pre}}^{\text{sci}}$.

System	$\langle \nu_{\text{pre}} \rangle$	$\langle E_{\text{npre}} \rangle$ (MeV)	$\langle E_{\text{n}} \rangle$ (MeV)	T_{n} (MeV)	$\langle B_{\text{n}} \rangle$ (MeV)
$^{50}\text{Cr} + ^{180}\text{W}$	2.7	11.5	3.5	1.7	8.065
$^{50}\text{Cr} + ^{186}\text{W}$	3.2	11.7	3.6	1.8	8.065
$^{52}\text{Cr} + ^{180}\text{W}$	2.4	11.4	3.3	1.7	8.065
$^{52}\text{Cr} + ^{184}\text{W}$	2.7	11.4	3.4	1.7	8.065
$^{54}\text{Cr} + ^{180}\text{W}$	2.3	11.3	3.2	1.6	8.065
$^{54}\text{Cr} + ^{182}\text{W}$	2.4	11.3	3.2	1.6	8.065
$^{54}\text{Cr} + ^{184}\text{W}$	2.5	11.3	3.3	1.6	8.065
$^{54}\text{Cr} + ^{186}\text{W}$	2.6	11.4	3.3	1.7	8.065

Table 4.3: Calculated values used in the determination of the $E_{\text{rot}}^{\text{sci}}$.

System	E_{rot}^0 (MeV)	T (MeV)	l (\hbar)
$^{50}\text{Cr} + ^{180}\text{W}$	2.54	1.79	25.19
$^{50}\text{Cr} + ^{186}\text{W}$	2.43	1.73	25.19
$^{52}\text{Cr} + ^{180}\text{W}$	2.50	1.73	25.19
$^{52}\text{Cr} + ^{184}\text{W}$	2.43	1.71	25.19
$^{54}\text{Cr} + ^{180}\text{W}$	2.47	1.74	25.19
$^{54}\text{Cr} + ^{182}\text{W}$	2.43	1.69	25.19
$^{54}\text{Cr} + ^{184}\text{W}$	2.40	1.70	25.19
$^{54}\text{Cr} + ^{186}\text{W}$	2.36	1.65	25.19

Table 4.4: Experimental mass widths σ_{exp} , statistical estimate for the pure fusion-fission mass width σ_{ff} , and the ratio of $\sigma_{\text{exp}}/\sigma_{\text{ff}}$ (upper limit of P_{CN}) for all 8 systems measured at the same $E_{\text{c.m.}}/V_{\text{B}} = 1.13$

System	Δ_{N}	σ_{exp}	error	σ_{ff}	$P_{\text{CN}}(UL) = \sigma_{\text{ff}}/\sigma_{\text{exp}}$
$^{50}\text{Cr} + ^{180}\text{W}$	0	98.0	16.4	18.19	0.186
$^{50}\text{Cr} + ^{186}\text{W}$	6	43.8	1.3	17.74	0.409
$^{52}\text{Cr} + ^{180}\text{W}$	2	65.4	4.0	18.11	0.274
$^{52}\text{Cr} + ^{184}\text{W}$	6	34.1	0.5	17.68	0.521
$^{54}\text{Cr} + ^{180}\text{W}$	4	55.8	2.1	17.96	0.321
$^{54}\text{Cr} + ^{182}\text{W}$	6	38.3	0.7	17.69	0.462
$^{54}\text{Cr} + ^{184}\text{W}$	8	39.9	0.8	17.77	0.446
$^{54}\text{Cr} + ^{186}\text{W}$	10	37.4	0.7	17.50	0.468

Cr + W system was taken to be the ratio of the calculated mass width for fusion-fission to the experimental mass widths as

$$\text{Upper Limit } P_{\text{CN}} \leq \frac{\sigma_{\text{ff}}}{\sigma_{\text{exp}}}. \quad (4.4)$$

The fractional values of the upper limit of P_{CN} determined for each system are listed in Table 4.4.

4.1.3 Angular Distributions

The angular distributions ($W(\theta)$) were determined for the eight Cr + W reactions measured in the present work. Each distribution was summed over all Φ . Each angular distribution was expressed as the differential fragment cross section at a given angle ($\frac{d\sigma}{d\Omega}(\theta)$). The angular

distribution and the differential fragment cross section are related by [51]

$$\frac{d\sigma}{d\Omega}(\theta) = \frac{W}{2\pi}(\theta)\sigma. \quad (4.5)$$

See Section 1.3.2 for more discussion. $\frac{d\sigma}{d\Omega}(\theta)$ was determined with a method developed by the reaction dynamics group at ANU. The method uses a normalization to an elastic scattering calibration measurement to determine the angular distribution while accounting for the thickness of the target and the efficiencies of the MWPCs and Si monitor detectors.

The angular distribution was only determined for $\theta_{c.m.}$ between 101° and 141° so only angles where the Back MWPC covered all mass ratios in the fission-like region were considered. The angular region is highlighted in Figures 4.8 and 4.9 by the dashed black box. $\frac{d\sigma}{d\Omega}(\theta)$ was determined for angular bins that were four degrees wide across this region. The $\theta_{c.m.}$ values reported in Figure 4.15 correspond to the center of each bin.

As described in Section 3.2.1, during the experiment at ANU, an elastic scattering calibration measurement was run with the reaction of $^{50}\text{Cr} + ^{184}\text{W}$ at $E_{\text{lab}} = 186.0$ MeV. The energy of the calibration run was selected to be below the Bass interaction barrier [9] of $^{50}\text{Cr} + ^{184}\text{W}$ of 196.04 MeV. At this energy, the nuclear reaction cross section goes to zero, so all of the reaction flux should be elastic scattering events.

The unsymmetrized MAD observed in the Back MWPC for the calibration measurement of $^{50}\text{Cr} + ^{184}\text{W}$ at $E_{c.m.} = 186.0$ MeV are shown in Figure 4.8. Only fragments with light mass ratios at 0.2 are observed in the Back MWPC because the heavy fragment did not have sufficient energy to get out of the target.

The unsymmetrized MAD observed in the Back MWPC for $^{50}\text{Cr} + ^{180}\text{W}$ at $E_{\text{lab}} = 284.6$ MeV is shown in Figure 4.9 as an example. The MAD after the mass ratio gate was applied

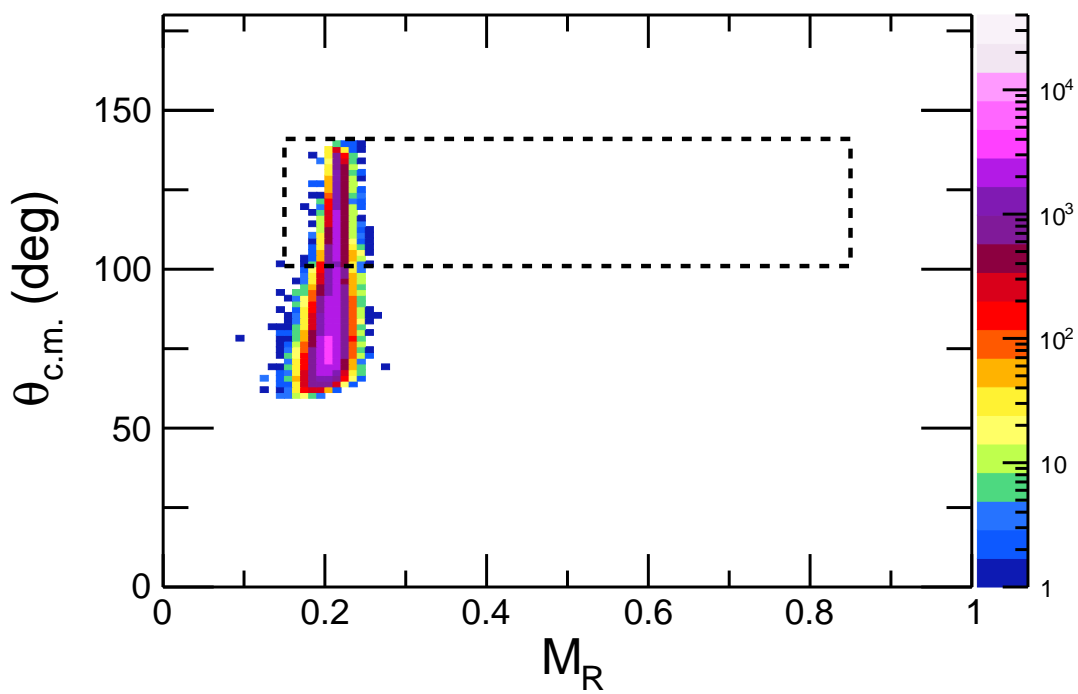


Figure 4.8: Unsymmetrized mass angle distribution for calibration run of $^{50}\text{Cr} + ^{184}\text{W}$ at $E_{\text{lab}} = 186.0$ MeV. The dashed, black box indicates the angular region included in the angular distribution calculations.

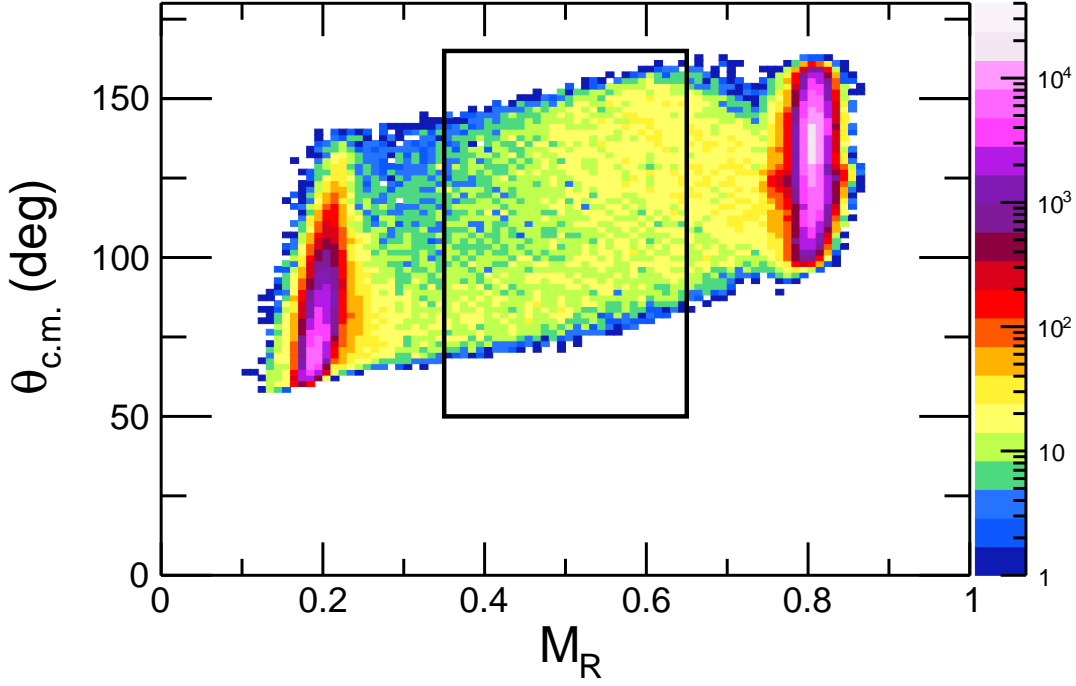


Figure 4.9: Unsymmetrized mass angle distribution for $^{50}\text{Cr} + ^{180}\text{W}$ at $E_{\text{lab}} = 284.6$ MeV as an example of the events included in the determination of the angular distribution. The solid, black box represents the gate used to exclude all events outside the fission-like region.

is shown in Figure 4.10 and the included angular region is highlighted by the dashed, black box.

4.1.3.1 Normalization of the Angular Distribution

The equation used for the normalization is

$$\frac{d\sigma(\theta_{\text{MWPC}}, E)}{d\Omega_{\text{MWPC}}} = Y_{\text{MWPC}}^{FF} * \frac{1}{Y_{\text{MWPC}, \text{Cal}}^{\text{Elastics}}} \frac{d\sigma(\theta_{\text{MWPC}}, E_{\text{Cal}})}{\delta\Omega_{\text{MWPC}}} * \frac{1}{Y_{\text{Mon}}^{\text{Elastics}}} \frac{d\sigma(\theta_{\text{Mon}}, E)}{\delta\Omega_{\text{Mon}}} * Y_{\text{Mon}, \text{Cal}}^{\text{Elastics}} \frac{\delta\Omega_{\text{Mon}}}{d\sigma(\theta_{\text{Mon}}, E_{\text{Cal}})}. \quad (4.6)$$

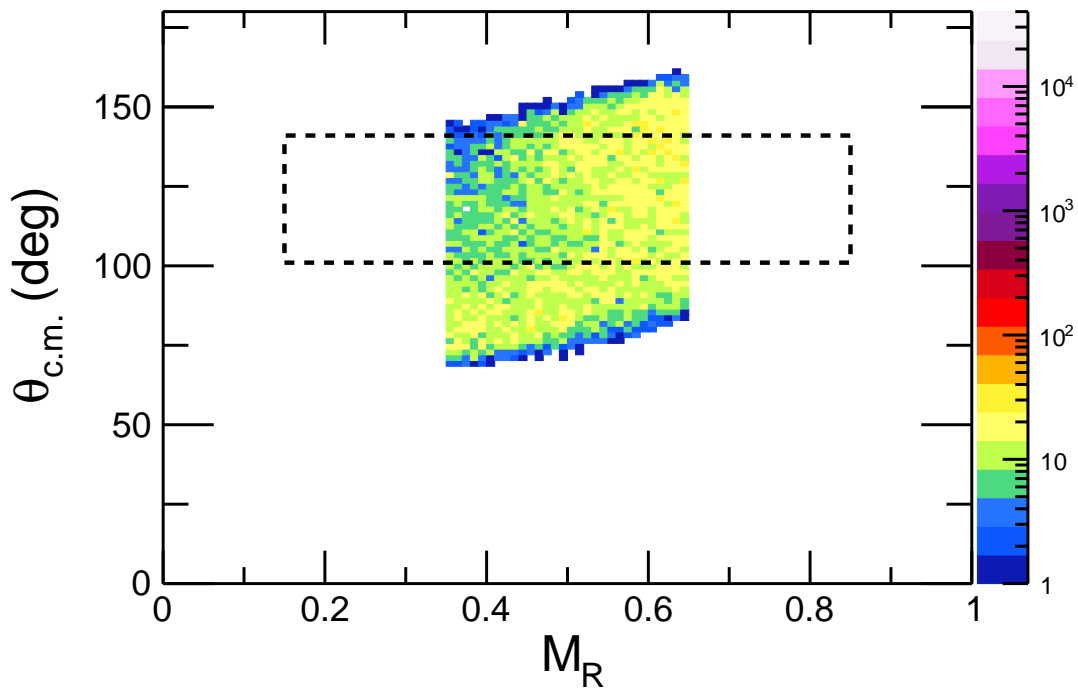


Figure 4.10: Unsymmetrized mass angle distribution after the gate on the fission-like region was applied to the data set for $^{50}\text{Cr} + ^{180}\text{W}$ at $E_{\text{lab}} = 284.6$ MeV as an example of the angular region included in the determination of the angular distribution. The dashed, black box represents the angular region included in the angular distribution calculations.

where Y_{MWPC}^{FF} was the yield in the MWPCs during the reaction of interest, $Y_{Mon}^{Elastic}$ is the yield in the Si monitor detectors during the reaction of interest, $Y_{MWPC,Cal}^{Elastic}$ is the yield in the MWPCs during the calibration run, and $Y_{Mon,Cal}^{Elastic}$ is the yield in the Si monitor detectors during the calibration run. Three Rutherford scattering cross sections were also necessary. (1) $d\sigma(\theta_{Mon}, E)/d\Omega$ is the deduced Rutherford scattering cross section in the monitors at the energy of the fission run. (2) $d\sigma(\theta_{lab}, E_{cal})/d\Omega$ is the Rutherford scattering cross section at the energy of the calibration run at a particular angle (θ_{lab}) in the MWPCs. (3) $d\sigma(\theta_{Mon}, E, Cal)/d\Omega$ is the deduced Rutherford cross section at the in the monitors at the calibration energy. Note that all angles are in the center-of-mass frame.

To quickly demonstrate that eq. 4.7 is dimensionally correct, consider the general case where the yield of a given reaction product in a detector can be calculated as $Y = I\rho_N\Delta x\Delta t\sigma\epsilon$ where I is the beam intensity, ρ_N is the particle density of the target, Δx is the effective target thickness, Δt is the time of the measurement, σ is the cross section of the reaction channel of interest, and ϵ is the detector efficiency. Therefore, σ can be determined for the experimental yield as $\frac{Y}{I\rho_N\Delta x\Delta t\epsilon}$. The differential cross section can then be determined as $\frac{d\sigma(\theta, \Phi)}{d\Omega} \sim \frac{Y}{I\rho_N\Delta x\Delta t\epsilon} \frac{1}{\Delta\Omega}$ where $\Delta\Omega$ is the solid angle of a given detector. The yield is determined from the measurement as discussed later and $I, \rho_N, \Delta x, \Delta t, \Delta\Omega$ and ϵ constants related to the measurements. While all these quantities should be known they can introduce large error into the angular distribution if not known well. The parameters in particular that are difficult to know in the present work are the thicknesses and particle densities of the tungsten targets.

The $\frac{d\sigma(\theta, \Phi)}{d\Omega} \frac{1}{Y}$ terms are replaced with their respective components, $\frac{1}{I\rho_N\Delta x\Delta t\epsilon} \frac{1}{\Delta\Omega}$, as below

$$\frac{d\sigma(\theta_{MWPC}, E)}{d\Omega_{MWPC}} = Y_{MWPC}^{FF} * \frac{1}{\rho_{N(Cal)} \Delta x_{Cal} I_{cal} \Delta t_{Cal} \epsilon_{MWPC} \Delta \Omega_{MWPC}} * \frac{1}{\rho_{N} \Delta x I \Delta t \epsilon_{Mon} \Delta \Omega_{Mon}} * \rho_{N(Cal)} \Delta x_{Cal} I_{Cal} \Delta t_{Cal} \epsilon_{Mon} \Delta \Omega_{Mon}. \quad (4.7)$$

and canceling terms leaves

$$\frac{d\sigma(\theta_{MWPC}, E)}{d\Omega_{MWPC}} = Y_{MWPC}^{FF} * \frac{1}{\epsilon_{MWPC} \Delta \Omega_{MWPC} \rho_N \Delta x I \Delta t}. \quad (4.8)$$

4.1.3.2 Quantities needed in Angular Distribution Determination

This section describes how the various quantities required for the determination of the angular distribution were deduced. The values relating to the monitors remained consistent for a given system, so they are described first.

The yield in the monitors, $Y_{Mon}^{Elastic}$ or $Y_{Mon,Cal}^{Elastic}$, was determined from the sum of the integrated counts in the monitor energy distributions. The monitor energy distributions for the example system of $^{50}\text{Cr} + ^{180}\text{W}$ at $E_{lab} = 284.6$ MeV are shown in Figure 4.11.

The normalization also required that two Rutherford scattering cross sections at the monitor angles ($\pm 22.5^\circ$) were calculated, one corresponding to the energy of the reaction of interest and one corresponding to the energy of the calibration run. The Rutherford cross sections were calculated as

$$\frac{d\sigma}{d\Omega} = \left(\frac{Z_1 Z_2 e^2}{4\pi \epsilon_0 E_{c.m.}^p} \right)^2 \frac{1}{\sin^4(\theta/2)} \quad (4.9)$$

where Z_i refers to the exit channel fragments, e is the charge of an electron, ϵ_0 is the

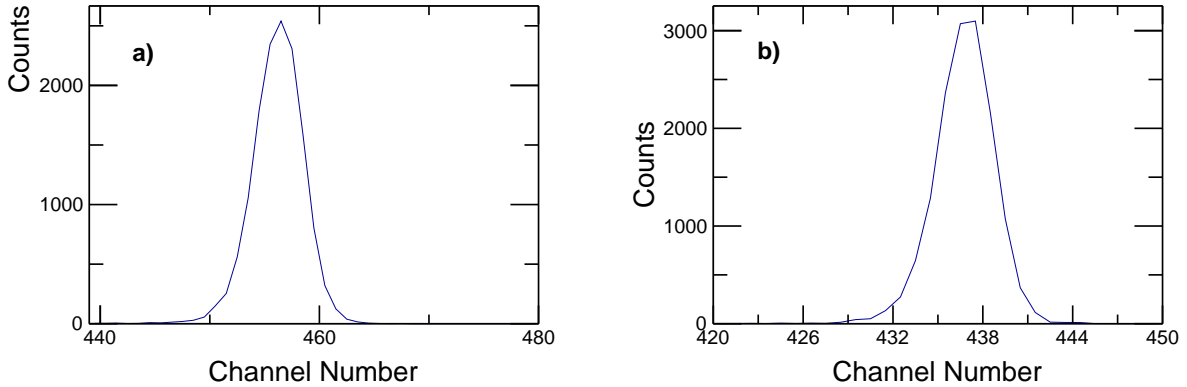


Figure 4.11: Counts in the two monitor detectors for the reaction of $^{50}\text{Cr} + ^{180}\text{W}$ at $E_{\text{lab}} = 284.6$ MeV shown as a function of channel number.

permittivity of free space, and θ is the angular location of the detector in the center-of-mass frame. The Si monitor detectors were located at $\theta_{\text{lab}} = \pm 23^\circ$ for all measurements. For elastic scattering events in the monitor detectors $E_{\text{c.m.}}^p$ is the center-of-mass energy of the projectile.

The rest of the quantities needed in eq. 4.6 were determined for a given four-degree range of the center-of-mass angle. The distribution of fission-like events over the center-of-mass angles ($\theta_{\text{c.m.}}$) covered by the Back MWPC is shown in Figures 4.12. To account for the efficiencies in the MWPC, which sits in the lab frame, the center-of-mass angles of the fission-like fragments needed to be converted to the lab frame angles (Θ_{lab}) so they could be normalized to the elastic scattering events at the same Θ_{lab} . The $\theta_{\text{c.m.}}$ values deduced for fission-like fragments for $^{50}\text{Cr} + ^{180}\text{W}$ at $E_{\text{lab}} = 284.6$ MeV as a function of their corresponding Θ_{lab} are shown in Figure 4.13. The spread in Θ_{lab} for each $\theta_{\text{c.m.}}$ results from the range of mass ratios for the fission-like fragments. The intensity scale in Figure 4.13 represents the number of events with a given combination of $\theta_{\text{c.m.}}$ and Θ_{lab} . The $\theta_{\text{c.m.}}$ versus θ_{lab} distribution was fit with a fourth degree polynomial. The result of that

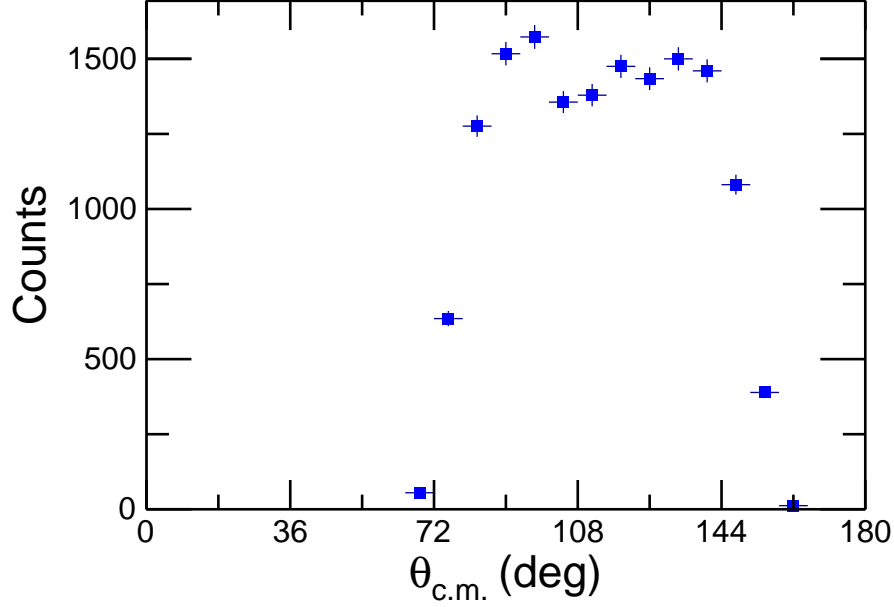


Figure 4.12: $\theta_{c.m.}$ distributions for the reaction of $^{50}\text{Cr} + ^{180}\text{W}$ at $E_{\text{lab}} = 284.6$ MeV.

fit for the example system of $^{50}\text{Cr} + ^{180}\text{W}$ at $E_{\text{lab}} = 284.6$ MeV is represented by the red line in Figure 4.13.

The normalization in eq. 4.6 was completed on a bin by bin basis for the distribution in Figure 4.13. For each $\theta_{c.m.}$ of fission-like fragments the corresponding Θ_{lab} was determined. This value of Θ_{lab} was then converted back into $\theta_{c.m.}(\text{Elas})$ for elastic scattering by the equation

$$\theta_{c.m.}(\text{Elas}) = \Theta_{\text{lab}} + \frac{180.0}{\pi} \text{asin} \left(\frac{A_p}{A_t} \sin \left(\Theta_{\text{lab}} \frac{\pi}{180.0} \right) \right) \quad (4.10)$$

where A_P is the mass of the projectile, A_T is the mass of the target, A_i is the mass of an emitted fragment, and TKE is the total kinetic energy calculated from Viola systematics (see eq. 3.25). $\theta_{c.m.}(\text{Elas})$ was then used in the determination of the Rutherford cross section $\frac{d\sigma(\theta_{\text{MWPC}, \text{Ecal}})}{\delta\Omega_{\text{MWPC}}}$ and the yield of elastics at a given angle in the Back MWPC ($Y_{\text{MWPC}, \text{Cal}}^{\text{Elastics}}$). The $\theta_{c.m.}(\text{Elas})$ distribution for the elastic scattering calibration measurement is shown in

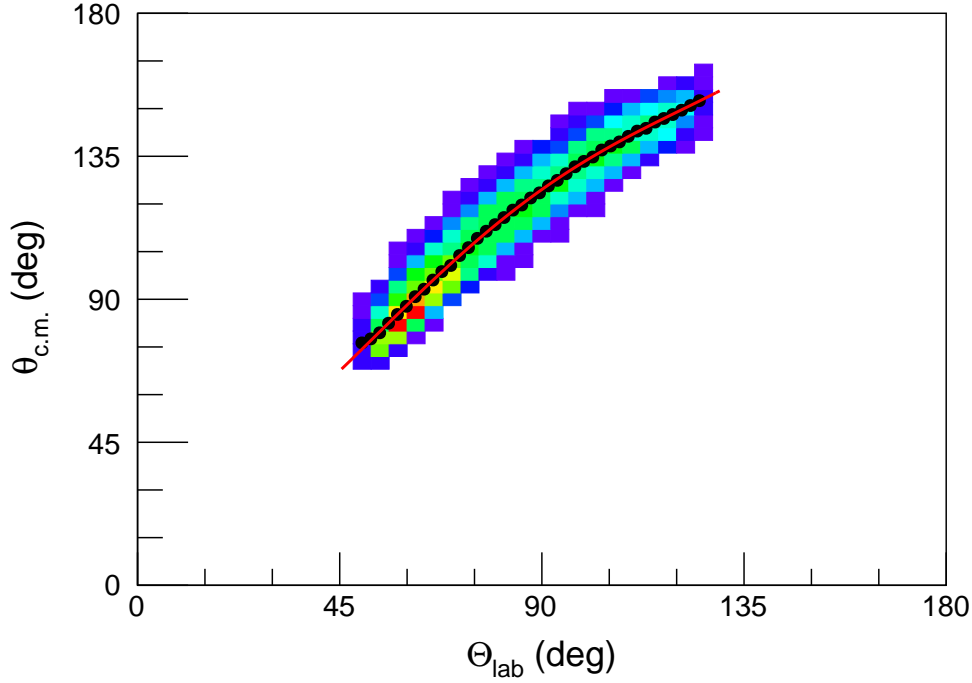


Figure 4.13: Distribution of $\theta_{c.m.}$ for each deduced θ_{lab} for the $^{50}\text{Cr} + ^{180}\text{W}$ at $E_{lab} = 284.6$ MeV. The solid, red line represents a fourth degree polynomial fit to the distribution.

Figure 4.14.

Now that all of the quantities have been determined for a given combination of $\theta_{c.m.}$ and Θ_{lab} a partial value of $\frac{d\sigma(E)}{d\Omega_{MWPC}}(\theta_{c.m.}, \Theta_{lab})$ can be calculated. This process was repeated for each possible Θ_{lab} for a given $\theta_{c.m.}$. Then all of the $\frac{d\sigma(E)}{d\Omega_{MWPC}}(\theta_{c.m.}, \Theta_{lab})$ were summed to deduce $\frac{d\sigma(\theta_{MWPC}E)}{d\Omega_{MWPC}}$ for given θ_{MWPC} in the Back MWPC. Repeating the process for each θ_{MWPC} region led to the determination of the final angular distributions shown in Figure 4.15 after the values were corrected for the relative detector efficiencies.

4.1.3.3 Relative Detector Efficiencies

During the primary Cr + W measurements and the calibration run a pulser signal (P, P_{Cal}) was added into the data acquisition system for the MWPCs at signal amplitudes that corre-

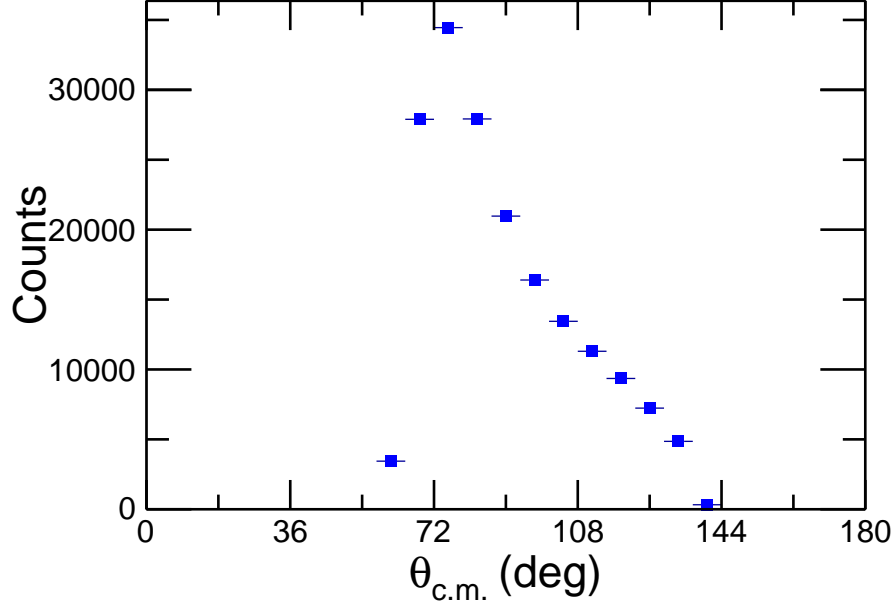


Figure 4.14: $\theta_{c.m.}$ distributions for the calibration measurement of $^{50}\text{Cr} + ^{184}\text{W}$ at $E_{\text{lab}} = 186.0$ MeV.

spond to channel numbers combinations in X and Y outside the active detector area. Scaler values were recorded for the pulser ($P_{\text{scal}}, P_{\text{scal,Cal}}$) and the two Si monitor detectors. The scalers from the two Si monitor detectors were summed to determine M_{scal} and $M_{\text{scal,Cal}}$ from the primary Cr + W measurements and the calibration run, respectively. The relative intrinsic peak efficiency ($Rel \epsilon_{peak,int}$) of the Front MWPC was determined between the reaction of interest and the calibration run of $^{50}\text{Cr} + ^{184}\text{W} \rightarrow ^{234}\text{Cf}$ at $E_{\text{lab}} = 186.0$ MeV. The relative intrinsic peak efficiency was determined for Cr + W measurement as

$$Rel \epsilon_{peak,int} = \frac{\frac{P_{\text{scal}}}{P} * \frac{M_{\text{scal,Cal}}}{M_{\text{Cal}}}}{\frac{M_{\text{scal}}}{M} * \frac{P_{\text{scal,Cal}}}{P_{\text{Cal}}}} \quad (4.11)$$

where M and M_{Cal} are the sum of the number of counts in the two monitors recorded in the data acquisition system for the primary C + W measurements and the calibration run,

Table 4.5: The number of counts in the two monitors (M), the number of pulser events in the Back MWPC (P), and the scalers values for the monitors (M_{scal}) and pulser (P_{scal}) from the measurement of $^{50}\text{Cr} + ^{180}\text{W}$ as an example and the calibration measurement of $^{50}\text{Cr} + ^{184}\text{W}$.

	$^{50}\text{Cr} + ^{180}\text{W}$	$^{50}\text{Cr} + ^{184}\text{W}$ (Cal)
P_{scal}	$7.45 \times 10^3 \pm 86$	$7.92 \times 10^3 \pm 89$
P	$7.24 \times 10^3 \pm 85$	$7.08 \times 10^3 \pm 84$
M_{scal}	$1.54 \times 10^4 \pm 1.2 \times 10^2$	$1.63 \times 10^4 \pm 1.3 \times 10^2$
M	$1.52 \times 10^4 \pm 1.2 \times 10^2$	$1.56 \times 10^4 \pm 1.3 \times 10^2$

respectively. For example, the values used in eq. 4.11 for $^{50}\text{Cr} + ^{180}\text{W}$ and the calibration measurement of $^{50}\text{Cr} + ^{184}\text{W}$ are provided in Table 4.5. Detector efficiency values for each system are provided in Table 4.6.

The solid, red line shown with the angular distribution in each panel of Figure 4.15 is a sine function fit to the data to highlight the general shape of the angular distribution. A χ^2 minimization was performed to determine the normalization of the sine function relative to the data. The sharp increase in the angular distribution data at large angles indicates the presence of quasifission.

4.2 Cr + W: $E^* = 52.0$ MeV

The results of the measurements of the eight Cr + W reactions at $E_{\text{CN}}^* = 52.0$ MeV are presented in this section. Reactions at the same excitation energy are particularly interesting for superheavy element production reactions as discussed in previous chapters (see 2.1.1).

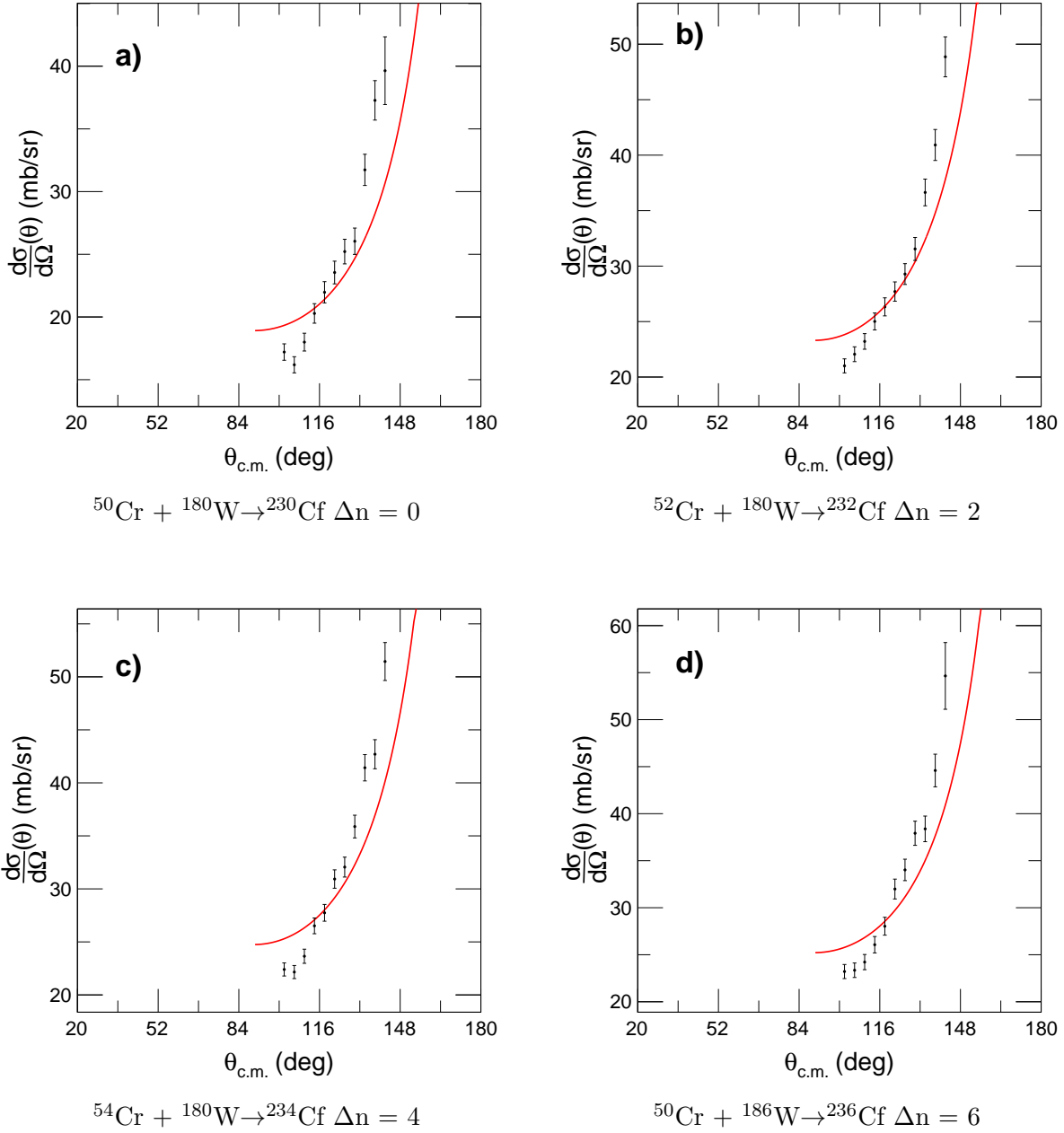


Figure 4.15: The angular distribution ($d\sigma(\theta_{\text{lab}}, E)/d\Omega$) for all eight Cr + W systems measure in the present work at $E_{c.m.}/V_B = 1.13$ shown as a function of $\theta_{c.m.}$ is represented by the black data points. The solid, red line is a sine function fit to the experimental data points using a χ^2 minimization.

Figure 4.15: (cont'd)

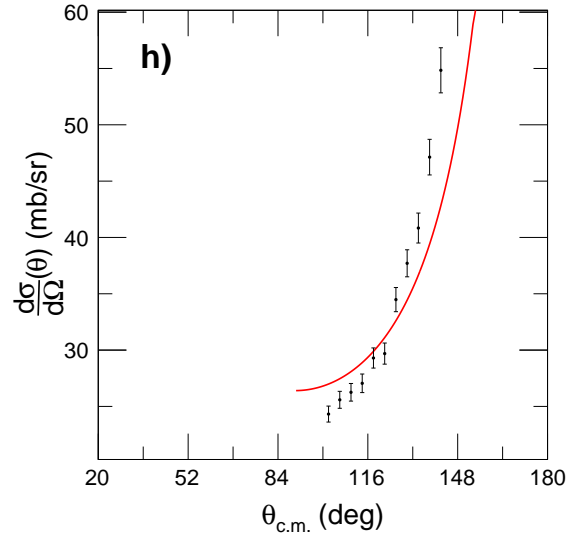
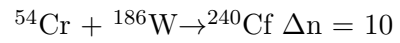
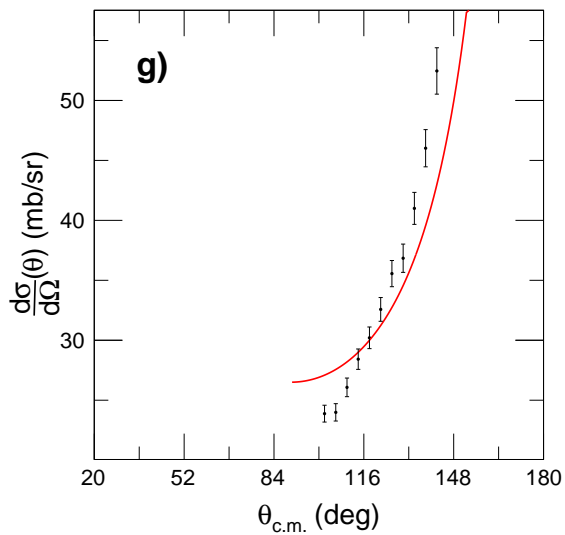
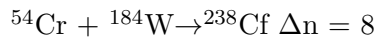
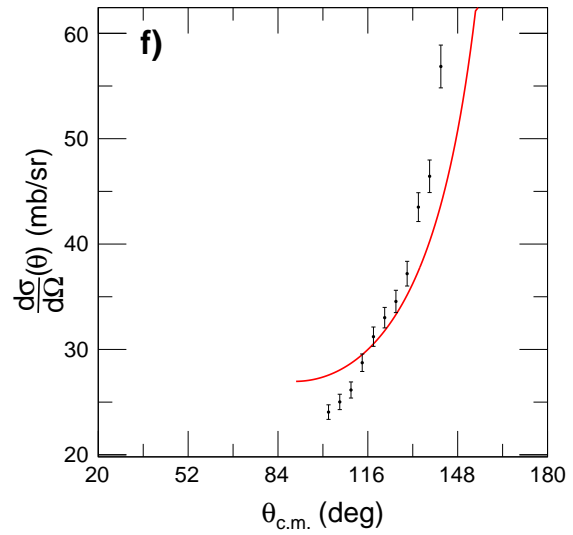
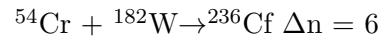
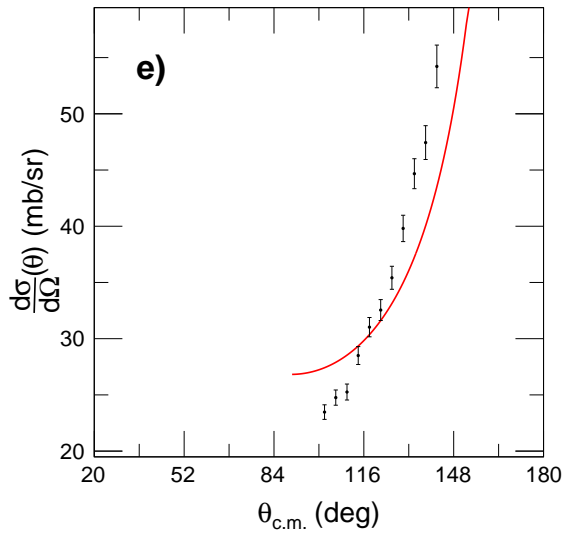
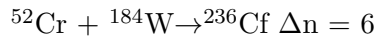


Table 4.6: Relative peak intrinsic efficiencies of the Back MWPC and the Si monitor detectors for all systems measured in the present work relative to the calibration run of $^{50}\text{Cr} + ^{184}\text{W} \rightarrow ^{234}\text{Cf}$ at $E_{\text{lab}} = 186.0$ MeV.

Reaction	ΔN	$E_{\text{c.m.}}/V_{\text{B}} = 1.13$	$E_{\text{CN}}^* = 52.0$ MeV
		<i>Rel</i> $\epsilon_{\text{peak,int}}(\text{MWPC0})$	<i>Rel</i> $\epsilon_{\text{peak,int}}(\text{MWPC0})$
$^{50}\text{Cr} + ^{180}\text{W} \rightarrow ^{230}\text{Cf}$	0	0.931 ± 0.030	0.954 ± 0.024
$^{50}\text{Cr} + ^{186}\text{W} \rightarrow ^{236}\text{Cf}$	6	0.931 ± 0.029	0.975 ± 0.022
$^{52}\text{Cr} + ^{180}\text{W} \rightarrow ^{232}\text{Cf}$	2	1.013 ± 0.025	1.028 ± 0.023
$^{52}\text{Cr} + ^{184}\text{W} \rightarrow ^{236}\text{Cf}$	6	1.024 ± 0.025	1.047 ± 0.021
$^{54}\text{Cr} + ^{180}\text{W} \rightarrow ^{234}\text{Cf}$	4	0.968 ± 0.035	0.958 ± 0.035
$^{54}\text{Cr} + ^{182}\text{W} \rightarrow ^{236}\text{Cf}$	6	0.980 ± 0.031	0.981 ± 0.032
$^{54}\text{Cr} + ^{184}\text{W} \rightarrow ^{238}\text{Cf}$	8	0.984 ± 0.027	0.999 ± 0.025
$^{54}\text{Cr} + ^{186}\text{W} \rightarrow ^{240}\text{Cf}$	10	0.964 ± 0.028	0.977 ± 0.025

4.2.1 Mass-Angle Distributions

Similar to the systems measured at $E_{\text{c.m.}}/V_{\text{B}} = 1.13$, the unsymmetrized MADs for the systems measured at $E_{\text{CN}}^* = 52.0$ MeV are shown in Figure 4.16 for the Back MWPC and in Figure 4.17 for the Front MWPC. The symmetrized MADs for all eight of the systems are shown in Figure 4.18. A correlation between mass and angle can be seen in each MAD, indicating the presence of quasifission. Again, the mass distributions were used in a quantitative determination of the contribution from quasifission.

4.2.2 Mass Distributions

The mass distributions for the eight systems measured at $E_{\text{CN}} = 52.0$ MeV are shown in Figure 4.19. A important feature to note in this set of mass distributions is the shape of the fission-like region. Three of the systems, $^{50}\text{Cr} + ^{180}\text{W}$ (Figure 4.19 panel A), $^{50}\text{Cr} + ^{186}\text{W}$ (Figure 4.19 panel D), and $^{52}\text{Cr} + ^{184}\text{W}$ (Figure 4.19 panel E) have a minimum or

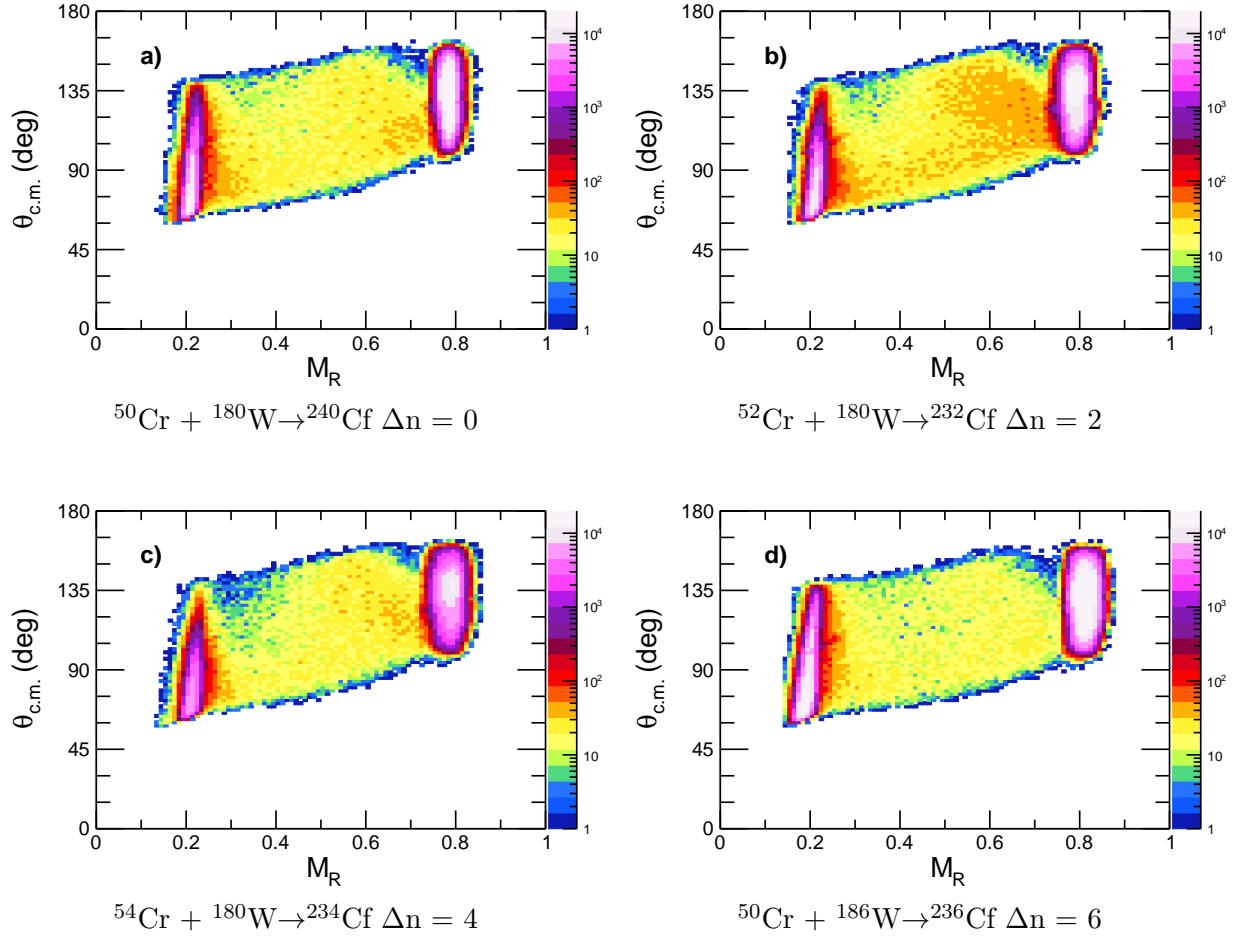
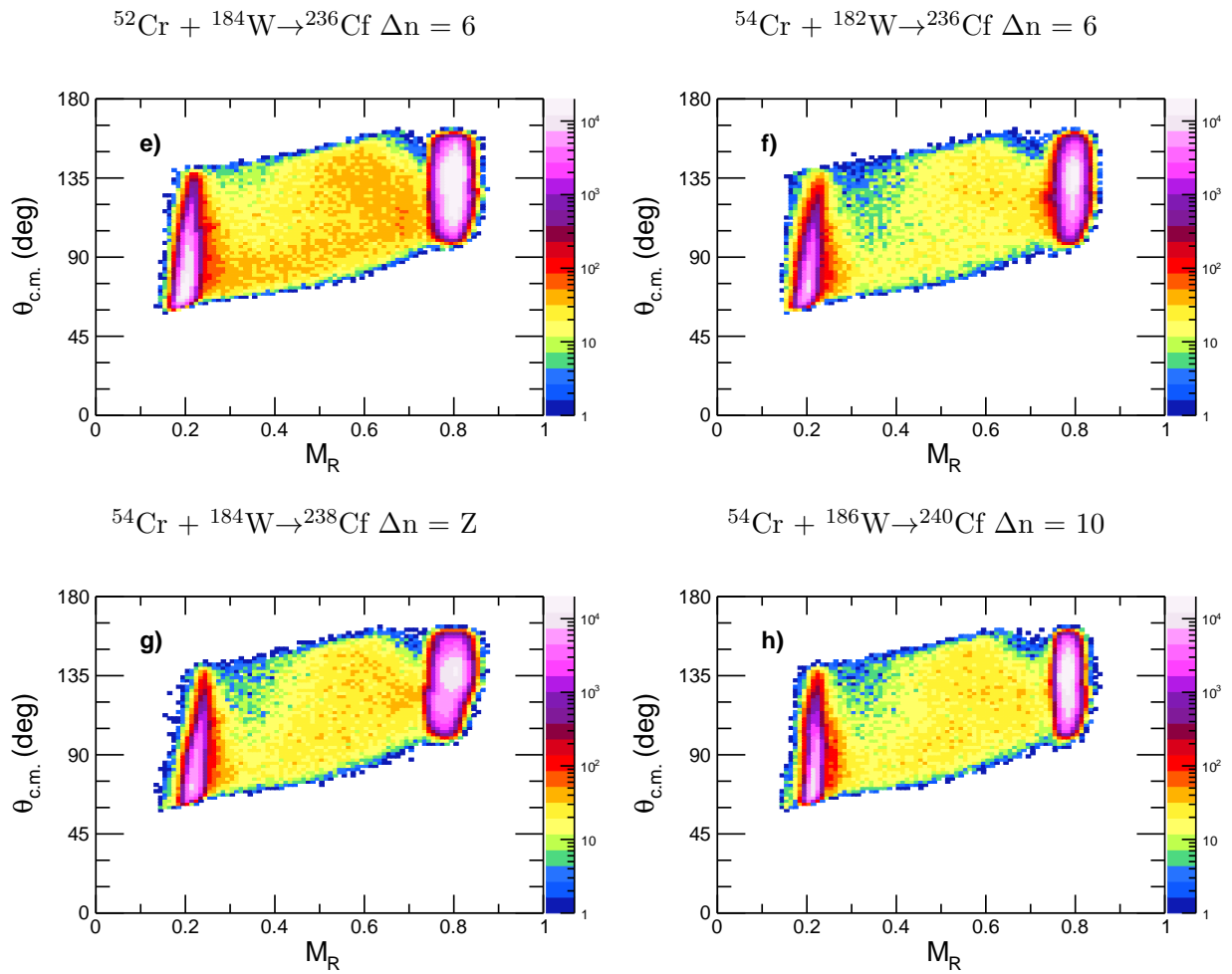


Figure 4.16: Unsymmetrized MADs observed in the Back MWPC for all eight systems presented in this work at $E_{\text{CN}}^* = 52.0$ MeV. Δn is the change in the number of neutrons in the compound nucleus relative to $^{50}\text{Cr} + ^{180}\text{W}$, where $N = 132$.

Figure 4.16: (cont'd)



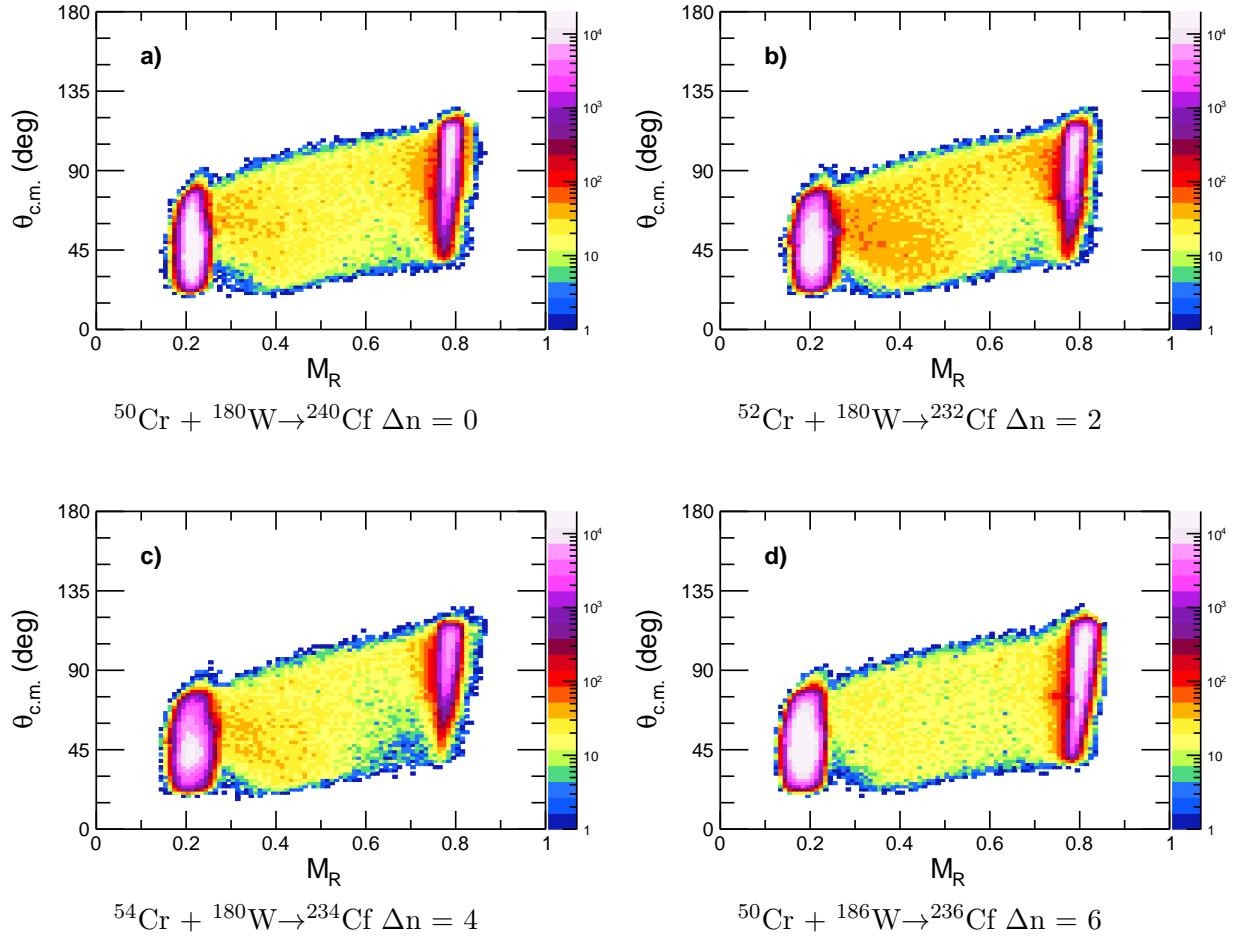
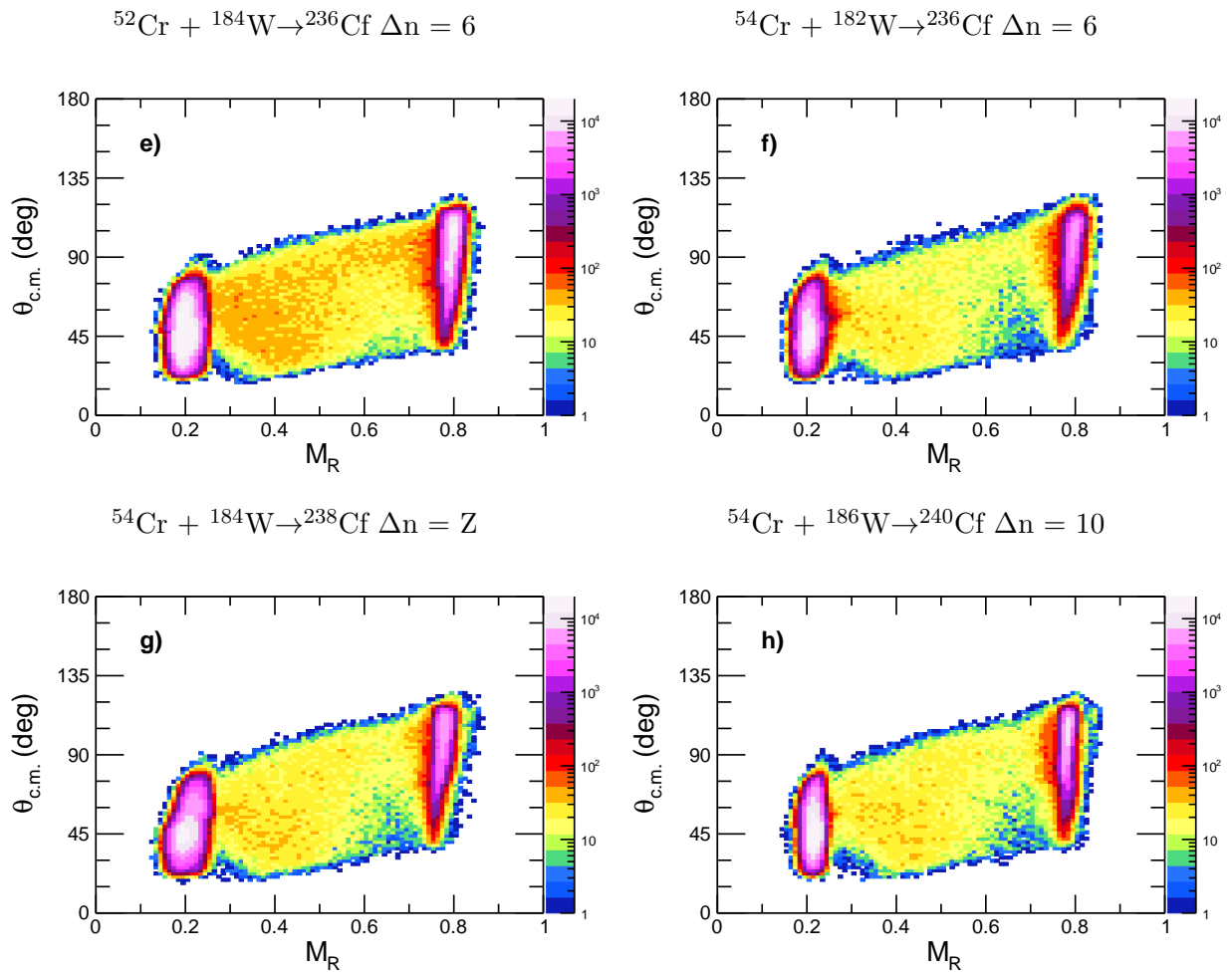


Figure 4.17: Unsymmetrized MADs observed in the Front MWPC for all eight systems presented in this work at $E_{\text{CN}}^* = 52.0$ MeV.

Figure 4.17: (cont'd)



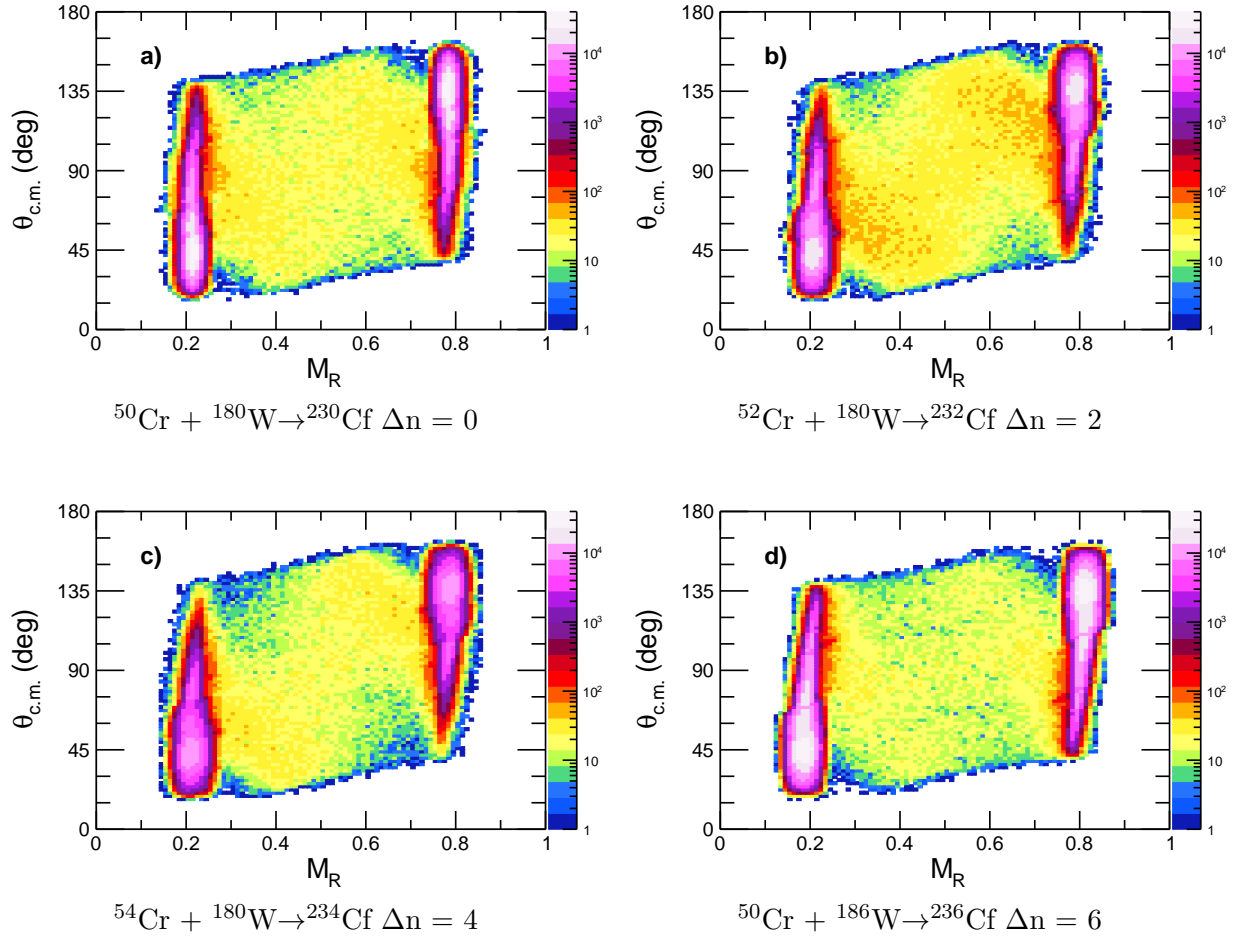
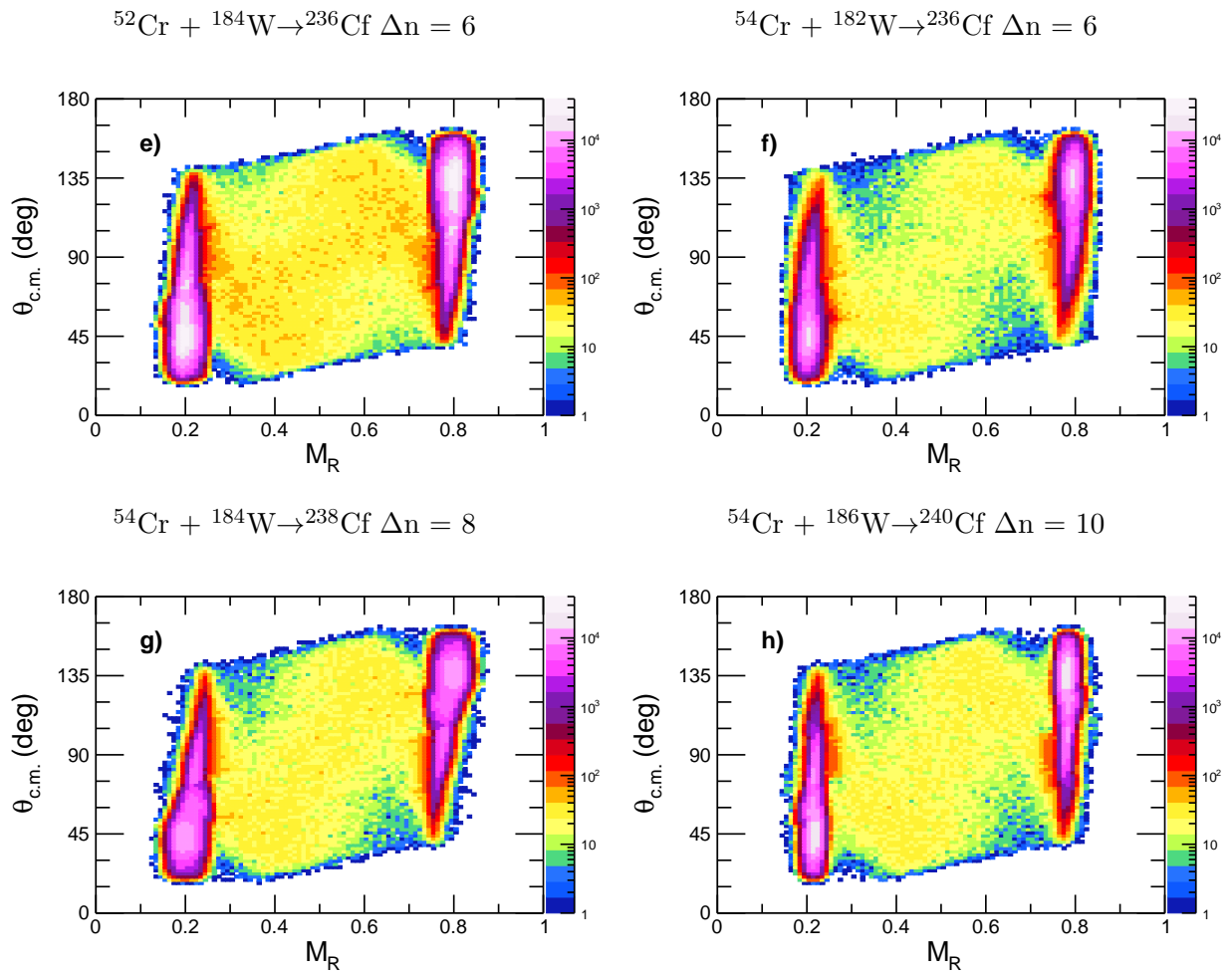


Figure 4.18: Symmetrized MADs for the Cr + W systems measured in this work at $E_{\text{CN}}^* = 52.0$ MeV.

Figure 4.18: (cont'd)



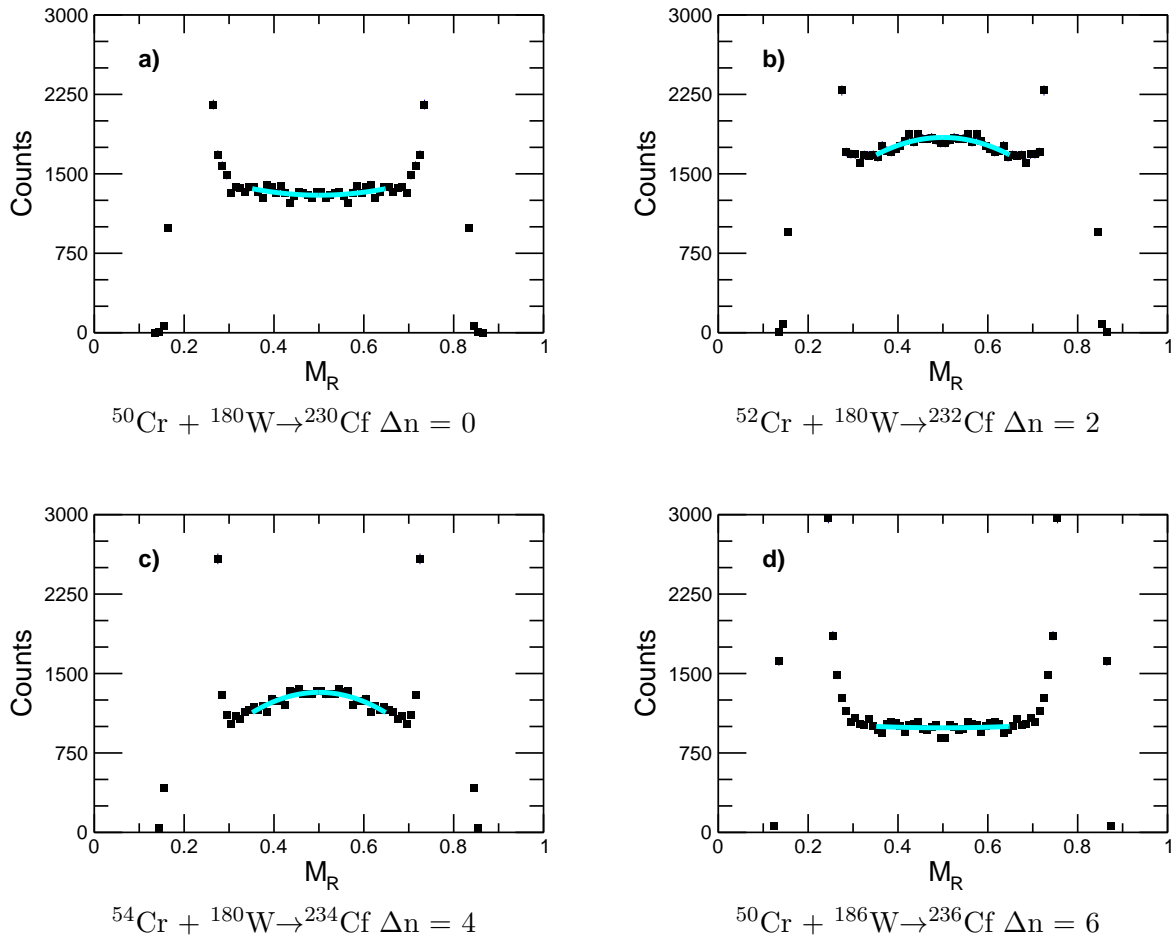
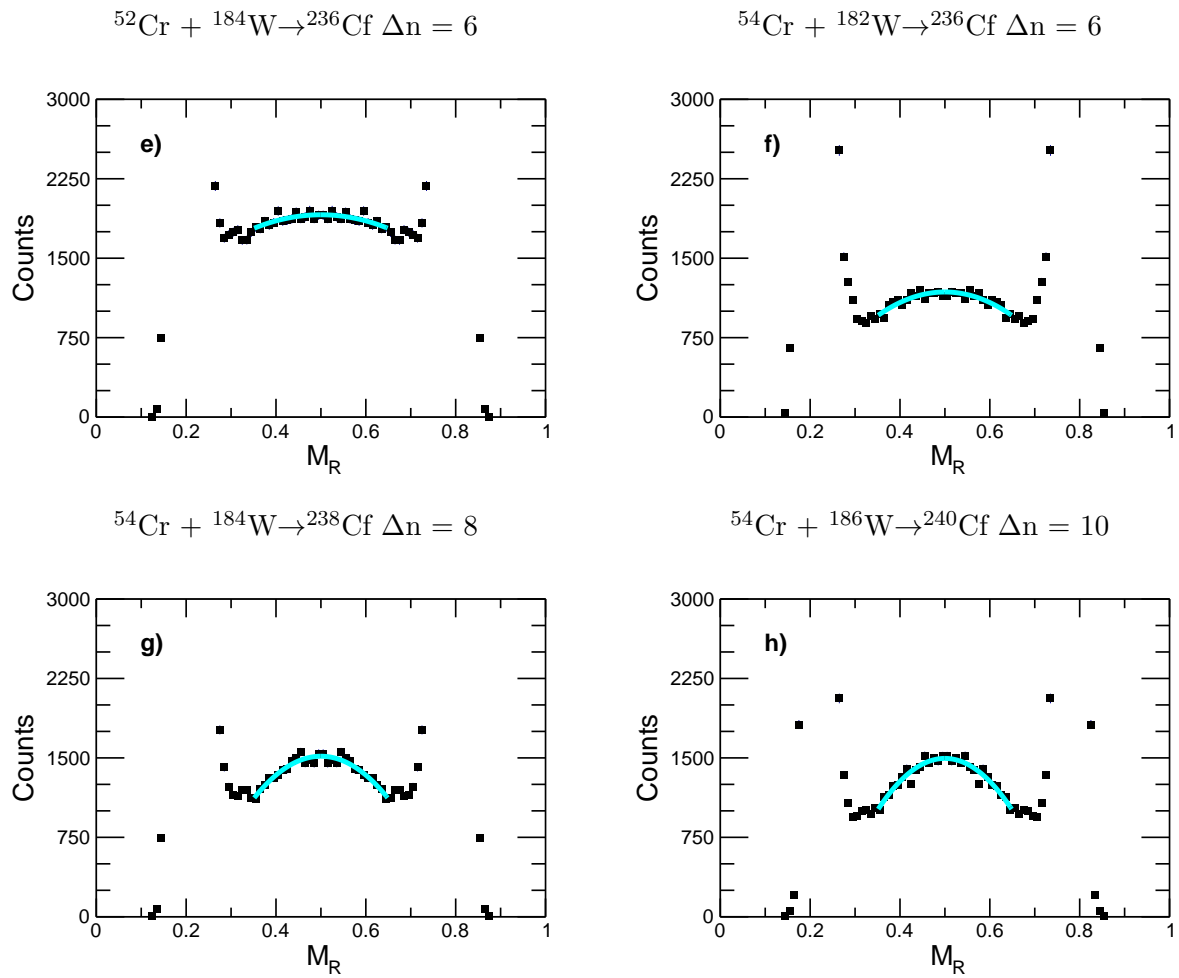


Figure 4.19: Mass distributions for Cr + W systems presented in this work at $E_{\text{CN}}^* = 52.0$ MeV. The solid green line represents the second degree polynomial fit to the data.

are flat at mass ratio of 0.5 rather than a maximum. This is very different from the systems measured at $E_{\text{c.m.}}/V_{\text{B}} = 1.13$ where all of the systems had a maximum at $M_{\text{R}} = 0.5$. The mass distributions observed for these systems appear to cross the boundary between Type II and Type III systems as discussed in Section 1.3.3.1 [40]. Due to this difference in the shapes of the mass distributions, fitting a Gaussian function to the data was not appropriate and a different analysis technique was necessary.

Figure 4.19: (cont'd)



4.2.2.1 Curvature Analysis Techniques

Rather than a Gaussian function, each mass distribution was fitted with a second degree polynomial function. The results of fitting second degree polynomials to the mass distributions for the systems measured at $E_{\text{CN}} = 52.0$ MeV are shown in each panel of Figure 4.19 as the solid, green line. The second derivative of the function resulting from the fit was calculated as two times the coefficient of the second-order coefficient to compare the relative shapes of the mass distributions and is referred to as the curvature parameter. The curvature parameter was then used as a means to quantitatively compare mass distributions generated for the systems at $E_{\text{CN}} = 52.0$ MeV in a similar manner to the widths from the Gaussian function used for the mass distributions for the systems measured at $E_{\text{c.m.}}/V_{\text{B}} = 1.13$. A larger curvature is equivalent to a smaller mass width and indicates a decrease in the amount of quasifission in the reaction. The values of the curvature parameter determined for the systems measured in the present work are listed in Table 4.7. The uncertainty associated with the second-order term of the second-degree polynomial fitted to the data was determined in a chi-squared minimization and is reported in Table 4.7. This technique was able to fit the systems that were nearly flat or had a minimum at $M_{\text{R}} = 0.5$. A positive curvature parameter is determined for the systems with a minimum at $M_{\text{R}}=0.5$. Systems that have nearly flat mass distributions will have curvature parameters near to zero. These systems fall into the Type I category identified by Du Rietz *et al.* [40] as described in Section 1.3.3.1. Short timescale quasifission dominates in reactions with positive curvature parameters.

4.2.2.2 Verification with $E_{\text{c.m.}}/V_{\text{B}} = 1.13$ systems

The validity of the curvature analysis technique was tested against the mass width technique with the systems that were measured at $E_{\text{c.m.}}/V_{\text{B}} = 1.13$. The eight systems measured at

Table 4.7: Curvature parameters and errors determined for all 8 systems measured at center-of-mass energies resulting in compound nuclei with $E_{\text{CN}} = 52.0$ MeV.

System	Curvature Parameter (arb. units)	error
$^{50}\text{Cr} + ^{180}\text{W}$	5.5×10^3	$\pm 1.9 \times 10^3$
$^{50}\text{Cr} + ^{186}\text{W}$	1.1×10^3	$\pm 1.7 \times 10^3$
$^{52}\text{Cr} + ^{180}\text{W}$	-1.50×10^4	$\pm 2.3 \times 10^3$
$^{52}\text{Cr} + ^{184}\text{W}$	-1.15×10^4	$\pm 2.3 \times 10^3$
$^{54}\text{Cr} + ^{180}\text{W}$	-1.73×10^4	$\pm 1.9 \times 10^3$
$^{54}\text{Cr} + ^{182}\text{W}$	-1.99×10^4	$\pm 1.7 \times 10^3$
$^{54}\text{Cr} + ^{184}\text{W}$	-3.57×10^4	$\pm 2.0 \times 10^3$
$^{54}\text{Cr} + ^{186}\text{W}$	-4.34×10^4	$\pm 1.9 \times 10^3$

$E_{\text{c.m.}}/V_{\text{B}} = 1.13$ were each fit with a second degree polynomial and the curvature parameter was determined. The result of that comparison is presented in Figure 4.20. The strong, linear correlation between the upper limits of P_{CN} and the curvature parameters indicates that overall the two methods are qualitatively consistent. For example, $^{50}\text{Cr} + ^{180}\text{W}$ has the lowest upper limit of P_{CN} (0.18 ± 0.3) and the largest curvature parameter ($-4.8 \times 10^3 \pm 1.6 \times 10^3$) among the systems, while $^{50}\text{Cr} + ^{180}\text{W}$ has a the largest upper limit of P_{CN} (0.521 ± 0.007) and the smallest curvature parameter ($-5.79 \times 10^4 \pm 2.0 \times 10^3$) among the systems.

4.2.3 Angular Distributions

The angular distributions for the eight Cr + W systems measured at $E_{\text{CN}}^* = 52.0$ MeV are shown in Figure 4.21. The angular distributions were obtained using the method described above in Section 4.1.3. Similar to the angular distributions for the systems with $E_{\text{c.m.}}/V_{\text{B}} = 1.13$, each is compared to a sine function fitted to the data, represented by the red line. The sharp increase in the angular distribution with increasing angle indicates the presence

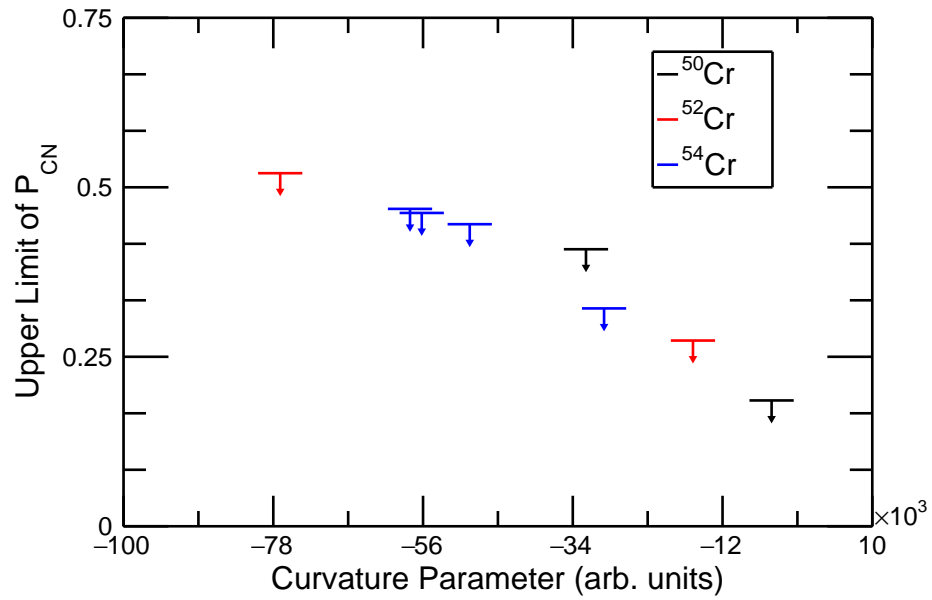


Figure 4.20: Comparison of the results from the two methods for determining the relative shapes experimental mass distributions applied to the Cr + W data at $E_{c.m.}/V_B = 1.13$.

of quasifission in all of the Cr + W systems measured at $E_{CN}^* = 52.0$ MeV.

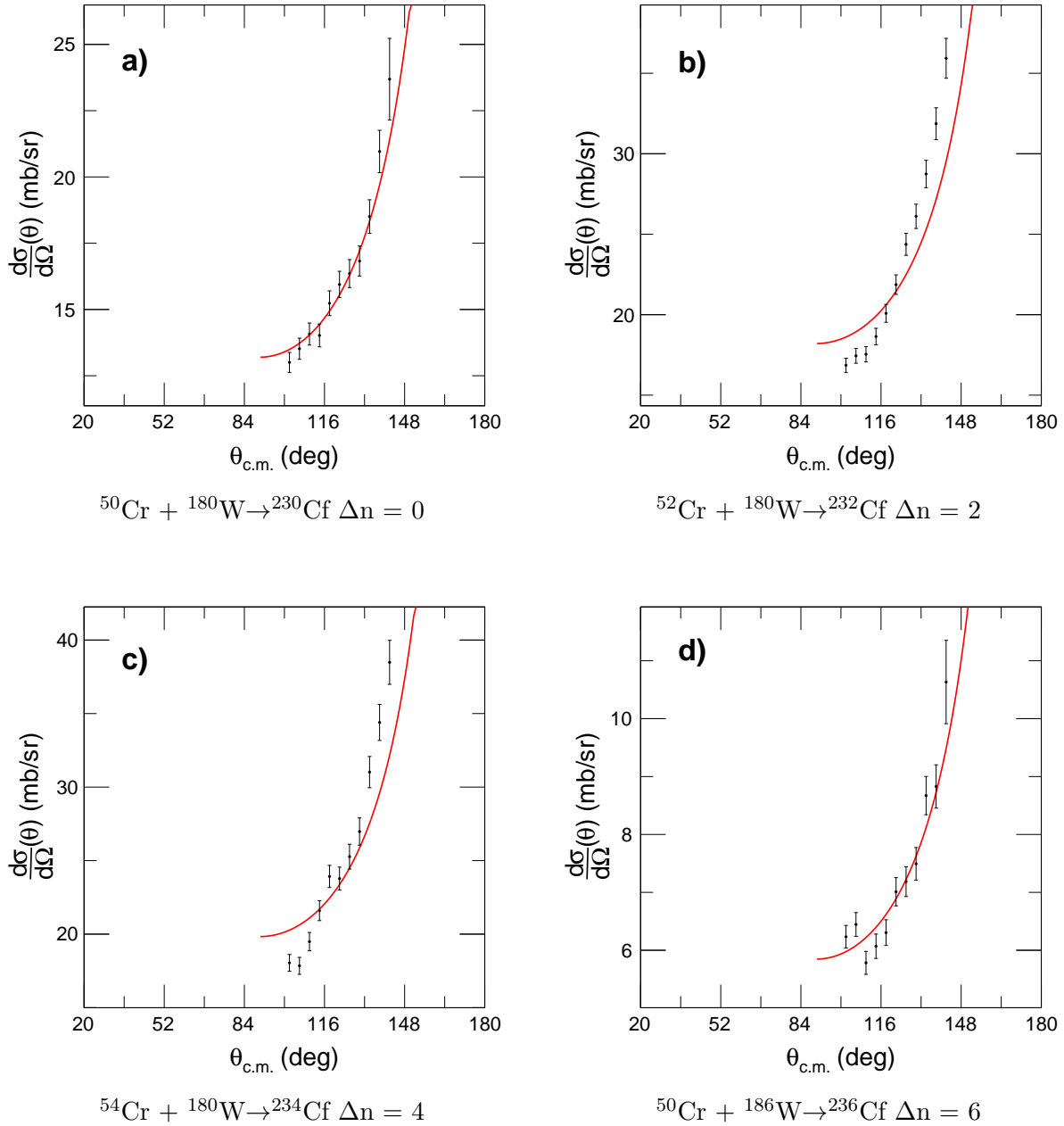
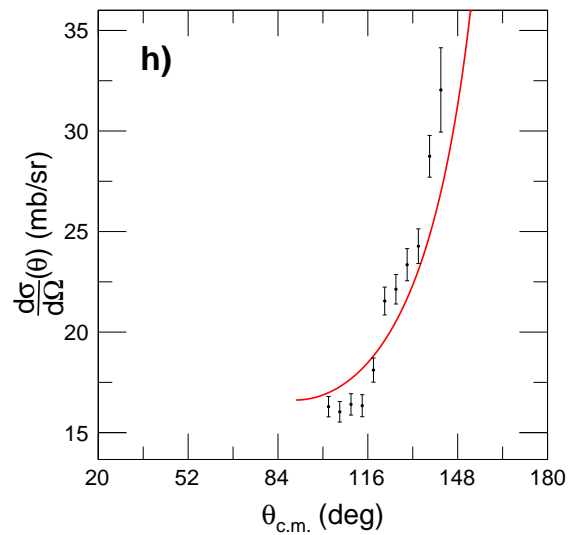
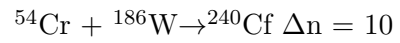
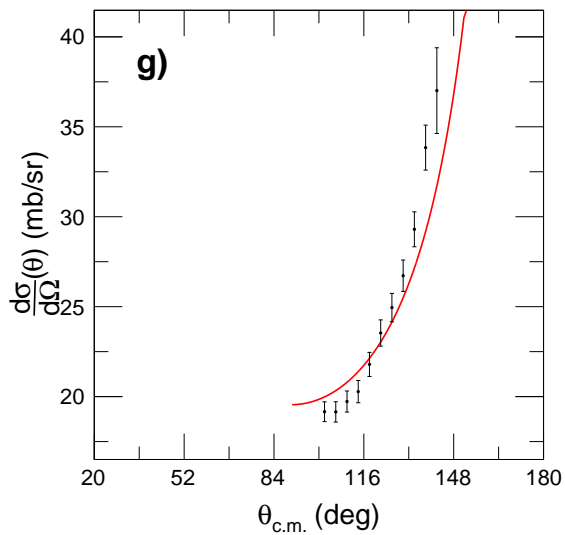
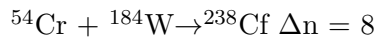
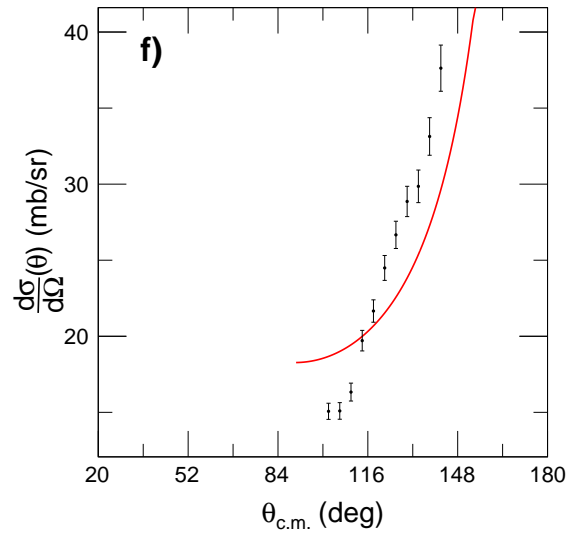
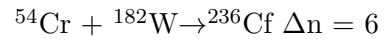
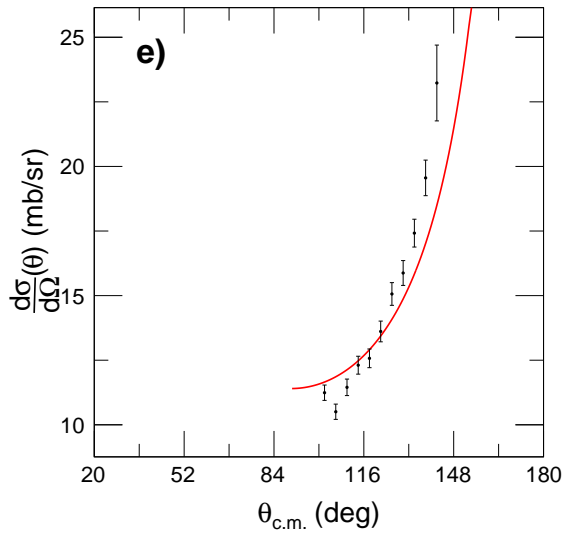
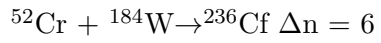


Figure 4.21: The angular distribution ($d\sigma(\theta_{lab}, E)/d\Omega$) for Cr + W systems measured in the present work at $E_{CN}^* = 52.0$ MeV shown as a function of $\theta_{c.m.}$ is represented by the black data points. The solid, red line is a sine function fit to the experimental data points using a χ^2 minimization.

Figure 4.21: (cont'd)



Chapter 5

Discussion

The primary goal of this work was to explore the effect of varying the neutron-richness of the reaction system on the reaction dynamics in a series of Cr + W reactions. In particular, the effect of varying the neutron-richness on the competition between the fusion-fission and quasifission reaction channels was examined. This chapter presents the interpretations of the results in Chapter 4 in the context of this goal. First, the subset of the systems forming the same compound nucleus are compared with the predictions of the Bohr independence hypothesis to demonstrate the presence of non equilibrium processes like quasifission in the systems measured in the present work. Then, the impact of increasing neutron-richness on the quasifission flux is discussed for both the systems measured at $E_{c.m.}/V_B = 1.13$ and $E_{CN}^* = 52.0$ MeV. In each case the underlying reaction dynamics are discussed. Finally, the systems measured in the present work are considered in a broader context through comparison with systems previously measured at ANU forming the same compound nuclei.

5.1 Bohr Independence Hypothesis

Bohr postulated that the decay mode of a compound nucleus should be independent of its mode of formation [113], which is termed the Bohr independence hypothesis. If the resulting compound nucleus reaches full equilibration of all degrees of freedom, then the Bohr independence hypothesis should hold true. In the case of the present work, it is expected that if the

systems were to fuse then the Bohr independence hypothesis would hold true. As quasifission is a non-equilibrium process, reactions with significant cross section in this exit channel would deviate from the Bohr independence hypothesis. In the present work, a subset of six Cr + W measurements form the same compound nucleus through three different entrance channels. Three different projectile and target combinations ($^{50}\text{Cr}+^{186}\text{W}$, $^{52}\text{Cr}+^{184}\text{W}$, and $^{54}\text{Cr}+^{182}\text{W}$) form the same compound nucleus ^{236}Cf . Each of these systems was measured at $E_{\text{c.m.}}/V_{\text{B}} = 1.13$ and $E^* = 52.0$ MeV to give six entrance channel combinations all forming the same compound nucleus. If the systems measured in the present work underwent equilibration fusion-fission, then the upper limits of P_{CN} from the three systems forming ^{236}Cf at each energy should be consistent.

The mass distributions for all six systems forming ^{236}Cf as the compound nucleus were shown in Panels D, E, and F of Figures 4.7 and 4.19. The measure of the relative amount of quasifission in the systems was determined with the techniques described previously. The upper limits of P_{CN} determined for the Cr + W systems forming ^{236}Cf are shown in Figure 5.1 as a function of the mass of the projectile at $E_{\text{c.m.}}/V_{\text{B}} = 1.13$ and the curvature parameter determined for the Cr + W systems forming ^{236}Cf is shown in Figure 5.2 as a function of the mass of the projectile $E_{\text{CN}}^* = 52.0$ MeV.

The upper limits of P_{CN} determined for the systems forming ^{236}Cf range from 0.41 to 0.52. So approximately half of the events are lost to the quasifission reaction channel and do not form a fully equilibrated compound nucleus. The curvature parameters determined for the systems forming ^{236}Cf vary significantly. Thus, the mass distributions from these three reactions have significantly different shapes. The fission-like region of the mass distribution generated for $^{52}\text{Cr}+^{184}\text{W}$ has a minimum at mass ratios of 0.5, while the fission-like region of the mass distribution measured for $^{50}\text{Cr}+^{186}\text{W}$ is essentially flat, and the mass distribution

measured for $^{54}\text{Cr}+^{182}\text{W}$ has a maximum at a mass ratio of 0.5. The Bohr independence hypothesis predicts that these systems should have similar mass distributions. There are two potential reasons for this discrepancy. On one hand, the independence hypothesis may not hold. On the other hand, compound nucleus formation may not be the only prominent reaction channel. If the system does not undergo compound nucleus formation then the Bohr Independence Hypothesis would not apply and the variation in the curvature parameter could be attributed to the quasifission reaction channel.

5.2 Cr + W: $E_{\text{c.m.}}/V_{\text{B}} = 1.13$

In this section the results from the systems measured at $E_{\text{c.m.}}/V_{\text{B}} = 1.13$ are discussed. The upper limit of P_{CN} is shown in Figure 5.3 as a function of $(N/Z)_{\text{CN}}$ determined as described in Section 4.1.2 for each of the systems measured at $E_{\text{c.m.}}/V_{\text{B}} = 1.13$.

Notice that the upper limit of P_{CN} increases with $(N/Z)_{\text{CN}}$. This trend indicates that in the more neutron-rich systems less flux is lost to quasifission compared to the loss in the neutron-deficient systems. For Cr+W at energies 13% above the interaction barrier [9], using more neutron-rich projectiles and targets is seen to increase the amount of fusion-fission. This result is promising for future superheavy nuclei production measurements with the most neutron-rich, radioactive beams. To understand the reaction dynamics that may be behind this relationship between quasifission and the change in neutron-richness, the effects of the fissility and mass asymmetry of the system are explored in the next section.

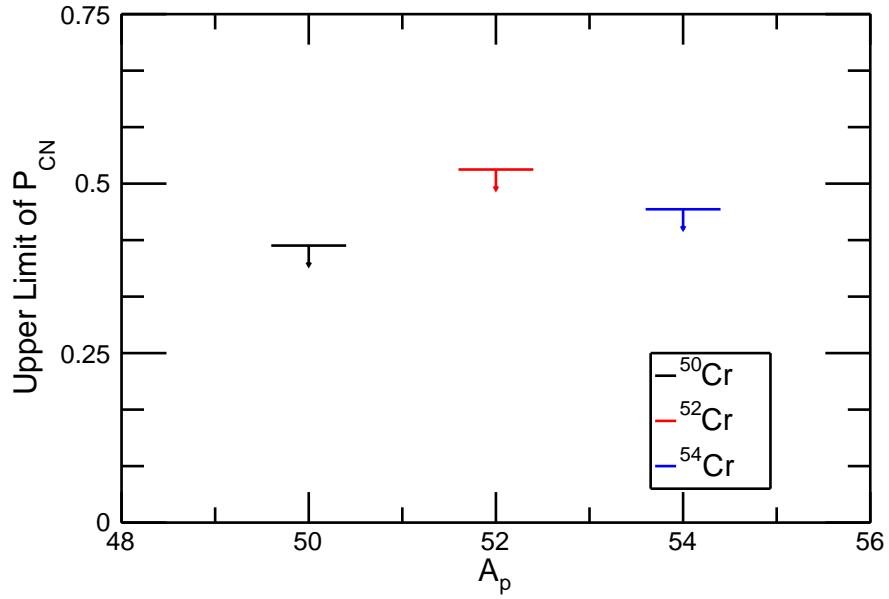


Figure 5.1: Upper limit of P_{CN} determined for the Cr + W systems forming ^{236}Cf measured in the present work as a function of the mass of the projectile. These systems were measured at $E_{c.m.}/V_B = 1.13$. The colors of the upper limit markers correspond to the projectile used in the reaction.

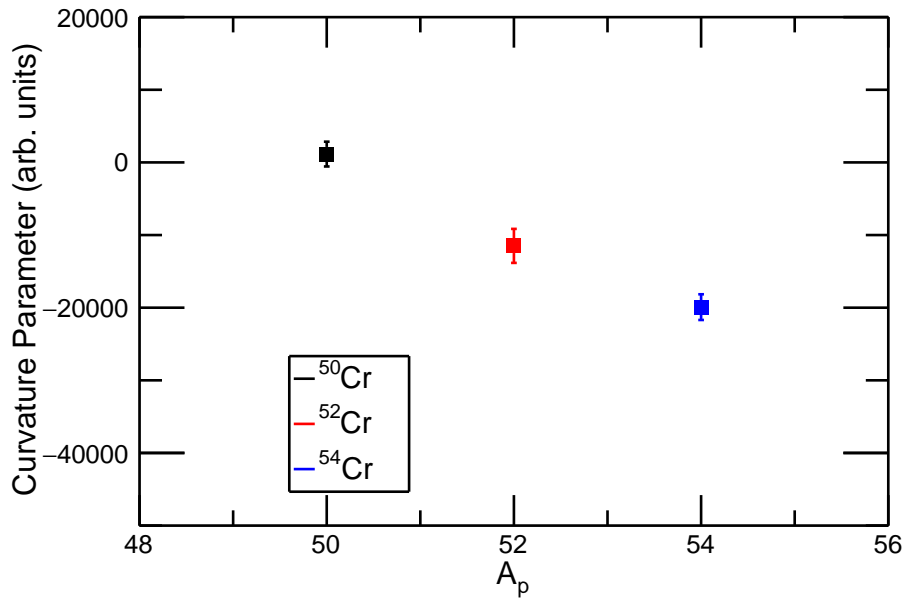


Figure 5.2: Curvature parameter determined for the Cr + W systems forming ^{236}Cf measured in the present work as a function of the mass of the projectile. These systems were measured at $E_{CN}^* = 52.0$ MeV. The colors of the upper limit markers correspond to the projectile used in the reaction.

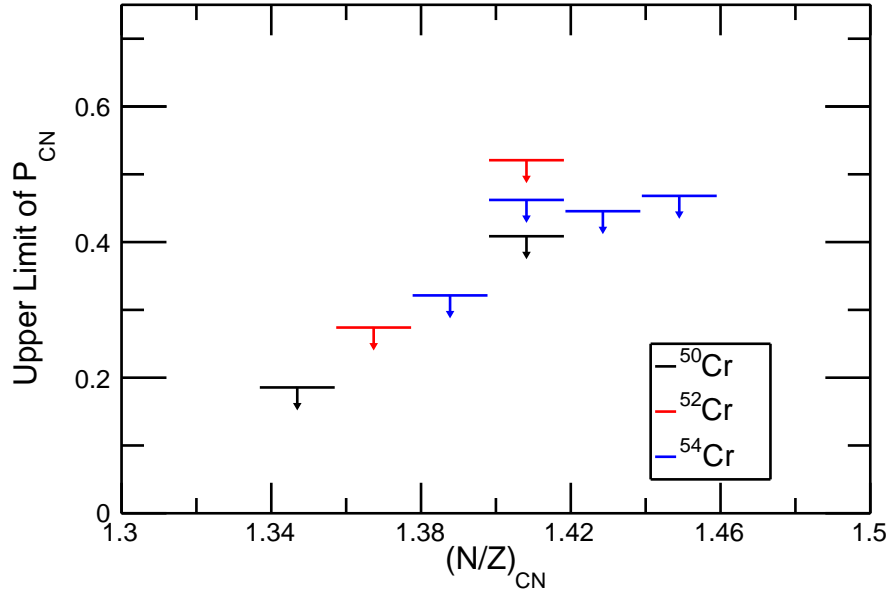


Figure 5.3: Upper limit of P_{CN} for each system measured at $E_{\text{c.m.}}/V_{\text{B}} = 1.13$ is shown as a function of $(N/Z)_{\text{CN}}$. The color of the upper limit markers correspond to the projectile used in the reaction.

5.2.1 Fissility and Mass Asymmetry

Both the compound nuclear fissility (χ_{CN}) and the mass asymmetry (α) are properties of a heavy-ion reaction system that have been shown to be dominant influences on the occurrence of quasifission in heavy-ion reactions [7, 74, 72]. Fissility is a scaling parameter that provides a measure of the ratio of the Coulomb and nuclear forces in a dinuclear system [38, 40, 56, 71] through the ratio of the Coulomb and surface terms in the liquid drop model. See the discussion in Section 1.2.2.1.

There are many related versions of the fissility parameter in the literature. The fissility parameter used here is the compound nuclear fissility, which has often been connected with

a change in the reaction dynamics. It is calculated as

$$\chi_{\text{CN}} = \frac{(Z^2/A)}{(Z^2/A)_{\text{crit}}} \quad (5.1)$$

where $(Z^2/A)_{\text{crit}} = 50.883(1 - 1.7826 I^2)$ and $I = (A - 2Z)/A$ [71, 30].

The mass asymmetry of the entrance channel is another variable often used in theoretical descriptions of heavy-ion reactions to determine the strength of the quasifission exit channel. The mass asymmetry of a dinuclear system is a dimensionless comparison of the size of the projectile to that of the target and is defined as

$$\alpha = \frac{A_{\text{target}} - A_{\text{projectile}}}{A_{\text{target}} + A_{\text{projectile}}}. \quad (5.2)$$

Note that when the neutron-richness of the reaction system is increased in the Cr + W systems both the fissility and the mass asymmetry decrease. For example, $^{50}\text{Cr} + ^{180}\text{W} \rightarrow ^{230}\text{Cf}$ is the most neutron-deficient system in this work and has χ_{CN} and α values of 0.854 and 0.565, respectively. The most neutron-rich system $^{54}\text{Cr} + ^{186}\text{W} \rightarrow ^{240}\text{Cf}$ has smaller χ_{CN} of 0.837 and α of 0.550. The χ_{CN} and α values for the reactions presented in this worked are listed in Table 5.1. The mass asymmetry is shown in Figure 5.4 as a function of the fissility of the systems measured in the present work. The fissility and mass asymmetry predict different outcomes in the present work, where the neutron-richness is varied for reactions between a constant pair of elements. It has been previously shown that as mass asymmetry increases, quasifission decreases [7], while other works have concluded that an increase in fissility leads to an increase in quasifission [80, 81, 54, 46, 8]. This leads to contradictory predictions for the effect of increasing the neutron-richness on quasifission. If the mass asymmetry is the variable with the most influence on the quasifission reaction channel, then

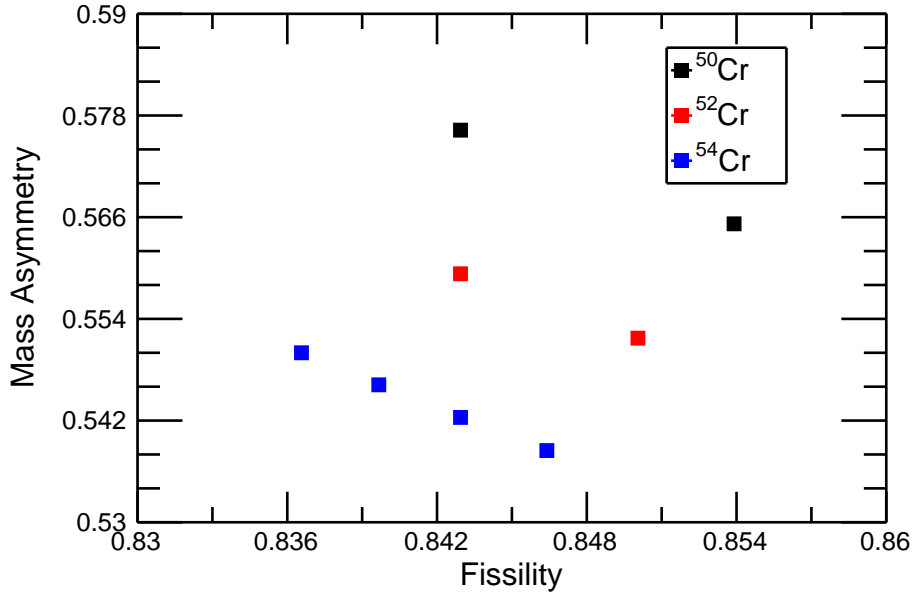


Figure 5.4: The mass asymmetry of the systems measured in the present work shown as a function of the systems fissility. The colors of the markers correspond to the projectile used in the reaction.

the prominence of the quasifission reaction channel should increase in the reaction of $^{54}\text{Cr} + ^{186}\text{W} \rightarrow ^{240}\text{Cf}$ (the most neutron-rich system) relative to the prominence of the quasifission reaction channel in the reaction of $^{50}\text{Cr} + ^{180}\text{W} \rightarrow ^{230}\text{Cf}$ (the most neutron-deficient system). Alternatively, if compound nuclear fissility is the variable with the dominant influence on the quasifission reaction channel, then the quasifission contribution should decrease in the reaction of $^{54}\text{Cr} + ^{186}\text{W} \rightarrow ^{240}\text{Cf}$ relative to the neutron-deficient systems. It is necessary to disentangle these two concepts and determine which effect dominates to fully understand how quasifission evolves with increasing neutron-richness.

The upper limit of P_{CN} determined for each of the systems in the present work at $E_{\text{c.m.}}/V_{\text{B}} = 1.13$ are shown in Figure 5.5 as a function of the compound nucleus fissility. Similarly, the upper limit of P_{CN} determined for each of the systems in the present work are shown in Figure 5.6 at $E_{\text{c.m.}}/V_{\text{B}} = 1.13$ as a function of the entrance channel mass asym-

Table 5.1: Compound nuclear fissility (χ_{CN}) and mass asymmetry (α) values of each of the eight Cr+W systems presented in this work. The determined upper limits of P_{CN} , capture cross section, and evaporation residue cross sections are also included.

System	ΔN	χ_{CN}	α
$^{50}\text{Cr} + ^{180}\text{W} \rightarrow ^{230}\text{Cf}$	0	0.854	0.565
$^{50}\text{Cr} + ^{186}\text{W} \rightarrow ^{236}\text{Cf}$	6	0.843	0.576
$^{52}\text{Cr} + ^{180}\text{W} \rightarrow ^{232}\text{Cf}$	2	0.850	0.552
$^{52}\text{Cr} + ^{184}\text{W} \rightarrow ^{236}\text{Cf}$	6	0.843	0.559
$^{54}\text{Cr} + ^{180}\text{W} \rightarrow ^{234}\text{Cf}$	4	0.846	0.538
$^{54}\text{Cr} + ^{182}\text{W} \rightarrow ^{236}\text{Cf}$	6	0.843	0.542
$^{54}\text{Cr} + ^{184}\text{W} \rightarrow ^{238}\text{Cf}$	8	0.840	0.546
$^{54}\text{Cr} + ^{186}\text{W} \rightarrow ^{240}\text{Cf}$	10	0.837	0.550

metry. A roughly linear relationship can be observed between the fissility of the compound nucleus and the upper limit of P_{CN} determined for each of the systems measured at $E_{\text{c.m.}}/V_{\text{B}} = 1.13$ while no clear trend can be observed with the determined upper limits of P_{CN} and the mass asymmetries of the systems. Thus, it can be suggested that fissility is the dominant variable influencing quasifission in these heavy-ion reactions as the neutron-richness increases in a reaction with a given elemental pair.

5.2.2 Mass Widths Compared to Theoretical Calculations

Recent work [87, 114, 115, 116] has shown that time dependent Hartree-Fock (TDHF) calculations can provide insight into the reaction dynamics of heavy-ion fusion reactions, in particular with regard to the competition between fusion-fission and quasifission. This section presents a comparison between the reactions measured in the present work at $E_{\text{c.m.}}/V_{\text{B}} = 1.13$ and recent TDHF calculations performed by Volker Oberacker and Sait Umar at Vanderbilt University [117]. TDHF is based on a mean-field formalism and uses a microscopic

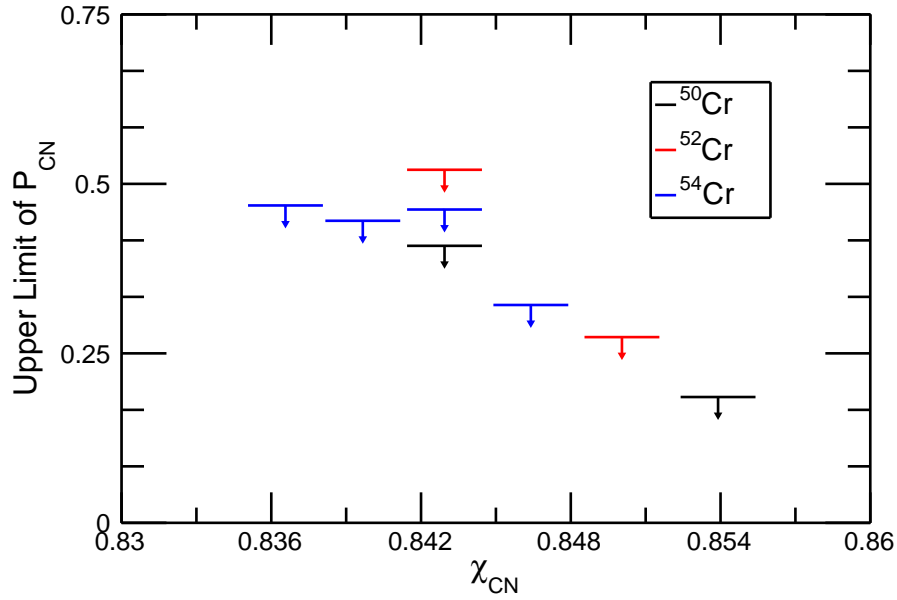


Figure 5.5: Deduced upper limits for P_{CN} shown as a function of the compound nuclear fissility for the systems measured at $E_{c.m.}/V_B = 1.13$. The colors of the upper limit markers correspond to the projectile used in the reaction.

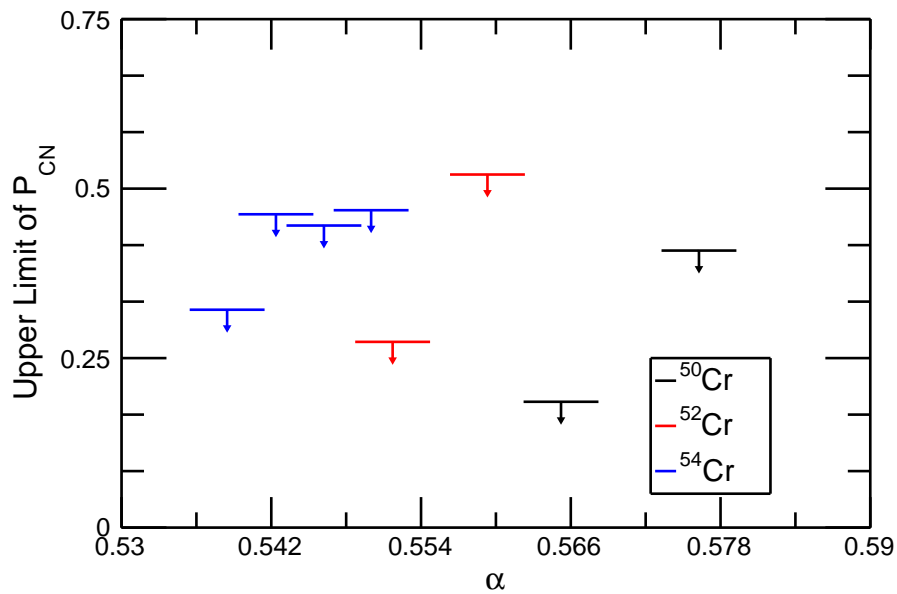


Figure 5.6: Deduced upper limits for P_{CN} shown as a function of the mass asymmetry for the systems measured at $E_{c.m.}/V_B = 1.13$. The colors of the upper limit markers correspond to the projectile used in the reaction.

approach to describe the evolution of a many-body system as a function of time [117].

TDHF calculations were completed for various impact parameters for the most neutron-deficient ($^{50}\text{Cr} + ^{180}\text{W} \rightarrow ^{240}\text{Cf}$) and the most neutron-rich ($^{54}\text{Cr} + ^{186}\text{W} \rightarrow ^{240}\text{Cf}$) systems in the present work [10]. The calculated mass ratio M_R and the charge ratio Z_R are shown in Panel A in Figure 5.7 and the contact time in Panel B as a function of impact parameter. An example of the evolution of the density distribution of a system over time is shown in the upper right corner of each panel in Figure 5.7. The evolution of the density distributions at an impact parameter of 3 fm where separation occurs is shown in Panel A in Figure 5.7. An example case at an impact parameter of 0 fm where the system was considered to eventually fuse is shown in Panel B in Figure 5.7. For the TDHF calculations presented here, fusion was considered to occur if the system did not separate during the first 35 zs after contact, based on previous calculations. The results of the calculations show the both systems fuse at the smallest impact parameters (i.e. below $b \sim 2$ fm). This limit is indicated by the boxes label “Fusion”. There was no mass ratio, charge ratio, or contact time in the calculations associated with the fusing systems so the boxes are placed at the mass ratio, charge ratio, or contact time corresponding to the first impact parameter at which fusion occurred. This choice is for visual clarity only. The differences between the two systems become apparent at impact parameters 2.5 and greater, where the separation of the dinuclear system occurs. The more neutron-rich system has larger mass and charge ratios and longer contact times relative to the neutron-deficient system. The longer the dinuclear system remains in contact the larger the probability it will not undergo quasifission. The results from the TDHF calculations agree with the experimental results from the upper limits of P_{CN} whereby increasing the neutron-richness of system increases the likelihood that the system will fuse. Note that TDHF provides an average result at each impact parameter. At impact parameters

where either fusion or quasifission may dominate, the other process may still be present because TDHF only provides the most likely exit channel.

5.2.3 Comparison with Analytical Calculations of P_{CN}

There has been much work attempting to calculate the value of P_{CN} empirically. However, the predictions vary by orders of magnitude as discussed in Section 1.2.3. Three of the commonly-used approaches in the literature to calculate P_{CN} are compared with the upper limits for P_{CN} determined for the Cr + W reactions measured in the present work. The three analytical calculations are described in the following sections. There are theoretical approaches beyond analytical calculations where dynamical models use potential energy surfaces to determine P_{CN} , however, these models require fitting parameters and were not explored in the present work [6, 118].

5.2.3.1 Armbruster's Analytical Description of P_{CN}

The results of the analytical calculations for P_{CN} and the upper limits of P_{CN} determined in the present work are shown in Figure 5.8. The first empirical prediction was based on a form developed by Armbruster, et al. [119] and fit to 63 hot-and cold-fusion data sets of heavy nuclei [29]. In this approach, P_{CN} is calculated as

$$P_{\text{CN}} = \frac{1}{2} \exp [-c(\chi_{\text{analytical}} - \chi_{\text{thr}})] \quad (5.3)$$

where χ_{thr} is the threshold fissility. A value of $\chi_{\text{thr}} = 0.72$ was determined in [119] and used in the present work. The scaling parameter c was set to -106 and was calculated from a fit to experimental data for the probability of fusion at the Bass barrier ($P(V_B)$)

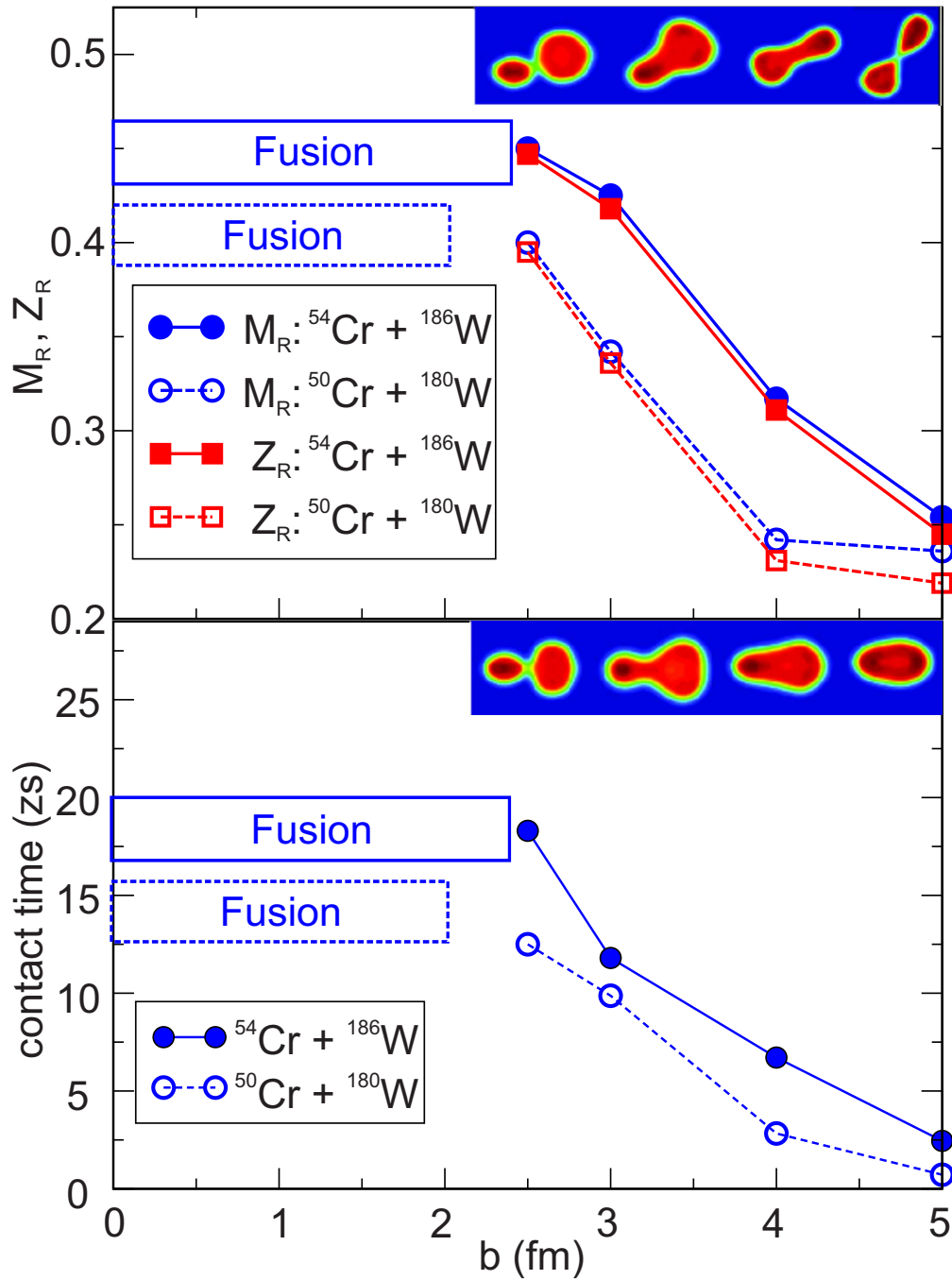


Figure 5.7: TDHF calculations for mass ratio M_R , charge ratio Z_R (a) and contact time (b) for $^{50}\text{Cr} + ^{180}\text{W} \rightarrow ^{240}\text{Cf}$ and $^{54}\text{Cr} + ^{186}\text{W} \rightarrow ^{240}\text{Cf}$ shown as a function of impact parameter b [10]. The insert in panel (a) shows an example of a density plot where the dinuclear system separates. The insert in panel (b) shows an example of a density plot where the system fuses, see the text. Reprinted figure with permission from [10] Copyright (2015) by the American Physical Society. <http://dx.doi.org/10.1103/PhysRevC.91.041602>

as a function of the average effective fissility. Armbruster *et al.* [119] fit the data with the function $c = -\ln P_{\text{CN}}/\Delta\chi$. Additional parameter sets have been proposed more recently in the literature [29]. The effective fissility used here is a variation of the fissility used earlier in eq. 5.1 and is written as

$$\chi_{\text{analytical}} = \left[\frac{(Z^2/A)}{(Z^2/A)_{\text{crit}}} \right] (1 - \alpha + \alpha f(k)) \quad (5.4)$$

where $(Z^2/A)_{\text{crit}}$ is calculated as in eq. 5.1, α is 1/3 and $f(k)$ is defined as

$$f(k) = \frac{4}{k^2 + k + \frac{1}{k} + \frac{1}{k^2}} \quad (5.5)$$

where $k = (A_1/A_2)^{1/3}$ is a parameter that characterizes the entrance channel asymmetry and A_1 and A_2 are the projectile and target mass numbers, respectively [119]. The results of this calculation of P_{CN} for the Cr + W systems measured in the present work are represented by the short-dashed, green line segments in Figure 5.8.

5.2.3.2 Zagrebaev's Analytical Description of P_{CN}

Zagrebaev *et al.* [36] proposed that P_{CN} could be analytically described by the function:

$$P_{\text{CN}}(E^*) = \frac{P_{\text{CN}}^0}{1 + \exp\left(\frac{E_B^* - E_{\text{int}}^*}{\Delta}\right)}, \quad (5.6)$$

where P_{CN}^0 is the fusion probability above the Bass barrier, E_B^* is the excitation energy of a compound nucleus resulting from a reaction at a center-of-mass beam energy equivalent to the Bass barrier energy [34], and Δ is equal to the width of the barrier distribution. This

width was taken in the present work to be 4.0 MeV as in [36]. P_{CN}^0 was calculated as

$$P_{\text{CN}}^0 = \frac{1}{(1 + \exp\left(\frac{(Z_1 Z_2 - \xi)}{\tau}\right))} = 0.272 \quad (5.7)$$

where $\xi = 45$ and $\tau = 1760$ were taken from a fit to experimental data [36] and Z_1 and Z_2 are the charge of the chromium and tungsten. The values of P_{CN} determined for the Cr + W systems in the present work using Zagrebaev's calculation are represented in Figure 5.8 by the dot-dashed, red line.

5.2.3.3 Siwek-Wilczyńska's Analytical Description of P_{CN}

In the third analytical approach considered here [120] a set of 28 reactions were considered where the evaporation-residue cross section data were previously measured. P_{CN} was deduced from its dependence on a Coulomb interaction parameter and the excess energy above the interaction barrier. The Coulomb interaction parameter, z , is defined as $z = Z_1 Z_2 / (A_1^{1/3} + A_2^{1/3})$. Siwek-Wilczyńska, *et al.* [120] proposed the following function of z as the best fit to the data:

$$P_{\text{CN}} = \exp\left(\frac{z}{a}\right)^k \quad (5.8)$$

where $k = 3.0$, and a is dependent on the excess energy above their barrier ($E_{\text{c.m.}} - V_{\text{B}}$). When $E_{\text{c.m.}} - V_{\text{B}} = 0$ MeV, eq. 5.8 best fit the data with $a \approx 135$ [120]. For $E_{\text{c.m.}} - B_0 = 10$ MeV the best fit was found with $a \approx 155$ [120]. For the systems measured in the present work $E_{\text{c.m.}} - V_{\text{B}}$ was on average 25 MeV. The values of P_{CN} were determined for the Cr + W systems in the present work using both $a = 135$ (indicated by the dot-long-dashed, light blue line segments) and $a = 155$ (indicated by the long-dashed, blue line segments).

Assuming a linear increase in a , at $E_{\text{c.m.}} - V_{\text{B}} = 25 \text{ MeV}$ a should equal to 185 (indicated by the dot-dashed, pink line segments). To fit the data in the present work a needs to be approximately 250. These P_{CN} values are included in Figure 5.8 for different a values.

5.2.3.4 Comparison of Results of Analytical Calculations

The values of P_{CN} calculated from the three analytical equations are shown in Figure 5.8 as a function of $(N/Z)_{\text{CN}}$. The upper limits of P_{CN} from the present work are also shown for comparison. The values of P_{CN} deduced in the present work are upper limits so they may not match the absolute values of P_{CN} calculated from the analytical equations. As shown in Figure 5.8, the calculated and deduced values of P_{CN} vary by orders of magnitude. Despite the lack of quantitative agreement, however, qualitative insight can be gained by comparing the general trends calculated from the analytical equations to the trend of deduced P_{CN} for the systems in the present work. In fact, all of the analytical calculations result in an increase in P_{CN} with neutron-richness.

5.3 Cr + W: $E^* = 52.0 \text{ MeV}$

The results from the subset of systems measured in the present work at the same compound nuclear excitation energy provide interesting insight that is relevant for superheavy production reactions. As discussed in Section 2.1.1, excitation energy is an important variable in superheavy production reactions because the excitation energy essentially determines the specific evaporation residues that can be produced. The interpretation of the results from the Cr + W reactions measured at $E^* = 52.0 \text{ MeV}$ are presented in Section 5.3 is discussed in this section.

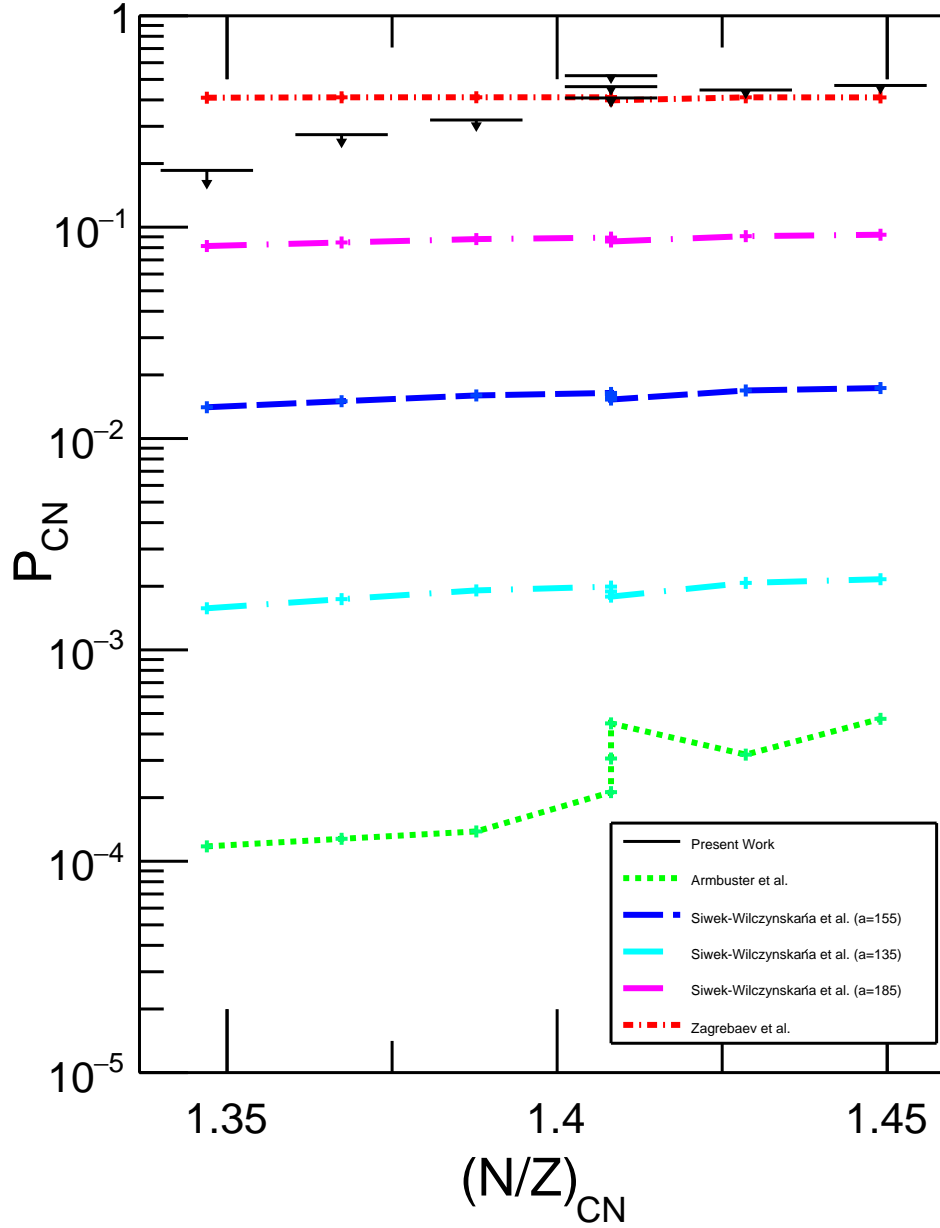


Figure 5.8: P_{CN} calculated from three analytical functions [119, 29, 120] shown as a function of $(N/Z)_{CN}$. The upper limits deduced for the systems in the present work are included as the horizontal lines.

In Section 5.3 the shape of the mass distributions were shown to be poorly described by a Gaussian function. In order to provide a measure of the relative amount of quasifission between the systems measured in the present work the curvature analysis technique (discussed in Section 4.2.2.2) was used. The curvature parameters determined for the systems measured in the present work at $E^* = 52.0$ MeV are shown in Figure 5.9 as a function of the $(N/Z)_{\text{CN}}$. Recall that a decrease in the curvature parameter is comparable to a decrease in P_{CN} and indicates a relative increase in the prominence of the quasifission reaction channel. A negative curvature parameter indicates that there was a maximum at $M_{\text{R}} = 0.5$ in mass distribution, while a positive curvature parameter indicates that there was a minimum at $M_{\text{R}} = 0.5$ in the mass distribution. For systems with nearly flat mass distributions, the curvature parameters will be near zero.

The two systems where ^{50}Cr was the projectile have a positive curvature parameter. The mass distributions from the two ^{50}Cr systems are similar in shape to those labeled by Du Rietz *et al.* [40] as Type I systems (See Section 1.3.3.1). In Type I systems short timescale quasifission dominates.

For the systems measured in the present work at $E^* = 52.0$ MeV there is no strong global trend with $(N/Z)_{\text{CN}}$ similar to that observed for the systems measured at $E_{\text{c.m.}}/V_{\text{B}} = 1.13$. There are clearly other factors involved in the reaction dynamics when the excitation energy is held constant at 52.0 MeV. Possible explanations for this difference are considered in the following section.

5.3.1 Angular Momentum

As discussed in Section 1.2.1.1, the angular momentum of the system plays an important role in the reaction dynamics. In Figure 5.10 the curvature parameters deduced for $\text{Cr} + \text{W}$

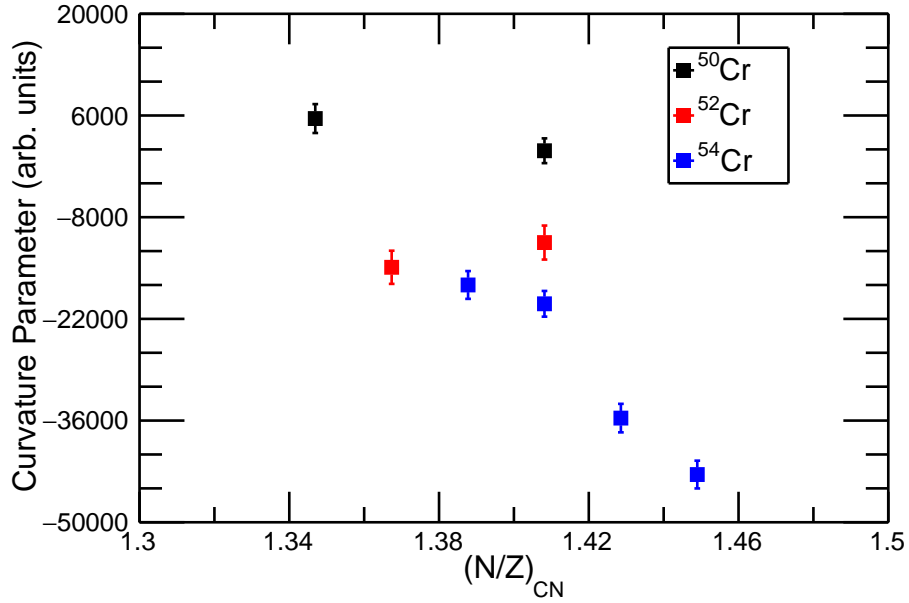


Figure 5.9: Curvature parameter in arbitrary units deduced from the mass distribution for each system measured at $E_{CN}^* = 52.0$ MeV as a function $(N/Z)_{CN}$.

systems are shown as a function of l_{\max} . In Figure 5.11 the curvature parameters deduced for Cr + W systems are shown as a function of l_{crit} . There is no simple correlation between the curvature parameters and either l_{\max} or l_{crit} . Generally, the systems with the lowest l_{\max} or l_{crit} have the highest curvature parameters, thus the strongest quasifission reaction channel.

5.3.2 Rotational Energy

In the set of systems measured at $E_{\text{c.m.}}/V_B = 1.13$ the entrance channel energy in the center-of-mass varied across the systems by only 5 MeV. However, in the systems measured at $E^* = 52.0$ MeV the center-of-mass energy varied by 14 MeV. As a result the energy available for rotation of the compound nucleus varied significantly among the systems measured at

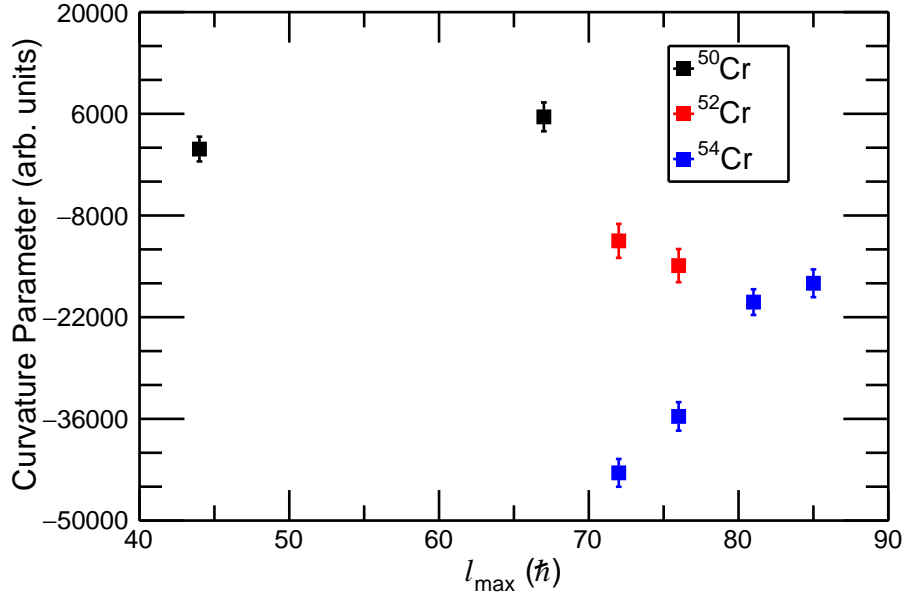


Figure 5.10: Curvature parameter deduced for the Cr + W systems at $E_{\text{CN}}^* = 52.0$ MeV in the present work as a function of the l_{max} . The colors of the data points indicate the projectile used in the reaction.

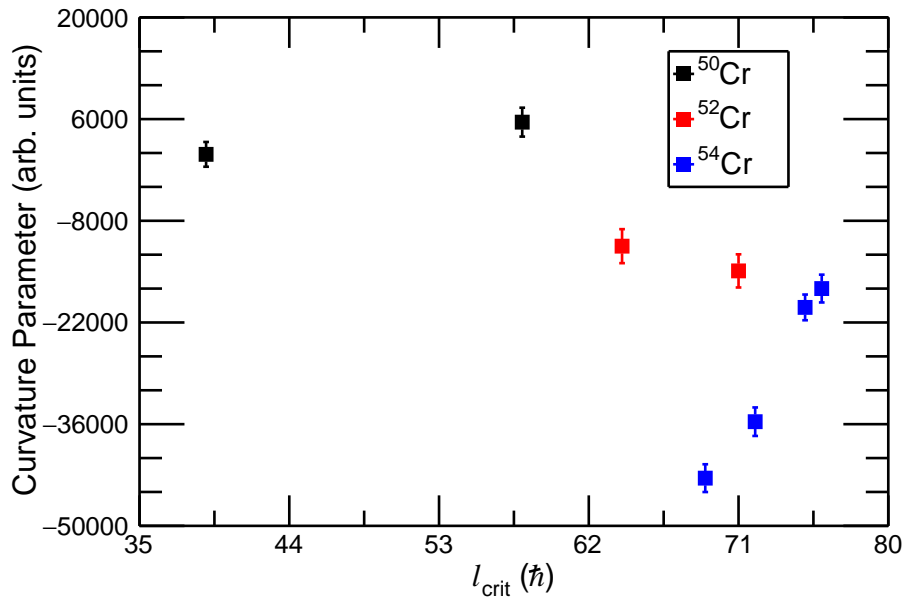


Figure 5.11: Curvature parameter deduced for the Cr + W systems at $E_{\text{CN}}^* = 52.0$ MeV in the present work as a function of the l_{crit} . The colors of the data points indicate the projectile used in the reaction.

$E_{\text{CN}}^* = 52.0$ MeV. The maximum energy available for rotation E_{rot} can be estimated as

$$E_{\text{rot}} = E_{\text{c.m.}} - V_{\text{B}} \quad (5.9)$$

where $E_{\text{c.m.}}$ is the entrance channel center-of-mass energy and V_{B} is the average Bass barrier [9, 35]. For the systems measured at $E_{\text{c.m.}}/V_{\text{B}} = 1.13$, E_{rot} varies by less than 1 MeV. By contrast, for the systems measured at $E_{\text{CN}}^* = 52.0$ MeV, E_{rot} varies from 5 to 22 MeV. The curvature parameter determined for each of the systems in the present work are shown in Figure 5.12 as a function of E_{rot} . Although there is no simple pattern, it is shown in Figure 5.12 that the systems with the lowest available rotational energy have the largest positive curvature parameters and the least “fusion-fission” like distributions. This indicates that the energy available for rotation and thus rotation of the dinuclear complex has an influence on the likelihood that the system will separate via the quasifission reaction channel. Note that the lowest curvature parameters were deduced for the two most neutron-rich systems ($^{54}\text{Cr}+^{184,186}\text{W}$) despite the fact that these two systems do not have the largest l_{max} , l_{crit} , or E_{rot} .

5.3.3 Effect of Nuclear Orientations

The physical shape of the nuclei involved in a heavy-ion fusion reaction, particularly a large deformation of the heavy reaction partner, has been shown to have a significant effect on the reaction dynamics especially at $E_{\text{c.m.}}$ near or below the interaction barrier [60, 41, 59, 64, 65, 39, 63, 62]. Many previous works have shown that the evaporation residue cross section is hindered at energies near the barrier [63, 62], when a deformed heavy nucleus takes part in the reaction. Similarly, hindrance of the related fusion-fission reaction channel has also

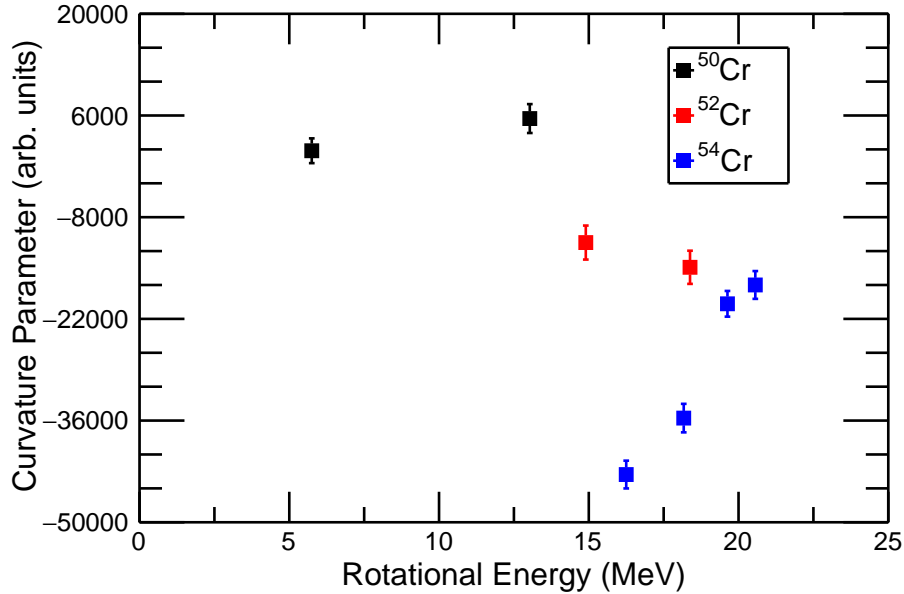


Figure 5.12: Curvature parameter determined for the Cr + W systems at $E_{\text{CN}}^* = 52.0$ MeV measured in the present work as a function of the maximum available rotational energy determined as in eq. 5.9 in MeV. The colors of the data points indicate the projectile used in the reaction.

been attributed to the presence of a deformed heavy nucleus in the entrance channel at center-of-mass energies near the barrier [60, 41, 59, 64, 65, 39]. This loss in fusion-fission and evaporation residue production then increases the strength of the quasifission reaction channel [60, 41].

Collisions between a spherical projectile and a prolate deformed nucleus occur with a continuous distribution between two extreme orientations (if the system is not able to reorient itself). For simplicity, the present discussion will consider collisions at impact parameter zero. In reality, there are many possibilities of impact parameter for each orientation. Two cartoon examples of the extreme orientations that will be considered in this discussion are shown in Figure 5.13. The case in which the nuclear symmetry axes (indicated by the dashed lines) are aligned is illustrated in Panel A of Figure 5.13. In this orientation, the projectile collides

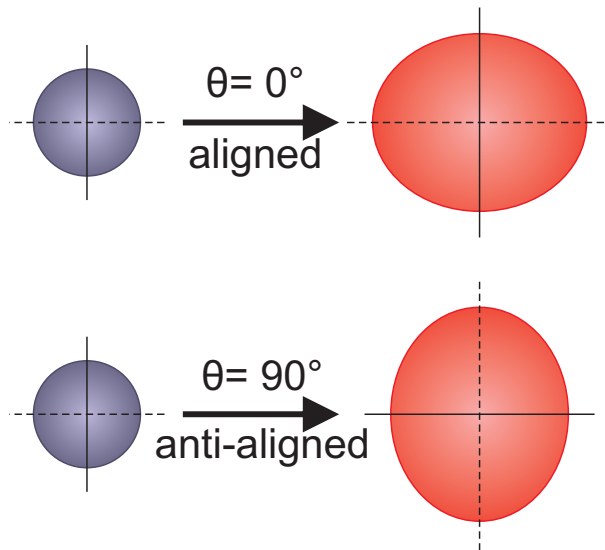


Figure 5.13: The two limiting case of collision with a deformed target nucleus. Panel A shows a collision where the nuclear symmetry axes are aligned. Panel B shows the case where the axes are anti-aligned.

with the “tip” of the prolate nucleus, forming an elongated dinuclear system. In the other extreme, the projectile collides with the elongated side of the deformed target such that the nuclear symmetry axes are perpendicular or anti-aligned as illustrated in Panel B of Figure 5.13. Note that the Coulomb energy is higher for the latter (Panel B) collision.

5.3.3.1 Shape Evolution and Mass Asymmetry

In previous works where hindrance of the fusion-fission or evaporation residues reaction channels was observed in reactions with deformed nuclei, the hinderance was attributed to the broadening of the interaction barrier due to the various possible nuclear orientations [121, 39]. Collisions like those illustrated in Panel A of Figure 5.13 with an elongated dinuclear system, were shown to preferentially lead to quasifission [121, 39]. Collisions like those illustrated in Panel B of Figure 5.13, where a more compact dinuclear system is formed, were shown to

preferentially lead to fusion-fission [121, 39]. The tungsten isotopes considered in the present work are all prolate deformed, while the chromium isotopes are all approximately spherical. The β_2 deformation parameter values for all nuclei discussed in the present work are listed in Table 5.2 [?].

To explore the effect of the deformation of the tungsten isotopes on the reaction dynamics of the systems measured in the present work, the interaction barriers must be calculated as a function of orientation. First, the principal radii of the deformed tungsten nuclei were determined. An axially deformed nucleus can be approximated as an ellipsoid of revolution where the various radii can be calculated from

$$R(\theta, \phi) = R_{\text{avg}}[1 + \beta \mathbf{Y}_{20}(\theta, \phi)] \quad (5.10)$$

where R_{avg} is the average radius of the two major axes, β is the deformation parameter along the semi-major axis of interest, and \mathbf{Y}_{20} is a spherical harmonic function (\mathbf{Y}_{LM}) where L is 2 and M is 0 [67]. In a prolate deformed nucleus, there are two axes of interest: (1) the elongated semi-major axis, along the nuclear symmetry axis indicated by the dashed, black line in the example prolate deformed nucleus in Figure 5.13, (2) the shortened semi-minor axis indicated by the solid, black line in the example prolate deformed nucleus in Figure 5.13. The limiting case of the semi-major and semi-minor axes can be calculated as:

$$\mathbf{Y}_{20}(\theta, \phi) = \frac{1}{4} \sqrt{\frac{5}{\pi}} (3\cos^2\theta - 1) \quad (5.11)$$

$$\mathbf{Y}_{20}(0^\circ, \phi) = \frac{1}{4} \sqrt{\frac{5}{\pi}} (3\cos^2(0) - 1) = \sqrt{\frac{5}{4\pi}} \quad (5.12)$$

$$\mathbf{Y}_{20}(90^\circ, \phi) = \frac{1}{4} \sqrt{\frac{5}{\pi}} (3\cos^2(90) - 1) = -\frac{1}{4} \sqrt{\frac{5}{\pi}} \quad (5.13)$$

$$R_{\text{semi-Major}}(\theta, \phi) = R_{\text{avg}} \left[1 + \beta * \left(-\frac{1}{4} \sqrt{\frac{5}{\pi}} \right) \right] \quad (5.14)$$

$$R_{\text{semi-Minor}}(\theta, \phi) = R_{\text{avg}} \left[1 + \beta * \sqrt{\frac{5}{4\pi}} \right] \quad (5.15)$$

$$(5.16)$$

The radius used in the present work was taken to be the Blocki half-density radius [9] defined as $R_{\text{avg}} = 1.16 * A^{1/3} - 1.39 * A^{-1/3}$. For each nucleus considered in the present work the average, semi-major, and semi-minor radii are listed in Table 5.2. Because of the strong deformation of the W nuclei, the semi-major and semi-minor axes change by more than 1 fm relative to the average radius, or by about 10% of the total. This has a large effect on the interaction barrier associated with each limiting case. The Bass barriers [9] were determined with the semi-major and semi-minor radii to examine the effect of this change in the radii and are listed in Table 5.3. The interaction radius was determined as $R_{\text{int}}(\text{orientation}) = R^{\text{Cr}}(\text{orientation}) + R^{\text{W}}(\text{orientation})$. The orientation of the deformed target reduced the barrier by 8% on average for the aligned collisions and increases the barrier by 5% for the anti-aligned collisions. In Figure 5.14, the curvature parameters determined for the systems measured in the present work are shown as a function of the aligned barrier in Panel A, the average barrier in Panel B, and the anti-aligned barrier in Panel C.

The enhanced curvature parameters of the two ^{50}Cr systems and the ^{52}Cr can be under-

Table 5.2: Average radii, β_2 values [86], semi-major radii, and semi-minor radii determined for chromium and tungsten isotopes considered in the present work.

Nucleus	R_B^i (average) (fm)	β_2 [86]	R_B^i (aligned) (fm)	R_B^i (anti-aligned) (fm)
^{50}Cr	3.89	0.0	–	–
^{52}Cr	3.96	0.0	–	–
^{54}Cr	4.02	0.0	–	–
^{180}W	6.30	0.258	7.33	5.79
^{182}W	6.33	0.259	7.36	5.81
^{184}W	6.35	0.24	7.32	5.87
^{186}W	6.38	0.23	7.30	5.92

stood in the context of the extreme barriers. For the anti-aligned collisions the $^{50}\text{Cr}+^{180}\text{W}$ and $^{50}\text{Cr}+^{186}\text{W}$ have $E_{\text{c.m.}}/V_B = 0.98$ and 1.01 , respectively. Thus, the anti-aligned configuration, which preferentially leads to fusion-fission, was suppressed for these systems because the entrance channel energy was below or barely above the interaction barrier. The hindrance to fusion of reactions at this orientation causes the quasifission flux to be high for these systems relative to the systems where the anti-aligned orientation is available. The combination of effects from rotational energy and change in the interaction barrier affect the reaction dynamics in the system measured in the present work at the fixed excitation energy.

5.4 Angular Distributions

In Sections 4.1.3 and 4.2.3 the angular distributions for the fission-like region for all of the systems measured in the present work at both energies were presented. Throughout the literature, angular distributions are often presented in terms of their anisotropy, where anisotropy is defined as the ratio of the observed cross sections at a given pair of angles.

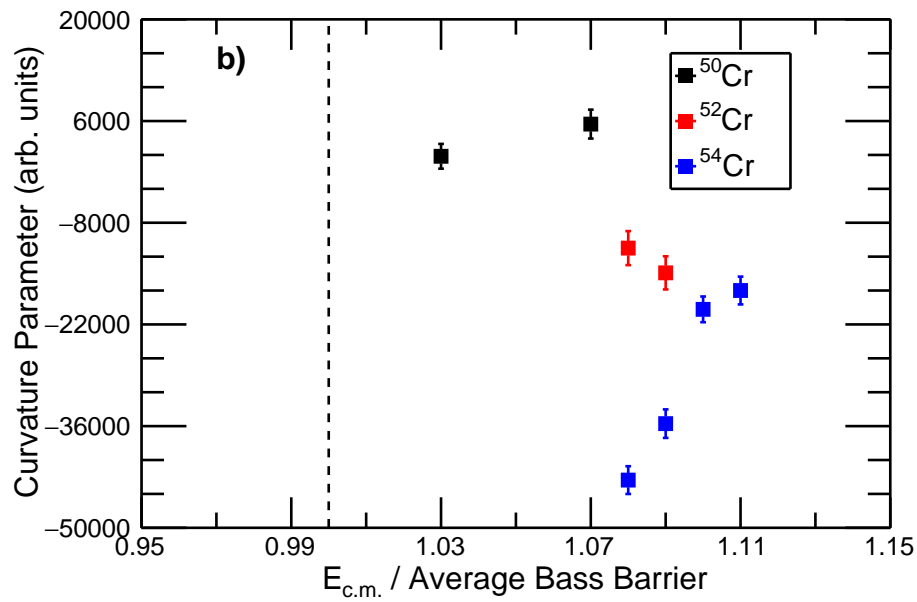
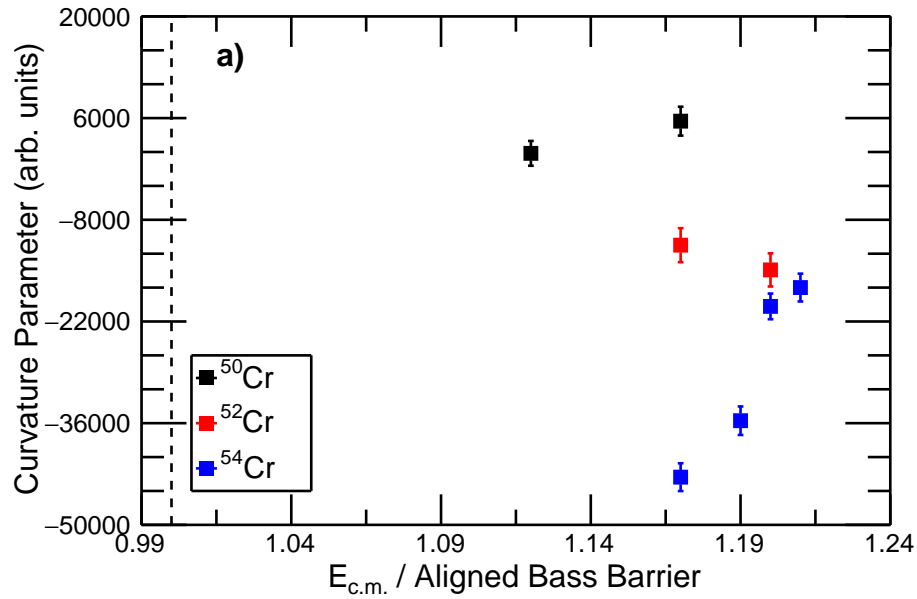


Figure 5.14: Curvature parameters determined for the Cr + W reactions measured in the present work as a function of $E_{c.m.}/V_B$ (aligned) in Panel A, $E_{c.m.}/V_B$ (average) in Panel B, and $E_{c.m.}/V_B$ (anti-aligned) in Panel C.

Figure 5.14: (cont'd)

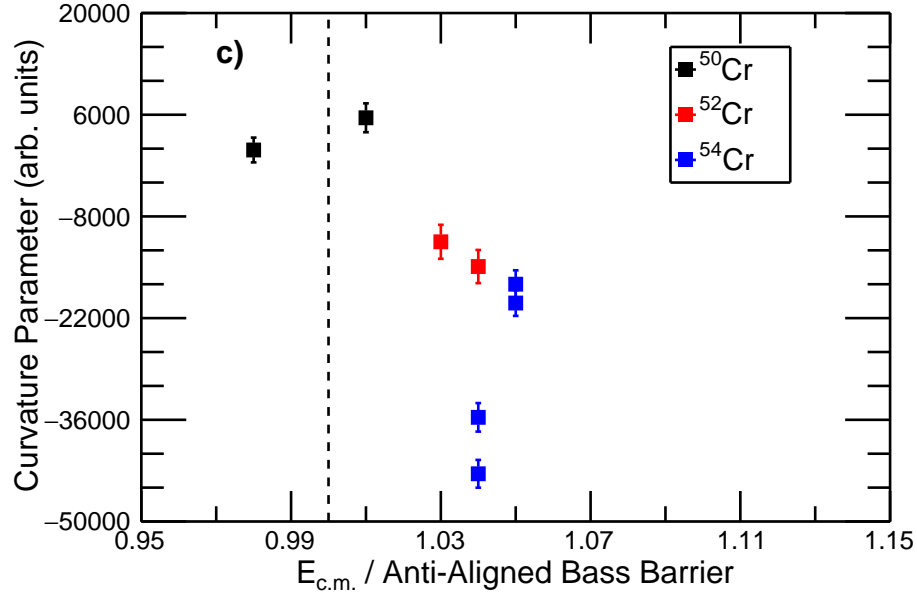


Table 5.3: Bass interaction barriers [9] for the average and limiting orientations determined for the Cr + W reactions considered in the present work.

System	$V_{\text{Bass}}(\text{average})$ (MeV)	$V_{\text{Bass}}(\text{aligned})$ (MeV)	$V_{\text{Bass}}(\text{anit-aligned})$ (MeV)
$^{50}\text{Cr} + ^{180}\text{W}$	196.95	179.84	207.21
$^{50}\text{Cr} + ^{186}\text{W}$	195.59	180.31	204.70
$^{52}\text{Cr} + ^{180}\text{W}$	195.75	178.86	205.83
$^{52}\text{Cr} + ^{184}\text{W}$	194.80	179.00	204.17
$^{54}\text{Cr} + ^{180}\text{W}$	194.56	177.89	204.51
$^{54}\text{Cr} + ^{182}\text{W}$	194.12	177.46	204.10
$^{54}\text{Cr} + ^{184}\text{W}$	193.67	178.05	202.86
$^{54}\text{Cr} + ^{186}\text{W}$	193.22	178.35	202.10

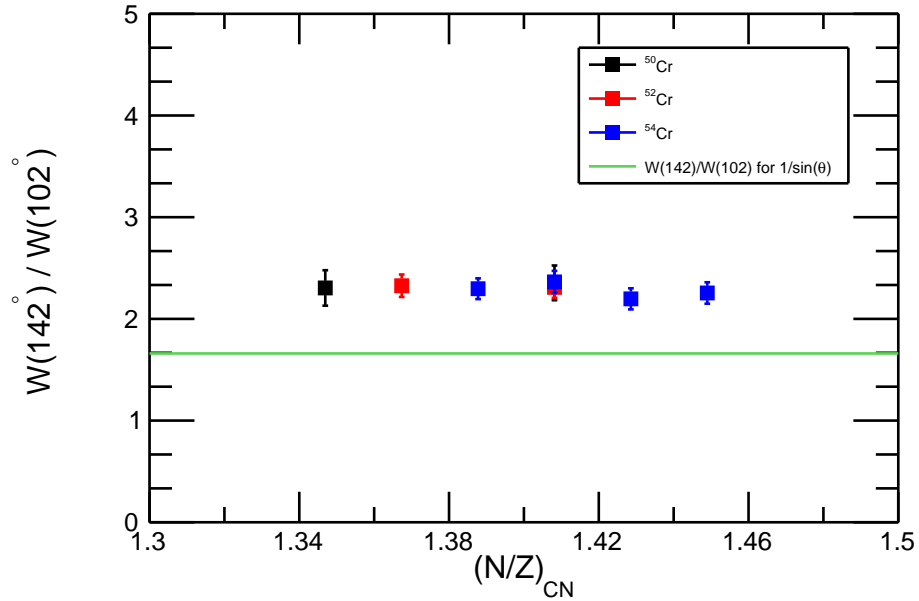


Figure 5.15: Angular anisotropy, determined as the ratio of $W(142^\circ)$ to $W(102^\circ)$ for the systems measured at $E_{c.m.}/V_B = 1.13$ shown as a function of $(N/Z)_{CN}$ in the present work. The colors of the data points correspond to the projectile used in the reaction. The solid, green line indicates the ratio of $W(142^\circ)$ to $W(102^\circ)$ for a $1/\sin(\theta)$ function.

Often, the anisotropy is defined as a ratio of the angular distributions function $W(\theta)$, such as $W(0^\circ)$ (or $W(180^\circ)$) to $W(90^\circ)$. In the present work, there was not full coverage of the fission-like mass ratios at $\theta = 90^\circ$ and 180° , thus, the anisotropy was taken as the ratio of $W(142^\circ)$ to $W(102^\circ)$.

The anisotropy determined from the angular distributions from the present work are shown in Figures 5.15 and 5.16. Clearly, there is little difference in the angular anisotropy among the present systems. The one feature of note in Figure 5.16 is the difference in the three systems that form ^{236}Cf , with $(N/Z)_{CN} = 1.41$ at $E_{CN}^* = 52.0$ MeV.

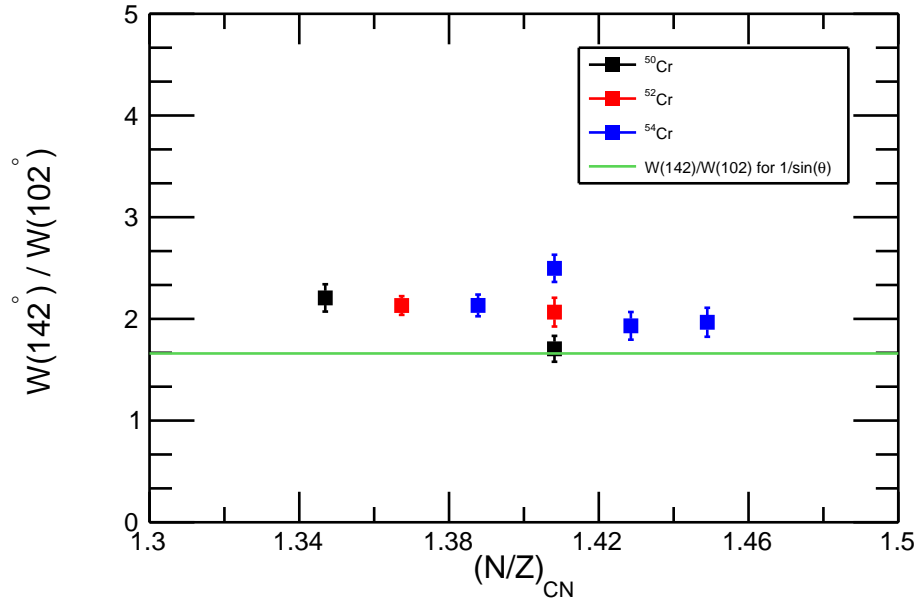


Figure 5.16: Angular anisotropy, determined as the ratio of $W(142^\circ)$ to $W(102^\circ)$ for the systems measured at $E_{\text{CN}}^* = 52.0$ MeV shown as a function of $(N/Z)_{\text{CN}}$ in the present work. The colors of the data points correspond to the projectile used in the reaction. The solid, green line indicates the ratio of $W(142^\circ)$ to $W(102^\circ)$ for a $1/\sin(\theta)$ function.

5.5 Previously Studied Reactions forming ^{238}Cf and ^{240}Cf

Additional insight into the reaction dynamics can be gained when the Cr+W systems are considered in the larger context of other reactions with different entrance channels that form the same compound nucleus. Previous experiments at ANU deduced the mass distributions for ^{238}Cf and ^{240}Cf with different entrance channels at comparable energies. Table 5.4 lists the entrance channels and energies of the systems previously measured at ANU forming ^{238}Cf and ^{240}Cf [46, 40].

The mass distributions from the reactions shown in Figure 5.17 indicate that the reaction dynamics for these systems are different than those for the Cr+W systems even though they form the same compound nucleus, especially at higher center-of-mass energies. For example, the most asymmetric entrance channels have the narrowest fission-fragment distribution.

The upper limits of P_{CN} determined for the systems measured in the present work and previously at ANU at energies with $E_{\text{c.m.}}/V_{\text{B}}$ was ≈ 1.13 are shown in Figures 5.19 and 5.18 as a function of the fissility and mass asymmetry, respectively. (Obviously, the fissility is the same for the systems forming the same compound nuclei.) In this representation, the difference between the values of P_{CN} for the most asymmetric system, $^{32}\text{S} + ^{208}\text{Pb}$, and the other systems is apparent. Additionally, the fusion-fission channel in $^{32}\text{S} + ^{208}\text{Pb}$ is expected to be favored due to the doubly magic ^{208}Pb [122, 119]. The curvature parameters determined for the systems in the present work and previously at ANU at energies where the compound nucleus was formed with $E_{\text{CN}}^* \approx 52.0$ MeV are shown in Figures 5.21 and 5.20 as a function of the fissility and mass asymmetry, respectively. Similar to the systems measured at $E_{\text{c.m.}}/V_{\text{B}} \approx 1.13$, the mass asymmetry is the defining variable, as in previous work [7] a significant change in change in entrance mass asymmetry has a large impact on the quasifission flux, when the system has the same fissility.

Table 5.4: Entrance channel system, fissility (χ_{CN}), mass asymmetry (α), center-of-mass energy, energy relative to the interaction barrier [9] ($E_{c.m.} / V_B$), excitation energy (E^*), and upper limit of P_{CN} for the relevant systems measured in the present work and the systems previously measured at ANU where the compound nucleus formed was ^{238}Cf or ^{240}Cf .

Entrance Channel	Compound Nucleus	χ_{CN}	α	$E_{c.m.}$ (MeV)	$E_{c.m.} / V_B$	E_{CN}^* (MeV)	Upper Limit P_{CN}
$E_{c.m.} / V_B \approx 1.13$							
$^{54}\text{Cr} + ^{184}\text{W}$	^{238}Cf	0.840	0.546	218.9	1.13	59.03	0.446 ± 0.009
$^{40}\text{Ca} + ^{198}\text{Pt}$ [40]	^{238}Cf	0.840	0.664	192.59	1.11	70.64	0.553 ± 0.002
$^{54}\text{Cr} + ^{186}\text{W}$	^{240}Cf	0.837	0.550	218.3	1.13	60.85	0.468 ± 0.009
$^{48}\text{Ti} + ^{192}\text{Os}$ [46]	^{240}Cf	0.837	0.600	207.94	1.14	65.54	0.451 ± 0.003
$^{32}\text{S} + ^{208}\text{Pb}$ [40]	^{240}Cf	0.837	0.733	166.4	1.13	60.61	0.448 ± 0.003
$E_{CN}^* \approx 52.0$ MeV							
							Curvature Parameter (arb. units)
$^{54}\text{Cr} + ^{184}\text{W}$	^{238}Cf	0.840	0.546	193.08	1.09	52.0	$-3.57 \times 10^4 \pm 2.0 \times 10^3$
$^{40}\text{Ca} + ^{198}\text{Pt}$ [40]	^{238}Cf	0.840	0.664	188.85	1.09	66.7	$-3.5 \times 10^4 \pm 1.4 \times 10^3$
$^{54}\text{Cr} + ^{186}\text{W}$	^{240}Cf	0.837	0.550	209.48	1.08	52.00	$-4.34 \times 10^4 \pm 1.9 \times 10^3$
$^{48}\text{Ti} + ^{192}\text{Os}$ [46]	^{240}Cf	0.837	0.600	196.0	1.07	53.06	$-3.6 \times 10^4 \pm 2.0 \times 10^3$
$^{32}\text{S} + ^{208}\text{Pb}$ [40]	^{240}Cf	0.837	0.733	158.17	1.07	52.37	$-2.7 \times 10^4 \pm 1.8 \times 10^3$

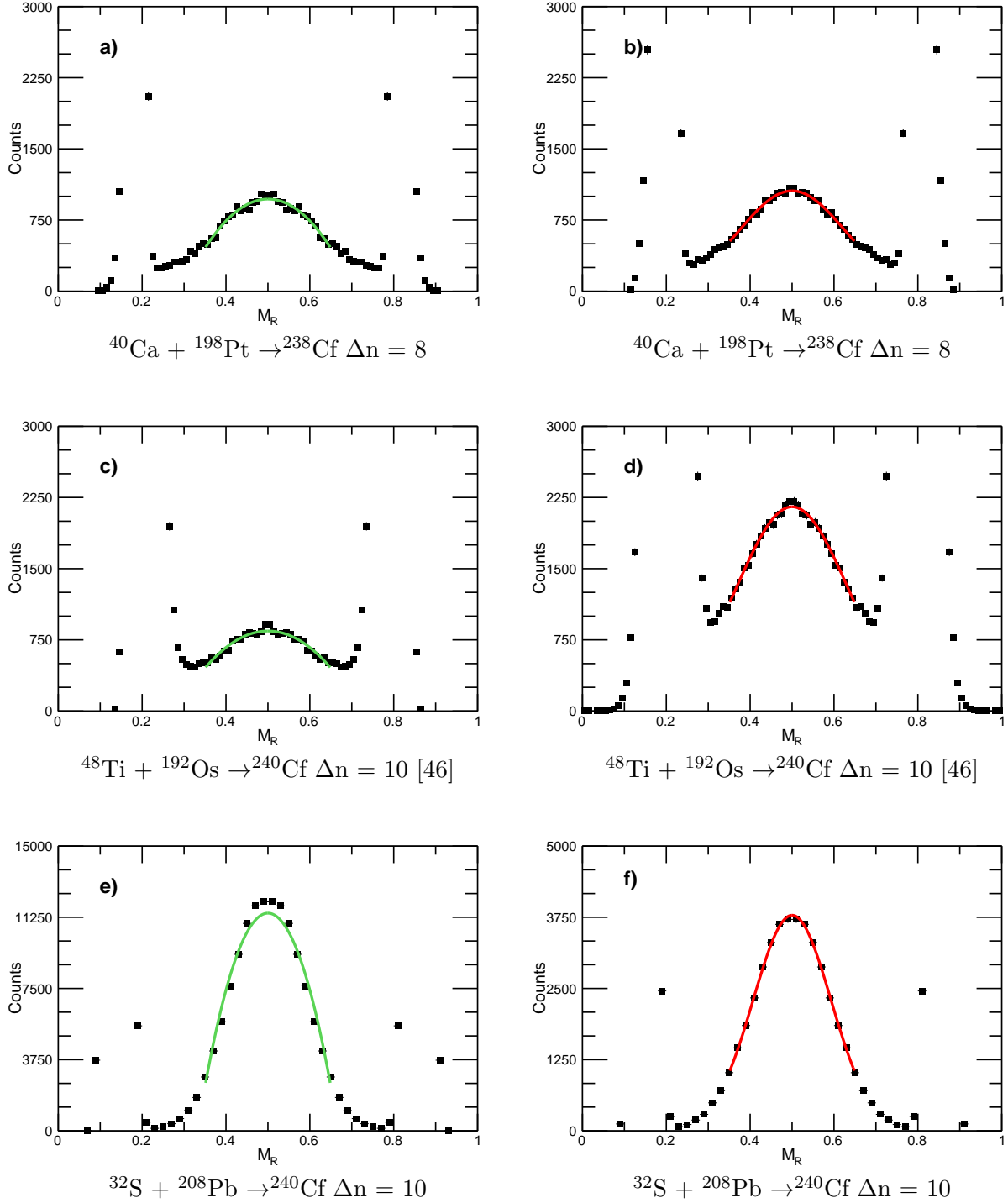


Figure 5.17: Mass distributions for previously measured systems forming ^{238}Cf or ^{240}Cf at comparable energies to the Cr+W systems measured at $E_{\text{c.m.}}/V_{\text{B}} \approx 1.13$ (panels A, C, and E) and $E_{\text{CN}}^* \approx 52.0$ MeV (panels B, D, and F).

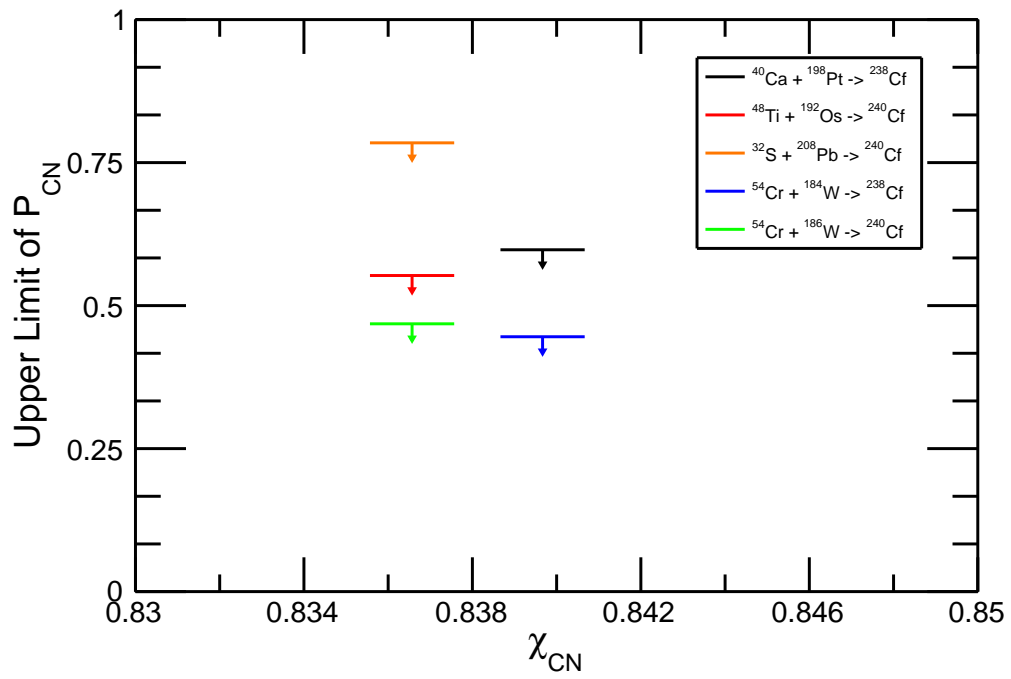


Figure 5.18: The upper limit of P_{CN} determined for the systems in the present work and previously measured at ANU forming ^{238}Cf or ^{240}Cf as the compound nucleus are shown as a function of the fissility of the compound nucleus. The systems are distinguished in the legend.

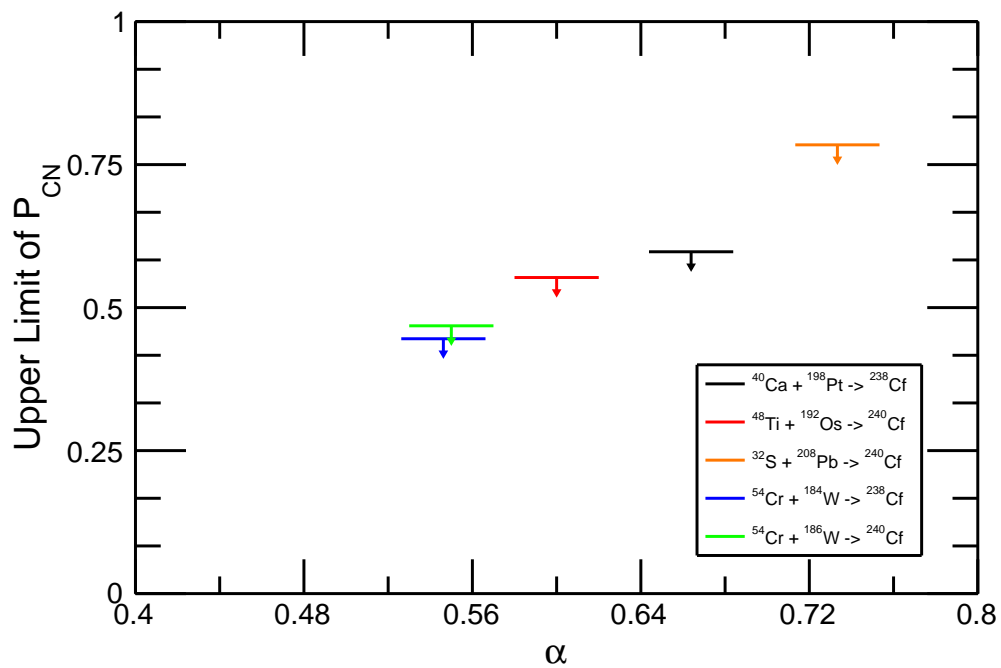


Figure 5.19: The upper limit of P_{CN} determined for the systems in the present work and previously measured at ANU forming ^{238}Cf or ^{240}Cf as the compound nucleus are shown as a function of the entrance channel mass asymmetry. The systems are distinguished in the legend.

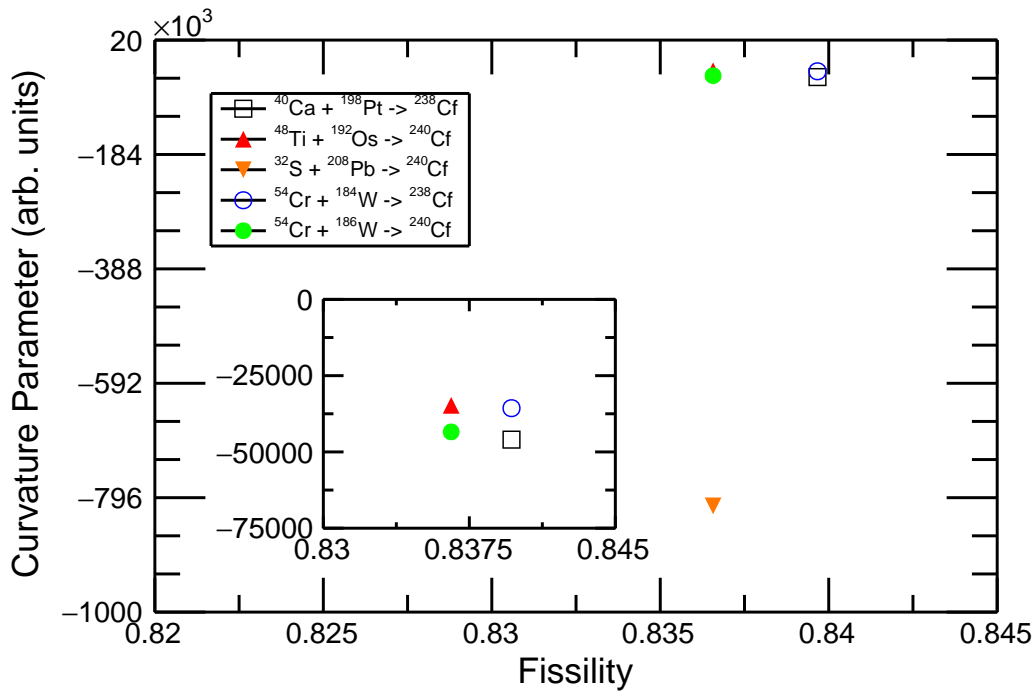


Figure 5.20: The curvature parameters determined for the systems in the present work and previously measured at ANU forming ^{238}Cf or ^{240}Cf as the compound nucleus are shown as a function of the fissility of the compound nucleus. The systems forming ^{238}Cf are indicated by the solid markers, while the systems forming ^{240}Cf are indicated by the open markers. The systems are distinguished in the legend. The inset in the lower right corner is the same plot zoomed in on the systems other than $^{32}\text{S} + ^{208}\text{Pb}$.

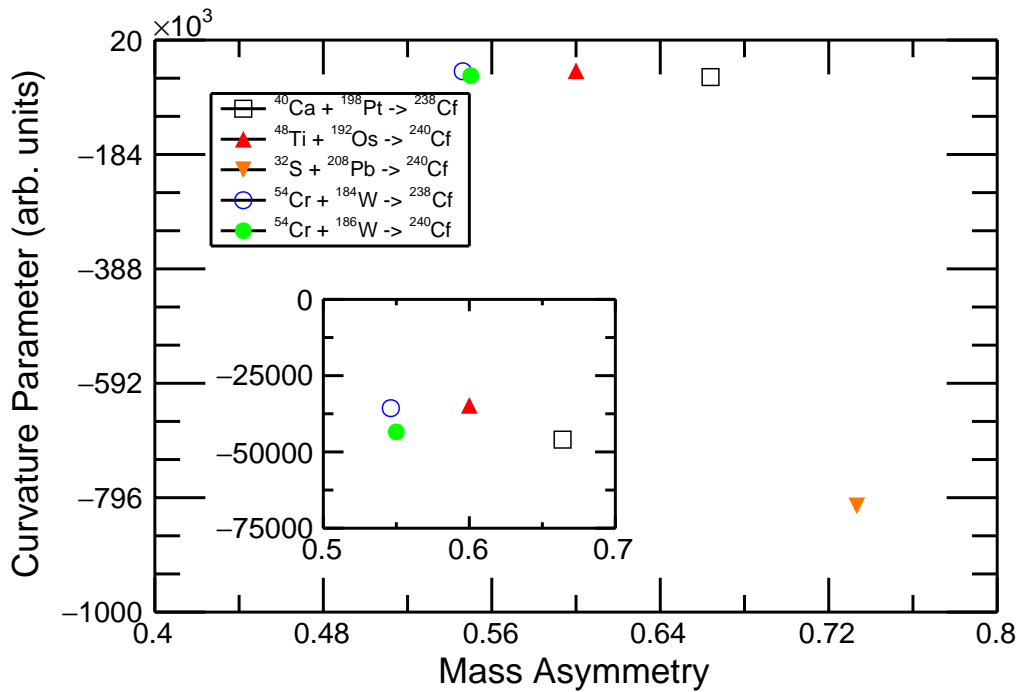


Figure 5.21: The curvature parameters determined for the systems in the present work and previously measured at ANU forming ^{238}Cf or ^{240}Cf as the compound nucleus are shown as a function of the entrance channel mass asymmetry. The systems forming ^{238}Cf are indicated by the solid markers, while the systems forming ^{240}Cf are indicated by the open markers. The systems are distinguished in the legend. The inset in the lower right corner is the same plot zoomed in on the systems other than $^{32}\text{S} + ^{208}\text{Pb}$.

Chapter 6

Conclusions

The mass angle distributions for eight isotopically different Cr + W reactions were successfully deduced and provided important insight about the reaction mechanism with increasing neutron-richness. The goal of the present work was to gain an understanding of the impact of increasing the neutron-richness on the reaction dynamics in heavy-ion fusion reactions. Two strongly competing exit channels in previously identified heavy-ion fusion reactions are fusion-fission and quasifission. The two reaction types compete with one another and make up the bulk of the reaction cross section for the formation of the heaviest nuclei. When quasifission is present a significant portion of the reaction flux is lost as a result of a failure to produce a compound nucleus. This loss is particularly detrimental to superheavy element formation reactions. Improved estimates of the cross sections of heavy-ion fusion reactions, particularly for superheavy element formation, require a full understanding of the quasifission component. The effect of neutron-richness has been suggested to be important for future superheavy element production reactions when more neutron-rich beams are used to produce nuclei in the predicted “Island of Stability”. In the present work, the reaction dynamics were explored with increasing neutron-richness.

Here, eight different isotopic combinations of the reaction of chromium and tungsten were measured. Each reaction was measured under two energy conditions, one at $E_{c.m.}/V_B = 1.13$ and E_{CN}^* of 52.0 MeV at the Heavy Ion Accelerator Facility at the Australia National University. The chromium beams were accelerated by the 14 UD tandem van de Graaf

accelerator and the superconducting LINAC. The position and timing information for fission fragments resulting from the Cr + W reactions was measured with the CUBE fission fragment detector system. The kinematic coincidence method was used to transform the position and timing information into mass ratios and center-of-mass angles. The resulting mass and angular distributions were used to deduce mass-angle distributions. The presence of a strong mass-angle correlation indicated the dominance of the quasifission exit channel for all reactions considered here. The projection of the mass angle distribution onto the mass axis was analyzed with two different methods, mass widths and curvature, to compare the relative distributions among the systems measured in the present work. At $E_{c.m.}/V_B = 1.13$ the broadening of the mass distribution decreased with increasing neutron-richness. At E_{CN}^* of 52.0 MeV the relationship between quasifission and neutron-richness was less clear. The variation of the interaction barrier due to the deformation of the tungsten nucleus may have a significant impact on the reaction dynamics at low E_{CN}^* . From the projection of the mass angle distribution onto the angle axis, the angular distribution was determined for the eight systems at each energy. The angular anisotropy was consistently larger than that expected for fusion-fission for each system indicating the dominance of quasifission in these reactions.

For the systems at 13% above interaction barrier, the experimental upper limits of P_{CN} were compared with the fissility (χ) and mass asymmetry (α) of the systems to distinguish between these two commonly used variables for predicating the presence of quasifission. From the upper limits determined for P_{CN} in the present work, it was concluded that, for the Cr + W system, the fissility is the primary predictor of the change in quasifission.

For the systems where the excitation energy of the compound nuclear was held constant at 52.0 MeV, it was found that the deformation of the heavy reaction partner is very important. The change in radius resulting from the deformation caused the center-of-mass energy of the

reaction to be right at the barrier for the configurations most likely to form a compound nucleus. Thus, the process of forming a compound nucleus was hindered relative to that of separating via quasifission. This is an important factor to consider for superheavy production reactions, where the excitation energy is important for the neutron evaporation likelihood leading to the desired evaporation residue.

Overall, the present work has shown that quasifission plays a significant role in the reaction dynamics for all of the Cr + W reactions. The observed decrease in quasifission with increasing neutron-richness for $E_{c.m.}/V_B = 1.13$ can be viewed as a positive result for future superheavy production reactions involving more neutron-rich, even radioactive, projectile beams. Based on the results of the present work, the increase in neutron-richness should increase the probability of forming a compound nucleus relative to a more neutron-deficient isotopic combination.

There is still much work to be done to understand the competition between fusion-fission and quasifission in heavy-ion fusion reactions. Heavy-ion fusion experiments with neutron-rich radioactive beams provide a new means of exploring the reaction mechanism. The first heavy-ion fusion reaction measurement with a radioactive beam produced by the NSCL ReA3 facility was measured in October 2015 [123]. The fusion excitation function was deduced for the reaction of $^{46}\text{K} + ^{181}\text{Ta}$ using the new Coincident Fission Fragment Detector [124]. This detector set up was based on the CUBE detector set up used in the present work. In future experiments with reaccelerated radioactive beams the Coincident Fission Fragment Detector could be used for studies comparable to the present work where reaction dynamics are explored through observed mass and angular distributions.

BIBLIOGRAPHY

BIBLIOGRAPHY

- [1] J. Hamilton, S. Hofmann, and Y. Oganessian, “Search for Superheavy Nuclei,” *Annual Review of Nuclear and Particle Science*, **63**, 383, (2013).
- [2] Y. T. Oganessian, F. S. Abdullin, C. Alexander, J. Binder, R. a. Boll, S. N. Dmitriev, J. Ezold, K. Felker, J. M. Gostic, R. K. Grzywacz, J. H. Hamilton, R. A. Henderson, M. G. Itkis, K. Miernik, D. Miller, K. J. Moody, A. N. Polyakov, A. V. Ramayya, J. B. Roberto, M. a. Ryabinin, K. P. Rykaczewski, R. N. Sagaidak, D. a. Shaughnessy, I. V. Shirokovsky, M. V. Shumeiko, M. A. Stoyer, N. J. Stoyer, V. G. Subbotin, A. M. Sukhov, Y. S. Tsyganov, V. K. Utyonkov, A. A. Voinov, and G. K. Vostokin, “Production and Decay of the Heaviest Nuclei $^{293,294}_{117}$ and $^{294}_{118}$,” *Physical Review Letters*, **109**, 162501, (2012).
- [3] Y. Oganessian, “Heaviest nuclei from ^{48}Ca -induced reactions,” *Journal of Physics G: Nuclear and Particle Physics*, **34**, R165, (2007).
- [4] J. Toke, R. Bock, G. X. Dai, A. Gobbi, S. Gralla, K. D. Hildenbrand, J. Kuzminski, W. F. J. Müller, A. Olmi, H. Stelser, “Quasi-Fission - The Mass-Drift Mode in Heavy-Ion Reactions,” *Nuclear Physics A*, **440**, 327, (1985).
- [5] B. B. Back, “Complete fusion and quasifission in reactions between heavy ions,” *Physical Review C*, **31**, 2104, (1985).
- [6] V. Zagrebaev, Y. Aritomo, M. Itkis, Y. Oganessian, and M. Ohta, “Synthesis of superheavy nuclei: How accurately can we describe it and calculate the cross sections?,” *Physical Review C*, **65**, 014607, (2001).
- [7] A. C. Berriman, D. J. Hinde, M. Dasgupta, C. R. Morton, R. D. Butt, and J. O. Newton, “Unexpected inhibition of fusion in nucleus-nucleus collisions.,” *Nature*, **413**, 144, (2001).
- [8] R. Yanez, W. Loveland, J. S. Barrett, L. Yao, B. B. Back, S. Zhu, and T. L. Khoo, “Measurement of the fusion probability, P_{CN} , for hot fusion reactions,” *Physical Review C*, **88**, 014606, (2013).
- [9] R. Bass, “Nucleus-Nucleus Potential Deduced from Experimental Fusion Cross Sections,” *Phys. Rev. Lett.*, **39**, 265, (1977).

- [10] K. Hammerton, Z. Kohley, D. J. Hinde, M. Dasgupta, A. Wakhle, E. Williams, V. E. Oberacker, A. S. Umar, I. P. Carter, K. J. Cook, J. Greene, D. Y. Jeung, D. H. Luong, S. D. Mcneil, C. S. Palshetkar, D. C. Rafferty, C. Simenel, and K. Stiefel, “Reduced quasifission competition in fusion reactions forming neutron-rich heavy elements,” *Physical Review C*, **91**, 041602(R) (2015).
- [11] Y. T. Oganessian, F. S. Abdullin, P. D. Bailey, D. E. Benker, M. E. Bennett, S. N. Dmitriev, J. G. Ezold, J. H. Hamilton, R. A. Henderson, M. G. Itkis, Y. V. Lobanov, a. N. Mezentsev, K. J. Moody, S. L. Nelson, A. N. Polyakov, C. E. Porter, A. V. Ramayya, F. D. Riley, J. B. Roberto, M. A. Ryabinin, K. P. Rykaczewski, R. N. Sagaidak, D. A. Shaughnessy, I. V. Shirokovsky, M. A. Stoyer, V. G. Subbotin, R. Sudowe, A. M. Sukhov, Y. S. Tsyganov, V. K. Utyonkov, A. A. Voinov, G. K. Vostokin, and P. A. Wilk, “Synthesis of a New Element with Atomic Number $Z=117$,” *Physical Review Letters*, **104**, 142502, (2010).
- [12] K. Morita, K. Morimoto, D. Kaji, T. Akiyama, S.-I. Goto, H. Haba, E. Ideguchi, R. Kanungo, K. Katori, H. Koura, H. Kudo, T. Ohnishi, A. Ozawa, T. Suda, K. Sueki, H. Xu, T. Yamaguchi, A. Yoneda, A. Yoshida, and Y. Zhao, “Experiment on the Synthesis of Element 113 in the Reaction,” *Journal of the Physical Society of Japan*, **72**, 2593, (2004).
- [13] Y. T. Oganessian, “Synthesis of the heaviest elements in 48 Ca-induced reactions,” *Radiochimica Acta*, **99**, 429, (2011).
- [14] Y. T. Oganessian, V. K. Utyonkov, Y. V. Lobanov, F. S. Abdullin, A. N. Polyakov, I. V. Shirokovsky, Y. S. Tsyganov, G. G. Gulbekian, S. L. Bogomolov, A. N. Mezentsev, S. Iliev, V. G. Subbotin, A. M. Sukhov, A. A. Voinov, G. V. Buklanov, K. Subotic, V. I. Zagrebaev, M. G. Itkis, J. B. Patin, K. J. Moody, J. F. Wild, M. A. Stoyer, N. J. Stoyer, D. A. Shaughnessy, J. M. Kenneally, and R. W. Lougheed, “Experiments on the synthesis of element 115 in the reaction $^{243}\text{Am}(^{48}\text{Ca}, xn)^{291-x}115$ x,” *Physical Review C*, **69**, 021601(R), (2004).
- [15] Y. T. Oganessian, V. K. Utyonkov, Y. V. Lobanov, F. S. Abdullin, A. N. Polyakov, R. N. Sagaidak, I. V. Shirokovsky, Y. S. Tsyganov, A. A. Voinov, G. G. Gulbekian, S. L. Bogomolov, B. N. Gikal, A. N. Mezentsev, S. Iliev, V. G. Subbotin, A. M. Sukhov, K. Subotic, V. I. Zagrebaev, G. K. Vostokin, M. G. Itkis, K. J. Moody, J. B. Patin, D. A. Shaughnessy, M. A. Stoyer, N. J. Stoyer, P. A. Wilk, J. M. Kenneally, J. H. Landrum, J. F. Wild, and R. W. Lougheed, “Synthesis of the isotopes of elements 118 and 116 in the ^{249}Cf and $^{245}\text{Cm}+^{28}\text{Ca}$ fusion reactions,” *Physical Review C*, **74**, 044602, (2006).
- [16] Y. T. Oganessian, Y. P. Tret'yakov, A. S. Il'inov, A. G. Demin, A. A. Pleve, S. P. Tret'yakov, V. M. Plotko, M. P. Ivanov, N. A. Danilov, Y. S. Korotkin, and G. N.

- Flerov, "Synthesis of neutron-deficient isotopes of fermium, kurchatovium, and element 106," *Journal of Experimental and Theoretical Physics Letters*, **20**, 265, (1974).
- [17] Y. Oganessian, A. Demin, A. Iljinov, S. Tretyakova, A. Pleve, Y. Penionzhkevich, M. Ivanov, and Y. Tretyakov, "Experiments on the synthesis of neutron-deficient kurchatovium isotopes in reactions induced by ^{50}Ti Ions," *Nuclear Physics A*, **239**, 157, (1975).
- [18] Y. Oganessian and V. Utyonkov, "Superheavy nuclei from ^{48}Ca -induced reactions," *Nuclear Physics A*, **944**, 62-98, (2015).
- [19] V. I. Zagrebaev, A. V. Karpov, and W. Greiner, "Possibilities for synthesis of new isotopes of superheavy elements in fusion reactions," *Physical Review C*, **85**, 014608, (2012).
- [20] A. J. B. Roberto, C. W. Alexander, R. A. Boll, J. D. Burns, J. G. Ezold, L. K. Felker, S. L. Hogle, and K. P. Rykaczewski, "Actinide targets for the synthesis of super-heavy elements," *Nuclear Physics A*, **944**, 99, (2015).
- [21] A. Sobiczewski, F. A. Gareev, and Kalinkin B N, "Closed Shells for $Z>82$ and $N>126$ in a Diffuse Potential Well," *Physics Letters*, **22**, 500, (1966).
- [22] M. Bender, K. Rutz, P.-G. Reinhard, J. A. Maruhn, and W. Greiner, "Shell structure of superheavy nuclei in self-consistent mean-field models," *Physical Review C*, **60**, 034304 (1999).
- [23] M. Bender, W. Nazarewicz, and P.-G. Reinhard, "Shell stabilization of super-and hyperheavy nuclei without magic gaps," *Physics Letters B*, **515**, 42, (2001).
- [24] W. Nazarewicz, M. Bender, S. Cwiok, P. H. Heenen, A. T. Kruppa, P.-G. Reinhard, and T. Vertse, "Theoretical description of superheavy nuclei," *Nuclear Physics A*, **701**, 165, (2002).
- [25] S. Hofmann, "Particle and Synthesis of Superheavy Elements Using Radioactive Beams and ' Targets Decay properties of SHE ' s," *Progress in Particle and Nuclear Physics*, **46**, 293, (2001).
- [26] National Research Council, "Scientific Opportunities with a Rare-Isotopes Facility in the United States," National Academic Press, Washington, DC, (2007).
- [27] National Research Council, "Nuclear Physics: Exploring the Heart of Matter," Decadal Survey of Nuclear Physics by the National Research Council, (2013).

- [28] Nuclear Science Advisory Committee, “The Frontiers of Nuclear Science: A Long Range Plan,” (2007).
- [29] W. Loveland, “Synthesis of transactinide nuclei using radioactive beams,” *Physical Review C*, **76**, 014612, (2007).
- [30] S. Bjørnholm and W. J. Swiatecki, “Dynamicsl aspects of nucleus-nucleus collisions,” *Nuclear Physics A*, **391**, 471, (1982).
- [31] R. K. Puri, M. K. Sharma, R. K. Gupta, and P. Schuck, “Isotopic dependence of fusion cross-sections – linear relationships,” *European Physics Journal A*, **3**, 277, (1998).
- [32] W. U. Schroeder and J. R. Huizenga, *Treatise on Heavy Ion Science*. New York: Plenum, vol. 2 ed., (1984).
- [33] R. Bass, *Nuclear Reactions with Heavy Ions*. Berlin: Springer, (1980).
- [34] R. Bass, “Threshold and Angular Momentum Limit in Complete Fusion of Heavy Ions,” *Physics Letters B*, **47**, 139, (1973Z).
- [35] R. Bass, “Fusion of Heavy Nuclei in a Classical Model,” *Nuclear Physics A*, **231**, 45, (1974).
- [36] V. Zagrebaev and W. Greiner, “Synthesis of superheavy nuclei: A search for new production reactions,” *Physical Review C*, **78**, 034610, (2008).
- [37] C. F. Weizsacker, “Zur Theorie der Kernmassen,” *Zeitschrift für Physik*, **96**, 431, (1935).
- [38] J. P. Blocki, H. Feldmeier, and W. J. Swiatecki, “Dynamical hinderance to compound-nucleus formation in heavy-ion reactions,” *Nuclear Physics A*, **459**, 145, (1986).
- [39] D. J. Hinde, R. du Rietz, M. Dasgupta, R. Thomas, and L. Gasques, “Two Distinct Quasifission Modes in the $^{32}\text{S}+^{232}\text{Th}$ Reaction,” *Physical Review Letters*, **101**, 092701, (2008).
- [40] R. du Rietz, E. Williams, D. J. Hinde, M. Dasgupta, M. Evers, C. J. Lin, D. H. Luong, C. Simenel, and A. Wakhle, “Mapping quasifission characteristics and timescales in heavy element formation reactions,” *Physical Review C*, **88**, 054618, (2013).

- [41] D. J. Hinde, M. Dasgupta, J. Leigh, J. Mein, C. Morton, J. Newton, and H. Timmers, “Conclusive evidence for the influence of nuclear orientation on quasifission,” *Physical review C: Nuclear physics*, **53**, 1290, (1996).
- [42] E. Prokhorova, A. A. Bogachev, M. Itkis, I. Itkis, G. Knyazheva, N. Kondratiev, E. Kozulin, L. Krupa, Y. Oganessian, I. Pokrovsky, V. Pashkevich, and A. Rusanov, “The fusion-fission and quasi-fission processes in the reaction $^{48}\text{Ca} + ^{208}\text{Pb}$ at energies near the Coulomb barrier,” *Nuclear Physics A*, **802**, 45, (2008).
- [43] E. Williams, D. J. Hinde, M. Dasgupta, R. du Rietz, I. P. Carter, M. Evers, D. H. Luong, S. D. McNeil, D. C. Rafferty, K. Ramachandran, and A. Wakhle, “Evolution of signatures of quasifission in reactions forming curium,” *Physical Review C*, **88**, 034611, (2013).
- [44] I. M. Itkis, E. M. Kozulin, M. G. Itkis, G. N. Knyazheva, A. A. Bogachev, E. V. Chernysheva, L. Krupa, Y. T. Oganessian, V. I. Zagrebaev, a. Y. Rusanov, F. Goennenwein, O. Dorvaux, L. Stuttgé, F. Hanappe, E. Vardaci, and E. de Goés Brennard, “Fission and quasifission modes in heavy-ion-induced reactions leading to the formation of Hs*,” *Physical Review C*, **83**, 064613, (2011).
- [45] M. G. Itki, J. Aystob, S. Beghini, A. A. Bogache, L. Corradid, M. G. Itkis, J. Aystob, S. Beghini, A. A. Bogachev, L. Corradi, O. Dorvaux, A. Gadea, G. Giardina, F. Hanappe, I. M. Itkis, M. Jandel, J. Kliman, S. V. Khlebnikov, G. N. Kniajeva, N. A. Kondratiev, E. M. Kozulin, L. Krupa, A. Latina, T. Materna, G. Montagnoli, Y. T. Oganessian, Pokrovsky. I. V., E. V. Prokhorova, N. Rowley, V. A. Rubchenya, A. Y. Rusanov, R. N. Sagaidak, F. Scarlassara, A. M. Stefanini, L. Stuttge, S. Szilner, M. Trotta, W. H. Trzaska, D. N. Vakhutin, A. M. Vinodkumar, V. M. Voskressenski, and V. I. Zagrebaev, “Shell effects in fission and quasi-fission of heavy and superheavy nuclei,” *Nuclear Physics*, **734**, 136–147, (2004).
- [46] C. J. Lin, R. du Rietz, D. J. Hinde, M. Dasgupta, R. G. Thomas, M. L. Brown, M. Evers, L. R. Gasques, and M. D. Rodriguez, “Systematic behavior of mass distributions in ^{48}Ti -induced fission at near-barrier energies,” *Physical Review C*, **85**, 014611, (2012).
- [47] A. Wakhle, “Experimental and Theoretical Studies of Quasifission”, PhD thesis, The Australia National University, (2013).
- [48] L. J. Colby, Jr., M. L. Shoaf, and J. W. Cobble, “Helium-Induced Fission Cross Sections of U^{233} and U^{238} and Nuclear Radii of Heavy Elements”, *Physical Review*, **121**, 1415, (1961).

- [49] K. F. Flynn and L. E. Glendenin, ‘*Rep. ANL-7749* Argonne National Laboratory, Argonne, Illinois (1970).
- [50] I. V. Ryzhov, S. G. Yavshits, G. A. Tutin, N. V. Kovalev, A. V. Saulski, N. A. Kudryashev, M. S. Onegin, L. A. Vaishnena, Yu. A. Gavrikov, O. T. Grudzevich, V. D. Simutkin, S. Pomp, J. Blomgren, M. Österlund, P. Andersson, R. Bevilacqua, J. P. Meulders, and R. Prieels, “Fragment-mass distributions in neutron-induced fission of ^{232}Th and ^{238}U at 33, 45, and 60 MeV”, *Physical Review C*, **83**, 054603, (2011).
- [51] R. Vandenbosch and J. R. Huizenga, “Nuclear Fission,” pp. 111–112, (1973).
- [52] J. A. Wheeler, “Channel Analysis of Fission,” in *Fast Neutron Physics* (J. B. Marion and J. L. Fowler, eds.), New York: Wiley, (1963).
- [53] G. E. Gordon, A. E. Larsh, T. Sikkeland, and G. T. Searorg, “Fission of Gold by Carbon Ions*,” *Physical Review*, **120**, 1341, (1960).
- [54] B. B. Back, R. R. Betts, J. E. Gindler, B. D. Wilkins, S. Saini, M. B. Tsang, C. K. Gelbke, L. W. G, M. A. McMahan, and P. A. Baisden, “Angular distributions in heavy-ion-induced fission,” *Physical Review C*, **32**, 195, (1985).
- [55] M. B. Tsang, H. Utsunomiya, C. K. Gelbke, W. G. Lynch, B. B. Back, S. Saini, P. A. Baisden, and M. A. McMahan, “Energy Dependence of Fission Fragment Angular Distributions for ^{19}F , ^{24}Mg , and ^{28}Si Induced Reactions on ^{208}Pb ,” *Physics Letters*, **129**, 18, (1983).
- [56] R. Bock, Y. T. Chu, A. Gobbi, E. Grosse, A. Olmi, H. Sann, D. Schwalm, U. Lynen, H. Esbensen, W. Wulfli, and E. Morenzoni, “Dynamics of the fusion process,” *Nuclear Physics A*, **388**, 334, (1982).
- [57] A. Heinz, K.-H. Schmidt, A. R. Junghans, P. Armbruster, J. Benlliure, C. Böckstiegel, H.-G. Clerc, A. Grewe, M. De Jong, J. Müller, M. Pfützner, S. Steinhäuser, and B. Voss, “Electromagnetic-induced fission of ^{238}U projectile fragments, a test case for the production of spherical super-heavy nuclei,” *Nuclear Physics A*, **713**, 3, (2003).
- [58] M. Dasgupta, D. J. Hinde, N. Rowley, and A. M. Stefanini, “Measuring Barriers to Fusion,” *Annual Review of Nuclear and Particle Science*, **48**, 401, (1998).
- [59] D. J. Hinde, M. Dasgupta, B. Fulton, C. Morton, R. Wooliscroft, A. Berriman, and K. Hagino, “Fusion Suppression and Sub-Barrier Breakup of Weakly Bound Nuclei,” *Physical Review Letters*, **89**, 272701, (2002).

- [60] D. J. Hinde, M. Dasgupta, J. Leigh, J. P. Lestone, J. Mein, C. R. Morton, J. O. Newton, and H. Timmers, “Fusion-Fission versus Quasifission: Effect of Nuclear Orientation,” *Physical Review Letters*, **4**, 1295, (1995).
- [61] J. Leigh, M. Dasgupta, D. J. Hinde, J. Mein, C. R. Morton, R. C. Lemmon, J. P. Lestone, J. O. Newton, H. Timmers, J. X. Wei, and N. Rowley, “Barrier distributions from the fusion of oxygen ions with $^{144,148,154}\text{Sm}$ and ^{186}W ,” *Physical Review C*, **52**, 3151, (1995).
- [62] S. Mitsuoka, H. Ikezoe, K. Nishio, K. Satou, and J. Lu, “Effects of neutron number and nuclear deformation on complete fusion of $^{60,64}\text{Ni}+^{154}\text{Sm}$ near the Coulomb barrier,” *Physical Review C*, **65**, 054608, (2002).
- [63] K. Nishio, H. Ikezoe, S. Mitsuoka, K. Satou, and S. C. Jeong, “Effects of nuclear deformation on fusion probability in the reactions of $^{82}\text{Se}+^{\text{nat}}\text{Ce}$ and $^{76}\text{Ge}+^{150}\text{Nd}$ near the Coulomb barrier,” *Physical Review C*, **63**, 044610, (2001).
- [64] R. Rafiei, R. G. Thomas, D. J. Hinde, M. Dasgupta, C. R. Morton, L. R. Gasques, M. L. Brown, and M. D. Rodriguez, “Strong evidence for quasifission in asymmetric reactions forming ^{202}Po ,” *Physical Review C*, **77**, 024606, (2008).
- [65] R. Thomas, D. J. Hinde, D. Duniec, F. Zenke, M. Dasgupta, M. Brown, M. Evers, L. Gasques, M. Rodriguez, and A. Diaz-Torres, “Entrance channel dependence of quasifission in reactions forming ^{220}Th ,” *Physical Review C*, **77**, 034610, (2008).
- [66] Y. X. Watanabe, A. Yoshida, T. Fukuda, T. Sekine, Y. Watanabe, H. Ikezoe, Y. Nagame, and T. Ikuta, “Measurement of fusion excitation functions of $^{(27,29,31)}\text{Al} + ^{197}\text{Au}$,” *The European Physical Journal A*, **379**, 373, (2001).
- [67] W. Loveland, D. Peterson, A. Vinodkumar, P. Sprunger, D. Shapira, J. Liang, G. Souliotis, D. Morrissey, and P. Lofy, “Fusion enhancement in the $^{38}\text{S}+^{208}\text{Pb}$ reaction,” *Physical Review C*, **74**, 044607, (2006).
- [68] K. Zyromski, W. Loveland, G. Souliotis, D. Morrissey, C. Powell, O. Batenkov, K. Aleklett, R. Yanez, and I. Forsberg, “Fusion enhancement in the $^{32,38}\text{S}+^{181}\text{Ta}$ reaction,” *Physical Review C*, **63**, 024615, (2001).
- [69] Y. Ts Oganessian, V. K. Utyonkov, Y. V. Lobanov, F. Sh Abdullin, A. N. Polyakov, I. V. Shirokovsky, Y. S. Tsyganov, A. N. Mezentsev, S. Iliev, V. G. Subbotin, A. M. Sukhov, K. Subotic, O. V. Ivanov, A. N. Voinov, V. I. Zagrebaev, K. J. Moody, J. F. Wild, N. J. Stoyer, M. A. Stoyer, and R. W. Lougheed, “Measurements of cross sections for the fusion-evaporation reactions $^{204,206,207,208}\text{Pb} + ^{48}\text{Ca}$ and $^{207}\text{Pb}+^{34}\text{S}$: Decay

- properties of the even-even nuclides ^{238}Cf and ^{250}No ,” *Physical Review C*, **64**, 054606, (2001).
- [70] Y. TS. Oganessian, V. K. Utyonkov, F. S. Abdullin, S. N. Dmitriev, R. Graeger, R. a. Henderson, M. G. Itkis, Y. V. Lobanov, a. N. Mezentsev, K. J. Moody, S. L. Nelson, A. N. Polyakov, M. A. Ryabinin, R. N. Sagaidak, D. A. Shaughnessy, I. V. Shirokovsky, M. A. Stoyer, N. J. Stoyer, V. G. Subbotin, K. Subotic, A. M. Sukhov, Y. S. Tsyganov, A. Türler, A. A. Voinov, G. K. Vostokin, P. A. Wilk, and A. Yakushev, “Synthesis and study of decay properties of the doubly magic nucleus ^{270}Hs in the $^{226}\text{Ra}+^{48}\text{Ca}$ reaction,” *Physical Review C*, **87**, 034605, (2013).
- [71] W. J. Swiatecki, “The Dynamics of the Fusion of two Nuclei,” *Nuclear Physics A*, **376**, 275, (1982).
- [72] J. F. Liang, C. J. Gross, Z. Kohley, D. Shapira, R. L. Varner, J. M. Allmond, A. L. Caraley, K. Lagergren, and P. E. Mueller, “Fusion probability for neutron-rich radioactive-Sn-induced reactions,” *Physical Review C*, **85**, 031601, (2012).
- [73] C. C. Sahm, H. G. Clerc, K. H. Schmidt, W. Reisdorf, P. Armbruster, F. P. Hessberger, J. G. Keller, G. Munzenberg, and D. Vermeulen, “Fusion probability of symmetric heavy, nuclear systems determined from evaporation-residue cross sections*,” *Nuclear Physics A*, **441**, 316, (1985).
- [74] K. T. Lesko, W. Henning, K. E. Rehm, G. Rosner, J. P. Schiffer, G. S. F. Stephans, B. Zeidman, and S. Freeman, “Fission following fusion of Ni+Sn,” *Physical Review C*, **34**, 2155, (1986).
- [75] A. Vinodkumar, W. Loveland, J. Neeway, L. Prissbrey, P. Sprunger, D. Peterson, J. Liang, D. Shapira, C. Gross, R. Varner, J. Kolata, A. Roberts, and A. Caraley, “ $^{132}\text{Sn}+^{96}\text{Zr}$ reaction: A study of fusion enhancement/hindrance,” *Physical Review C*, **78**, 054608, (2008).
- [76] C. Wang, J. Zhang, Z. Z. Ren, and C. W. Shen, “How the projectile neutron number influences the evaporation cross section in complete fusion reactions with heavy ions,” *Physical Review C*, **82**, 054605, (2010).
- [77] G. G. Adamian, N. V. Antonenko, and W. Scheid, “Characteristics of quasifission products within the dinuclear system model,” *Physical Review C*, **68**, 034601, (2003).
- [78] N. Antonenko, E. Cherepanov, A.K. Nasirov, V. Permjakov, and V. Volkov, “Competition between complete fusion and quasi-fission in reactions between massive nuclei. The fusion barrier,” *Physics Letters B*, **319**, 425, (1993).

- [79] N. V. Antonenko, E. A. Cherepanov, A. K. Nasirov, V. P. Permjakov, and V. V. Volkov, “Carnpaund nucleus forxnatian in reactions between massive nuclei: Fusion barrier,” *Physical Review C*, **51**, 2635, (1995).
- [80] D. J. Hinde, M. Dasgupta, and A. Mukherjee, “Severe Inhibition of Fusion by Quasi-fission in Reactions Forming ^{220}Th ,” *Physics Review Letters*, **89**, 282701, (2002).
- [81] A. Y. Chizhov, M. G. Itkis, I. M. Itkis, G. N. Kniajeva, E. M. Kozulin, N. A. Kondratiev, I. V. Pokrovsky, R. N. Sagaidak, V. M. Voskressensky, A. V. Yerebin, L. Corradi, A. Gadea, A. Latina, A. M. Stefanini, S. Szilner, M. Trotta, A. M. Vinodkumar, S. Beghini, G. Montagnoli, F. Scarlassara, A. Ya Rusanov, F. Hanappe, O. Dorvaux, N. Rowley, and L. Stuttgé, “Unexpected entrance-channel effect in the fission of $^{216}\text{Ra}^*$,” *Physical Review C*, **67**, 011603(R), (2003).
- [82] M. Itkis, A. A. Bogachev, I. Itkis, J. Kliman, G. Knyazheva, N. Kondratiev, E. Kozulin, L. Krupa, Y. Oganessian, I. Pokrovsky, E. Prokhorova, and A. Rusanov, “The processes of fusion-fission and quasi-fission of superheavy nuclei,” *Nuclear Physics A*, **787**, 150, (2007).
- [83] C. Simenel, D. J. Hinde, R. du Rietz, M. Dasgupta, M. Evers, C. Lin, D. Luong, and A. Wakhle, “Influence of entrance-channel magicity and isospin on quasi-fission,” *Physics Letters B*, **710**, 607, (2012).
- [84] J. P. Greene and Z. Kohley, “Isotopic Tungsten Targets,” *Journal of Radioanalytical and Nuclear Chemistry*, **305**, 743, (2015).
- [85] J. K. Tuli, “Nuclear Wallet Cards,” (2011).
- [86] P. Möller, J. R. Nix, W. D. Myers, and W. J. Swiatecki, “Nuclear Ground-State Masses and Deformations,” *Atomic Data and Nuclear Data Tables*, **59**, 185, (1995).
- [87] A. Wakhle, C. Simenel, D. J. Hinde, M. Dasgupta, M. Evers, D. H. Luong, R. du Rietz, and E. Williams, “Interplay between Quantum Shells and Orientation in Quasifission,” *Physical Review Letters*, **113**, 182502, (2014).
- [88] O. B. Tarasov and D. Bazin, “Development of the program LISE: application to fusion-evaporation,” *Nuclear Instruments and Methods in Physics Research, B*, **204**, 174, (2003).
- [89] R. Middleton and C. T. Adams, “A close to universal negative ion source,” *Nuclear Instruments and Methods*, **118**, 329, (1974).

- [90] R. Middleton, "A Negative-Ion Cookbook," University of Pennsylvania, Philadelphia, (1990).
- [91] D. A. Bromley, "The development of electrostatic accelerators," *Nuclear Instruments and Methods*, **122**, 1, (1974).
- [92] R. G. Herb, "Pelletron accelerators for very high voltage," *Nuclear Instruments and Methods*, **122**, 267, (1974).
- [93] T. R. Ophel, J. S. Harrison, J. O. Newton, R. H. Spear, E. W. Titterton, and D. C. Weisser, "The 14UD pelletron accelerator at the Australian National University," *Nuclear Instruments and Methods*, **122**, 227, (1974).
- [94] R. Middleton, "A survey of negative ion sources for tandem accelerators," *Nuclear Instruments and Methods*, **122**, 35, (1974).
- [95] R. Middleton, "A Versatile High Intensity Negative Ion Source," *Nuclear Instruments and Methods*, **214**, 139, (1983).
- [96] A. B. Wittkower and H. D. Betz, "Equilibrium-charge-state distributions of energetic ions ($Z > 2$) ion gaseous and solid media*," *Atomic Data and Nuclear Data Tables*, **5**, 113, (1973).
- [97] V. S. Nikolaev and I. S. Dmitriev, "On the Equilibrium Charge Distributions in Heavy Element Beams," *Physics Letters A*, **28**, 277, (1968).
- [98] J. L. Yntema, "Heavy Ion Stripping in Tandem Accelerator Terminals," *Nuclear Instruments and Methods*, **122**, 45, (1974).
- [99] G. Charpak, R. Bouclier, T. Bressani, J. Favier, and C. Zupancic, "The use of multiwire proportional counters to select and localize charged particles," *Nuclear Instruments and Methods*, **62**, 262, (1968).
- [100] G. Charpak, F. Sauli Cern, and G. Switzerland, "Multiwire proportional chambers and drift chambers," *Nuclear Instruments and Methods*, **162**, 405, (1979).
- [101] R. Fourme, "Position-sensitive gas detectors: MWPCs and their gifted descendants," *Nuclear Instruments and Methods in Physics Research A*, **392**, 1, (1997).
- [102] G. F. Knoll, *Radiation Detection and Measurement*. Hoboken, NJ: Wiley, 4th ed., (2010).

- [103] D. J. Hinde, *Private Communication*. (2016).
- [104] R. Brun and F. Rademakers, “ROOT– An object oriented data analysis framework,” *Nuclear Instruments and Methods in Physics Research Section A: Accelerators, Spectrometers, Detectors and Associated Equipment*, **389**, 81, (1997).
- [105] R. du Rietz, D. J. Hinde, M. Dasgupta, R. G. Thomas, L. R. Gasques, M. Evers, N. Lobanov, and A. Wakhle, “Predominant Time Scales in Fission Processes in Reactions of S, Ti and Ni with W: Zeptosecond versus Attosecond,” *Physical Review Letters*, **106**, 052701, (2011).
- [106] D. Y. Jeung, E. Williams, D. J. Hinde, M. Dasgupta, R. Du Rietz, M. Evers, C. J. Lin, D. H. Luong, C. Simenel, and A. Wakhle, “Dynamical approach to heavy ion-induced fission,” *European Physics Journal Web of Conferences*, **91**, 5, (2015).
- [107] V. E. Viola, “Correlation of fission fragment kinetic energy data,” *Nuclear Data Tables A*, **1**, 391, (1966).
- [108] V. E. Viola, M. Walker, and K. Kwiatkowski, “Systematics of Fission Fragment Total Kinetic Energy Release,” *Physical Review C* **31**, 1550, (1985).
- [109] M. G. Itkis and A. Y. Rustamov, “The fission of heated nuclei in reactions involving heavy ions: static and dynamical aspects,” *Physics of particles and nuclei*, **29**, 160, (1998).
- [110] I. V. Pokrovsky, L. Calabretta, M. G. Itkis, N. A. Kondratiev, E. M. Kozulin, C. Maiolino, E. V. Prokhorova, A. Y. Rusanov, and S. P. Tretyakova, “Three fission modes of ^{220}Ra ,” *Physical Review C*, **60**, 041304(R), (1999).
- [111] K. Hagino, N. Rowley, and a.T. Kruppa, “A program for coupled-channel calculations with all order couplings for heavy-ion fusion reactions,” *Computer Physics Communications*, **123**, 143, (1999).
- [112] K. Hagino and N. Takigawa, “Subbarrier Fusion Reactions and Many-Particle Quantum Tunneling,” *Progress of Theoretical Physics*, **128**, 1001, (2012).
- [113] N. Bohr, “Neutron Capture and Nuclear Constitution,” *Nature*, **137**, 344, (1936).
- [114] C. Simenel and A. S. Umar, “Formation and dynamics of fission fragments,” *Physical Review C*, **89**, 031601, (2014).

- [115] V. E. Oberacker, A. S. Umar, and C. Simenel, “Dissipative dynamics in quasifission,” *Physical Review C*, **90**, 054605, (2014).
- [116] A.S. Umar and V. Oberacker, “Time-dependent HF approach to SHE dynamics,” *Nuclear Physics A*, **944**, 238, (2015).
- [117] A.S. Umar and V. Oberacker, “Three-dimensional unrestricted time-dependent Hartree-Fock fusion calculations using the full Skyrme interaction,” *Physical Review C*, **73**, 054607, (2006).
- [118] V. Zagrebaev and W. Greiner, “Unified consideration of deep inelastic, quasi-fission and fusion-fission phenomena,” *Journal of Physics G: Nuclear and Particle Physics*, **31**, 825, (2005).
- [119] P. Armbruster, “Nuclear structure in cold rearrangement processes in fission and fusion,” *Reports on Progress in Physics*, **62**, 465, (1999).
- [120] K. Siwek-Wilczyńska, A. Borowiec, I. Skwira-Chalot, and J. Wilczyński, “Entrance channel effects in suppression of fusion of heavy nuclei,” *International Journal of Modern Physics E*, **17**, 12, (2008).
- [121] D. J. Hinde, M. Dasgupta, N. Herrald, R. G. Neilson, J. O. Newton, and M. A. Lane, “Isotopic dependence of fusion barrier energies in reactions forming heavy elements,” *Physical Review C*, **75**, 1, (2007).
- [122] D. J. Hinde and M. Dasgupta, “A new framework to investigate the systematics of fusion probabilities in heavy element formation: Application to Th isotopes.” *Physics Letters B*, **622**, 23 (2005).
- [123] A. Wakhle, W. Loveland, D. Morrissey, K. Hammerton, K. Stiefel, and R. Yanez, *In Preparation*, 2017.
- [124] A. Wakhle, K. Hammerton, Z. Kohley, and J. Yurkon, *In Preparation*, 2017.